Soil gas analytics in geothermal exploration and monitoring

kumulative Dissertation von
M. Sc.
Anna Jentsch

an der Mathematisch-Naturwissenschaftlichen Fakultät in der
Wissenschaftsdisziplin Geowissenschaften
der Universität Potsdam und dem deutschen GeoForschungsZentrum
GFZ Potsdam in der Sektion 4.8 Geoenergie
zur Erlangung des Akademischen Grades

Doctor rerum naturalium
-Dr. rer. nat.-

Potsdam 2021

Supervisor:	Prof. Dr. Uwe Altenberger
Supervisor:	Dr. Egbert Jolie
Referee:	Prof. Dr. Uwe Altenberger
Referee:	Dr. Egbert Jolie
Referee:	Dr. Maren Brehme
Date of PhD defense:	10th December 2021

https://doi.org/10.25932/publishup-54403
https://nbn-resolving.org/urn:nbn:de:kobv:517-opus4-544039

Life is in flux

Acknowledgements

It’s a long, long, long way... it was a long way, that I would not have been able to travel without the many dear people by my side.

This list is by no means complete and the order of people mentioned does not make them less or more important.

I am very grateful for having had the chance to start my journey as a young researcher in section 4.8 Geoenergy at the German Research centre for Geosciences, long before I got the opportunity to write this PhD thesis. I thank Ernst and David, who first hired me as a research assistant and then offered me a PhD position. You are by far the most supportive, calm, open-minded seniors I have met.

I am greatly thankful to Egbert Jolie. You already guided and mentored me during my master thesis and you continued to do so with unconditional support during my time as a PhD student. Thank you for your trust and open ear during the times when things did not look so ’rosy’. You definitely got to know me in my good, my bad, my excited, my disappointed, and my sad times. I am very much looking forward to continue our collaboration, which is build on trust, respect, appreciation and the common pursuit of a goal developed over the past years.

Also, I would like to express my gratitude to my Professor Uwe Altenberger who has been accompanying me since I started studying at the University of Potsdam. You definitely join the group of people who have given me a lot of confidence and support whenever it was needed. Despite the many commitments, you always keep a cool head and you are a very positive person.

My GFZ colleagues Tania, Katrin, Kemal, Henning, and Stefan. Without you, my days at work would have not been the same. You all listened to my ideas, doubts, and motivated me to keep on going. I appreciate the innumerable creative discussions about work and life. I am happy to consider you not only colleagues but also my friends.

Thanks also to everyone else from section 4.8 for providing an enjoyable and warm work environment throughout the past years I have spent with you.

This PhD thesis heavily relied on field- and maintenance work as without these there would have been no data to work with. Many thanks to the local partners from Mexico, Ethiopia, and New Zealand for logistical and organisational support during field work. Also, I would like to express my gratitude to the many students and technicians for their continuous and unresting dedication in supporting my fieldwork.

Thanks to the GFZ for the opportunities to exchange knowledge, share ideas, and have access to a great research infrastructure. Riding my bike up to the Telegrafenberg and arriving at this forested and quiet workplace is definitely a good way to start your day.

My deepest gratitude goes to my family and friends. Thank you for ALWAYS being there for me. I am blessed to be surrounded by such amazing people in my life with whom I can share my passion for science but who also inspire me on so many other levels. Each and every one of you contributed to this work and without you I would never have finished it. To Muuts, Maria, and Omi. You are the women in my life that I look up to and who have always believed in me. Thank you.

Zusammenfassung

Zu den großen Herausforderungen bei der Erkundung und Nutzung geothermischer Ressourcen, gehören die strukturgeologische Charakterisierung eines geothermischen Systems sowie die Anwendung nachhaltiger Überwachungskonzepte, um Veränderungen im geothermischen Reservoir während der Förderung und/oder Injektion von Fluiden zu verstehen. Bei unzureichender Permeabilität des Reservoirgesteins stellen Verwerfungen und Kluftnetzwerke bevorzugte Bohrziele dar, da sie potentielle Wegsamkeiten für heiße und/oder kalte Fluide sind. Entlang dieser fluidführenden Strukturen können in vulkanisch-geothermischen Systemen auch erhebliche Mengen an Gasemissionen an der Erdoberfläche freigesetzt werden.

Im Rahmen dieser Arbeit wurden verschiedene methodische Ansätze und Messkonzepte entwickelt und getestet, um die räumliche und zeitliche Variation verschiedener Bodengasparameter zu bestimmen und diese im Kontext struktureller Permeabilitäten zu interpretieren. Um das Potential der Bodengasanalytik als innovative geothermische Explorations- und Überwachungsmethode zu validieren, wurden die methodischen Ansätze auf drei verschiedene vulkanisch-geothermische Systeme angewendet. Diesbezüglich wurde für jeden Standort ein individueller Messansatz hinsichtlich der bekannten strukturgeologischen Merkmale und standortspezifischen Fragestellung entwickelt.

Die erste Studie präsentiert Ergebnisse aus der kombinierten Messung des CO_2-Flusses, der Bodentemperatur und der Analyse von Isotopenverhältnissen ($\delta^{13}C_{CO2}$, $^3He/^4He$), welche systematisch und flächendeckend in der geothermischen Produktionszone des Geothermalfeldes Los Humeros, Mexiko, gemessen wurden. Ziel war es, Bereiche mit einer Verbindung zum überkritischen ($T > 374°C$ and $P > 221$ bar) und bisher noch ungenutzten geothermischen Reservoir zu identifizieren. Das mit großem Punktabstand und systematisch generierte Messnetz (25 x 200 m) für die Bestimmung des CO_2-Flusses erwies sich als schnelle und flexible Anwendung zur Identifizierung von Gebieten mit anomaler CO_2-Entgasung. Basierend auf diesen Ergebnissen wurde anschließend mit geringeren Messabständen die genaue Ausdehnung und das heterogene Muster der anomalen Entgasungsgebiete aufgelöst. Dadurch war es möglich, die Entgasungsmuster mit der internen strukturgeologischen Heterogenität einzelner Störungssegmente in Verbindung zu bringen, wodurch Bereiche, die den Gasfluss besonders begünstigen, wie z.B. Störungsschnittpunkte, ermittelt werden konnten. Schließlich wurden vorher unbekannte, geothermisch interessante Bereiche, die eine erhöhte strukturelle Permeabilität aufweisen und eine Verbindung zum überkritischen Reservoir darstellen, identifiziert. Diese Bereiche gelten als besonders vielversprechend für die zukünftige geothermische Exploration und Entwicklung des Geothermalfeldes.

In der zweiten Studie wird ein neuartiger Überwachungsansatz vorgestellt, bei dem kontinuierlich der CO_2-Fluss gemessen wurde, um Veränderungen im Reservoir zu überwachen,

die durch die Reinjektion von kaltem Thermalwasser verursacht werden. Zu diesem Zweck wurde ein automatisiertes Mehrkammer-CO_2-Flusssystem innerhalb der Bruchzone einer Hauptstörung aufgebaut. Die Grundlage eines geeigneten Standortes wurde durch die Ergebnisse der CO_2-Explorationsuntersuchungen gegeben. Es war von großer Wichtigkeit, dass der Standort eine Verbindung zum geothermischen Reservoir aufweist, erkennbar an hydrothermaler CO_2-Entgasung und heißen Bodentemperaturen (> 50 °C). Die Ergebnisse zeigten ein Sinken der Gasemissionen als Reaktion auf Änderungen der Reinjektionsraten innerhalb von 24 h, was auf eine aktive hydraulische Kommunikation zwischen dem geothermischen Reservoir und der Erdoberfläche hinweist. Dies ist ein vielversprechende Methode, da nahezu in Echtzeit und in situ Daten über Veränderungen im Reservoir angezeigt werden und eine rechtzeitige Reaktion auf unerwünschte Veränderungen (z.B. Druckabfall, Seismizität) möglich ist.

Die dritte Studie präsentiert Ergebnisse aus dem Aluto-Geothermiefeld in Äthiopien, bei dem eine flächendeckende, Multiparameter-Analyse, bestehend aus CO_2-Fluss, ^{222}Rn- und ^{220}Rn-Aktivitätskonzentrationen und Bodentemperaturen durchgeführt wurde, um verborgene fluidführende Strukturen zu erkennen. Die ^{222}Rn- und ^{220}Rn-Aktivitätskonzentrationen wurden als ergänzende Bodengasparameter zum CO_2-Fluss verwendet, um ihr Potenzial als zusätzliche Explorationsparameter zu bewerten. Die kombinierte Messung aller Parameter ermöglichte die Entwicklung von Bodengas Fingerabdrücken – ein neuartiger Visualisierungsansatz. Dadurch lässt sich in Abhängigkeit von der Menge an Gasemissionen und deren Fließgeschwindigkeiten das Untersuchungsgebiet in vulkanisch (Wärme), tektonisch (Strukturen) und vulkanisch-tektonisch dominierte Gebiete unterteilen. Basierend auf diesem Konzept stellen vulkanisch-tektonisch dominierte Gebiete die vielversprechendsten Ziele für die zukünftige geothermische Exploration und Entwicklung an diesem Standort dar, da hier heiße hydrothermale Fluide entlang durchlässiger Strukturen migrieren. Zwei solche, bisher nicht berücksichtigte Gebiete wurden im Süden und Südosten identifiziert. Darüber hinaus konnten zwei bisher unbekannte Gebiete mit strukturell bedingter Durchlässigkeit anhand der Aktivitätskonzentrationen von ^{222}Rn und ^{220}Rn identifiziert werden.

Schließlich wird in der vierten Studie ein neuartiger Messansatz zum Nachweis der strukturbedingten CO_2-Entgasung im geothermischen Gebiet Ngapouri, Neuseeland, vorgestellt. Zum ersten Mal wurde die Tunable-Diode-Laser-Methode (TDL) in einem geothermischen Gebiet mit geringer Entgasung angewandt, um ihr Potenzial als geothermische Explorationsmethode zu bewerten. Obwohl der Messansatz auf Profilmessungen basiert, was zu einer geringen räumlichen Auflösung führt, zeigen die Ergebnisse einen Zusammenhang zwischen bekannten und unbekannten Störungen sowie erhöhten CO_2-Konzentrationen. Somit erwies sich die TDL-Methode bei der Bestimmung der strukturbedingten Permeabilität auch in solchen Gebieten als erfolgreich, in denen keine offensichtliche geothermische Aktivität vorhanden ist. Mit systematischen und kleinskaligen CO_2-Fluss-Messungen, kann anschließend die räumliche Auflösung der Abschnitte eines Profils mit erhöhten CO_2-Konzentrationen, verfeinert werden.

Mit den Ergebnissen dieser Arbeit konnte ich die Anwendbarkeit systematischer und flächendeckender Bodengasmessungen für geothermische Explorations- und Überwachungszwecke nachweisen. Die Kombination von verschiedenen Bodengasen und deren Messung anhand verschiedener Messnetze ermöglicht die genaue Identifizierung und Charakterisierung fluidführender Strukturen und wurde bisher noch nicht standardmäßig eingesetzt und/oder erprobt. Mit den Ergebnissen der jeweiligen Studien werden effiziente und kostengünstige Arbeitsabläufe dargelegt, die einen praxisorientierten Ansatz zeigen, der zu einer erfolgreichen und nachhaltigen Exploration und Überwachung geothermischer Ressourcen beitragen kann. Letztlich wird somit das Ressourcenrisiko bei der geothermischen Projektentwicklung minimiert. Um das Verständnis der komplexen Struktur und Dynamik geothermischer Systeme voranzutreiben, ist schließlich eine Kombination aus innovativen und flächendeckenden geologischen, geochemischen und geophysikalischen Methoden unerlässlich.

Abstract

Major challenges during geothermal exploration and exploitation include the structural-geological characterization of the geothermal system and the application of sustainable monitoring concepts to explain changes in a geothermal reservoir during production and/or reinjection of fluids. In the absence of sufficiently permeable reservoir rocks, faults and fracture networks are preferred drilling targets because they can facilitate the migration of hot and/or cold fluids. In volcanic-geothermal systems considerable amounts of gas emissions can be released at the earth surface, often related to these fluid-releasing structures.

In this thesis, I developed and evaluated different methodological approaches and measurement concepts to determine the spatial and temporal variation of several soil gas parameters to understand the structural control on fluid flow. In order to validate their potential as innovative geothermal exploration and monitoring tools, these methodological approaches were applied to three different volcanic-geothermal systems. At each site an individual survey design was developed regarding the site-specific questions.

The first study presents results of the combined measurement of CO_2 flux, ground temperatures, and the analysis of isotope ratios ($\delta^{13}C_{CO2}$, $^3He/^4He$) across the main production area of the Los Humeros geothermal field, to identify locations with a connection to its supercritical ($T > 374°C$ and $P > 221$ bar) geothermal reservoir. The results of the systematic and large-scale (25 x 200 m) CO_2 flux scouting survey proved to be a fast and flexible way to identify areas of anomalous degassing. Subsequent sampling with high resolution surveys revealed the actual extent and heterogenous pattern of anomalous degassing areas. They have been related to the internal fault hydraulic architecture and allowed to assess favourable structural settings for fluid flow such as fault intersections. Finally, areas of unknown structurally controlled permeability with a connection to the superhot geothermal reservoir have been determined, which represent promising targets for future geothermal exploration and development.

In the second study, I introduce a novel monitoring approach by examining the variation of CO_2 flux to monitor changes in the reservoir induced by fluid reinjection. For that reason, an automated, multi-chamber CO_2 flux system was deployed across the damage zone of a major normal fault crossing the Los Humeros geothermal field. Based on the results of the CO_2 flux scouting survey, a suitable site was selected that had a connection to the geothermal reservoir, as identified by hydrothermal CO_2 degassing and hot ground temperatures (> 50 °C). The results revealed a response of gas emissions to changes in reinjection rates within 24 h, proving an active hydraulic communication between the geothermal reservoir and the earth surface. This is a promising monitoring strategy that provides nearly real-time and in-situ data about

changes in the reservoir and allows to timely react to unwanted changes (e.g., pressure decline, seismicity).

The third study presents results from the Aluto geothermal field in Ethiopia where an area-wide and multi-parameter analysis, consisting of measurements of CO_2 flux, ^{222}Rn, and ^{220}Rn activity concentrations and ground temperatures was conducted to detect hidden permeable structures. ^{222}Rn and ^{220}Rn activity concentrations are evaluated as a complementary soil gas parameter to CO_2 flux, to investigate their potential to understand tectono-volcanic degassing. The combined measurement of all parameters enabled to develop soil gas fingerprints, a novel visualization approach. Depending on the magnitude of gas emissions and their migration velocities the study area was divided in volcanic (heat), tectonic (structures), and volcano-tectonic dominated areas. Based on these concepts, volcano-tectonic dominated areas, where hot hydrothermal fluids migrate along permeable faults, present the most promising targets for future geothermal exploration and development in this geothermal field. Two of these areas have been identified in the south and south-east which have not yet been targeted for geothermal exploitation. Furthermore, two unknown areas of structural related permeability could be identified by ^{222}Rn and ^{220}Rn activity concentrations.

Eventually, the fourth study presents a novel measurement approach to detect structural controlled CO_2 degassing, in Ngapouri geothermal area, New Zealand. For the first time, the tunable diode laser (TDL) method was applied in a low-degassing geothermal area, to evaluate its potential as a geothermal exploration method. Although the sampling approach is based on profile measurements, which leads to low spatial resolution, the results showed a link between known/inferred faults and increased CO_2 concentrations. Thus, the TDL method proved to be a successful in the determination of structural related permeability, also in areas where no obvious geothermal activity is present. Once an area of anomalous CO_2 concentrations has been identified, it can be easily complemented by CO_2 flux grid measurements to determine the extent and orientation of the degassing segment.

With the results of this work, I was able to demonstrate the applicability of systematic and area-wide soil gas measurements for geothermal exploration and monitoring purposes. In particular, the combination of different soil gases using different measurement networks enables the identification and characterization of fluid-bearing structures and has not yet been used and/or tested as standard practice. The different studies present efficient and cost-effective workflows and demonstrate a hands-on approach to a successful and sustainable exploration and monitoring of geothermal resources. This minimizes the resource risk during geothermal project development. Finally, to advance the understanding of the complex structure and dynamics of geothermal systems, a combination of comprehensive and cutting-edge geological, geochemical, and geophysical exploration methods is essential.

Table of Contents

List of Figures

List of Tables

Glossary

Advective degassing	describes the process of rapid gas migration favoured by pronounced structural discontinuities in the subsurface
CO_2 degassing	is the natural release of CO_2 from geological systems which can be either from biogenic or geogenic sources
CO_2 emissions	is equivalent to CO_2 degassing
CO_2 flux	describes the process of CO_2 flowing out at the earth surface and is calculated by the increase of CO_2 concentration inside a chamber of known volume as a function of time
CO_2 efflux	is equivalent to CO_2 flux
Diffuse soil degassing	occurs across wide areas, is less visible and characterized by low migration velocities towards the surface
Exploration survey	means large-scale soil gas sampling across a geothermal system and beyond
Natural gas emissions	are composed of biogenic and geogenic gas emissions measured at/in the (sub)surface
Scouting	is equivalent to exploration survey
Targeting	describes high-resolution soil gas sampling at selected sites

1

Introduction

1.1 General background

Since the beginning of the 19th century, accelerated industrialisation, the global spread of extractive economies, and an ever-growing world population have generated steady increases in carbon emissions, reaching today 9.7 ± 0.5 GtC yr^{-1} largely induced by the burning of fossil fuels (*Friedlingstein et al.*, 2020). With the start of continuously monitoring atmospheric carbon dioxide (CO_2) concentrations in 1958, it has become evident that enormous amounts of CO_2 are being released into the atmosphere, which boosted its concentration from 316 ppm in 1959 to 409 ppm in 2019 (*Dlugokencky and Tans*, 2020). While CO_2 and methane (CH_4) are the main contributors to the increase of global greenhouse gas (GHG) emissions, further GHG with serious implications for our society are nitrous oxide (N_2O), and fluorinated gases (F-gases) (*IPCC*, 2013).

In addition to anthropogenic emissions, natural degassing occurs widespread and with significant amounts from volcanic and non-volcanic (not directly connected to active volcanism) to active tectonic areas (*Chiodini et al.*, 2020; *Frondini et al.*, 2018; *Fu et al.*, 2017).

Volcanic emissions discharge through a central conduit/conduits, hot springs, fumaroles, crater lakes or diffuse flank degassing (*Oppenheimer et al.*, 2014), whereas non-volcanic degassing can be related to active tectonic settings and geothermal systems where discharge can occur along faults and fractures (*Brune et al.*, 2017; *Buttitta et al.*, 2020; *Tamburello et al.*, 2018). Thus, the migration of gases from the earth's interior to the atmosphere is controlled by the crustal and structural conditions of the respective geological-tectonic setting. The different types of natural emissions can also have a local to global impact on the atmospheric and terrestrial environment.

Both, anthropogenic and natural gas emissions are of great importance in atmospheric and climate research (*Brune et al.*, 2017; *Etiope and Klusman*, 2010; *Mörner and Etiope*, 2002), volcanic hazard and risk analysis (*Battaglia et al.*, 2019; *Carapezza et al.*, 2009; *Jolie et al.*, 2019), mining (*Azadi et al.*, 2020; *Noack*, 1998), or in the exploration/exploitation of conventional resources (*Karion et al.*, 2013; *Pinti et al.*, 2016) and geothermal energy (*Bertrami et al.*, 1990; *Gunnarsson et al.*, 2014; *Lewicki and Oldenburg*, 2004).

The continuous demand for renewable and locally produced energy and the reduction in GHG emissions drives the development of geothermal exploration projects worldwide (*IRENA*, 2020). Geothermal energy, stored in form of heat below the surface, is certainly one of the few sustainable alternatives to fossil energy, capable of generating base-load heat and power, independent of daytime, weather, or climatic phenomena. In 2020, the global installed geothermal power generation was 15,950 MWe (*Huttrer*, 2020), while the installed thermal power for direct utilization (e.g. space and greenhouse heating) reached 107,727 MWt (*Lund and Toth*, 2020).

Virtually geothermal energy is available around the world, however the higher the temperature of the produced fluid, the greater the potential for power generation. Fluids of these so called medium- to high enthalpy geothermal systems (250 °C $<$ T $<$ 350°C and 1100 kJ/kg $<$ h$<$ 2800 kJ/kg; *Kamila et al.* (2021)) are found in tectonically and volcanically active areas predominantly at plate tectonic boundaries such as volcanic arcs above subduction zones (e.g. Sunda arc, Indonesia), mid-ocean ridges (e.g. Iceland), rift valleys (e.g. East African Rift) or near hot spot magmatism (e.g. Hawaii) (*DiPippo*, 2016; *Nicholson*, 1993). Several classifications of geothermal systems exist in the literature regarding geological-hydrological controls and thermodynamic state (*Henley and Ellis*, 1983; *Kaya et al.*, 2011; *Moeck*, 2014; *Sanyal*, 2005; *Williams et al.*, 2011) and will be discussed in chapter 2.2.

In the context of geothermal research, many definitions are used to describe certain parts of a geothermal system, which can sometimes lead to confusion. For this reason, the terms frequently used in this thesis will be explained below.

i) A geothermal field refers to the geographical position at the Earth's surface either marked by geothermal surface manifestations (e.g. fumaroles, hydrothermal alteration) or in the case of a blind/hidden geothermal field (without visible surface activity) confined by its reservoir below.

ii) A geothermal system describes the totality of geologically relevant conditions in the Earth crust at a location that is used or intended to be used for geothermal purposes.

iii) A geothermal reservoir describes the part of the underground from which geothermal energy can be extracted either by fluid or steam *Saemundsson* (2016); *Toth and Bobok* (2017).

For the exploitation of geothermal energy, fluids, heat and sufficient permeability, either formation or structural controlled, play a decisive role and determine the utilisation potential and economic viability of a geothermal resource (*DiPippo*, 2007; *Lautze et al.*, 2017). Structural permeability in form of extensive faults and fracture networks can promote the migration of hydrothermal fluids (water + gas) within a geothermal system to Earth's surface. The determination of their chemical and isotope composition gives information on their origin and formation as well as valuable insights into chemical and physical processes operating in the mantle, the crust, and the hydrosphere (*Chiodini et al.*, 2008; *Daskalopoulou et al.*, 2019). Consequently, gas emissions at the surface present invisible fingerprints of these systems.

Several studies proved the connection between structural control over degassing and suggest the mapping of gas emissions as an indicator for structural discontinuities in the subsurface

(*Bennati et al.*, 2011; *Camarda et al.*, 2020; *Fairley and Hinds*, 2004b; *Jolie et al.*, 2016; *Lombardi and Voltattorni*, 2010). Geothermal exploration takes advantage of this finding (*Bertrami et al.*, 1990; *Fridriksson et al.*, 2016; *Klusman et al.*, 2000) as structural controlled permeability is one of the main targets for geothermal wells, especially when formation permeability of reservoir rocks is low (*Bignall et al.*, 2010; *Faulds et al.*, 2018). For this reason, one of the main objectives of geothermal exploration campaigns is to locate permeable faults and fracture networks, among others. Over the last 50 years, various geological, geochemical, and geophysical exploration methods have been developed to build robust conceptual models to understand the structure and dynamics of geothermal systems. However, one of the biggest challenges remains, the identification of suitable drilling targets. Area-wide soil gas analysis offers the fast investigation of large areas during a short amount of time and as mentioned before, they can carry useful information from the deep geothermal reservoir without drilling a well. In addition, the continuous monitoring of gas emissions proved to be a powerful method in the characterization of local background signals to forecast changes in volcanic activity (volcano monitoring) (*Laiolo et al.*, 2016; *Sabbarese et al.*, 2020). In fact, other studies could also show a link between earthquake activity and changes in gas flux, prior or during periods of anomalous seismicity related to stress changes and fluid pressure fluctuations in the crust (*Chiodini et al.*, 2020; *Cigolini et al.*, 2007). This makes soil gas analysis an interesting and promising method to be applied as a geothermal exploration and monitoring tool.

The overall aim of this thesis is thus to test and evaluate best practices of soil gas analytics for sustainable geothermal exploration and monitoring purposes. This was achieved by the measurement of the spatial and temporal distribution, composition and relative magnitude of gas emissions at Earth's surface. Depending on the objective of the investigation, different sampling concepts (regular grids vs. profiles), analytical methods (alpha spectroscopy or efflux measurements) and gas species (carbon dioxide or helium), were tested and measured. Moreover, this thesis aims to understand how structural permeabilities control gas emissions at the surface of different geothermal systems and which processes affect their formation and migration.

1.2 Thesis outline

This cumulative thesis demonstrates the investigation and mapping of various gas parameters in three different geothermal areas located in Ethiopia, New Zealand and Mexico, using a variety of measurement concepts and tools. Both the overall concepts and each individual method are applicable approaches to quantify gas emissions at the shallow (sub)surface to improve the understanding of gas release in volcanic-geothermal systems associated to structural permeabilities and geothermal reservoir activity. The experiences gained throughout this thesis contribute to a safe and sustainable exploration and monitoring of geothermal resources, and thus to the energy transition which requires urgent action on global scale to tackle the climate crisis.

Part I of this thesis gives an introduction to the three research areas that are linked in this thesis: Geothermal systems (Chapter 2.2), Structural geology (3.1), and Gas geochemistry

(Chapter 4.1). I briefly present the gas parameters measured in this work and the respective sampling and measurement techniques used with them (Chapter 5.4).

Part II consists of four manuscripts listed in section 1.3.

Each of the chapters contains its own introduction, geological context, results and discussion while I have summarized a complete bibliography of the entire thesis at the end. My contribution to the preparation of the manuscripts is outlined in section 1.3. Supplementary data related to the manuscripts are attached at the end of the corresponding chapter along with links to associated data publications. Chapter 6 presents results of the measurement of different soil gas parameters from the Los Humeros geothermal field, where sampling grids at different point spacing were tested to investigate and resolve the structural control on gas emissions. Furthermore, high resolution gas emission patterns where interpreted in relation to the internal fault zone architecture. The aim was to identify areas connected to the superhot geothermal reservoir. Chapter 7 presents the use of a continuous CO_2 flux measurement system as a geothermal monitoring concept to detect changes in the deep geothermal reservoir associated with fluid reinjection. Chapter 8 shows results from a multi-parameter study at the Aluto Volcanic Complex in Ethiopia to improve the understanding of tectonic and volcanic controls on the existing geothermal system and the identification of hidden structures. A soil gas fingerprint was developed to understand the spatial distribution of soil gases in specific domains and thus identify promising drilling targets. Finally, chapter 9 investigates the application of the tunable diode laser method to detect fault related permeability by measuring CO_2 concentrations in a low degassing geothermal area in New Zealand.

Part III includes an individual discussion of each publication and and a cumulative discussion in synthesis with the other publications (Chapter 10. Finally, it ends with a workflow based on the results obtained in this thesis, as a guide for future exploration and monitoring campaigns. The thesis ends with an overall conclusion (Chapter 11).

1.3 List of Publications and Contributions

This cumulative thesis reflects the close collaboration with my co-authors during my time as a PhD-student. The four manuscripts have been published in peer-reviewed scientific journals (Chapter 6, 7 8, and 9). I have listed an additional manuscript in section (1.3.1) that is not part of this thesis, but some of the results in chapter 6 have been integrated into this publication for a comprehensive interpretation of the Los Humeros geothermal system. It presents results obtained during the GEMex project which funded my PhD position.

Chapter 6

Anna Jentsch, Egbert Jolie, David G. Jones , Helen Taylor-Curran, Loïc Peiffer, Martin Zimmer, Bob Lister (2020), Magmatic volatiles to assess permeable volcano-tectonic structures in the Los Humeros geothermal field, Mexico, *Journal of Volcanology and Geothermal Research*, 394, https://doi.org/10.1016/j.jvolgeores.2020.106820

- Associated data publication: **Anna Jentsch**, Egbert Jolie, David G. Jones , Helen Taylor-Curran, Loïc Peiffer, Martin Zimmer, Bob Lister (2020), CO_2 efflux, soil temperature and carbon/helium isotope results from the Los Humeros geothermal field, Mexico, *GFZ Data Services* https://doi.org/10.5880/GFZ.4.6.2020.001

Contributions: I developed the sampling concepts and was leading the field work. Furthermore, I processed the data, performed the statistical analysis, wrote the manuscript, prepared figures, and discussed the final results. All co-authors corrected and improved the manuscript. The paper considerably benefited from discussions with Egbert Jolie, Loïc Peiffer, and Martin Zimmer. The field work was supported by David G. Jones, Helen Taylor-Curran, and Bob Lister. The corresponding data publication was prepared by me according to the guidelines of the GFZ data services.

Chapter 7

Anna Jentsch, Walter Duesing, Egbert Jolie, Martin Zimmer (2021), Monitoring the response of volcanic CO_2 emissions to changes in the Los Humeros hydrothermal system, *Scientific Reports*,

- Associated data publication: **Anna Jentsch**, Walter Duesing, Egbert Jolie, Martin Zimmer (2021), Continuous monitoring of soil CO_2 flux and atmospheric parameters at the Los Humeros Volcanic Complex, Mexico, *GFZ Data Services*, http://doi.org/10.5880/GFZ.4.8.2021.003

Contributions: As a first author, I processed the data, wrote the manuscript and prepared the figures. The data evaluation and statistical analysis was performed by Walter Duesing and me. Egbert Jolie and Martin Zimmer contributed to the deployment of the monitoring station. The discussion of the final results received valuable comments from Walter Duesing and Egbert Jolie. All co-authors corrected and improved the manuscript. The corresponding data publication was prepared by me according to the guidelines of the GFZ data services.

Chapter 8

Egbert Jolie, W. Hutchinson, D.L. Driba, **Anna Jentsch**, B. Gizaw (2019), Pinpointing deep geothermal upflow in zones of complex tectono-volcanic degassing: New insights from Aluto Volcano, Main Ethiopian Rift, *Geochemistry, Geophysics, Geosystems*, 20, 4146–4161, https://doi.org/10.1029/2019GC008309

Contributions: I was involved in the preparation of the field study and participated in the field work. Furthermore, I contributed to the data processing and helped with the evaluation.

Chapter 9

Agnes Mazot, Andrew Rae, **Anna Jentsch**, Karen Britten (2019), Testing the tunable diode laser system in extreme environments: Measuring high and low CO_2 concentrations in both active volcanic and geothermal settings, *Journal of Volcanology and Geothermal Research*, 376, 1-14, https://doi.org/10.1016/j.jvolgeores.2019.03.011

Contributions: I conducted the main part of the field work at Ngapouri geothermal area and processed the data. I assisted in the analysis of the data and helped write the introduction, results, and discussion section on the Ngapouri geothermal area.

1.3.1 Additional Manuscript

Tania Toledo, Emmanuel Gaucher, Philippe Jousset, **Anna Jentsch**, Christian Haberland, Hansruedi Maurer, Charlotte Krawczyk, Marco Calò, Ángel Figueroa (2020), Local Earthquake Tomography at Los Humeros Geothermal Field (Mexico), *Journal of Geophysical Research: Solid Earth*, 125, https://doi.org/10.1029/2020JB020390

Contributions: I assisted with the integration of available geological, geochemical, and geophysical data collected at Los Humeros and with the results interpretation. Furthermore, I have contributed to the generation of figures regarding the results interpretation.

Part I

Scientific background

2

Geothermal System Classification

Geothermal systems occur in different geological settings all over the world and during the past 40 years numerous classification schemes have been proposed (*Hochstein*, 1988; *Kaya et al.*, 2011; *Lee*, 2001; *Moeck*, 2014; *Muffler and Cataldi*, 1978; *Williams et al.*, 2011). However, widely applied classification schemes are usually based on geological, hydrogeological, temperature, and heat transfer regime. These parameters, as well as the fluid type, liquid or steam, are strongly controlled by the plate tectonic setting (*DiPippo*, 2016). In a nutshell, all the aforementioned factors need to be evaluated during geothermal resource assessment as they provide essential implications for geothermal exploration and utilization strategies. Figure 2.1 provides an overview of high-temperature geothermal areas used for power generation including the three field sites examined in this thesis. In the following paragraph, I will give a brief summary of geothermal systems following the classification scheme developed by *Moeck* (2014), who proposed a classification in terms of the heat source of geothermal systems and their tectonic setting.

2.1 Convection-dominated geothermal systems

The greatest potential for geothermal energy utilization can be found in high enthalpy, convection-dominated geothermal systems related to active tectonic settings at convergent and transform plate boundaries (e.g. Trans Mexican Volcanic Belt, Mexico), within spreading centers and rifts (e.g. Basin and Range Province, Nevada), and over mantle hot spots (e.g. Hawaii) (*DiPippo*, 2016; *Stimac et al.*, 2015). Their heat source either originates from an active magma chamber, recent magmatic intrusions ($<$ 50,000 years old) or is related to elevated heat flow in extensional areas of thin crust caused by the upwelling of mantle material (*Moeck*, 2014).

Consequently, reservoir temperatures between 150 °C up to 350 °C in shallow depth (1-3 km) are not exceptional and often cause two-phase conditions (liquid and vapour) within the central upflow zone (*Henley and Ellis*, 1983; *Hochstein*, 1988).

In the majority of these systems, geothermal activity is evidenced by gases and fluids discharging at the surface in form of fumaroles, hot springs, steaming ground, and sulfataras.

Diffuse degassing is less visible across wide areas, but sometimes it is recognizable by changes in vegetation and by soil alteration. These volatile emissions are the result of complex chemical and physical interactions between magmatic fluids, meteoric water (groundwater), seawater, and rocks during the upward migration along complex fault and fracture networks (*Nicholson*, 1993). Especially in non-magmatic regions where geothermal systems are influenced by regional extension, permeability and fluid flow are controlled by active faults. Faults and fracture networks present favourable targets for geothermal production and injection wells. However, a thorough understanding of their structural architecture and the state of stress in the crust are essential to assess whether they are permeable to fluids or not (*Faulds and Hinz*, 2015). Soil gas analysis complements these methods as permeable zones can be identified by increased degassing (*Chiodini et al.*, 2007; *Fridriksson et al.*, 2006; *Jentsch et al.*, 2020). Hydrothermal fluids are typical for convection-dominated geothermal systems and are responsible for advective heat transfer processes resulting in extremely high geothermal gradients way above the crustal average of 30 °C/km and increased heat flow between 150 to 300 mW m^{-2} (*Stimac et al.*, 2015; *Stober and Bucher*, 2013). The geothermal areas investigated in this thesis are all characterised by active or recent magmatic intrusions, which are also referred to as volcanic-geothermal systems.

2.2 Conduction-dominated geothermal systems

The thermal regime in conduction-dominated geothermal systems is characterized by the normal crustal heat flow (65 mW m^{-2} which corresponds to a temperature gradient of 30 °C/km, (*DiPippo*, 2016) in passive plate tectonic settings such as rift and foreland basins (e.g. Molasse Basin in Germany). In some areas, for example Soultz-sous-Forêt in France, local thermal anomalies can be associated to intruded plutons of granitic composition generating heat through the radioactive decay of uranium (^{238}U,^{235}U), thorium (^{232}Th), and potassium (^{40}K) (*Stimac et al.*, 2015). Overall, conduction-dominated systems are associated with low and medium enthalpy resources (50 - 150 °C). The crustal heat flow is influenced by the temperature gradient between the different lithologies of a geological system. The ability of rocks to transport heat is called thermal conductivity λ and varies considerably between crystalline rocks, which conduct heat up to three times better than sediments (*Schön*, 2015). Potential surface manifestations are mineral springs, mofettes, and diffuse soil degassing (*Kämpf et al.*, 2013; *Moeck*, 2014).

Another subdivision of these systems is related to the presence of water and permeability. In sedimentary basins fluid flow is facilitated by certain litho- and biofacies with sufficient porosity and permeability that occur in carbonates, shales or sandstones acting as potential aquifers. Similarly, faults also play an important role in heat transfer processes as they allow meteoric water to infiltrate to the deep subsurface. They are formed during the increase of crustal thickness in front of orogens related to the accumulation of erosional products or during basin evolution (*Moeck*, 2014).

On the contrary, in Hot Dry Rock (HDR) systems i.e. crystalline intrusive areas, fluids are usually absent and natural permeability is insufficient. Therefore, a great effort has been made in recent decades to develop these unconventional geothermal resources, also called Enhanced

Geothermal Systems (EGS). In EGS systems, fluids are injected under high pressure, also known as hydraulic stimulation, to create permeability by either inducing artificial fractures or increasing the permeability of the existing structural network (*DiPippo*, 2016). This enabled the heat extraction from these low to medium enthalpy geothermal systems (< 150 °C) used for direct heat and in some cases for electricity generation. Although conduction-dominated systems are characterized by low permeabilities and buried faults at several kilometers depths, the application of soil gas analysis in these systems proved to be successful method for the identification of deep reaching faults (*Ciotoli et al.*, 1998; *Duddridge et al.*, 1991; *Kämpf et al.*, 2013).

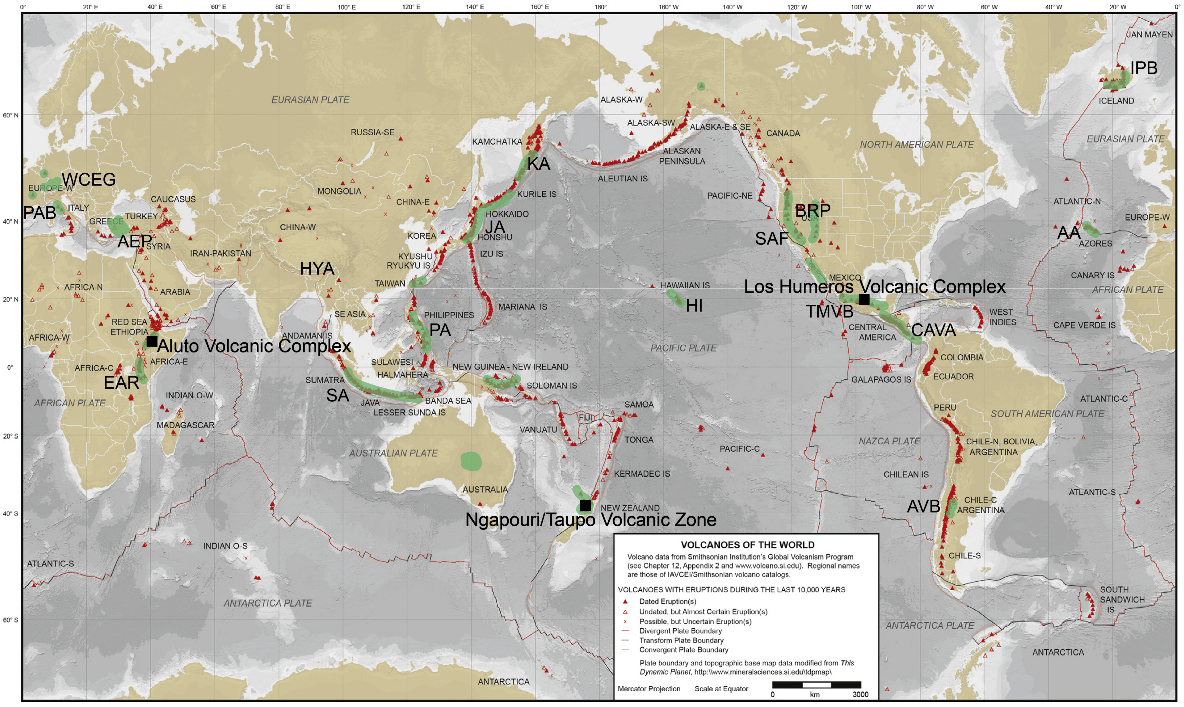

Figure 2.1: Overview of major tectonic plate boundaries, volcanoes with eruptions during the last 10,000 years and high-temperature geothermal provinces currently used for power generation (light green *Huttrer*, 2020). These high-temperature geothermal systems typically occur in magmatic, extensional and transtensional settings along active plate tectonic boundaries and close to volcanoes. Black solid squares indicate the study sites of this thesis. Names of key geothermal provinces with large geothermal power generation potential are indicated by capital letters taken from *Jolie et al.* (2021). AA, Azores archipelago; AEP, Aegean extensional province; AVB, Andean Volcanic Belt; BRP, Basin and Range Province; CAVA, Central American Volcanic Arc; EAR, East African Rift; HI, Hawaii archipelago; HYA, Himalaya; IPB, Iceland plate boundary; JA, Japanese arc system; KA, Kuril arc; PA, Philippine arc; PAB, pre-Apennine belt; SA, Sunda arc; SAF, San Andreas Fault Zone; TMVB, Trans-Mexican Volcanic Belt; WCEG, western/central European geothermal systems. The map has been modified from *Sigurdsson et al.* (2015).

3

Faults & Fractures

3.1 The role of faults and fractures in geothermal systems

The economic success of a geothermal project depends critically on the geological conditions at great depth, more specifically on the availability of natural fluids and their potential to flow through the geothermal reservoir. It is commonly known that fault and fractures can promote fluid migration from depth into the geothermal reservoir to Earth's surface, making them favourable targets for geothermal wells (*Fairley and Hinds*, 2004a; *Faulds and Hinz*, 2015; *Rossetti et al.*, 2011). It is not only important to define the location and spatial extent of faults and fracture networks but also to understand their heterogeneous behaviour which can favour or hamper fluid flow.

According to *Fossen* (2010), a fault is a tabular volume of rock consisting of a central slip surface or core, formed by intense shearing, and a surrounding volume of rock that has been affected by more gentle brittle deformation spatially and genetically related to the fault. Already a single fault can reach considerable depth and length up to several kilometers indicating its potential to circulate large amounts of fluids. Brittle deformation is also responsible for the development of fractures, which involve displacements in the mm- to dm-scale. The term fault zone describes multiple subparallel faults that represent highly complex and heterogeneous structural discontinuities. In fact, there will be no fault or fault zone without the occurrence of extensive fracture networks.

Following the definition by *Fossen* (2010) and early work by *Caine et al.* (1996), the anatomy of faults can be distinguished into i) the fault core, ii) the fault damage zone, and iii) the relatively undeformed protolith zone. Depending on the size of a fault, the fault core and damage zone can vary from a few centimeters up to several meters. The fault core hosts most of the displacement and can consist of a clay-rich fault gouge, cohesive cataclasites, and different types of breccias often representing a barrier to fluid flow. In contrast, the fault damage zone is characterized by enhanced permeability facilitating fluid migration due to the high density of brittle structures. Typical structures include deformation bands, shear and tensile fractures, small faults and veins (*Caine et al.*, 1996; *Chester and Logan*, 1986).

If volcanic-tectonic forces act within a hydrothermal system, slip on a fault can occur, releasing stress. These stresses concentrate near the fault rupture but can also be transferred and promote further displacement along fractures or faults, respectively (*Siler et al.*, 2018). The prevailing stress field in a geothermal system controls the orientation and mode of fractures and faults and thus the fluid flow (*Rowland and Sibson*, 2004; *Sibson*, 1996). Numerous studies (*Curewitz and Karson*, 1997; *Faulds and Hinz*, 2015; *Rowland and Sibson*, 2004; *Siler and Pepin*, 2021) investigated the geological and structural controls on fluid flow in geothermal systems. Their aim was to evaluate favourable settings for the occurrence of geothermal resources. Figure 3.1 presents conceptual models of common structural settings from the Basin and Range Province in Nevada from *Faulds and Hinz* (2015). However, they are applicable to other geothermal systems worldwide. Sill, many geothermal systems show a combination of different structural settings rather than one normal fault or fault bend being responsible for increased permeability.

In general, areas characterized by multiple fault strands that overlap or intersect correspond to critically stressed areas. In these areas the chances are good that fluid pathways will remain open, reopen or new pathways will be created supported by the occurrence of hot springs at the surface, intense hydrothermal alteration, or increased degassing. Past hydrothermal activity can be evidenced by older deposits and allows to track fluid migration history. In this context, the interaction of hydrothermal fluids with rocks needs to be discussed, as hot and often acidic fluids from high temperature geothermal systems dissolve minerals during their upward migration along permeable pathways and thus can enhance permeability. On the other hand, dissolved minerals can also precipitate as quartz, calcite and others, in shallower parts of the system and reduce permeability (*Bense et al.*, 2013). These processes are driven by pressure and temperature changes and geochemical reactions between fluids and fluids and rocks (*Rossetti et al.*, 2011; *Townend et al.*, 2017; *Yehya and Rice*, 2020).

Finally, fracture networks and fault zones are characterized by very heterogeneous and anisotropic behaviour resulting in either a fluid conduit, a fluid barrier or in many cases a combination of both. Sometimes, an individual fault segment can present a high permeable flow path whereas the total average flow of that fault would be considered as low (*Fairley and Hinds*, 2004a). Despite the important role of faults and fractures in geothermal systems and various methods to locate them, the challenge remains to evaluate the influence of a fault's hydraulic architecture on fluid flow and to estimate its permeability. This is where soil gas analysis complements traditional methods. It helps to improve the understanding of the internal fault structure by the application of domain-based sampling grids (small point distance) to better constrain potential drilling targets.

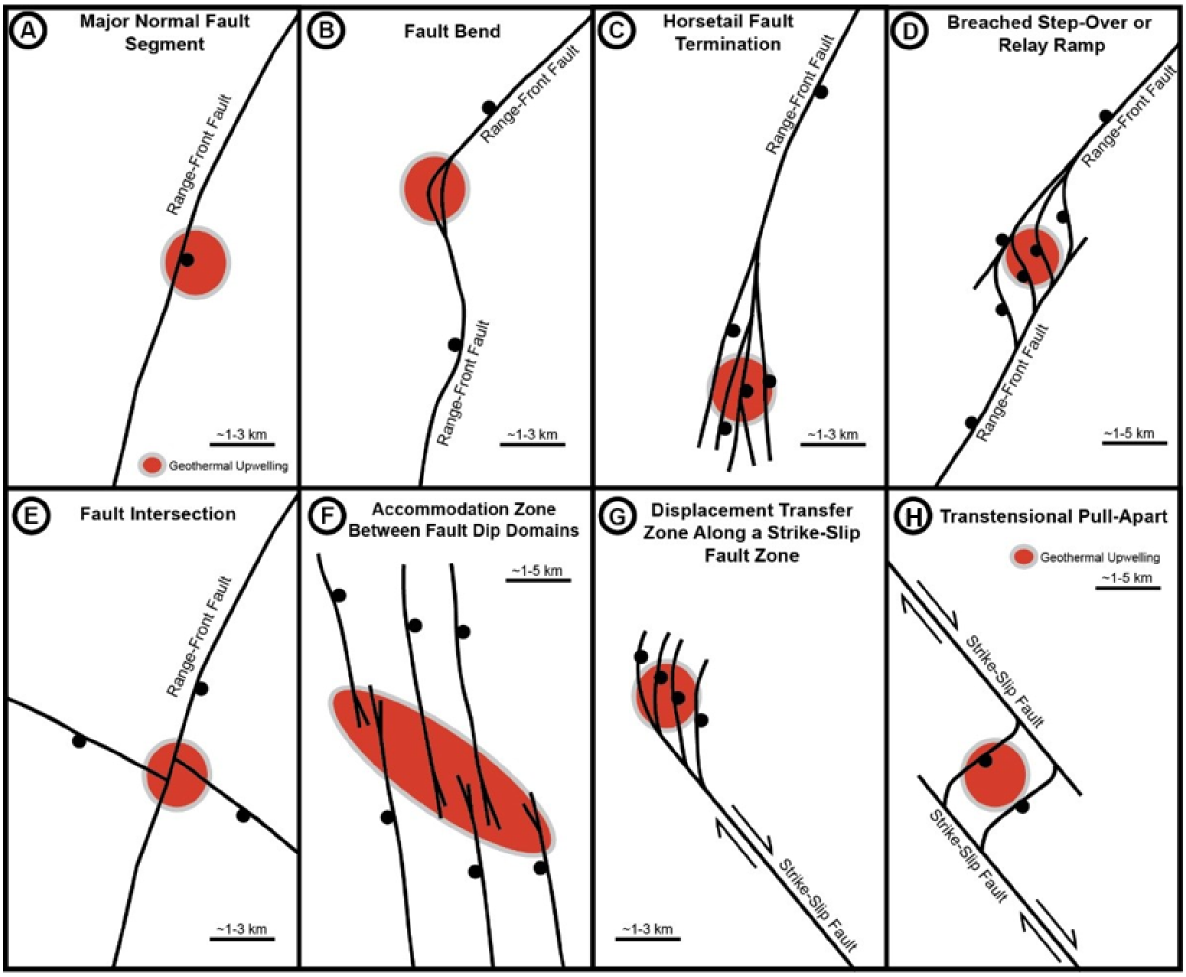

Figure 3.1: Conceptual models of typical structural settings occurring in geothermal systems from *Faulds and Hinz* (2015). Red circles/ellipse indicate areas of enhanced geothermal fluid flow.

4

Volatiles

4.1 Origin and processes affecting volatiles in high-temperature geothermal areas

The mantle is one of the most important volatile reservoirs of the earth and steadily supplies significant amounts of gases to the overlying crust and atmosphere. During magma ascent towards shallow depths, the pressure decreases, which is accompanied by a decrease of gas solubility in the melt. Consequently, gases are released into a vapour phase as they rise to the surface (*Aiuppa and Gaillard*, 2016; *Francis and Oppenheimer*, 2004).

The most abundant volatile species in volcanic-geothermal systems are CO_2 and H_2O followed by CH_4, N_2, NH_3, H_2, and H_2S also referred to as non-condensable gases (NCG). Whereas volcanic gas emissions directly released by active volcanoes are richer in sulfur species and halogens (*Nicholson*, 1993; *Stimac et al.*, 2015). In addition, great attention has been paid to noble gases like helium (He), argon (Ar), or neon (Ne), since they are present in small quantities in high temperature geothermal systems and due to their inert behaviour, allow the determination of the final origin of gases (*Ozima, M. and Podosek*, 2002; *Sano and Fischer*, 2013). Thus, geothermal and volcanic gases present a cocktail of different contributions from the mantle, crustal fluids, rocks, and the atmosphere (*Mason et al.*, 2017; *Oppenheimer et al.*, 2014).

The origin of fluids circulating within the crust can be distinguished by meteoric, magmatic, and connate waters. The reaction of waters and gas with the surrounding rocks alters the composition of reservoir fluids (steam and liquid) and additional gases can form favoured by the presence of carbonates or sedimentary rocks in the reservoir. A typical process in high-temperature geothermal systems is phase separation, i.e. boiling, in which reservoir fluids are separated into a liquid and a vapor phase due to the reduction in hydrostatic pressure during upward migration. In this context, the solubility of gases (depending on reservoir temperature and pressure) should be mentioned, since it determines the composition and quantity of gas passing into the vapor phase in the event of boiling. A general order for solubility of common geothermal gases in water is $NH_3 > H_2S > CO_2 > CH_4 > H_2 > O_2 > N_2$ with ammonia dissolving first and nitrogen last (*D'Amore and H. Truesdell*, 1988; *Nicholson*, 1993).

Especially at shallow depth, geothermal fluids and gases may condense, mix, and oxidize. This results in the generation of acid to alkaline fluids and provokes a variety of geothermal surface manifestations such as intense argillic alteration, steaming ground, fumaroles, travertine deposits, or widespread diffuse degassing. These manifestations are directly linked to different transport mechanisms that control fluid migration in the subsurface. *Etiope and Martinelli* (2002) classified two types of fluid transport, in which advection describes the process induced by pressure gradients, resulting in the fast migration of gases from the high to the low pressure zone, whereas diffusion aims to equalize concentrations within a system ascribed by much lower migration velocities. In geothermal systems, the term convection is often used when talking about advective fluid flow linked to geothermal gradients. In most cases, gas movement is a combination of advection and diffusion (*Carapezza and Granieri*, 2004; *Chiodini et al.*, 1998). This paragraph has reviewed some of the main volatile species and processes influencing their chemical and isotopic composition. Not only the chemistry but also the amount of gas emissions at the surface provide valuable insights to preferential pathways and the thermodynamic state of high temperature geothermal systems.

5

Gas parameters & Methods

The following sections provide a brief introduction to the gases that will be discussed in this thesis followed by the respective measurement methods for determining their content or isotopic composition. In particular, I discuss the measurement methods and their application in the field (individual advantages and disadvantages), the average measurement time and influencing factors. General limitations to the measurement of soil gases include low permeable or solid surface rocks, and heavy rainfall.

5.1 Carbon dioxide

CO_2 can be found in various geological settings. However, in high temperature volcanic-geothermal systems it often represents more than 85 % both volume and weight of the total gas content (*Mahon*, 1970; *Nicholson*, 1993; *Stimac et al.*, 2015). This is mainly due to its low solubility in silicate melts (*Keppler et al.*, 2003) making it an important geochemical tracer gas to determine subsurface fluid pathways and flow rates. Deep/geogenic CO_2 can have different origins resulting from magma degassing, thermal alteration of carbonate rocks and minerals, or the degradation of organic matter within sedimentary rocks (*Henley and Ellis*, 1983). Shallow/biogenic CO_2 is the result of solutes in meteoric water and near-surface metabolic processes between soil organic matter, microbes, organic decomposition, and atmospheric dilution (*Raich and Tufekcioglu*, 2000; *Widén and Majdi*, 2011).

5.1.1 Soil CO_2 flux

Soil CO_2 flux can be either measured in-situ by single measurements or continuously by an automated CO_2 flux monitoring system connecting up to 16 long-term chambers with a maximum diameter of 30 m. It is calculated by the increase of CO_2 concentration inside a chamber of known volume (between 0.002 - 0.006 m^3) as a function of time following the accumulation chamber method (*Chiodini et al.*, 1998; *Parkinson*, 1981). The accumulation chamber is placed on the ground and a small air pump circulates gas through a closed loop from the chamber to a non-dispersive infra-red analyzer, which measures in the range of 0 -

20,000 ppm (depending on the analyzer). The signal is converted by an analog-digital converter and transmitted to a small palmtop computer, where the result is plotted in real time. By the manual selection of a regression interval a linear regression line is fitted onto the exponential curve.

Any disturbing effects on CO_2 caused by e.g atmospheric contamination can be immediately revealed by the curve progression. Thus the user has a direct control on the quality of each measurement. Atmospheric parameters recorded at each sampling site are air temperature and barometric pressure, as they are required for the unit conversion from the original unit ppm s^{-1} to g m^2 d^{-1}. During continuous monitoring campaigns, the aforementioned atmospheric parameters are usually complemented by air and soil humidity, precipitation, wind speed and direction, and soil temperature to quantify possible changes induced by environmental parameters on soil CO_2 flux (*Jentsch et al.*, 2021; *Oliveira et al.*, 2018; *Viveiros et al.*, 2015). On average a flux measurement requires between 60 to 240 seconds resulting in extensive data sets within a very short time.

Area-wide soil CO_2 flux surveys are useful to understand the spatial variability of CO_2 flux and allow the spontaneous adaption of sampling networks regarding a particular area of interest. In addition, the total CO_2 output from a study area can be calculated. This contributes to the understanding of CO_2 emissions from volcanic-geothermal areas to the global carbon budget. An excellent evaluation of temporal and small-scale spatial variations is enabled by the permanent monitoring of soil CO_2 flux. Fundamental research on the occurrence of abundant amounts of CO_2 in volcanic geothermal systems and the commercial availability of the robust equipment paved the way for the regular application of soil CO_2 flux measurements linked to active geothermal areas during the past 30 years (*Bergfeld et al.*, 2001; *Bertrami et al.*, 1990; *Chiodini et al.*, 1995; *Jolie et al.*, 2016; *Taussi et al.*, 2021; *Voltattorni et al.*, 2010).

5.1.2 CO_2 concentration

CO_2 concentrations were measured with the tunable diode laser spectroscopy technique (TDL) based on the absorption of infra-red radiation by using a light source that is tunable over a narrow wavelength range (1.3 - 1.7 nm). The instrument consists of a transmitter/receiver unit that measures CO_2 mixing ratios over a linear open paths of up to 1 km distance. A laser light is emitted from a transceiver, propagates through the atmosphere to a retro-reflector mirror (single or triple gold plated corner cube), where the light is reflected and returns to the transceiver onto a photodiode detector. The TDL performs continuous and automatic calibration as a portion of the emitted beam passes through a reference cell of known CO_2 concentration. The two signals, one from the measured sample path and the other from the reference cell, are converted into electrical waveforms and processed to obtain CO_2 column amounts in ppm m. These values are then converted into average CO_2 mixing ratios in ppmv by including the known path length. The light level (dimensionless) is the amount of energy returned by the retro-reflector and registered by the transceiver. For a linear behaviour of the TDL, the ideal working range of the light level is between 2000 - 12000 (*Pedone et al.*, 2014a). A high temporal resolution of 1 Hz is set as the sampling rate. To obtain robust results a measurement takes between 3 to 10 minutes depending on the dynamics in the atmosphere. Especially changing insolation (clouds), humidity, wind speed/direction and dense fog can disturb or extent measurement time as the laser can loose its signal strength. In addition, topographical changes can reduce the path length of a measurement.

The TDL technique enables the measurement of wide areas in a relatively short amount of time with high sensitivity ($\sim$ 2 ppm) to distinguish between background and anomalous CO_2 concentrations (*Mazot et al.*, 2019). Once an area of interest has been identified along a section, a more accurate location of increased CO_2 emissions can be be achieved by reducing the path length. This also makes it possible to measure over mud pools and fumaroles. Furthermore, TDL also provides continuous monitoring of CO_2 concentrations. However, compared to the measurement of soil CO_2 flux, TDL is much more influenced by atmospheric parameters, so its application is recommended in stable atmospheric conditions and outside of areas where many vehicles are operated and livestock are present. So far, TDL has been used mainly for studies in volcanically active areas, to monitor gas concentrations (*De Natale et al.*, 2001; *De Rosa et al.*, 2007) but the study by *Mazot et al.* (2019) shows its great potential to detect structural controlled permeability in geothermal areas.

5.1.3 Carbon isotopes

Isotopes are atoms where the nuclei contains the same amount of protons but a different number of neutrons. This results in a difference in atomic mass and thus affects the chemical and physical properties of the isotopes (*Hoefs*, 2004).

Carbon has two stable isotopes, ^{12}C and ^{13}C and their ratio together with a reference standard (Pee Dee Belemnite - V-PDB) is used to describe the isotopic composition of a sample in terms of delta δ values as per mille (‰). Stable isotopes do not decay naturally instead the variation in isotope abundance is the result of isotope fractionation due to a large variety of natural processes that take place at equilibrium or kinetic conditions e.g. precipitation, dissolution, and diffusion (*Sharp*, 2017).

Sampling of carbon isotopes at diffuse soil degassing sites is conducted by inserting a metal probe in 1 m depth and aspirating the gas through a syringe. Depending on the rate of flux the metal probe is flushed three to four times before taking the final sample which is injected into an evacuated 12 ml glass vial with a pierceable septum. Finally, the analysis is performed at the laboratory with an isotopic ratio mass spectrometer under continuous flow.

All mass spectrometers are based on the principle of deflecting an energetic, focused ion beam to separate charged atoms and molecules based on their mass and motion in a magnetic/electrostatic field. The primary components exist of i) an ion source, where a sample is ionized, accelerated and focused into a beam, ii) a mass analyzer, which deflects the ions based on their mass and charge, and finally iii) a collector assembly where the relative intensities of ion beams are measured and are than used to calculate isotope ratios (*Sharp*, 2017).

Carbon isotopes yield valuable information about the origin of a gas (biogenic/geogenic). Depending on the tectonic setting the composition of high CO_2 flux discharges can represent a mixture of relative contributions from the mantle, subducted carbonates and organic sediments (*Allard*, 1983). An extensive database of $\delta^{13}C_{CO_2}$ values from global volcanic and hydrothermal gas discharges along volcanic arcs has been developed over the past 30 years and reveals a large range of carbon isotopic values with the majority of samples falling between -6‰ to -2‰ indicative for upper mantle values (*Marty and Zimmermann*, 1999; *Oppenheimer et al.*, 2014).

The combined analysis of soil CO_2 flux and $\delta^{13}C_{CO_2}$ at the same location proved to be a reliable concept to determine soil CO_2 origin and revealed that isotopically derived thresholds for CO_2 fluxes can change the thresholds of simple statistical analysis of CO_2 flux data and the associated division into populations. This approach also revealed that low soil CO_2 fluxes (< 30 g m^2 d^{-1}) have carbon isotopic values of hydrothermal/mantle origin (*Chiodini et al.*, 2008; *Hanson et al.*, 2014; *Jentsch et al.*, 2020).

This has a direct influence on the spatial interpretation of CO_2 emissions in the context of structural controlled gas release. Further data from carbon isotopic values of carbonate rocks inside the reservoir or steam discharge from production wells are very useful for the interpretation of soil $\delta^{13}C_{CO_2}$ values. Eventually, the exact origin of carbon (mantle/crust) is not of too much importance in geothermal exploration, as long as the CO_2 flux and the associated carbon isotope value can be used to infer migration from deep areas.

5.2 Radon and Thoron

Radioactive decay is a natural, spontaneous process in which an atom of one element decays or breaks down to form another element by losing atomic particles. Radon (^{222}Rn) and thoron (^{220}Rn) are two gaseous, radioactive isotopes naturally-occurring in the Earth's crust from the radioactive decay of their parent nuclides uranium (^{238}U decay series) and thorium (^{232}Th decay series) and can be already detected at extremely low concentrations (*Baskaran*, 2016). Substantial amounts of uranium and thorium are found in granites, rhyolites, shales and sandstones. Felsic igneous rocks are found to have higher radon content than mafic rocks (*Belin*, 1959; *Regmi and Agah*, 2018). How fast an element decays is measured in terms of the element half-life. The half-life of radon before it decays to its daughter product ^{218}Po is 3.8 days, whereas thoron decays into ^{216}Po in a relatively short half-life of 55 s. Radon is chemically inert and thus it moves either as a gas or is transported by fluids, steam or other carrier gases such as carbon dioxide over long distances to the surface. This explains its abundance in especially convection-dominated geothermal systems (*Belin*, 1959; *Hernández et al.*, 2004; *Whitehead*, 1984).

5.2.1 ^{222}Rn and ^{220}Rn activity concentration

During the last decades a number of techniques have been developed for the measurement of ^{222}Rn and ^{220}Rn activity concentrations. Both isotopes decay by alpha particle emission at nuclide specific energies. The most common methods rely on the measurement of their short living daughter products ^{218}Po for ^{222}Rn and ^{216}Po for ^{220}Rn. A single-detector system analyses (^{222}Rn) and (^{220}Rn) simultaneously. Directly after the decay, the remaining ^{218}Po and ^{216}Po nuclei become charged positively. The set-up of an electrical field forces the ions to accumulate on the surface of a semiconductor silicon detector. The number of collected ions is equal to the radon and thoron concentration inside the measurement chamber. ^{218}Po decays with a half-life of 3.05 minutes and ^{216}Po in less than 1 s, therefore the equilibrium state between gas concentration and daughter products is reached after five half-lives for radon and immediately for thoron. This corresponds to a total measurement time of 15 minutes at each sampling point (*Baskaran*, 2016). A metal probe is installed 1 m in the ground and connected by a tube with the gas monitor. Soil gas is then pumped with a constant flow rate. A condensation flask is interconnected to avoid condensation and water from entering the tool directly. The unit of radioactivity is becquerel (Bq), which is equal to one atom decaying per second. Radon activity concentrations in soil gas are given in Bq m^{-3}.

It is well known that changes in atmospheric conditions such as barometric pressure, precipitation and wind speed show an influence on soil gas radon concentrations (*Gingrich*, 1984). Therefore, area-wide soil gas surveys over several days should take place during stable weather conditions. An increased spatial distribution can provide evidence of structural pathways that facilitate its migration, presuming the source is at greater depth (*Davidson et al.*, 2016; *Erees et al.*, 2006; *Jolie et al.*, 2015a). Due to the different half-life of ^{222}Rn and ^{220}Rn fluid migration velocities can be estimated and give evidence to hydrothermal upflow zones in geothermal reservoirs (*Giammanco et al.*, 2007; *Jolie et al.*, 2019). The continuous measurement of radon concentrations can also reveal information about subsurface fluid dynamics and increased seismic and volcanic activity (*Cigolini et al.*, 2007; *Sabbarese et al.*, 2020).

5.3 Helium

Helium is one of the most popular noble gases to interpret the origin of volcanic and hydrothermal gases. This has to do with its unambiguous origin from the crust and mantle traced by the two naturally occurring stable isotopes ^{3}He and ^{4}He and because it is chemically inert. Only a very low helium concentration (5.4 ppm) can be found in air. While ^{3}He is primordial and a remnant from the formation of the earth, ^{4}He has its source from the radioactive alpha decay of ^{238}U, ^{235}U and ^{232}Th. In nature the two isotopes occur in a ratio of 1:1000000 (^{3}He :^{4}He). Usually, the ^{3}He/^{4}He ratio (R) is normalized to the air value $R_A = 1.386 \times 10^{-6}$ and expressed as R/R_A (*Ozima, M. and Podosek*, 2002; *Sano and Wakita*, 1985). Living evidence of ongoing degassing of primordial ^{3}He from the Earth is found along ocean ridges and islands, most notably Iceland and Hawaii having the highest observed helium ratios of 28 R/R_A (*Graham*, 2002). The global average of volcanic arcs is 5.4 R/R_A (*Hilton et al.*, 2002) . Thus mantle-derived fluids and lavas present the main source of ^{3}He. Nevertheless, a wide range of ^{3}He/^{4}He values exists from various volcanic and hydrothermal discharges in the world (*Daskalopoulou et al.*, 2019; *Fischer and Chiodini*, 2015; *Karlstrom et al.*, 2013; *Notsu et al.*, 2001).

5.3.1 Helium isotopes

As explained above in 5.1.3, mass spectrometers can be optimized depending on the gases to be measured. For noble gas analysis, a gas sample is introduced to the mass spectrometer through a cryogenic preparation and purification line for the removal of water, permanent gases, and the separation of helium from neon. Than a source is ionizing the gas atoms by electron bombardment, which are accelerated and focused through a system of electric lenses by an ion optic and in the case of noble gases a magnetic field is applied to deflect ions by their mass to charge ratio. Finally, one detector measures large ion beams (^{4}He) in a Faraday cup, whereas smaller ion beams (^{3}He) are measured by an electron multiplier connected to an ion counting system (*Niedermann et al.*, 1997).

For the analysis of ^{3}He/^{4}He ratios in geothermal systems, samples should be taken from active degassing sites as we know that ^{4}He is the dominant isotope and contamination with addional ^{4}He from air should be avoided. Therefore, an inverted funnel is burried a few centimeters within the soil and positioned on top of an active steaming point. The funnel is connected to a tube and than a copper pipe with stainless-steel cramps on both sides. Once the copper pipe has been flushed with the gas sample, it is closed at both ends and the sample is analysed in the laboratory. The sampling time varies according to the gas flow but takes on average 10 minutes. Suitable sampling sites are limited due to the previously mentioned conditions that must be present. If active geothermal surface manifestations are absent, sampling of production steam from wells can be a reliable source for understanding the origin of geothermal fluids within a reservoir (*Kennedy and van Soest*, 2006; *Pinti et al.*, 2017).

5.4 Ground temperatures

Ground temperature measurements provide a very fast and easy way to detect geothermal activity in the shallow subsurface as the equipment is simply a thermocouple probe connected to a digital thermometer. Ground temperature is a function of heat transfer by means of radiation, convection, and conduction and is predominantly affected by the the structure and physical properties of the soil. Sufficient measurement depth (at least 50 cm) is necessary to reduce the influence of diurnal temperature cycles and thermal equilibrium is usually reached after 3-5 minutes. The determination of the spatial distribution of ground temperatures proved to be a promising indicator for structural controlled hydrothermal circulation (*Fairley and Hinds*, 2004a; *Rissmann et al.*, 2011) together with soil gas emissions (*Chiodini et al.*, 2015; *Taussi et al.*, 2021) but also for the estimation of geothermal heat flow (*Hernández et al.*, 2012; *Rissmann et al.*, 2012). However, anomalous ground temperatures can also occur without increased gas emissions due to conduction. This provides additional information about the circulation of hot geothermal fluids at shallow depths that are impeded in their vertical upflow by low-permeable rocks/soil (*Hanson et al.*, 2014; *Jentsch et al.*, 2020).

Part II

Applications

6

Los Humeros Scouting

Magmatic volatiles to assess permeable volcano-tectonic structures in the Los Humeros geothermal field, Mexico

Anna Jentsch, Egbert Jolie, David G. Jones , Helen Taylor-Curran, Loïc Peiffer, Martin Zimmer, Bob Lister

Article published in *Journal of Volcanology and Geothermal Research*, 2020.
`https://doi.org/10.1016/j.jvolgeores.2020.106820`

Abstract: Magmatic volatiles can be considered as the surface fingerprint of active volcanic systems, both during periods of quiescent and eruptive volcanic activity. The spatial variability of gas emissions at Earth's surface is a proxy for structural discontinuities in the subsurface of volcanic systems. We conducted extensive and regular spaced soil gas surveys within the Los Humeros geothermal field to improve the understanding of the structural control on fluid flow. Surveys at different scales were performed with the aim to i) identify areas of increased gas emissions (reservoir scale), ii) their relation to (un)known volcano-tectonic structures (fault scale) favoring fluid flow, and iii) determine the origin of gas emissions. Herein, we show results from a CO_2 efflux scouting survey, which was performed across the main geothermal production zone (6 km x 4 km) together with soil temperature measurements. We identified five areas with increased CO_2 emissions, where further sampling was performed with denser sampling grids to understand the fault zone architecture and local variations in gas emissions. CO_2 efflux values range from below detection limit of the device to 1,464 g m^{-2} d^{-1} with a total output of 87 t d^{-1} across an area of 13.7 km^2. Furthermore, $\delta^{13}C_{CO2}$ and $^3He/^4He$ analyses complemented the dataset in order to assess the origin of soil gases. Carbon isotopic data cover a broad spectrum from biogenous to endogenous sources. Determined $^3He/^4He$ ratios indicate a mantle component in the samples of up to 65 % being most evident in the northwestern and southwestern part of the study area. We show that a systematic sampling approach on reservoir scale is necessary for the identification and assessment of major permeable fault segments. The combined processing of CO_2 efflux and $\delta^{13}C_{CO2}$ facilitated the detection of permeable structural segments with a connection to the deep, high-temperature geothermal reservoir, also in areas with low to intermediate CO_2 emissions. The results of this study complement existing geophysical datasets and define further promising areas for future exploration activities in the north- and southwestern sector of the production field.

6.1 Introduction

Volcanic-hosted geothermal systems comprise a vast amount of thermal energy with the potential to reach supercritical conditions ($T > 374°C$ and $P > 221$ bar for pure water) nearby magmatic intrusions (*Scott et al.*, 2015). The identification, characterization, assessment, and development of exploitation concepts for the Los Humeros superhot geothermal resource is the focus of the Mexican-European collaborative project GEMex (*Jolie et al.*, 2018). The successful utilization of the superhot reservoir is expected to increase the overall productivity of the field. However, technical challenges associated with reservoir fluids of aggressive physicochemical characteristics, drilling into high-temperature zones $> 350°C$, and insufficient formation permeability need to be overcome (*Gutierrez-Negrin and Izquierdo-Montalvo*, 2010). The structural control of permeability and fluid flow in volcanic-geothermal reservoirs like Los Humeros has a substantial influence on the geothermal potential of the system (*Jafari and Babadagli*, 2011). Hydrothermal fluid flow occurs preferentially along major subsurface discontinuities (*Curewitz and Karson*, 1997; *Jolie et al.*, 2016, 2019; *Rossetti et al.*, 2011; *Rowland and Sibson*, 2004).

Previous studies at Los Humeros focused already on the structural architecture of the large silicic caldera (*Campos-Enriquez and Arredondo-Fragoso*, 1992), but thick layers of post caldera volcanic material are expected to cover many faults and fractures (*Norini et al.*, 2015a). Fluid migration is mainly controlled by a pronounced fault network (*Arellano et al.*, 2003; *Norini et al.*, 2015a; *Peiffer et al.*, 2018), while petrophysical analyses of samples from the reservoir units indicate low to medium permeability (*Weydt et al.*, 2018). Geophysical surveys (e.g., resistivity, gravity, seismicity) are commonly used in geothermal exploration, but cannot resolve single permeability structures rather than wide zones. More importantly, resistivity imaging is limited in its differentiation between active and past hydrothermal activity. In this context, soil gas surveys substantially complement established geophysical exploration techniques by indicating recent volcanic-geothermal activity. Spatial variations of gas emissions and their isotopic composition can be related to permeable segments of the structural framework in a volcanic complex, and provide clear evidence of an active geothermal system with hydrothermal fluid circulation. Therefore, we performed an extensive, regularly-spaced CO_2 efflux survey at Los Humeros Volcanic Complex (LHVC) with the aim to identify and quantify areas of increased gas emissions as indicator of permeable pathways connecting the deep volcanic-geothermal system with Earth's surface.

CO_2 is one of the most abundant gases in volcanic-geothermal systems as it exsolves from magma at greater depth (*Edmonds and Wallace*, 2017). CO_2 emissions can be measured in-situ by the accumulation chamber technique (*Parkinson*, 1981) with a sampling time of only 2-3 min per site. Additionally, we sampled from selected sites for carbon and helium isotope analyses to determine the origin of fluids and assess transport processes of CO_2 and He. Helium isotopes ($^3He/^4He$) are excellent tracers to differentiate between crustal or mantle derived fluids, since both isotopes are stable, chemically inert and insoluble in water (*Ozima, M. and Podosek*, 2002). ^3He was trapped in the mantle during Earth accretion, while ^4He is a decay product of the natural occurring radionuclides (^{238}U, ^{235}U, ^{232}Th) and present in the crust and atmosphere (*Karlstrom et al.*, 2013; *Notsu et al.*, 2001; *Ozima, M. and Podosek*, 2002). Based on results from the large-scale CO_2 efflux scouting survey, multiple domains with increased CO_2 emissions were identified for a more specific assessment by smaller grids. The domain-based approach was applied to gain a high-resolution picture across areas with increased gas emissions, to identify segments of highest permeability, and to understand the heterogeneity of gas emission over short distances, especially along fault damage zones (*Caine et al.*, 1996; *Jolie et al.*, 2016).

6.2 Geology

The Trans-Mexican Volcanic Belt (TMVB) is a 1,000 km long Neogene volcanic arc resulting from the subduction of the two oceanic plates, Cocos and Rivera, under the North American Plate (*Pérez-Campos et al.*, 2008, Figure 6.1a). Three of the five geothermal production fields used for power generation in Mexico are located within the TMVB (*Gutiérrez-Negrín*, 2019). The LHVC is the largest, silicic caldera complex in the eastern part of the TMVB (*Carrasco-Núñez et al.*, 2017b, Figure 6.1a) and hosts a high-temperature geothermal system, which is currently utilized by a geothermal power plant with an installed capacity of 95 MWe (*Gutiérrez-Negrín*, 2019).

6.2.1 Geological history

The Los Humeros caldera has a complex geological and tectonic evolution studied in detail during the early stages of exploration by *Ferriz and Mahood* (1984), who dated the beginning of the caldera forming volcanism to 460 ± 40 ka lasting until 50 ± 20 ka ago. Recently, *Carrasco-Núñez et al.* (2018) determined a much shorter time frame for the caldera forming stage (164 ± 4.2 ka until 69 ± 16 ka ago) and concluded that the existence of such a high enthalpy geothermal system must be related to a young heat source. The following stratigraphic description refers mainly to the work of *Carrasco-Núñez et al.* (2017a,b, 2018) and references therein. The pre-, syn-, and post-caldera evolution is marked by alternating episodes of explosive and effusive eruptions producing a large range of volcanic rocks from different sources and depths (*Lucci et al.*, 2019). The basement of the LHVC is comprised of a thick layer of Paleozoic granites and Mesozoic limestones with major mafic and silicic intrusion overlain by andesitic and basaltic lavas (Teziutlan Formation; 1.44 – 2.65 Ma) (*Carrasco-Núñez et al.*, 2017a). The onset of the caldera forming period was dominated by an immense, explosive eruption 164 ± 4.2 ka ago causing the irregular shaped Los Humeros caldera with a diameter of approximately 20 km (*Carrasco-Núñez et al.*, 2018, Figure 6.1b). Followed by a period of plinian eruptions producing different pumice fallouts known as the Faby Tuff, a second major caldera forming event formed the Los Potreros caldera 69 ± 16 ka ago (*Carrasco-Núñez et al.*, 2017a). This semicircular caldera with a diameter of around 10 km hosts the present-day active geothermal system. During the post-caldera episode, volcanic activity inside the caldera moved from the central part of the geothermal field to the northern and southern areas where volcanic activity mainly occurred along ring faults (monogenetic eruptive centers). Another significant eruption inside the Los Humeros caldera occurred 7.3 ± 0.1 ka ago and left the oval shaped Xalapazco crater (approx. 1.7 km in diameter, Fig.1b) in the south of the complex (*Carrasco-Núñez et al.*, 2018; *Ferriz and Mahood*, 1984; *Willcox*, 2011). The youngest activity occurred 2.8 ± 0.03 ka ago, which produced a trachytic lava flow in the vicinity of the SW caldera rim (*Carrasco-Núñez et al.*, 2017a).

6.2.2 Structural evolution

The Los Humeros geothermal reservoir, hosted by the pre-caldera andesites, is characterized by medium to low matrix permeability (*Gutierrez-Negrin and Izquierdo-Montalvo*, 2010). Hence, main geothermal fluid flow can only be controlled by a dense fault/fracture network resulting from different periods of volcano-tectonic activity (*Norini et al.*, 2019). Early structural analysis by *Campos-Enriquez and Garduño-Monroy* (1987) concentrated on the regional tectonic regime and its impact on the local fault system within the LHVC, which revealed two dominant regional structural systems of NW-SE and NE-SW orientation. Further extensive structural fieldwork by *Norini et al.* (2015a, 2019) across the LHVC and surrounding areas confirmed the influence of the two dominant regional structural systems on faults inside the caldera. The initial regional fault system evolved from a NE-SW compressive orogenic phase resulting in the Mexican Fault and Thrust Belt (MFTB) leaving NW-SE/NNW-SSE oriented folds and thrust faults in the sedimentary basement (S_{Hmax} = NE-SW; S_{hmin} = NW-SE). These basement structures favored the later development of the main NW-SE/NNW-SSE normal fault system (e.g., Los Humeros and Maztaloya fault), which developed during caldera collapse and post caldera volcanic activity under an extensional regime (NE-SW). The second fault system is related to the TMVB evolution, which evolved under a regional NE-SW extensional stress regime (S_{Hmax} = NW-SE; S_{hmin} = NE-SW) evolving NE-SW striking normal faults. Faults like Pedernal or Cueva Ahumada (Figure 6.1c) are local volcanotectonic faults, which were generated after the Los Potreros caldera collapse but their morphology may be a heritage of TMVB regional faults as they follow a NE-SW strike. The present-day faulting activity is influenced by an extensional (regional) and radial (local) stress field, which relates to the shallow magmatic/hydrothermal system with recent normal and reverse faulting (Figure 6.1c; *Norini et al.*, 2019). Past and recent hydrothermal fluid flow is indicated along known deep-rooted faults (e.g., La Cuesta, Los Humeros, Arroyo Grande) connected with the geothermal reservoir (secondary permeability) (*Norini et al.*, 2019). Deep-rooted regional faults within the basement of the caldera are indicated by water isotopic analyses of fluid samples from springs and wells in and around the LHVC, suggesting a regional recharge of the geothermal system (*Lelli and Villanueva Alfaro Cuevas*, 2019).

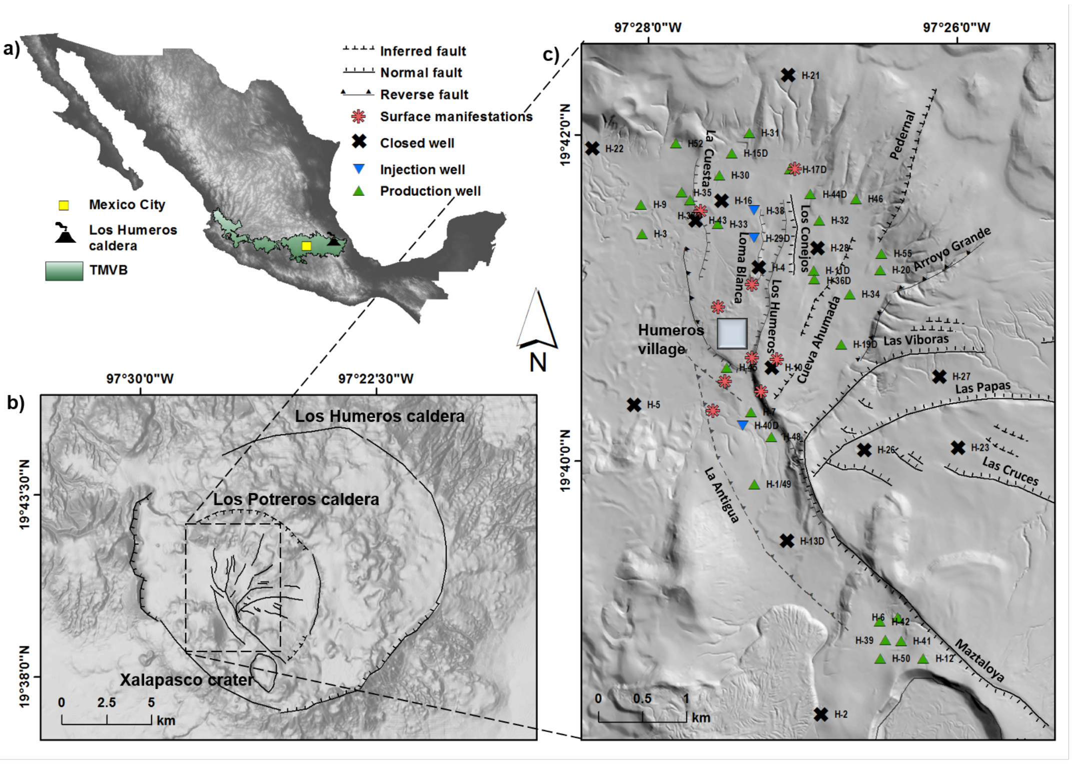

Figure 6.1: a) Map of Mexico showing the location of the Los Humeros caldera within the Trans Mexican Volcanic Belt (TMVB). b) Digital elevation model (DEM) reproduced with permission of Instituto Nacional de Estadística y Geografía (INEGI) showing mapped and inferred scarps of the Los Humeros and Los Potreros caldera originating from the two main caldera forming events. The youngest evidence for active volcanism inside the caldera is the Xalapasco crater (7.3 ± 0.1 ka) in the south. c) High resolution DEM (1m) of the study area from *Carrasco-Núñez et al.* (2017a) showing all injection (green triangle down) and production wells (blue triangle up). Solid and dashed black lines represent the fault network transferred from *Norini et al.* (2015a). Red asterisks show locations of surface manifestations e.g. advanced argillic alteration, weak steam vents, sulfatara, and warm ground (own observation). Light grey square indicates the location of Humeros village.

6.3 Methods

6.3.1 Sampling approach

Systematic soil gas surveys in volcanic and geothermal areas require the development of site-specific sampling concepts. The decision of whether or not an area is investigated by transects or (ir)regular grids depends on the objective of the survey, time, accessibility to the area, and site-specific characteristics such as the presence of fumaroles, alteration, known structures and other factors (*Fridriksson et al.*, 2006; *Hernández et al.*, 2012; *Parks et al.*, 2013; *Rodríguez et al.*, 2015). Specific areas with obvious gas emissions are often sampled with a higher density of measurements for a more accurate detection of variations in soil gas emissions and delineation, whereas areas with less obvious gas emissions are often not taken into account (*Chatterjee et al.*, 2019; *Werner et al.*, 2000) despite the chance of missing permeable structures (hidden faults). Multiple studies showed the advantage of regular spaced surveys (*Jolie et al.*, 2019; *Werner et al.*, 2000). Systematic grid sampling is an effective and unbiased concept to collect spatially correlated data over a large area (geothermal reservoir scale) whilst avoiding interpolation artefacts (*Isaaks and Srivastava*, 1989) and allowing a detailed estimation of the total CO_2 output (combined advective and diffuse degassing) (*Lee et al.*, 2016).

For the CO_2 scouting survey (2017), we developed a regular sampling network for an area of 6 km × 4 km adapted specifically to the structural setting. The network consists of 2,700 CO_2 efflux-sampling points with the purpose to detect spatial variability of soil gas emissions across major parts of the geothermal production field. The sampling grid is defined by 25 m × 200 m spacing with the small point spacing oriented perpendicular to the major fault strike (NNW-SSE) within the caldera (Table 6.1, Figure 6.3a). CO_2 efflux was measured in-situ (60–120 s) by means of the accumulation chamber method (*Chiodini et al.*, 1998). Due to expected anthropogenic disturbances no CO_2 efflux measurements were performed in Humeros village.

Based on the results of the CO_2 efflux scouting survey, five main areas have been identified with increased CO_2 emissions. These areas (Figure 6.3a) were investigated at higher resolution in 2018 (Table 6.2) by the accumulation chamber method. The domain-based approach facilitated a more detailed estimation of CO_2 output for the investigated areas.

6.3.2 CO_2 efflux and soil temperature

CO_2 efflux measurements were performed with portable LICOR LI-820 infrared gas analyzers being connected through a closed loop to an accumulation chamber Type A. The LI-820 is a non-dispersive, infrared (NDIR) gas analyzer based upon a single path, dual wavelength detection system. The measuring range is between 0 and 20,000 ppm with a maximum gas flow rate of 1 l min^{-1} (*West Systems*, 2019). A detailed description of the accumulation chamber method is defined by (*Chiodini et al.*, 1998). All measurements and sampling took place under dry weather conditions. Soil temperatures were measured at 50 cm depth with a Greisinger GMH 285-BNC thermometer (accuracy ± 0.1 °C) coupled to a 620 mm long stainless steel probe. For the domain-based surveys a Hanna HI-93510® thermistor thermometer (accuracy ± 0.4 °C) fitted to a 500 mm temperature probe was used.

The statistical evaluation of CO_2 efflux data was performed by the graphical statistical analysis (GSA) introduced by (*Sinclair*, 1974, Figure 6.2). This method is commonly used to separate large datasets by plotting the logarithmic CO_2 efflux values against the cumulative frequency and identifying major inflection points as a key indicator of different populations. By identifying multiple log-normal populations different gas sources and/or transport mechanisms can be inferred. A detailed description of the GSA method was compiled by (*Chiodini et al.*, 1998, 2008). Both datasets (scouting and domain-based CO_2 surveys) have been merged for statistical analyses.

The interpolated maps of CO_2 efflux and soil temperature were generated by means of sequential Gaussian simulations (sGs) using ESRI ArcGIS®10.5 software. The sGs algorithm was introduced by *Deutsch and Journel* (1998), who emphasize that sGs respects original data without smoothing extreme values in order to preserve spatial variations. In total, 100 realizations were performed for the sGs based on a simple kriging model. The sGs procedure requires a gaussian distribution of data. Therefore, all data were normal score transformed and declustered to correct data distribution before the generation of omnidirectional variograms. All variograms and related model parameters can be found in the supplementary material.

Interpolated maps have been computed up to 97 g m^{-2} d^{-1}, since merely 3% of the data show values $\geq$ 97 g m^{-2} d^{-1}. The strong variation of effluxes over short distances respects high values more than low resulting in a different appearance of anomalies. Through the comparison of the different interpolations (map including all values versus map including only values up to 97 g m^{-2} d^{-1}), we assessed that the exclusion of values $\geq$ 97 g m^{-2} d^{-1} in our interpolation method emphasizes the spatial extent of lower degassing areas with hydrothermal signatures, which play a major role regarding structural related degassing. This way of data presentation still respects all information since values above 97 g m^{-2} d^{-1} are illustrated as graduated black triangles on maps.

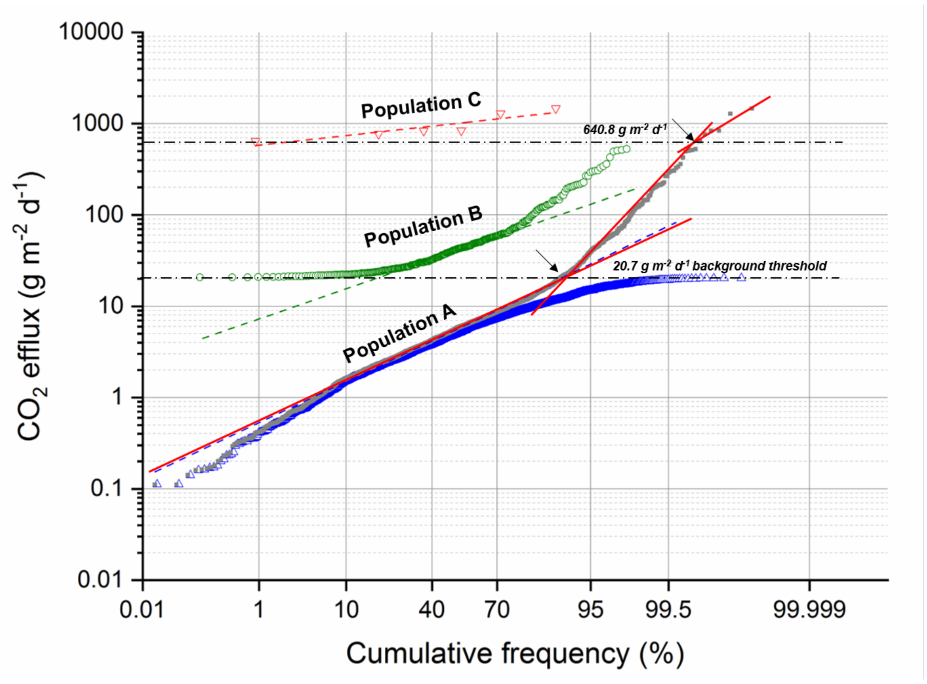

Figure 6.2: Probability plot for the entire CO_2 efflux dataset. Black arrows point on the inflection points, which divide the dataset in to three populations. Lower dashed black line indicates the threshold value for background CO_2 efflux and the upper one indicates the threshold between population B and C.

6.3.3 $\delta^{13}C_{CO_2}$

94 soil gas samples were collected for $\delta^{13}C_{CO_2}$ isotopic analyses (Table 6.1 and Table 6.2) from areas of low, intermediate and high CO_2 efflux to constrain the origin of CO_2 emissions by their isotopic signatures (biogenous, endogenous). A hollow metal probe was installed in 1 m depth for gas sampling. To avoid any contamination with ambient air, the metal probe was flushed five times with a 60 ml syringe before collecting a gas sample. The sample was injected into an evacuated 12 ml glass vial with a pierceable septum. Analyses were performed with a GC-C-IRMS system consisted of a GC (6890N, Agilent Technology, USA) connected to a GC-C/TC III combustion device coupled via open split to a MAT 253 mass spectrometer (ThermoFisher Scientific, Germany) under continuous flow. The quality of the carbon isotope measurements was checked by direct injection a CO_2-reference gas with known δ^{13}C into the mass spectrometer during each run as well as by daily measurements of n-alkane gas standard (n-C1 to n-C6). The standard deviation is <0.5 ‰. Herein, all results are reported in the

standard notation δ as per mille (‰) deviations relative to the PDB (Pee Dee Belemnite) standard.

6.3.4 ^{3}He/^{4}He ratios

To further constrain the origin of gas emissions, six helium samples were taken from selected sites to determine the ^{3}He/^{4}He ratios. Samples were taken on steam vents to reduce the contribution of ^{4}He from ambient air by placing a funnel on the outlet of the steam vent, which was connected via a flexible tube to a 40 cm copper pipe. If steam flow was insufficient, gas was aspirated with a hand pump for about two minutes. Metal clamps were fixed to each end of the copper tube and tightly closed for a safe storage of the gas. The samples were analyzed with a VG-5400 mass spectrometer. Results were normalized to the air ratio ($R/R_A = 1.386 \times 10^{-6}$).

Table 6.1: Summary of all measured parameters and sampling specifications including their minima, maxima and mean values from the survey in 2017 (May-June); Lab = laboratory; b.s. = below surface; a.s. = at surface

Parameters	Dimension of study area [km]	Grid spacing [m]	N	Sampling procedure/Analysis	Sampling time [min]	Min	Max	Mean
CO_2 efflux [g $m^{-2}d^{-1}$]	6 × 4	25 × 200	2,823	a.s./ In-situ	1-2	0	839	8.5
$\delta^{13}C$-CO_2 [δ ‰ vs. VPBD]	Selected sites	Single points	38	1m b.s./ Lab	approx. 10	-19.2	-1.2	-7.9
Ts [°C]	5.8 × 2.4	50/100 × 200	858	50 cm b.s./ In-situ	approx. 10	5.9	91.3	17.5
$^3He/^4He$ [R/R_A]	Selected sites	Single points	6	Variable depth (max. 30 cm b.s)/ Lab	10	2.31	4.88	3.4

6.4 Results

A summary of the different parameters is presented in Table 6.1 and Table 6.2. CO_2 efflux values from the two field campaigns show a wide range and vary from below detection limit to 1,464.2 g m^{-2} d^{-1}. By applying the GSA method two inflection points have been identified at the 90 % and 99.8 % cumulative percentile, which separate the dataset into three populations with a gently sloping central segment (Figure 6.2). Sinclair (1974) explains this kind of shape as characteristic for an overlap of two populations (A+B). Population A corresponds to low background efflux values (0.1 – 20.7 g m^{-2} d^{-1}). Population B is a mixed population with a wide range of values (20.7 – 640.8 g m^{-2} d^{-1}), and Population C includes the highest measured values (670.8 – 1,464.2 g m^{-2} d^{-1}) in the study area. Statistical parameters obtained by the GSA method are reported in Table 6.3. The low fraction of high degassing values is related to our sampling approach, which follows a regular sampling grid rather than mapping exclusively areas of high CO_2 emissions with only a few sites of background values. In consequence, the domain-based survey in 2018 resulted in more data points assigned to population C as the focus was on areas of increased CO_2 emissions.

6.4.1 CO_2 efflux scouting survey and soil temperatures

Figure 6.3a shows the result of sequential Gaussian simulations (mean out of 100 simulations) from the CO_2 efflux scouting survey in 2017. Bold capital letters in Figure 6.3a refer to results explained in the following paragraph. Zones with gas emissions exceeding the background threshold ($>$ 20.7 g m^{-2} d^{-1}) occur across the entire study area (Area A to G). Areas A, C, D, and E define a well pronounced NNW-SSE corridor (3 km × 1.5 km) of increased gas emissions $>$ 100 g m^{-2} d^{-1}. The maximum CO_2 efflux was measured in Area E with 839 g m^{-2} d^{-1} (Figure 6.3a). La Cuesta fault in Area A and Los Humeros fault in Area D show increased CO_2 degassing in their foot- and hanging walls ($<$ 200.9 g m^{-2} d^{-1}). Areas A to E are characterized by major CO_2 emissions, which occur together with geothermal surface manifestations, such as weak steam vents, sparse solfatara, and hot ground with temperatures up to 91°C, and argillic alteration (*Gutierrez-Negrin and Izquierdo-Montalvo*, 2010). However, areas of increased CO_2 emissions are not limited to these features. There are no significant CO_2 emissions or geothermal surface expressions in the south of the study area (Area H, Figure 6.3a). Almost no gas emissions have been detected in Area I, which is covered by a young basalt flow (*Carrasco-Núñez et al.*, 2017a).

Soil temperatures at 50 cm depth vary from 5.7 °C to 91.3 °C (Table 6.1). The histogram (Figure 6.4) shows a right skewed frequency distribution for soil temperatures illustrating that the majority of values were low, while the probability plot indicates a prominent inflection point at 22 °C. Increased soil temperatures ($>$ 22 °C) occur in or close to areas of increased degassing (Area A-E; Figure 6.5a). In addition, Area J and K show increased temperatures of 41 °C and 26 °C, respectively (Figure 6.5a). The maximum measured soil temperature of 91.3 °C occurred in Area C, where active solfatara is located.

Table 6.2: Summary of all measured parameters with minimum, maximum and mean values from the surveys in 2018 (February & April – Area D). The analysis and sampling procedure are given in Table 6.1. Location of Areas A to F can be seen in Figure 6.3a. Note that results of Area F are not shown in Figure 6.3b, since emissions are mainly background ($\leq 22.\ 4$ g m^{-2} d^{-1}) and carbon isotopic values indicate a biogenic origin of CO_2. VPBD = Vienna Pee Dee Belemnite

			CO_2 emissions				Carbon isotopes				Soil temperatures			
	Dimension of study area [m]	Grid spacing [m]	N CO2 efflux [g m^{-2}d^{-1}]	Min	Max	Mean	N δ^{13}C-CO2 [δ ‰ vs. VPBD]	Min	Max	Mean	N Ts [°C]	Min	Max	Mean
Area A	400 × 300	25 - 30 × 90 - 120	64	0.71	1,464.2	61.1	7	-18.0	-2.9	-5.9	10	12.2	22.1	18.1
Area B	300 × 200	25 - 30 × 90 - 120	40	2.12	63.8	22.7	10	-20.5	-3.7	-9.8	39	13.1	52.3	27.2
Area D	140 × 260	10 × 10	480	0.16	526.2	25.2	6	-18.4	-2.4	-7.2	-	-	-	-
Area E	770 × 500	25 - 30 × 90 - 120	131	0.49	1,285.5	44.5	23	-19.8	-1.6	-6.5	128	8.3	36	18.1
Area F	500 × 350	25 - 30 × 90 - 120	83	1.88	22.4	8.55	8	-23.2	-12.7	-18.4	83	5.7	22.6	14.1

Table 6.3: Statistical parameters of the total CO_2 efflux dataset obtained by the graphical statistical analysis.

Population	Proportion [%]	N	Mean CO_2 efflux [g m^{-2} d^{-1}]	CO_2 efflux range [g m^{-2} d^{-1}]
Background Population (A)	90.2	3,203	6	0.1 – 20.7
Mixed Population (B)	9.7	344	66.4	20.7 – 640.8
Hydrothermal Population (C)	0.1	5	1,038.1	640.8 – 1,464.2

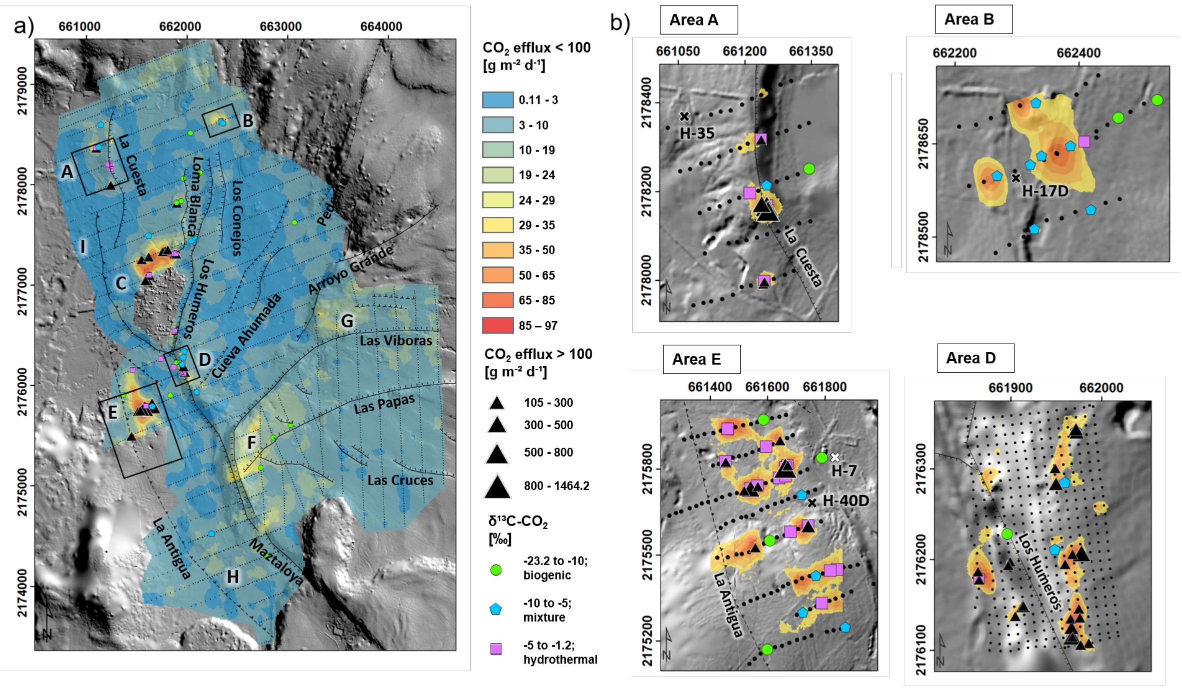

Figure 6.3: Results of sequential Gaussian simulation for CO_2 efflux a) from 2017 showing the distribution of low, intermediate and elevated degassing sites up to 97 g m^{-2} d^{-1}. Black squares (A, B, D, E) show the location and size of the small scale surveys performed in 2018. b) CO_2 efflux maps for Area A, B, E, and D. Values lower than 29 g m^{-2} d^{-1} are masked. Labeled black crosses show location of production wells. The white cross in Area E shows an injection well. Graduated black triangles (all maps) illustrate CO_2 efflux values >97 g m^{-2} d^{-1}. The classification of carbon isotopic measurements and related symbols applies to all maps. Small black dots represent CO_2 efflux sampling sites. Solid and dashed black lines illustrate known and inferred faults. The grey cutout between Area C and D shows Humeros village where no measurements were performed to avoid artificial effects.

6.4.2 Domain-based CO_2 efflux and soil temperature survey

Figure 3b shows diffuse CO_2 emissions of four selected domains out of five. All values below 29 g m^{-2} d^{-1} are masked. Highest CO_2 efflux values of 1,285.5 g m^{-2} d^{-1} and 1,464.2 g m^{-2} d^{-1} were measured in Area E and A, respectively. All three areas (A, D, E) are characterized by a general NNW-SSE orientation of increased CO_2 emissions. Area D is an excellent example of highly variable CO_2 emissions over short distances resolved by a grid spacing of 10 m × 10 m. In comparison to the large-scale scouting survey, where increased CO_2 degassing appears less variable, the domain-based surveys improved the spatial resolution in these areas. Nevertheless, both sampling concepts provide similar results for the occurrence of major diffuse CO_2 emissions despite different grid spacing. During domain-based sampling, soil temperatures

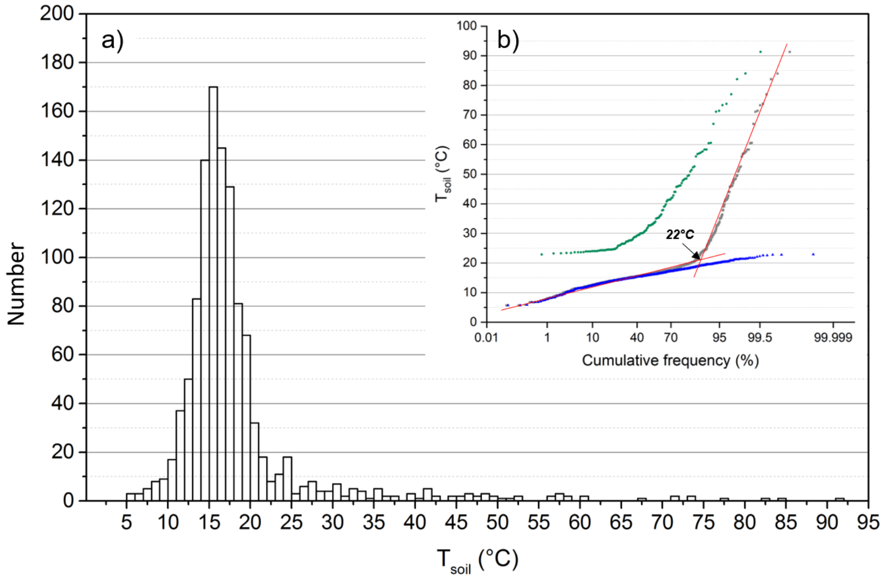

Figure 6.4: a) Histogram showing a right skewed frequency distribution of soil temperatures. The majority of values (87.9%) range between 5.9 °C and 22 °C. b) Probability plot of soil temperatures indicating a major inflection point at 22 °C, which separates the dataset into background and anomalous soil temperatures.

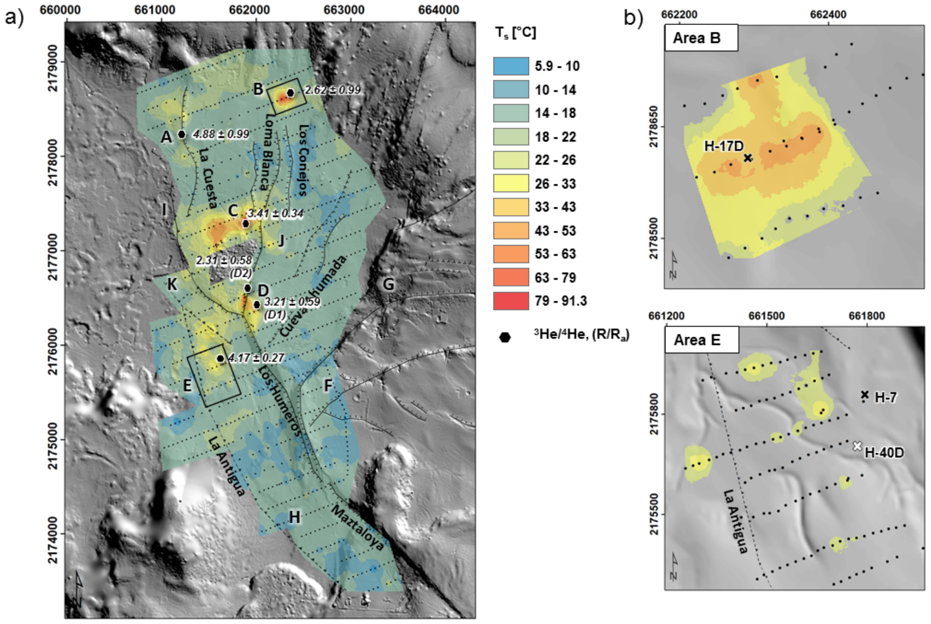

Figure 6.5: Results of sequential Gaussian simulation a) for all measured soil temperatures in 2017. Black small dots represent soil temperature sampling sites. Black hexagons illustrate sampling sites and re-sults for air-corrected helium ratios at weak to moderate steam vents. Note that two helium samples were taken in Area D (D1 and D2). Black squares show the location of the small scale surveys for Area B and E. b) Soil temperature maps for Area B, and E. Temperatures below 25°C are masked. Black and white crosses illustrate production and injection wells, respectively.

were solely measured in Area B and E (Figure 6.5b and Table 6.2). A maximum temperature

Table 6.4: Summary of CO_2 output estimations from the large-scale and small-scale surveys at Los Humeros. For comparison we included values from the study of *Peiffer et al.* (2018) as well as other volcanic/geothermal systems worldwide.

Study Area	Area [km^2]	Total CO_2 output [t d^{-1}]	Standard deviation	Reference
Total study area	13.6	87.3	10.2	This study
Total study area above background threshold	0.5	26.1	0.078	
Area A	0.13	1.6	8×10^{-5}	
Area B	0.06	1.3	9.1×10^{-5}	
Area D	0.04	0.7	1.2×10^{-4}	
Area E	0.43	10.6	1.5×10^{-4}	
Humeros North	0.06	13.5	3.9	*Peiffer et al.* (2018)
Humeros South	0.012	2.66	0.3	
Xalapasco	0.0045	1.38	0.05	
Volcanic/Geothermal system Kos, Greece	0.4	74.7a	n/a	*Daskalopoulou et al.* (2019)
Volcanic/geothermal system Monte Amiata, Italy	0.22	221	25	*Frondini et al.* (2009)
Volcanic/geothermal system Reykjanes, Iceland	0.23	13.9	1.7	*Fridriksson et al.* (2006)
Geothermal system Ohaaki, New Zealand	12.7	111	6.7	*Rissmann et al.* (2012)

[a] Only CO_2 efflux values above biogenic threshold are included

of 52.9 °C was measured in Area B coinciding with increased CO_2 emissions. In Area E well defined cluster have been identified with soil temperatures up to 35 °C.

6.4.3 Isotopic analyses

Carbon isotopic values range from -23.2‰ to -1.2‰ ± 0.07‰ (Table 6.1 and Table 6.2), covering a broad spectrum of sources (Figure 6.3a and Figure 6.3b). Steam vents were selected for $^3He/^4He$ ratio analyses (Figure 6.5a). $^3He/^4He$ ratios deviate for all samples from the air helium isotopic ratio (R_A = 1.386 × 10-6) and confirm a mantle contribution. The measured ratios range from 2.31 ± 0.58 to 4.88 ± 0.99. Highest $^3He/^4He$ ratios were identified in Area A and E, coinciding with maximum measured CO_2 emissions.

6.4.4 CO_2 output estimations

Based on the sequential Gaussian simulation maps for the investigated areas, a CO_2 output estimation was computed. Each CO_2 degassing rate is the sum of the product of each grid cell by the cell surface. The total CO_2 output (biogenous plus endogenous) is estimated to be 87.6 t d^{-}1, whereas the CO_2 output calculated above the biogenic threshold only accounts for 26.1 t d^{-}1. A detailed summary of results from all areas is given in Table 6.4, which also includes CO_2 degassing rates computed by *Peiffer et al.* (2018). It is noteworthy that their results are based on random and dense sampling points concentrating on known high degassing areas in Los Humeros. For comparison, we included further CO_2 output estimations from other volcanic-geothermal systems worldwide (Table 6.4). A comprehensive data compilation of CO_2 output estimations from various active, dormant, and inactive volcanic regions worldwide is summarized in a study of (*Kis et al.*, 2017).

6.5 Discussion

6.5.1 CO_2 efflux and $\delta^{13}C_{CO_2}$

6.5.1.1 Population A

The majority of measured CO_2 efflux values belong to population A with a mean of 6.6 g m^{-2} d^{-1} (Table 6.3). The inflection point separating the background population from the remaining values is defined at 20.7 g m^{-2} d^{-1} (Figure 6.2). Such low efflux values typically originate from biogenic sources (i.e. plant and microbial respiration and organic decomposition; see also (*Cardellini et al.*, 2003; *Hutchison et al.*, 2015; *Jolie et al.*, 2019; *Peiffer et al.*, 2014; *Werner et al.*, 2000). In fact, maximum CO_2 efflux values reported for biogenic sources generally range from below detection limit of the device up to a few tens of grams per square meter and day in highly vegetated areas, but never exceed 100 g m^{-2} d^{-1} (*Chiodini et al.*, 2007; *Raich and Tufekcioglu*, 2000; *Widén and Majdi*, 2011). *Peiffer et al.* (2018) report similar results for areas without any apparent geothermal manifestations in the Los Humeros caldera with a mean of 7.4 g m^{-2} d^{-1}. The overall vegetation within the survey area is very sparse and dominated by shrubs and dry grasses growing on loose soil consisting of pumice tuff mixed with organic material. However, to some extend the northern part is used for maize cultivation, whereas the south is partly forested by pine trees. Additionally, most $\delta^{13}C_{CO_2}$ samples acquired in this study confirm this observation by heavier $\delta^{13}C_{CO_2}$ values < -10‰. Figure 6 illustrates the relation between CO_2 efflux and corresponding carbon isotopic composition in context to previously published carbon isotopic data from Los Humeros (*González-Partida et al.*, 1993; *Peiffer et al.*, 2018; *Portugal et al.*, 1994; *Richard et al.*, 2019; *Truesdell and Quijano*, 1988).

We have identified seven locations with CO_2 efflux values lower than 20.7 g m^{-2} d^{-1}, but with a $\delta^{13}C_{CO_2}$ isotopic composition ranging from -3.9‰ to -7‰ (Area A, D, E) indicating a clear contribution of hydrothermal and mantle-derived CO_2 (Figure 6.6). The identified locations are up to 200 m distant to areas with increased gas emissions, which indicates that the actual dimension of geothermally active areas is larger than expected. This finding agrees with *Chiodini et al.* (2008), who estimated a larger size of a diffuse degassing structure at Solfatara of Pozzuoli by using the biogenic threshold resulting from $\delta^{13}C_{CO_2}$ analysis of respective CO_2 effluxes. Following the approach of *Chiodini et al.* (2008) our carbon isotopic dataset is separated in three populations (Table 6.5; Figure 6.3 in the supplementary data). The range for biogenic CO_2 effluxes determined by the separation of carbon isotopes shows a similar range based on the statistical separation of the CO_2 efflux dataset (Population A). Whereas the range of CO_2 effluxes resulting from $\delta^{13}C_{CO_2}$ analysis in the mixed and hydrothermal groups, show much lower minimum values (1 g m^{-2} d^{-1}) than those identified by the statistical separation of the CO_2 efflux dataset in population B and C (Table 6.5). These low emissions occurring in the mixed and hydrothermal group are likely caused by advection at low rates, similar to biogenic emission rates, due to low permeability of soil/rocks and/or low-pressure gradients from the reservoir to the surface. Diffusion of hydrothermal CO_2 can also explain low emissions, if CO_2 concentration gradients are present within the soil system (*Peiffer et al.*, 2014). The combined analysis of CO_2 efflux and carbon isotopes for a differentiation of carbon sources is a powerful approach to estimate the actual extent of geothermally active areas.

Almost no gas emissions have been detected in Area I (Figure 6.3a), where a young and compact basalt flow (3.8 ka) covers the area (*Carrasco-Núñez et al.*, 2017a). The presence of permeable structures with increased gas emissions could not be proven, but cannot be ruled out as gas efflux measurements are hardly possible to perform on compact bedrock. This is supported by a 10 m topographic scarp displacing the lava flow in Area I identified by *Norini et al.* (2019) which is clearly visible on the high-resolution DEM. Thermal imagery from drones could complement gas emission data in this area, as well as CO_2 concentration measurements with a TDL system (Tunable Diode Laser), which helps to discriminate ambient from elevated CO_2 concentrations possibly linked to hidden structures as also shown by *Mazot et al.* (2019).

6.5.1.2 Population B

The relatively large range of CO_2 emissions in population B (20.7 - 640.8 g m^{-2} d^{-1}) results from multiple CO_2 sources and transport mechanisms. Corresponding $\delta^{13}C_{CO_2}$ values range from -18 ‰ up to -1.2 ‰. All CO_2 efflux values between 20.7 and 29 g m^{-2} d^{-1} are characterized by biogenic $\delta^{13}C_{CO_2}$ values. The mixed and hydrothermal $\delta^{13}C_{CO_2}$ groups have corresponding CO_2 efflux values from 20.7 – 76.3 g m^{-2} d^{-1} and 22.2 – 640.8 g m^{-2} d^{-1}, respectively (Figure 6.6). This suggests that CO_2 emissions originate from biogenic sources, volcanic degassing, and contributions from the sedimentary basement driven by diffusive and advective transport mechanisms.

6.5.1.3 Population C

Population C (640.8 g m^{-2} d^{-1} – 1,468 g m^{-2} d^{-1}) is characterized by the heaviest $\delta^{13}C_{CO_2}$ values (-3.9‰ to -3‰), indicating the contribution of the volcanic-hydrothermal system. Similar $\delta^{13}C_{CO_2}$ values are reported by Peiffer et al. (2018) for areas with CO_2 emissions > 675 g m^{-2} d^{-1}. Separation between Population B and C is the result of solely advective gas transport, also supported by a small deviation of corresponding $\delta^{13}C_{CO_2}$ values due to high CO_2 efflux (*Camarda et al.*, 2007).

Table 6.5: Statistical parameters of $\delta^{13}C$-CO_2 obtained by the GSA method and corresponding CO_2 efflux values.

Population	Proportion [%]	N	$\delta^{13}C$-CO_2 range [δ ‰ vs. VPBD]	Mean $\delta^{13}C$-CO_2 [δ ‰ vs. VPBD]	Associated CO_2 efflux range [g m^{-2} d^{-1}]	Associated Mean CO_2 efflux [g m^{-2} d^{-1}]
Biogenic (A)	13	12	-23.2 to -18	-19.9	2.6 – 20.6	9
Mixed (B)	46	36	-17.9 to -5.96	-10.8	1.7 – 839	49.3
Hydrothermal (C)	40	42	-5.92 to -1.2	-3.6	1.0 – 1,464.2	190.1

6.5.2 Carbon isotopes - Origin and processes influencing their variability

6.5.2.1 Sources

Various studies at Los Humeros present comprehensive datasets on carbon isotope data from well fluids, calcite scales analyzed from well cuttings, and limestone from analogue outcrops of the basement (*González-Partida et al.*, 1993; *Portugal et al.*, 1994; *Truesdell and Quijano*, 1988). *Richard et al.* (2019) sampled production steam from 20 wells and found $\delta^{13}C_{CO_2}$ values ranging from -5.3 to -2.2‰. *Peiffer et al.* (2018) conducted three domain-based CO_2

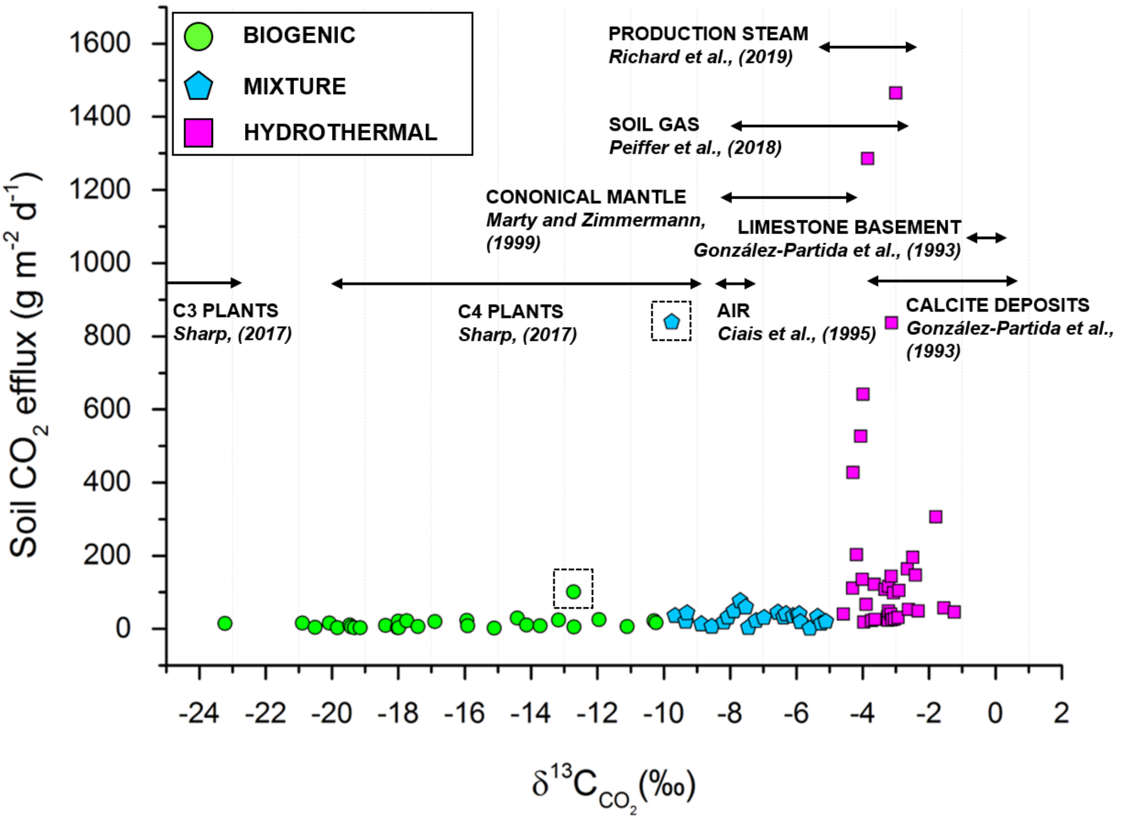

Figure 6.6: Plot illustrating soil CO_2 efflux versus all carbon isotopic composition of soil CO_2. Their spatial distribution can be seen in Figure 6.3. We illustrate the range of measured carbon isotopes from various studies at Los Humeros for comparison. $\delta^{13}C_{CO_2}$ values from increased soil gas emissions and production steam are in accordance with our values from the hydro-thermal and mixed groups. Two samples likely show a contamination with air (surrounded by black dashed rectangle). One sample was taken close to injection well H-29 with a CO_2 efflux of 100.8 g m^{-2} d^{-1} and a corresponding $\delta^{13}C_{CO_2}$ value of -12.7‰, whereas the other sample was taken in Area E with a CO_2 efflux of 839 g m^{-2} d^{-1} and a $\delta^{13}C_{CO_2}$ value of -9.8‰ (Figure 6.3)

efflux surveys at Los Humeros complemented by carbon isotopic analyses of samples from areas with increased CO_2 emissions ($\delta^{13}C_{CO_2}$ between -7.8 and -2.7‰). We assigned measured $\delta^{13}C_{CO_2}$ values to three groups according to characteristic $\delta^{13}C_{CO_2}$ ranges for biogenic, mixed, and hydrothermal gases from literature mentioned above. The biogenic group (-23 to -10‰) is consistent with derivation of carbon from C4 (-16 to -9‰, e.g., maize; *Hoefs*, 2009) and C3 plants (-33 to -23‰, e.g., high latitude grasses; from *Kohn*, 2010; *Sharp*, 2017), both present at Los Humeros. The mixed group ranges from -10 to -5‰, indicating a combination of different sources such as atmospheric (-8.3 to -7.2‰; from *Ciais et al.*, 1995) and mantle derived CO_2 (-6 ± 2‰ canonical mantle value; from *Marty and Zimmermann*, 1999) with a small overlap to C4 plants. The hydrothermal group includes $\delta^{13}C_{CO_2}$ values from -5 to -1.2‰, comprising values from the hydrothermal system (-3.3 ‰; average value of production steam from LHVC; from *Richard et al.*, 2019) as well as sedimentary decarbonation resulting from the underlying pre-volcanic limestone basement (0.7 to -3.9‰ from calcite in well-cuttings and 0.3 to -0.8‰ from limestone basement; *González-Partida et al.*, 1993). Following the approach of *Chiodini et al.* (2008), who sampled carbon isotopes from fumaroles to define a characteristic $\delta^{13}C_{CO_2}$ value representative for a 'pure' magmatic fluid, we calculated a mean value for $\delta^{13}C_{CO_2}$ of -3.6‰ from six anomalous degassing sites (in Area A to E) at Los Humeros. This value represents the average hydrothermal component of CO_2 from the reservoir, comparable to the mean $\delta^{13}C_{CO_2}$ of -3.3 from production steam determined by *Richard et al.* (2019). Thus, $\delta^{13}C_{CO_2}$ values with hydrothermal indications derived from surficial gas emissions provide a vital tool for the identification of areas with a connection to the deep reservoir. Our results prove that reliable reservoir information can already be obtained by surface exploration methods without the necessity of drilling costly wells.

6.5.2.2 Processes

There are different processes causing a range of endogenous $\delta^{13}C_{CO_2}$ values, which is subduction of the Rivera and Cocos plate under the North-American plate (*Richard et al.*, 2019) and isotopic fractionation processes. During the subduction process, the lithospheric mantle is mixing with fractions of the mantle wedge and carbon from different sources seems to reach the upper crust (*Richard et al.*, 2019). *Mason et al.* (2017) and *Peiffer et al.* (2018) discuss the spread of $\delta^{13}C_{CO_2}$ values by different carbon isotopic fractionation processes and propose following possibilities: (i) diffusion, (ii) partial dissolution of CO_2 into groundwater (both processes are present in the shallow subsurface), (iii) carbon remobilization during subduction through metamorphic decarbonation, (iv) dissolution of meta-carbonates in the basement accompanied by crustal carbon assimilation as a result of magma interaction with the crust, and (v) boiling causing calcite precipitation. *Camarda et al.* (2007) explain that it is crucial at which depths $\delta^{13}C_{CO_2}$ samples are taken. Fractionation in the uppermost soil layers (<1 m) due to diffusion can be neglected for our study due to sufficient sampling depth (1 m) of carbon isotopes. *Verma* (2000) reported results from geochemical and radiogenic isotope analyses of basaltic and rhyolitic volcanic rocks, which evidence the assimilation of crustal material in the upper mantle during magma formation at Los Humeros. Independent of a mantle, hydrothermal, or limestone carbon isotopic signature, all values evidence a permeable connection to the high-temperature geothermal reservoir.

6.5.3 Origin of helium

Air-normalized helium isotopic ratios range from 2.31 ± 0.58 to 4.88 ± 0.99 R_A. All samples show mixing between mantle and atmosphere as illustrated by mixing curves after *Sano and Wakita* (1985) (Figure 6.7a). Mantle contribution ranges between 30 and 65%. The maximum contribution is related to strong degassing in Area A and E (Figure 6.3a and Figure 6.7b). Pinti et al. (2017) report a mean $^3He/^4He$ ratio from 22 production wells in Los Humeros of 7.03 ± 0.4 R_A being very close to the canonical $^3He/^4He$ ratio from mid-oceanic ridge basalts (8 ± 1 R_A; *Graham*, 2008, Figure 6.7a). $^3He/^4He$ ratios decrease due to the decay of uranium and thorium associated with the formation of ^4He within the crust. The subsurface stratigraphy in Los Humeros is dominated by alternating layers of volcanic rocks, rich in uranium (up to 4.8 ppm) and thorium (up to 19.7 ppm), especially in andesitic and rhyolitic-dacitic rocks (*Carrasco-Núñez et al.*, 2017b). Hence, the difference between our ratios determined from steaming ground and the ones reported by (*Pinti et al.*, 2017) from fluid samples of the geothermal reservoir (between 1,600 to 3,100 m depth) results from the enrichment of ^4He

during slow upward migration of fluids within the shallow crust along permeability structures, compared to the rapid flow rates of steam in production wells.

6.5.3.1 Spatial correlation of CO_2 efflux, $\delta^{13}C_{CO_2}$ and $^3He/^4He$

In Figures 7b and 7c two diagrams of air normalized $^3He/^4He$ ratios against CO_2 efflux and $\delta^{13}C_{CO_2}$ values are illustrated, where the positive correlation between all three investigated parameters becomes apparent. The most prominent permeable connection from Earth's surface to the high-temperature geothermal system is indicated at sampling sites along a NNW-oriented, structure-dominated corridor with deep-rooted faults, in particular in Area A and E. Area C, D1, and D2 are also characterized by a hydrothermal source of CO_2. $^3He/^4He$ indicates a significant mantle component between 20 and 50% (Figure 6.7a). The location of these data points occurs between Area A and E within this well-defined NNW-SSE corridor suggesting that this is the main permeability zone of Los Humeros geothermal field. Area B is located northeast of the structural corridor, also with mantle components in $^3He/^4He$ and $\delta^{13}C_{CO_2}$. Production wells south of Area B (Fig. 1c) may target another N-S oriented fault zone (hidden faults), east of Los Conejos fault without further evidence of anomalous degassing.

6.5.3.2 Thermal anomalies

Anomalous soil temperatures ($\geq$ 22 °C) correlate with areas of increased degassing, except for Area K and J (Figure 6.3 and Figure 6.5), where only low CO_2 emissions ($\sim$11-21 g m^{-2} d^{-1}) have been determined, but still stand out from the surrounding background efflux ($\sim$1-6 g m^{-2} d^{-1}) in these areas. Increased temperatures of 26.3 °C (Area K) and 41.2°C (Area J) occur close ($<$ 50 m) to known faults, where hot fluids circulate at depth and heat could be transferred primarily by thermal conduction. *Bloomberg et al.* (2012) and *Finizola et al.* (2003) observed similar effects, which they explain with hydrothermal alteration preventing degassing in areas of previously high permeability. For that reason, soil temperatures can be an additional indicator for the presence of hot fluids in the shallow subsurface, even without increased gas emissions at the surface.

The gas sample from the site with the highest measured soil temperature (91.3 °C; Area C) has a $\delta^{13}C_{CO_2}$ value of -2.5‰ and is surrounded by solfatara being the most obvious indicator for magmatic degassing (*Francis and Oppenheimer*, 2004). *Espinosa-Paredes and Garcia-Gutierrez* (2003) estimated static formation temperatures (SFT) for selected wells in Los Humeros (1,500 - 3,265 m). The high SFT for well H-29 (433.6 °C; depth 2,186 m, Fig. 1c), drilled into the footwall of Loma Blanca fault might explain maximum soil temperature in Area C, which is favored by the near-vertical upflow of hydrothermal fluids. Strong alteration along Loma Blanca fault supports this observation.

6.5.4 Deep-derived gases in context to fault zone architecture and geothermal production

While some of the faults in Los Humeros have prominent fault scarps, their continuation into the deep geothermal reservoir often remains unknown (*Norini et al.*, 2015a). Geophysical resistivity

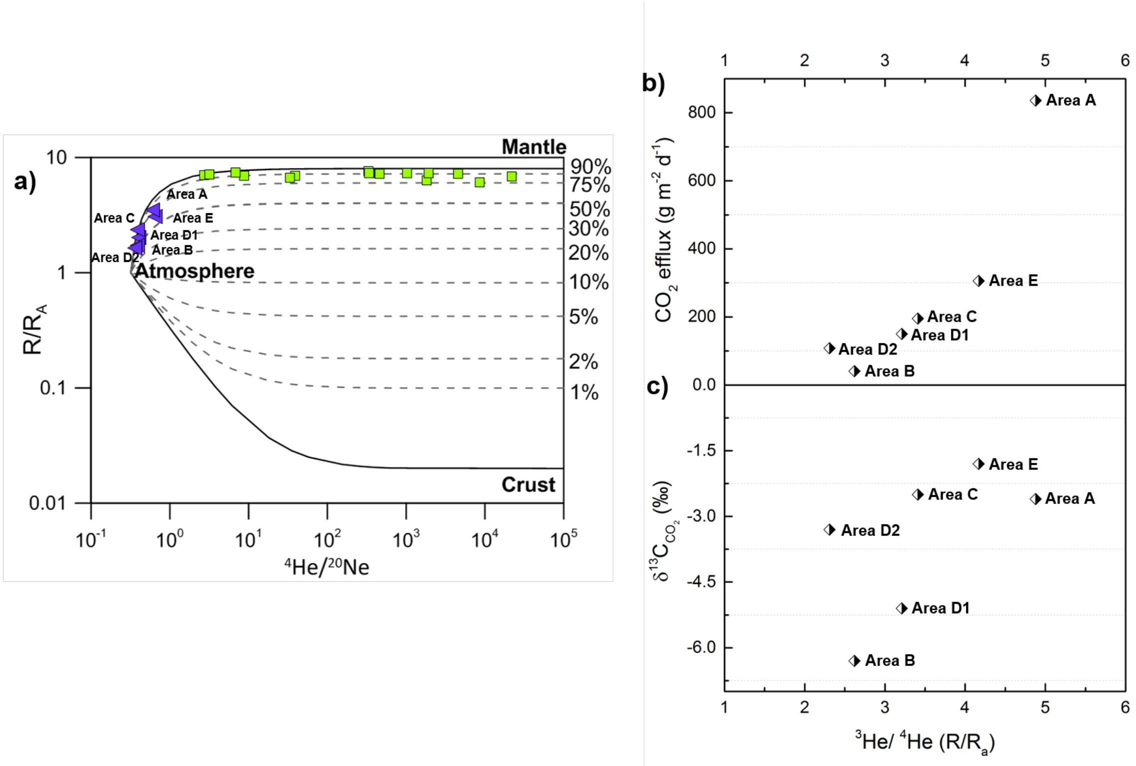

Figure 6.7: a) Binary plot of R/R$_A$ vs. ^{4}He/^{20}Ne of samples from steam vents (purple triangles, this study) and geothermal production steam (green squares from *Pinti et al.*, 2017). Dashed lines represent mixing between atmosphere and end-members (crust or mantle) with different percentages of mantle contribution (after *Sano and Wakita*, 1985). Our results show a clear mixing between atmosphere and up to 65% mantle. b) ^{3}He/^{4}He (R/R$_A$) ratios versus CO$_2$ efflux. There is a positive correlation of the two parameters. The highest measured efflux coincides with the highest measured ^{3}He/^{4}He ratio. Only Area B shows a slightly higher ^{3}He/^{4}He ratio but lower CO$_2$ emissions. c) ^{3}He/^{4}He (R/R$_A$) ratios versus carbon isotopic composition of soil CO$_2$. The highest measured ^{3}He/^{4}He ratios coincide with $\delta^{13}C_{CO_2}$ values of hydrothermal origin representing the deep geothermal system. Each area is represented by a half-filled diamond. In all diagrams Area A and E show the most evident relation to the superhot geothermal system

studies indicate zones of increased alteration as a result of intense fluid-rock interaction in the subsurface of Los Humeros reaching up to 5-6 km depth (*Arzate et al.*, 2018; *Benediktsdóttir et al.*, 2019). Different studies have shown that faults can act as major conduits for fluid-flow and are responsible for secondary permeability in geothermal systems (*Caine et al.*, 1996; *Jolie et al.*, 2016; *Rossetti et al.*, 2011; *Rowland and Sibson*, 2004), but can also reduce permeability and act as a barrier due to mineral precipitation or comminution (*Aben et al.*, 2016; *Rossetti et al.*, 2011; *Rowland and Sibson*, 2004). Our study shows that CO$_2$ degassing is typically not limited to single fault planes, instead it is influenced by wide fault damage zones or multiple, interconnected faults with anisotropic and heterogeneous properties. Los Humeros fault system was influenced by different periods of volcano-tectonic activity under changing stress conditions (Section 6.2.2). *Faulds and Hinz* (2015) assessed different structural settings (e.g., fault steps, intersections, tips) in the Basin and Range Province favoring the formation of geothermal systems. In the following paragraphs, we have related some of our observations to structural settings described in their study (Figure 6.8a-e).

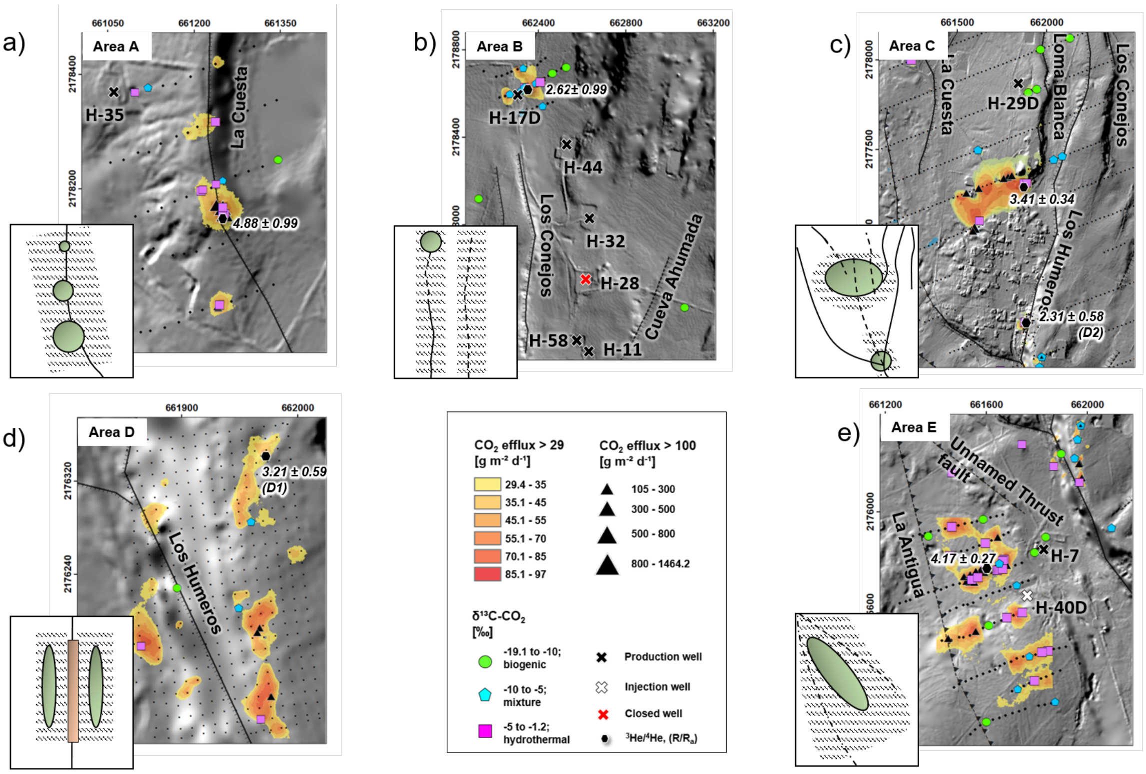

Figure 6.8: Detailed view of degassing in Area A, B, C, D, and E. Inset maps provide a schematic (not to scale) structural interpretation based on the catalogue of favorable structural settings for fluid flow by *Faulds and Hinz* (2015). Possible dimensions of fault damage zones are outlined (diagonal, dashed, black lines), Green ellipses (upwelling of geothermal fluids) correlate to highest CO_2 emissions, impermeable fault core (orange rectangle), known faults (black solid lines), inferred fault (black, dashed lines). a) Shows a typical major normal fault with highest gas emissions at the fault bend. b) Hidden fault or fault continuation of Los Conejos fault. The zoomed out map shows also the location of many production wells drilled along N-S corridor parallel to Los Conejos indicating another structural corridor. c) A horsetail fault termination starting in the south of Humeros village with faults (i.e. La Cuesta, Loma Blanca, and Los Conejos) forming the horse tail. d) Permeable fault damage zone and a less permeable fault core along Los Humeros fault e) Fault intersection or linkage of two fault damage zones favoring increased degassing in Area E

6.5.4.1 Area A – Normal fault

Degassing at La Cuesta fault follows an N-S orientation along a 400 m-long and 150 m-wide segment (Figure 6.8a). La Cuesta is a normal fault promoting fluid upflow from the deep reservoir, preferentially in its footwall. This is supported by highest $^3He/^4He$ values and hydrothermal $\delta^{13}C_{CO_2}$. Since well H-35 is drilled nearly vertical and proved to be suitable as a geothermal production well, another permeable segment is indicated to the west of La Cuesta.

6.5.4.2 Area B – Hidden fault/Fault continuation

Increased soil gas emissions in Area B are limited in its extent, but might be the result of a hidden fault structure. A possible continuation of Los Conejos fault at depth towards the north cannot be excluded, unless another, hidden structural corridor, parallel to the east of Los Conejos fault is present. This could be indicated by multiple production wells targeting the geothermal reservoir at a depth of ∼2800 m (Figure 6.8b).

6.5.4.3 Area C – Horsetail fault termination

Degassing in Area C is observed in a 550 m E-W × 250 m N-S wide zone north of Humeros village with clustered gas emissions and soil temperatures up to 91.3°C, as well as signatures of mantle derived helium and hydrothermal carbon. The clustered gas emissions may be indicative for the existence of further structural elements, hidden beneath Humeros village. We suggest that increased fluid flow might be accommodated by a horsetail fault termination where the break up into multiple fault strands favors geothermal fluid flow (Figure 6.8c). Additional CO_2 efflux measurements by *Peiffer et al.* (2018) towards the north of Area C show a continuation of increased degassing along Loma Blanca and Los Humeros fault.

6.5.4.4 Area D – Fault damage zone

The Los Humeros fault in Area D has a vertical escarpment up to 80 m with evident heterogeneous degassing in its fault damage zone (Figure 6.8d and Figure 6.9). Degassing along the fault core is low, typically the result of hydrothermal alteration and mineral precipitation (*Wyering et al.*, 2014). Increased soil temperatures have been measured along the fault scarp (thermal conduction). Gas emissions along Los Humeros fault are limited to a 700 m-long NNW-SSE segment and point to the most permeable part of this large normal fault.

6.5.4.5 Area E – Fault intersection

Area E hosts the largest zone of increased gas emissions (600 m E-W × 1,000 m N-S) and hydrothermal signals (^{3}He/^{4}He, $\delta^{13}C_{CO_2}$) along a well-confined corridor (Figure 6.3b and Figure 6.8e). Increased degassing could be related to a fault intersection between La Antigua and an unnamed thrust fault (Figure 6.8e). However, also the linkage of damage zones from the unnamed thrust fault, La Antigua and maybe Los Humeros fault at depth might promote increased fluid flow in that area (Figure 6.9). In some parts of Area E, we noticed superficial argillic alteration (e.g., kaolinite), a result of upward migration of geothermal fluids to the surface (*Bernard et al.*, 2011). The orientation of the zone with anomalous degassing reflects the typical NNW-SSE orientation of faults in this structural corridor of the LHVC.

6.6 Conclusion and Outlook

We present results of a comprehensive multi-scale soil gas survey in the Los Humeros geothermal field to identify areas of increased permeability as a result of structural discontinuities in the subsurface. Our findings demonstrate that the majority of increased diffuse CO_2 emissions are hydrothermal/mantle derived with some contribution from metamorphic decarbonation. The combined analysis of CO_2 efflux and $\delta^{13}C_{CO_2}$ showed that areas of background diffuse CO_2 emissions could still be related to fluid pathways with a connection to the deep reservoir. Helium isotopic analyses at selected locations complement results from the area-wide CO_2 efflux survey and prove the existence of deep-rooted faults down to the high-temperature geothermal reservoir. Independent of the source, increased gas emissions always indicate the presence of a fault-controlled fluid migration along permeable segments of fault zones. This is an important information for the definition of input parameters for dynamic models of geothermal systems.

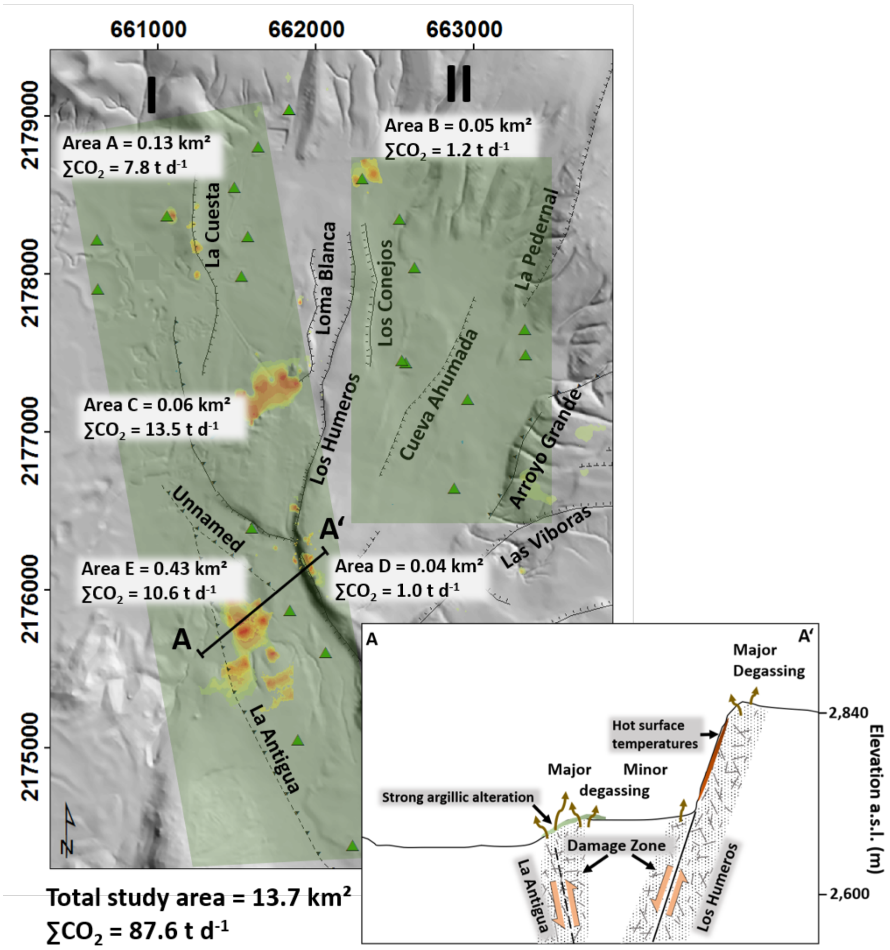

Figure 6.9: Simplified map showing two structural corridors (highlighted in green; corridor I = NNW-SSE and corridor II= N-S oriented), which favor hydrothermal fluid flow within the main production zone of the geothermal field. Our interpretation is based on increased CO_2 emissions (extracted from Figure 6.3) and the location of production wells (green triangles). The total CO_2 output and size for each area is shown. Please note that values from Area C are taken from *Peiffer et al.* (2018) who focused on localized areas of increased degassing rates and a high number of measuring points resulting in a high CO_2 emission rate. The cross-section A-A' shows our interpretation of the structural framework in Area D and E. (Legend for CO_2 emissions can be found in Figure 6.8)

The further identification of migration pathways of hydrothermal fluids in the subsurface can be acquired by soil temperature measurements at sufficient depth even without increased gas emissions. One of the most significant areas for geothermal power generation in Los Humeros is a permeable, NNW-SSE oriented structural corridor, which is targeted by a large number of the geothermal production wells (Figure 6.9) and shows the strongest mantle contribution in helium and carbon isotopes. Furthermore, we suggest another N-S oriented, structurally confined compartment, which includes Area B and is also targeted by many of the production wells (Figure 6.9). A promising area of enhanced structural permeability was identified in Area E, making it a possible target for future geothermal exploration activities.

We demonstrate that the application of large-scale CO_2 efflux surveys with suitable sampling distance is a successful approach for geothermal exploration. Domain-based surveys with higher resolution (smaller grid spacing) improve the assessment of spatial variability of gas emissions along specific faults. Some structures are characterized by increased fluid flow along deep-rooted faults such as La Cuesta and La Antigua fault. Others may act to some extent as barriers, for example Las Papas or Los Humeros fault.

Soil gas studies are suitable exploration techniques in volcanic-geothermal systems before costly drilling operations and should become an integral part in the overall exploration strategy in new and undeveloped geothermal fields to complement established methods, e.g., geological mapping and geophysical exploration. Gas measurements in combination with bathymetric and ground temperature surveys have even proven their suitability to indicate geothermal fluid flow in unconventional geothermal settings, e.g., limnic environments (*Jolie*, 2019). Although, CO_2 emissions from anomalous degassing sites play an important role when calculating the CO_2 output from an area, we could show that two-thirds of the CO_2 emissions in Los Humeros are related to background values and should not be neglected when calculating the total CO_2 output (Figure 6.9), which has a significant contribution to the global CO_2 budget.

Furthermore, the continuous monitoring of volcanic gas emissions will improve the understanding of temporal variations, their relation to seismic and/or volcanic activity, and effects of geothermal exploitation at Los Humeros, which is the focus of another publication currently in preparation. Further work should focus on variable sampling grids and integrated approaches, and confirm their reliability in different volcanic-geothermal settings.

Acknowledgements

This paper presents results of the GEMex Project, funded by the European Union's Horizon 2020 research and innovation programme under Grant Agreement No.727550, and by the Mexican Energy Sustainability Fund CONACYT-SENER, Project2015-04-268074. The authors wish to thank the Comisión Federal de Electricidad of Mexico (CFE) for their support, and access to Los Humeros geothermal field. A special thank you to all people from Mexico, Argentina, and Germany who supported us to collect this comprehensive dataset: Esteban Silva, Sonia Vargas Pineda, Romel González, Ana Maria Dávalos Pérez, Jorge Alejandro Guevara Alday, Ruth Alfaro Cuevas Villanueva, Rojeh Khleif, Tanja Ballerstedt, Camila Espinoza, Leandra Weydt, and Adrian Lechel. Thank you to the GEMex consortium, to Gianluca Norini and Kyriaki Daskalopoulou for fruitful discussions. Thank you to the Universidad Michoacana de San Nicolás de Hidalgo for providing vehicles for the fieldwork. We would also like to thank Section 4.3: Climate Dynamics and Landscape Evolution with the laboratory for compound-specific isotope analysis and Section 3.1: Inorganic and Isotope Geochemistry with the noble gas laboratory at the German Research Center for Geoscience (GFZ) in Potsdam as well as Charles Belanger and Steve Brookes (Iso-Analytical Limited) for analysis of carbon isotopes in CO_2 samples collected during the BGS campaign.

Electronic supplementary data

All datasets generated and analyzed for this study can be found on the repository of the GFZ Data Service under the following DOI: `http://doi.org/10.5880/GFZ.4.6.2020.001`

Appendix 6.A Figures

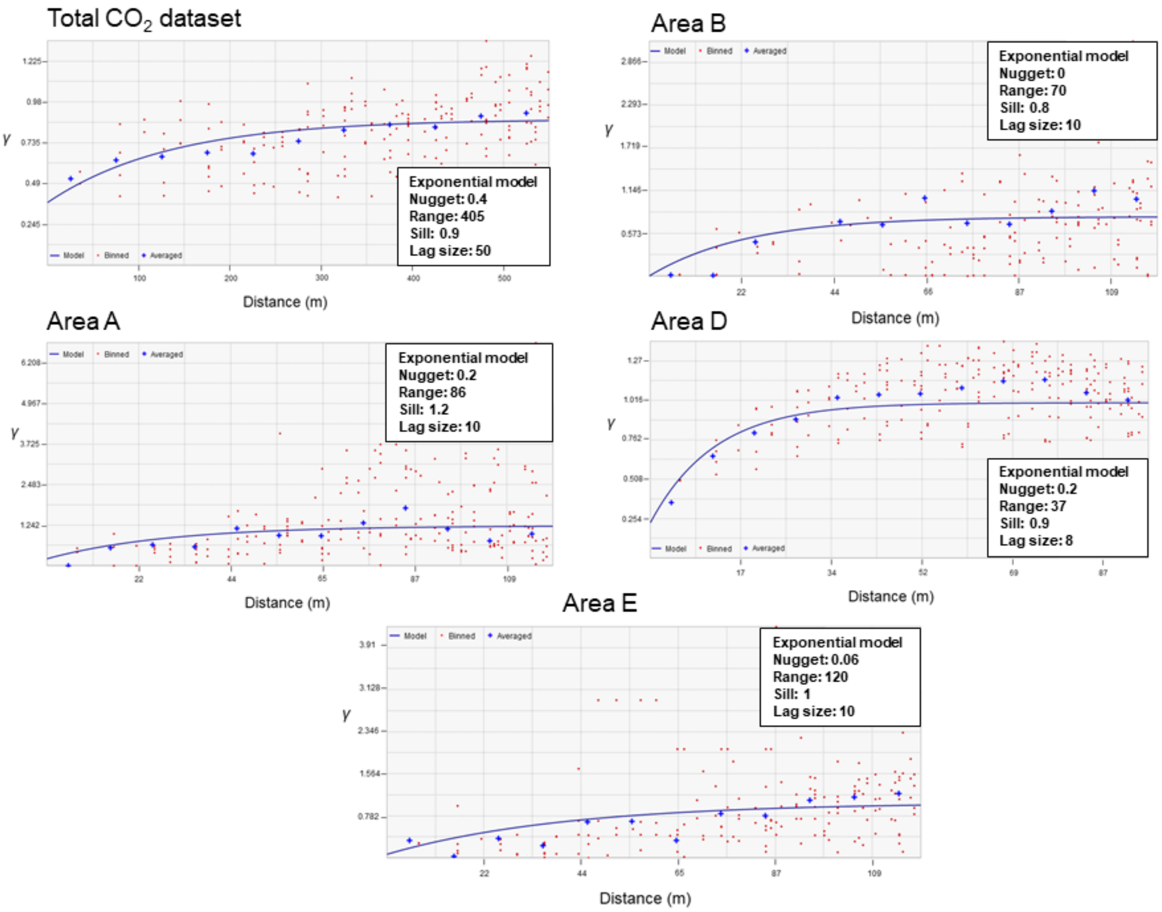

Figure 6.10: Experimental and modeled variograms of the CO_2 efflux maps for the total study area and the small-scale surveys

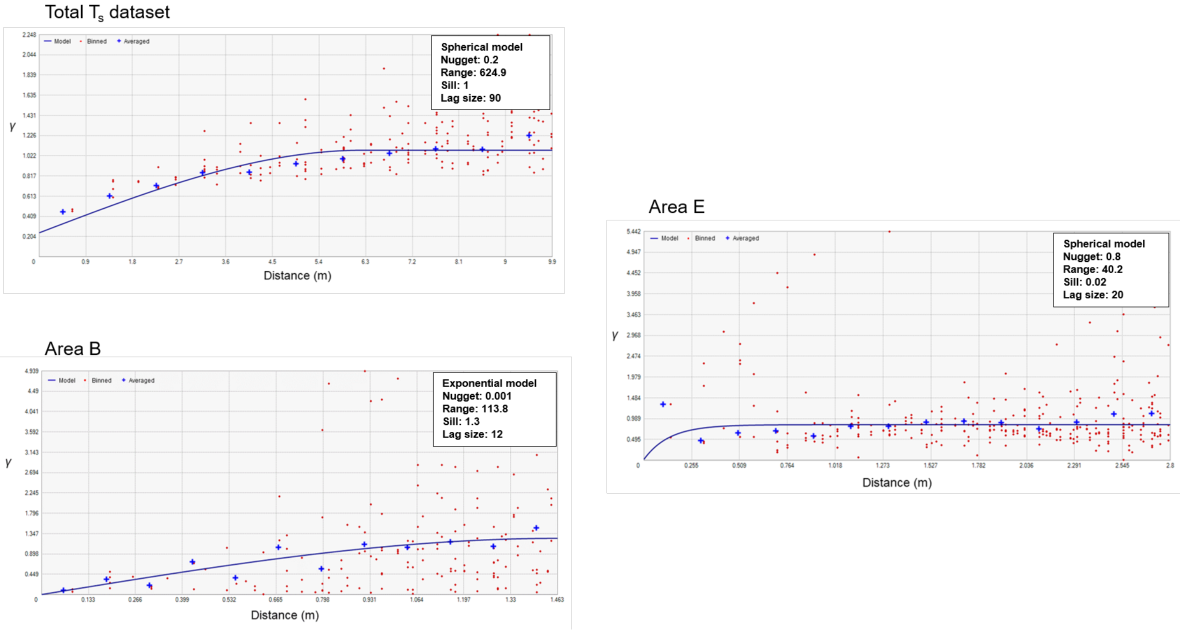

Figure 6.11: Experimental and modeled variograms of soil temperature maps for the total study area, Area B, and Area E.

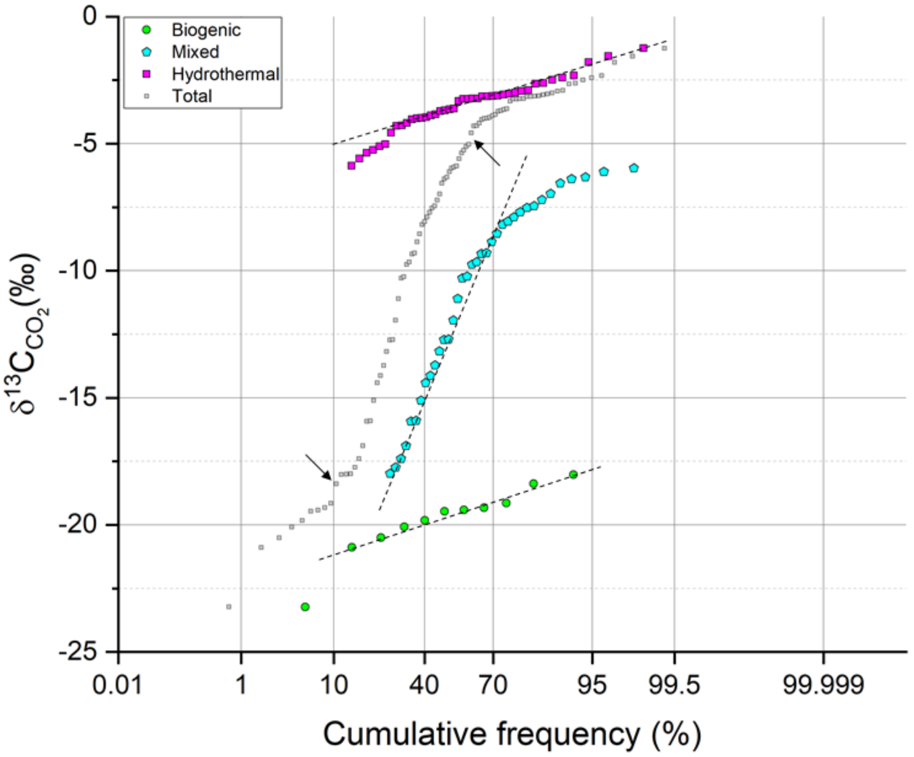

Figure 6.12: Probability plot of carbon isotopes. Based on the identification of two inflection points (black arrows), three populations (biogenic, mixed, and hydrothermal) could be identified.

7

Los Humeros Monitoring

Monitoring the response of volcanic CO_2 emissions to changes in the Los Humeros hydrothermal system

Anna Jentsch, Walter Duesing, Egbert Jolie, Martin Zimmer

Article published in *Scientific Reports*, 2021.

Abstract: Carbon dioxide is the most abundant, non-condensable gas in volcanic systems, released into the atmosphere through either diffuse or advective fluid flow. The emission of substantial amounts of CO_2 at Earth's surface is not only controlled by volcanic plumes during periods of eruptive activity or fumaroles but also by soil degassing along permeable structures in the subsurface. Monitoring of these processes is of utmost importance for volcanic hazard analyses, and is also relevant for managing geothermal resources. Fluid bearing faults are key elements of economic value for geothermal power generation. Here, we describe for the first time how sensitively and quickly natural gas emissions react to changes within a deep hydrothermal system due to geothermal fluid reinjection. For this purpose, we deployed an automated, multi-chamber CO_2 flux monitoring system within the damage zone of a deep-rooted major normal fault in the Los Humeros Volcanic Complex (LHVC) in Mexico and recorded data over a period of five months. After removing the atmospheric effects on variations in CO_2 flux, we calculated correlation coefficients between residual CO_2 emissions and reinjection rates, identifying an inverse correlation ρ = -0.51 to -0.66. Our results indicate that gas emissions respond to changes in reinjection rates within 24 hours, proving an active hydraulic communication between the hydrothermal system and Earth's surface. This finding is a promising indication not only for geothermal reservoir monitoring but also for advanced long-term volcanic risk analysis. Response times allow for estimation of fluid migration velocities, which is a key constraint for conceptual and numerical modelling of fluid flow in fracture-dominated systems.

7.1 Introduction

Worldwide, a large number of caldera-hosted geothermal systems are located along volcanic arcs, such as the Los Humeros Volcanic caldera (LHVC) in the Trans-Mexican Volcanic Belt (Mexico) or Onikobe in the Honshu Arc (Japan). Such geothermal systems contain a vast potential of geothermal energy (*Carrasco-Núñez et al.*, 2018; *Stelling et al.*, 2016). Calderas are very complex, large-sclae geological structures (*Suñe-Puchol et al.*, 2019) and provide elevated heat flow within relatively shallow depths (< 2 km) lasting for several thousands of years. This makes them a preferred target in geothermal exploration (*Amanda et al.*, 2019; *Sorey*, 1985; *Wohletz and Grant*, 1992). Their structural evolution is of particular interest, since a comprehensive understanding of the localization of permeable fluid pathways, as well as of their structural controls, are key objectives for the successful utilization of geothermal energy (*Banerjee et al.*, 2011; *Jolie et al.*, 2016).

Deep-rooted fault zones and fracture networks connecting geothermal reservoirs to Earth's surface channel vast amounts of hydrothermal fluids (*Batista Cruz et al.*, 2019; *Chiodini et al.*, 1998; *Taussi et al.*, 2021; *Werner and Cardellini*, 2006). In undisturbed conditions, migrating fluids can form stable and long-lasting geothermal surface manifestations such as fumaroles or hot springs, which provide valuable information about the reservoir conditions (*Jolie et al.*, 2021; *Kristmannsdóttir and Ármannsson*, 2003). However, volcano-tectonic activity or the development of geothermal resources for power generation can change this equilibrium.

A sustainable field management requires comprehensive monitoring of physical and chemical changes in geothermal reservoirs during production and reinjection of fluids for a timely reaction to pressure decline and temperature depletion, respectively (*DiPippo*, 2016). Reinjection of extracted geothermal fluids (brine) into the feed, or loss zones, of a geothermal system is essential to maintain reservoir pressure and fluid recharge, control subsidence and avoid contamination of local ground water (*Kamila et al.*, 2021; *Stefansson*, 1997). This requires site-specific strategies for reinjection at suitable locations, thus avoiding any interference in the production zone by thermal breakthrough, mineral precipitation or induced seismicity (*Gaucher et al.*, 2015; *Horne*, 1985).

For the first time, in this study we investigated the relationship between induced CO_2 flux variability and changes in reinjection rates in a geothermal system. We deployed a multi-chamber CO_2 flux monitoring system within the damage zone of a large normal fault crossing the Los Humeros geothermal field, in combination with an on-site meteorological station. After we quantified the variations in CO_2 flux induced by atmospheric parameters, we used the time series of residual CO_2 emissions to calculate their correlation coefficients with daily reinjection rates. The results show an inverse correlation between the two parameters within a time window of ≤ 24 hours. We additionally discuss further unmonitored variables and nonlinear processes that could have a potential impact on CO_2 variations. Our approach combines geochemical surface data and physical subsurface data in order to develop a thorough understanding of induced fluid migration from the geothermal reservoir along specific flow paths to the Earth's surface.

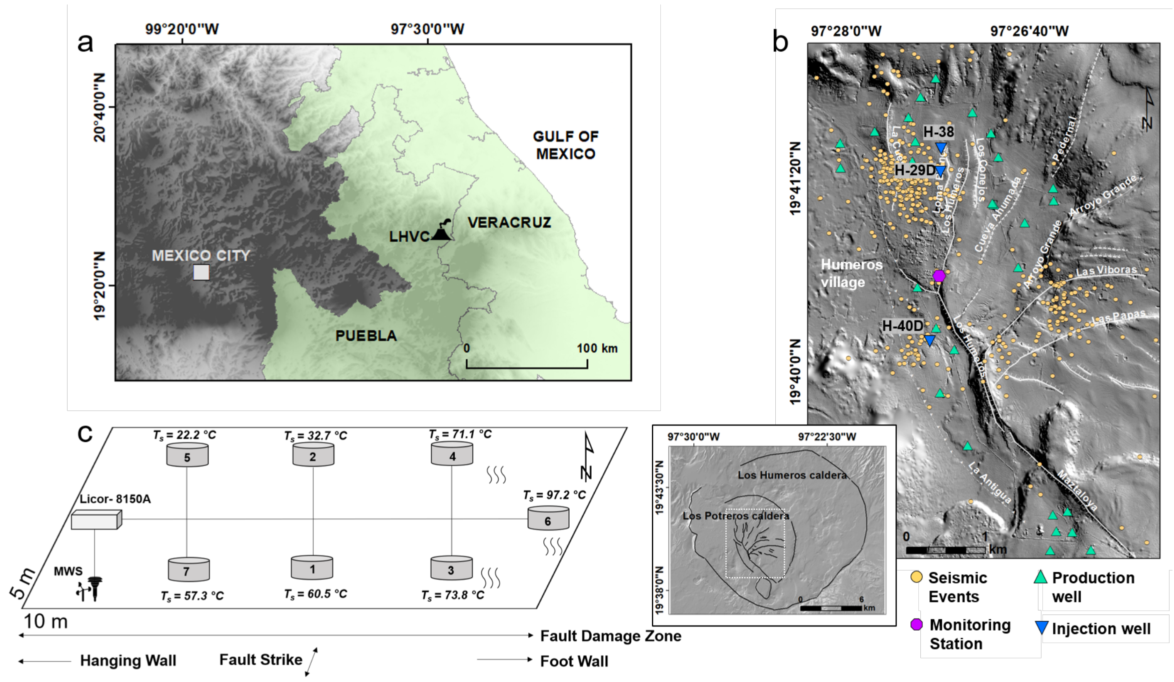

Figure 7.1: a) Location of the Los Humeros Volcanic Complex (LHVC) on the border of the federal states Puebla and Veracruz on a 120 m-resolution digital elevation model (DEM), available at https://www.inegi.org.mx/app/geo2/elevacionesmex/. b) Overview of the main production field of Los Humeros (Installed capacity 93.9 MWe; *Gutiérrez-Negrín* (2019)) on a shaded relief image obtained from a 1 m-resolution DEM from *Carrasco-Núñez et al.* (2017b). White solid and dashed lines illustrate known and inferred faults, respectively. Orange circles represent locations of seismic events from September 2017 to September 2018 (*Toledo et al.*, 2020a). The inset map, illustrated by the white dashed rectangle, shows the extent of the LHVC and Los Potreros caldera hosting the active geothermal field. The maps were generated using ArcGIS 10.4.1 software. c) Setup of the CO_2 monitoring array within the fault damage zone of the Los Humeros fault. $T_S$values indicate ground temperatures measured during the initial site selection survey, while black arrows show the direction and extension of fault geometry parameters.

7.1.1 Los Humeros Geothermal System

The Los Humeros Volcanic Complex (LHVC) is the result of the largest caldera-forming eruption in the 1000 km long Trans-Mexican Volcanic Belt (TMVB) (Fig. 7.1a). *Cavazos-Álvarez and Carrasco-Núñez* (2020) determined that the LHVC contains a volume of 290 km^3 of erupted ignimbrites, marking the onset of the formation of the Los Humeros caldera (LHC) 164 ± 4.2 ka, followed by a long period (approx. 95 ka) of explosive and effusive volcanic activity. During this period, another smaller-scale caldera-forming event occurred 69 ± 16 ka, which imbedded the Los Potreros caldera (LPC) in the 19 km-wide LHC (Fig. 7.1b). The LPC hosts the high-temperature (approx. 380 °C at $>$ 2100 m below surface), two-phase, liquid-dominated Los Humeros geothermal reservoir, which is controlled by secondary permeability, e.g., faults and fractures (*Elders et al.*, 2014). The reservoir fluids are rich in CO_2 and other non-condensable gases (*González-Partida et al.*, 1993; *Prol-Ledesma*, 1998). Helium isotopic ratios, determined in fluid samples from wells, are characteristic of the sub-continental mantle and suggest heat supply from an active magmatic system (*Pinti et al.*, 2017). Both volcanic activity and regional tectonics are the dominant forces on the structural architecture of the caldera. The volcano-tectonic interaction is responsible for the fault system's complexity (*Norini et al.*, 2019). Formation permeability of the andesitic to basaltic geothermal reservoir is very low (K <10^{-16} m^2; *Weydt et al.*, 2018). Thus, fluid migration is mainly favoured by fault zones and fracture networks that cut through the overlying volcanic rocks. Macro-fracture permeability, characterized by regional faults in the geothermal system, can either enhance or impede fluid migration through the formation of fluid conduits or barriers (*Norini et al.*, 2019).

Two of the most distinctive faults, the Los Humeros and Maztaloya faults, merge in the central part of the geothermal reservoir. Several smaller fault strands in the northern part of the Los Humeros fault (e.g., La Cuesta, Loma Blanca, Los Conejos) build a horsetail structure forming a wide zone of substantial hydrothermal alteration (*Norini et al.*, 2019). Within this structure, increased CO_2 degassing and multiple thermal anomalies with ground temperatures up to 92 °C at 50 cm depth are observed (*Jentsch et al.*, 2020; *Peiffer et al.*, 2018). The Los Humeros fault is a deep-seated, permeable fault zone facilitating the migration of geothermal fluids. It is therefore targeted by both production and reinjection wells (Fig.7.1b). This makes the fault an ideal location in which to study the response of natural gas emissions at Earth's surface to reinjection-induced changes in the geothermal reservoir.

7.2 Data and methods

We installed an LI-COR Li-8100 automated soil CO_2 flux monitoring system with seven accumulation chambers on an area of 50 m^2 in combination with an on-site weather station (MWS 9-5; Fig. 7.1c, 7.7; Table 7.1 in the supplemental material) for continuous observation of air temperature, barometric pressure, air humidity, precipitation, and wind speed and direction. The monitoring site was chosen to be well linked to a fault displaying thermal anomalies and increased degassing, distinctive from background CO_2 emissions. For this reason, CO_2 flux and ground temperatures at 50 cm depth were measured before the monitoring network was deployed. The vegetation cover of the study site is sparse and characterized by irregular tufts of grass, small shrubs, cacti and agaves. Several pine trees border the eastern side of the monitoring area thus, we cannot exclude the influence of root respiration on CO_2 flux at stations 3, 4 and 6 (Fig. 7.7). Most of the study site lacks a surficial organic layer due to anomalous ground temperatures ($T_S > 30°C$) that control the distribution of argillic alteration, as recognized by clay minerals such as kaolinite (*Gutierrez-Negrin and Izquierdo-Montalvo*, 2010). The subsurface consists of alternating layers of unconsolidated pumice and scoria lapilli, which have a wide range of grain sizes (*Dávila-Harris and Carrasco-Núñez*, 2014). Each monitoring station measured soil CO_2 flux on an hourly basis following the accumulation chamber method (*Cardellini et al.*, 2017; *Chiodini et al.*, 1998; *Parkinson*, 1981) over a period of five months, from April to September 2018. The setup with multiple accumulation chambers was chosen due to the following advantages compared to single monitoring stations:

i) monitoring CO_2 fluxes of different magnitudes and origins (hydrothermal/biogenic), ii) continuous datasets for benchmarking between individual sampling sites, iii) robust quantitative assessment of the influence of meteorological parameters on gas flux, and iv) understanding the spatial variability of CO_2 flux on small areas in relation to (sub)surface heterogeneities (fault zone architecture, soil type, alteration).

The geothermal reservoir has been the site of more than 60 wells in the past 40 years (*Aragón-Aguilar et al.*, 2017). Infield reinjection began five years after the commercial utilization of geothermal energy started in 1990 (*Arellano et al.*, 2015). Currently, three wells with depths of 2200 m are used to reinject geothermal fluids at a total average rate of 171 t/hr and 28 production wells with a production of 663 t/hr (2018, unpublished data from CFE Comisión Federal de Electricidad; Fig. 7.1b). The amount of reinjected fluids at Los Humeros depends on the available brine, which has always been low compared to the amount of produced fluids (liquid and steam). An increase in reinjection rates usually occurs in response to an observed decline in productivity, but it is a balancing act to inject the appropriate amount of fluids without decreasing production enthalpies. In recent years, geothermal operators at Los Humeros have incorporated condensing technologies into the power units to increase the amount of fluids used for reinjection (personal communication). Daily reinjection and monthly production rates were provided by the geothermal power plant operator CFE. From September 2017 to September 2018, seismic activity was continuously monitored using 25 broadband and 20 short-period stations across the Los Humeros geothermal field (*Toledo et al.*, 2020a). Three distinct clusters of induced/natural seismicity (MLV $\leq$ 2.1) are indicated in the vicinity of production and reinjection wells (Fig. 7.1b) at depths between 1 and 3.5 km, corresponding to the depth of the geothermal reservoir. During CO_2 flux monitoring, the magnitude of seismic events (124 in total) ranged from -0.61 to 2.1 MLV (unpublished data).

The collected datasets were statistically analysed using MATLAB software version R2019b. The statistical correlations among i) the CO_2 flux chambers and ii) each CO_2 flux chamber and the meteorological parameters was calculated using a spearman's rank correlation matrix. Removing atmospheric effects on CO_2 flux data is crucial for determining the influence of endogenous processes on CO_2 variations (*Cannata et al.*, 2010; *Liuzzo et al.*, 2013; *Rinaldi et al.*, 2012). This was conducted by computing a stepwise multiple linear regression model (SMLRM) (*Oliveira et al.*, 2018). For the SMLRM, we excluded all data gaps, thereby reducing the multidimensional data set from 3552 to 2971 data points. The stepwise regression is a systematic method that describes the relationship between the response variable (CO_2 flux) and the predictor variables (atmospheric parameters) by first adding and then removing one variable at a time to the model. The final model is reached when the residual sum of squares (R^2) no longer changes. The adjusted R^2 value explains the amount of variation computed by the linear regression model. The p-value is a criterion which defines whether variables should be removed or added to the model, with the default threshold set to 0.05. A p-value below 0.05 is usually considered a sufficient rejection of the null hypothesis (*Wilks*, 2006). The major advantage of this algorithm is that only predictor variables which significantly influence the response variable are included in the model.

To further interpret the results from the SMLRM, we generated several continuous wavelet transformations (CWTs) from the hourly-measured CO_2 flux time series and the residuals of the stepwise regression models. Finally, we calculated the Spearman correlation coefficients (ρ) between residual CO_2 time series and fluid reinjection rates. In order to compare the two different time series, we reduced the hourly-measured CO_2 fluxes to daily averages. This was done in two steps. We first used a 24-hour Gaussian filter providing zero phase shift by running in both the forward and reverse directions, smoothing the hourly measured CO_2 fluxes. As a second step, we used a shape-preserving piecewise cubic interpolation, to identify adequate numbers of sampling points from the hourly-measured CO_2 data and down sample the CO_2

fluxes to the time series of the lower-resolution daily injection data (Fig. 7.2). Additionally, a linear regression analysis was performed to model the relationship between CO_2 flux residuals and reinjection rates and calculate a 95 % confidence interval.

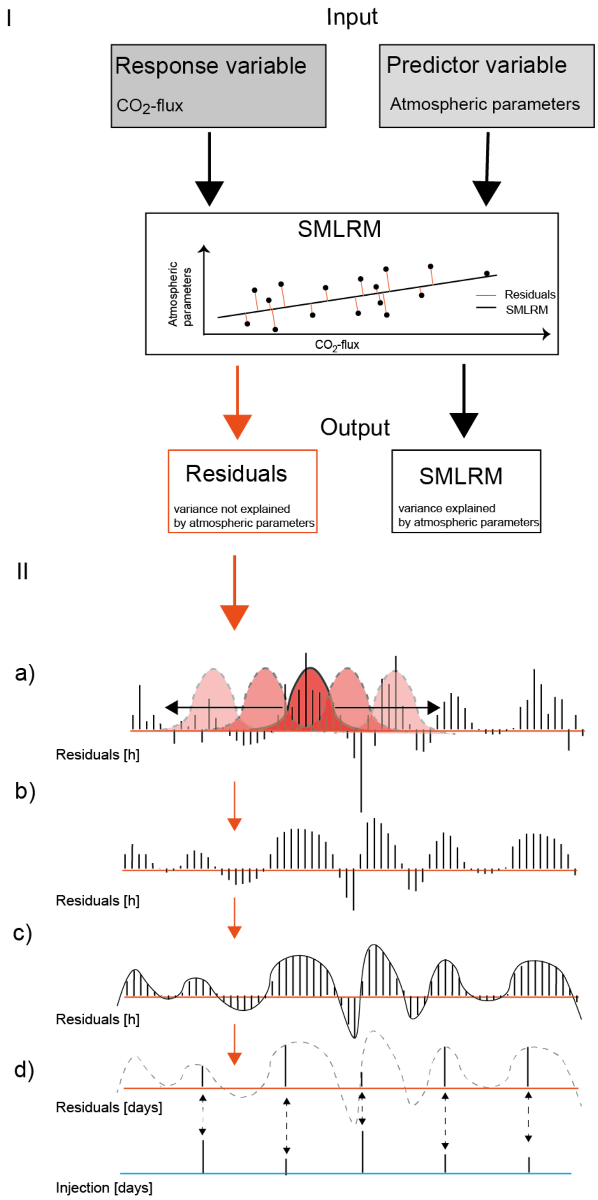

Figure 7.2: Workflow of the statistical analysis of the monitored data. Part I shows a flow chart of the stepwise multiple linear regression model (SMLRM). The SMLRM requires two input variables, the predictor variable, and the response variable. While the predictor variable usually consists of a multidimensional data set, as in our case atmospheric parameters (e.g., air temperature, wind speed), the response variable is a one-dimensional data set (measured CO_2 flux). The output of the SMLRM is a linear regression model that represents the variability of the response variable according to the predictor variables. The remaining residuals represent the variability of the response variable which is not explained by the predictor variables. In this study we focused on the residuals. Part II visualizes the resampling of the residuals. a) describes the application of the 24 h gauss-filter running in both, forward and reverse directions, b) to smooth the hourly measured CO_2 fluxes. c) shows the application of a shape-preserving piecewise cubic interpolation and finally d) resampling of hourly resolved residuals of the SMLRM to daily resolution. Consequently, we obtain daily resolved residuals that now can be correlated with the daily injection rates.

7.3 Results and Discussion

Each CO_2 emissions time series is characterized by strong variability in daily mean flux rates and a decrease at all stations from April to June, followed by a moderate increase from July to September (Fig. 7.3a, 7.8 and Table 7.2). Despite the close proximity of the seven monitoring stations, the different time series do not always indicate coherent behaviour. Given that background/biogenic CO_2 fluxes at Los Humeros usually do not exceed 20 g m^{-2} d^{-1}, the mean CO_2 flux value of each station suggests input from hydrothermal degassing, as also supported by carbon isotopic samples taken at two sites within the monitoring area ($\delta^{13}C_{CO_2}$ = -3.3 and -3.1 ‰; *Jentsch et al.*, 2020). In fact, hydrothermal degassing at rates similar to biogenic fluxes can result from low permeability of soil/rocks or low-pressure gradients (*Peiffer et al.*, 2014). At Station 6, CO_2 flux values were observed to be twice as high compared to values at the other monitoring stations. Along with a ground temperature of 97.2 °C, this is indicative of advective fluid transport. However, low degassing rates, as observed at station 2, 4 and 5, provide evidence for mixed diffusive-advective gas transport. Diurnal variations between 130-475 g m^{-2} d^{-1} (Station 6) demonstrate the dynamic behaviour of fluid migration within this highly-permeable fault zone.

The strong variations of CO_2 flux in such a constrained area are affected by i) different transport mechanisms of fluid flow (advective/diffusive), ii) variable intensities of hydrothermal alteration, iii) subsurface heterogeneities, iv) fault zone architecture/migration pathways, and eventually v) atmospheric parameters. Stations 1, 5, 6 and 7 demonstrate similar behavior to each other and also to meteorological parameters (Fig. 7.3b).

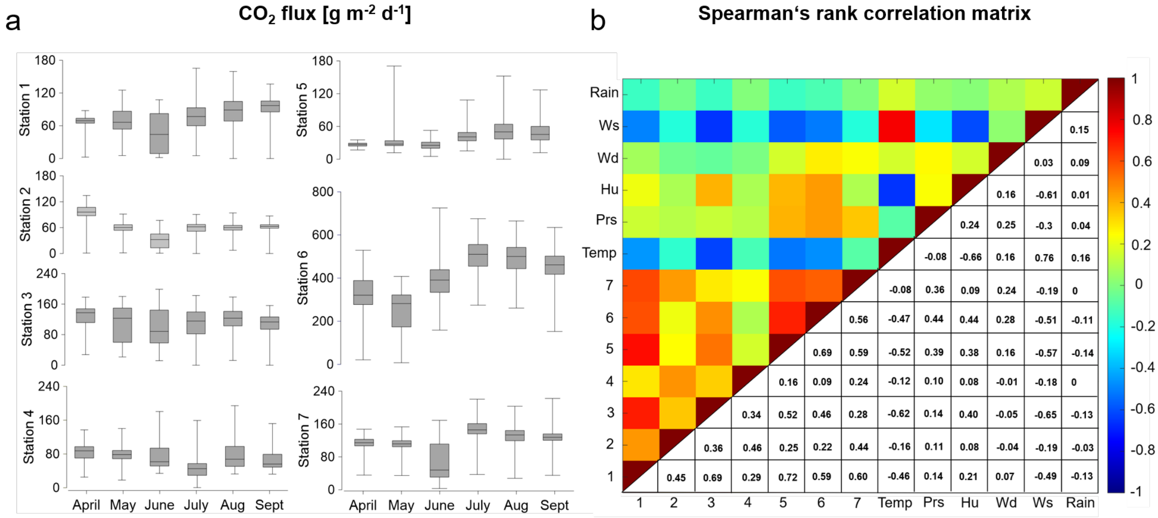

	1	2	3	4	5	6	7	Temp	Prs	Hu	Wd	Ws	Rain
Rain													
Ws													0.15
Wd												0.03	0.09
Hu											0.16	-0.61	0.01
Prs										0.24	0.25	-0.3	0.04
Temp									-0.08	-0.66	0.16	0.76	0.16
7								-0.08	0.36	0.09	0.24	-0.19	0
6							0.56	-0.47	0.44	0.44	0.28	-0.51	-0.11
5						0.69	0.59	-0.52	0.39	0.38	0.16	-0.57	-0.14
4					0.16	0.09	0.24	-0.12	0.10	0.08	-0.01	-0.18	0
3				0.34	0.52	0.46	0.28	-0.62	0.14	0.40	-0.05	-0.65	-0.13
2			0.36	0.46	0.25	0.22	0.44	-0.16	0.11	0.08	-0.04	-0.19	-0.03
1		0.45	0.69	0.29	0.72	0.59	0.60	-0.46	0.14	0.21	0.07	-0.49	-0.13

Figure 7.3: a) Box-plots showing the variability of CO_2 flux values during the monitoring period. b) Spearman correlation coefficients showing the relationship between stations and atmospheric parameters. The y-axis labels are defined as follows: Temp - Air temperature [°C], Prs - Barometric pressure [hPa], Hu - Air humidity [%], Wd - Wind direction [°N], Ws - Wind speed [km/h], Rain [mm].

7.3.1 Atmospheric effects on CO_2 flux

The Spearman's rank correlation revealed that the strongest negative correlations occurred between CO_2 flux and wind speed as well as air temperature. Both of these atmospheric parameters are strongly positively correlated with each other. Atmospheric pressure, on the other hand, shows only a weak positive correlation with CO_2 flux at stations 5, 6, and 7, while at the other station no correlation is detected (Fig. 7.3b). Wind speed demonstrates the greatest influence on CO_2 flux for the majority of stations (Tables 7.4 - 7.10). The moderate to strong inverse correlation between wind speed and CO_2 flux at stations 1, 3, 5 and 6 shown in blue (Fig. 7.3b), suggests that either high wind speeds inhibit the migration of CO_2 from the soil or that CO_2 is diluted with ambient air, that penetrates the shallow and partially porous subsurface favoured by topography. In fact, the west-facing topographic scarp of the NNE-SSW-striking Los Humeros fault is exposed to the main wind directions measured during the monitoring period (Fig 7.10). A possible link between surface topography and CO_2 flux has already been discussed in a study performed at Mammoth Mountain in California (*Lewicki and Hilley*, 2014; *Lewicki et al.*, 2007). Considering that barometric pressure was relatively stable during the monitoring period (Fig. 7.9 and Table 7.3), we suspect that the positive correlation with CO_2 flux (stations 5, 6, 7) is either a spurious correlation or a superposition by stronger atmospheric parameters, such as wind speed, that masks the barometric pumping effect (*Viveiros et al.*, 2015). Although rainfall and CO_2 flux do not have significant correlation coefficients (Fig. 7.3b), we observe an effect of heavier rain periods on CO_2 emissions (Fig. 7.8). We assume that with increased precipitation, the upper, altered soil layer becomes saturated with water, forming a gas seal that prevents CO_2 degassing. To protect the equipment from condensation, no measurements were taken when air humidity exceeded 90%, resulting in a few data gaps during the end of June and in the first half of August. An overview of the statistical distribution of atmospheric parameters is provided in the supplementary material (Table 7.3).

Application of the SMLRM revealed that 7 to 39% of CO_2 flux variations can be explained by atmospheric parameters, with less than 10% of the variations explained by atmospheric parameters at stations 2 and 4. In comparison to the other stations, station 4 shows more spike-like variations and no cyclic behavior (Fig. 7.8, 7.11). A detailed summary of the results at each station can be found in Tables 7.4 - 7.10 in the supplementary material.

The results of the CWT on CO_2 flux and model residuals show that a 24-hour cycle is evident at nearly all stations, while semi-diurnal cycles are less pronounced (Fig. 7.4, 7.11). It is not surprising that stations 2 and 4 do not show any cyclic behavior, as the results of the SMLRM show the least influence from atmospheric parameters, thus emphasizing the impact of unmonitored variables on their variations. The residual CO_2 flux rates at stations 1 and 5 show no cyclic behavior, while for stations 3, 6 and 7 the strengths of 12-hour and 24-hour cycles become weaker but are still visible. Consequently, the SMLRM and CWT prove that further unmonitored variables affect CO_2 flux variations, which are discussed in the following paragraph.

7.3.2 Effects of the shallow subsurface on CO_2 flux

Soil porosity and intrinsic permeability play major roles in the vadose zone, since they determine fluid flow mechanisms (advection/ diffusion) and flow directions (*Forde et al.*, 2020; *Rinaldi*

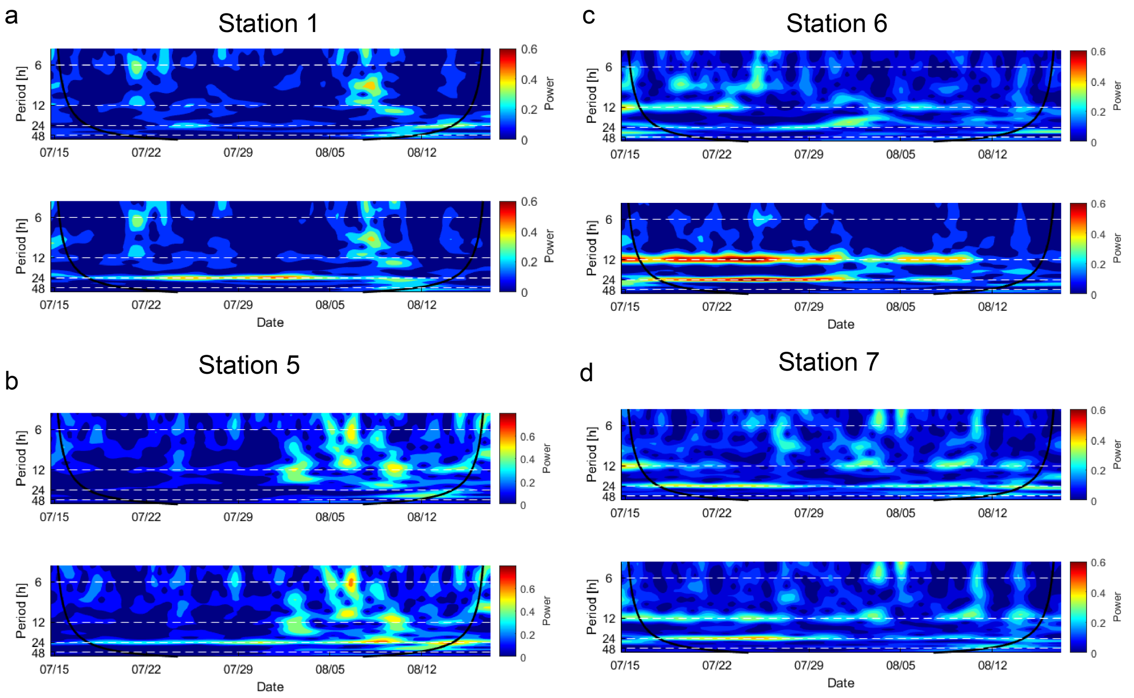

Figure 7.4: Wavelet power spectrum for the period from mid-July to mid-August at: a) station 1, b) station 5, c) station 6, and d) station 7. The lower spectrogram at each station shows the initial CO_2 flux, while the upper spectrogram shows the residual CO_2 flux. The time period shown here was chosen because of its continuous data coverage. Black solid lines represent the cone of influence, with areas outside the black line potentially affected by edge-effect artifacts. The wavelets were created with the MATLAB software, version R2019b.

et al., 2012; *Viveiros et al.*, 2015). On average, the uppermost layer in the geological succession of the Los Humeros geothermal reservoir consists of 100 m-thick, unconsolidated pumice and scoria fall deposits with porosities of up to 50% (*Weydt et al.*, 2018). Hydrothermal alteration of varying intensity, as seen throughout the study area, is induced by fluid-rock interactions and affects petrophysical rock properties (*Prol-Ledesma and Browne*, 1988).

Some studies have shown that soil temperature and soil water content contribute significantly to variations in CO_2 flux due to increased biological oxidation, or near-surface steam condensation (*Reth et al.*, 2005; *Viveiros et al.*, 2015, 2020), while others did not identify any significant relationship (*Lewicki and Hilley*, 2014). These parameters have not been measured continuously at our study site due to technical difficulties with the sensors. However, a strong correlation between ground temperatures and mean CO_2 flux is supported by data from the initial site selection survey (e.g., station 1: 73 g m^{-2} d^{-1}, 60.5 °C; station 3: 109 g m^{-2} d^{-1}, 73.8 °C; station 6: 418 g m^{-2} d^{-1}, 97.2 °C; and station 7: 120 g m^{-2} d^{-1}; 57.3 °C; Fig. 7.1c) and reinforces the assumption that ground temperatures may explain some of the CO_2 flux variation. Ultimately, the damage zone of the Los Humeros fault substantially influences fluid migration from the hydrothermal reservoir to the surface, as indicated by the strong variability of increased CO_2 fluxes and hot ground temperatures. The increase in permeability of fault damage zones as a result of extensive fracture networks has previously been noted (*Bense et al.*, 2013; *Caine et al.*, 1996; *Curewitz and Karson*, 1997; *Rowland and Sibson*, 2004). We relate heterogeneities and anisotropies in the shallow subsurface to a complex fracture network, acting as a fluid conduit-barrier system with the geometry and distribution of fractures related to normal dip-slip kinematics and recent uplift of small magma bodies (*Urbani et al.*, 2020). Mineral precipitation of quartz and calcite in fractures and faults is the result of silica-rich geothermal waters and loss of CO_2 at the boiling point (*Gutierrez-Negrin and Izquierdo-Montalvo*, 2010; *Martínez-Serrano*, 2002). Together with hydrothermal alteration at the surface, these processes may impede lateral and vertical fluid migration in certain areas, while directing fluid flow to areas of higher permeability as previously observed in other geological systems (*Yehya and Rice*, 2020).

7.3.3 CO_2 flux vs. fluid reinjection – Implication for geothermal reservoir management

The key finding of this study is the inverse correlation between the rate of low-temperature (approx. 90°C) reinjected fluids and residual CO_2 flux (Fig. 7.5). We identified this inverse correlation by removing the effects of measured atmospheric parameters and calculating the Spearman's rank correlation coefficients between both time series. For this purpose, we used the summarized flow rate of all three reinjection wells, referred to as total reinjected fluids (Fig. 7.12), and obtained moderate to strong negative correlation coefficients (ρ = -0.51 to -0.66) at stations 1, 5, 6, and 7 (Fig. 7.5). These stations are also intercorrelated and show intermediate to strong correlations with atmospheric parameters (Fig. 7.3b).

The spectral signatures of the residual time series from stations 1 and 5, visualized in their respective wavelet power spectra, no longer show diurnal variations (Fig. 7.4). These results demonstrate that the SMLRM successfully modelled atmospheric influences and that the residual time series are free of variations caused by atmospheric changes. Therefore, they may represent variability related to changes in the geothermal reservoir, which could explain the stronger correlation to reinjection of stations 1 and 5 compared to other stations. For example, the lowest mean CO_2 flux (40 g $m^{-2}d^{-1}$) of all stations was measured at station 5. However, a temporal relationship between low degassing rates, similar to those at station 5, and deep seismic activity has been monitored at Piton de la Fournaise (*Boudoire et al.*, 2018) and supports our finding that lower CO_2 emissions can provide information about dynamic changes at depth.

At stations 2, 3 and 4 no significant correlations to reinjection rates were calculated (Fig. 7.13). As mentioned earlier, stations 2 and 4 differed in their response to daily atmospheric variations. They showed strongly reduced power within the 24- and 12-hour bands, indicating that those fluxes may not correspond as strongly to atmospheric changes as other stations (Fig. 7.11). Station 3 shows strong 24- and 12-hour cycles and a low correlation to reinjection rates of the respective residual CO_2 flux time series. Comparing the wavelet power spectrum of station 3 with the wavelet power spectrum of its residuals, strong 24- and 12-hour cycles remain, indicating that an atmospheric influence is still present (Fig. 7.11).

We assume that stations not correlated with reinjection rates are more strongly influenced by unmonitored variables, e.g., soil temperature or soil humidity, as well as nonlinear processes such as: i) fluid-rock interactions (dissolution, mineralization) leading to changes in fracture permeability and soil/rock properties (*Gutierrez-Negrin and Izquierdo-Montalvo*, 2010; *Zhang et al.*, 2008), ii) changes in effective stresses by pore pressure perturbations from ascending fluids (*Talwani et al.*, 2007), and iii) local and regional stress field changes due to volcanic-tectonic forces influencing fracture distribution and geometry (*Norini et al.*, 2015b, 2019). It is therefore unreliable to consider only one parameter when trying to understand which processes are affecting CO_2 in the subsurface, as complex physical, thermal, chemical and mechanical (THCM) processes occur during the reinjection of cold geothermal brine into geothermal systems (*Bodvarsson*, 1989; *Bödvarsson and Tsang*, 1982; *Kaya and Zarrouk*, 2017; *Parisio et al.*, 2019). To understand the inverse correlation of surface CO_2 emissions and reinjection of cold water, we will discuss some hypotheses below. However, we want to point out that none of these hypotheses is true on its own, but rather they become valid when combined

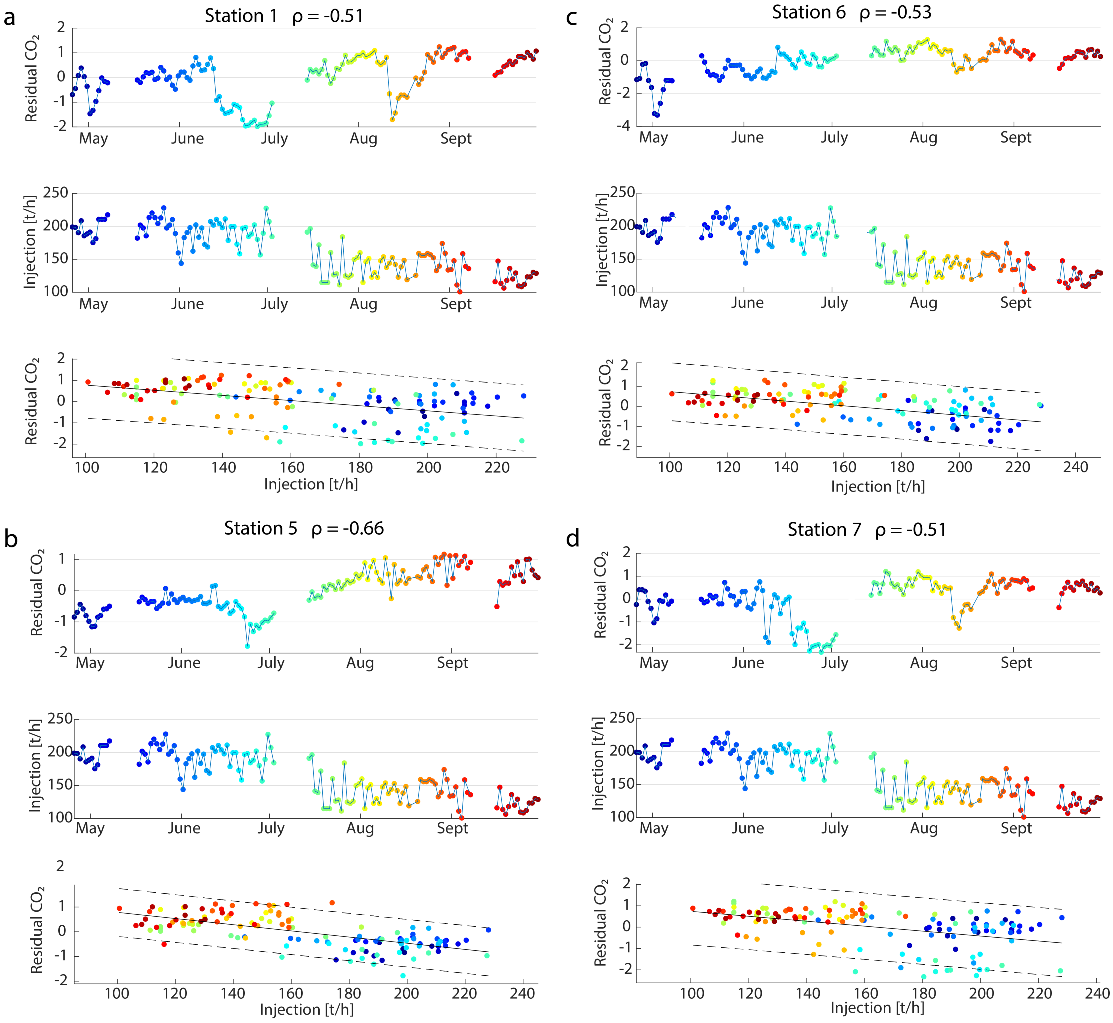

Figure 7.5: Temporal relationship between daily residual CO_2 flux (upper plot) and total reinjected fluids (middle plot) at: a) station 1, b) station 5, c) station 6, and d) station 7 and corresponding spearman correlation coefficients (ρ). Linear regression analysis (bottom plots) illustrates the relationship between the CO_2 flux residuals and reinjection rates within the 95% confidence interval. Colours are used to visualize the data of the respective time periods. The interrupted lines in the CO_2 flux and reinjection curves represent data gaps that are not considered in the determination of correlation coefficients.

1st hypothesis: The natural upflow of andesitic and fossil fluids from the deep volcanic system can be suppressed by high reinjection rates, reducing the ascendance of CO_2 into the geothermal reservoir. This process has already been described by a numerical model reported in *Kaya and Zarrouk* (2017).

2nd hypothesis: *Kaya and Zarrouk* (2017) also determined that a large amount of non-condensable gases such as CO_2 can be stored in reservoir rocks through mineral dissolution and precipitation. Dissolved CO_2 reacts with divalent cations such as Ca2+ and precipitates calcite, which is in agreement with hydrothermal zones composed of calcite and other hydrothermal minerals found in well cuttings at Los Humeros (*Martínez-Serrano*, 2002). This trapping mechanism can be numerically modelled by either chemical or physical adsorption of gases on the rock matrix (*Kaya and Zarrouk*, 2017).

3rd hypothesis: The deep reinjection of fluids into the low permeable rock matrix at 2000 m depth results on the one hand in a pressure buildup, causing CO_2 to remain in the dissolved phase and on the other hand a reduction in boiling, which also has a positive effect on CO_2 solubility (*Pistone et al.*, 2011). Future studies should focus on numerical models of coupled THCM processes, in order to evaluate the proposed hypotheses and the role of discrete fracture networks and multi-phase fluid flow.

However, the response of CO_2 emissions to a decrease or increase in reinjection rates within 24 hours indicates that the Los Humeros fault is a highly permeable structure, connecting the geothermal reservoir and Earth's surface. To exclude a potential time delay between the response of CO_2 emissions and fluid reinjection, we also calculated correlation coefficients when testing variable time lags, and did not observe an increase in correlation. Consequently, we can define the response time of gas emissions to changes in reinjection rates as ≤ 24 hours. A global review paper on tracer tests summarizes that tracer velocities in the order of one to several tens of meters per hour are not exceptional (*Bodvarsson*, 1989). Increased fluid migration velocities are also indicated by tracer studies performed in wells at Los Humeros (*Iglesias et al.*, 2015), thus supporting our results.

7.3.4 Natural gas emissions vs. seismic activity

Induced seismicity triggered by geothermal exploitation causes changes in the thermal and poroelastic stresses of a reservoir (*Urban and Lermo*, 2017). During our monitoring period, recorded seismicity did not exceed a local magnitude of MLV 2.1 (unpublished data) with the majority of hypocentres located at >2 km depth, corresponding to the depth of the exploited geothermal reservoir (*Toledo et al.*, 2020a). In this study, we found no clear relationship between residual CO_2 flux and seismicity rate or associated magnitudes. However, we suggest further study involving longer observation periods and seismic tremor analyses to validate this relationship. In addition, CO_2 flux could be compared with more sensitive data such as structural changes obtained with coda wave interferometry (*Obermann et al.*, 2015). For this purpose, we would place the gas monitoring system along the fault trace of seismically active faults with geothermal surface activity.

7.4 Conclusion

The characterization of fluid migration in geothermal fields plays an important role for the safe and sustainable management of a reservoir. In this study, we have discussed various factors

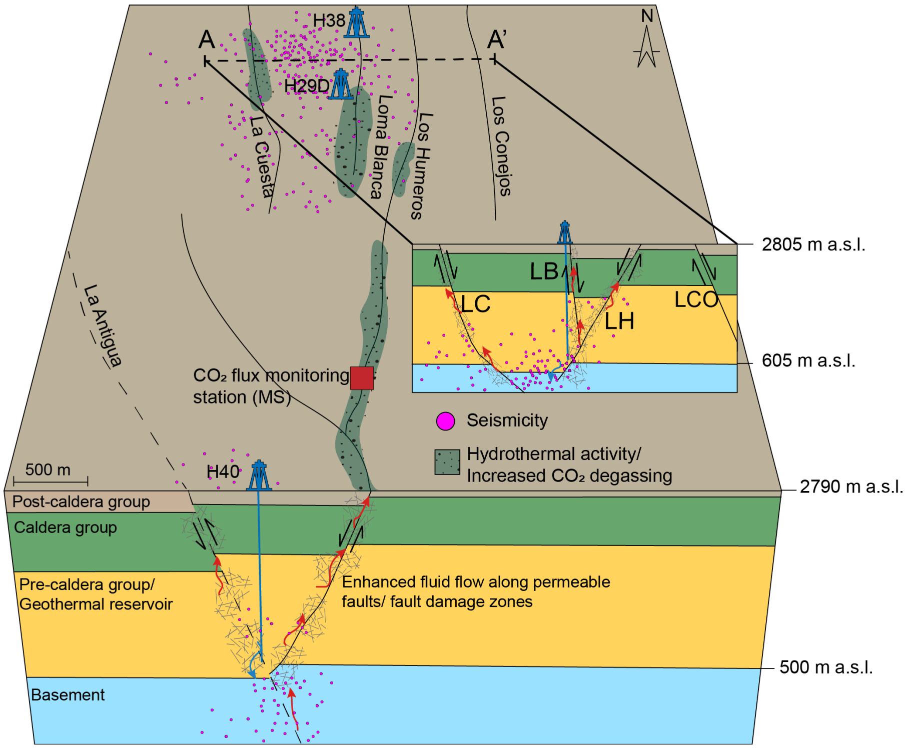

Figure 7.6: A simplified conceptual model showing enhanced fluid migration along steeply-dipping faults/fault damage zones cutting through the Los Humeros geothermal system. Cross sections show the orientation and connectivity of injection wells to faults. Red arrows illustrate the migration of hot reservoir fluids, while blue arrows show the migration of colder reinjected fluids. Note that cross section A-A' is located between injection well H29D (deviated to the NW) and H38 and is intended to represent a buffer zone for this area. For the exact location of seismicity, the reader is referred to Figure 7.1b. The abbreviations are defined as follows: LH - Los Humeros, LB - Loma Blanca, LC - La Cuesta, LCO - Los Conejos; a.s.l. above sea-level. Detailed descriptions of lithologies referring to the different caldera groups can be found in *Carrasco-Núñez et al.* (2017b).

influencing the variation on CO_2 emissions and demonstrated the effect of fluid reinjection on surface gas emissions. Our results indicate an active hydraulic communication between the target zones of reinjection wells and hydrothermal surface manifestations along the Los Humeros fault, as illustrated by a simplified conceptual model (Fig. 7.6). This finding has implications for novel reservoir monitoring concepts, including automated gas analytics for real-time analyses of reservoir responses to geothermal reservoir operations (including stimulations). Multi-chamber systems provide a fundamental tool for studying the high spatial and temporal variability of surface CO_2 flux due to external factors, particularly within active structural settings where fluid flow is controlled by extensive fracture networks. Several open questions remain; therefore future studies should investigate long-term monitoring of gas emissions ($\geq$ 12 months, ideally 24 months) and multiple gas monitoring systems should be installed across geothermal fields. In addition, coupled THCM models considering discrete fracture networks, integrated multi-phase flow and reactive transport simulations could model the complexities discussed here, which is beyond the scope of this publication. Nevertheless, we have provided important evidence that surface CO_2 flux responds to reservoir-induced changes caused by reinjection of cold geothermal brine. Regular sampling of carbon and noble gas isotopes using automated sampling techniques could complement the analysis of changing reservoir conditions driven by geothermal exploitation. Geochemical and geophysical methods should be more commonly combined in integrated monitoring systems for optimized reservoir management. This also applies to other utilization concepts of the geological underground, such as carbon capture storage systems.

Acknowledgements

This paper presents results of the GEMex Project, funded by the European Union's Horizon 2020 - Research and Innovation Program under Grant Agreement No. 727550, and by the Mexican Energy Sustainability Fund CONACYT-SENER, Project 2015-04-268074. We wish to thank the Comisión Federal de Electricidad of Mexico (CFE) for their support and access to Los Humeros geothermal field. In particular, we thank Rafael Alfaro and Elidee Juárez Hilarios for regularly downloading data and maintaining the monitoring station. We would also like to thank Guido Blöcher, Mauro Cacace and Henning Francke for valuable discussions during the review process.

Electronic supplementary data

All datasets generated and analyzed for this study can be found on the repository of the GFZ Data Service under the following DOI: `http://doi.org/10.5880/GFZ.4.8.2021.003`

Appendix 7.A Tables and Figures

Table 7.1: Technical data of sensor from the MWS 9-5 microprocessor weather station

Variable	Sensor Type	Range	Accuracy
Temperature	PT-100 (Platinum resistance)	-40 to 50 °C	± 0.3 °C
Barometric pressure	monolithic, laser trimmed absolute pressure sensor (thick film ceramic)	600 to 1100 hPa	± 0.8 hPa (btw. -40 to 50 °C)
Humidity	Monolithic, capacitive sensor	10-100 %	± 2 % (btw. -40 to 50°C)
Windspeed	Three-shell anemometer with magnetic scanning measuring contactless using a Hall sensor (V1.2) or a Reed-contact.	0 to 150 km/h	± 2 km/h
Rain	Water is collected on an area of 200 cm2 and is drained through a funnel to the bucket. The bucket tilts whenever a defined quantity of water has been collected. The tilting creates pulses which are counted.	0 to 5000 mm (0.1 mm resolution)	± 0.2 mm
Wind direction	A weather vane with an endless precision potentiometer of 10 kOhms and a rotation angle of 360 °	0 to 359,9 °N, (resolution 0.1°)	± 5° (at -10°C to 50°C), Hysteresis <8°

Table 7.2: Descriptive statistics of CO_2 flux from seven monitoring stations. Note: Soil CO_2 flux was measured with a Licor-8100A automated monitoring system with 20 cm survey chambers. The analyzer control unit consists of an infrared gas analyzer and a connection panel to interface with monitoring chambers and the LI-8150 Multiplexer measuring the gas exchange. Measurement Range CO_2: 0 ppm to 20,000 ppm; Accuracy: 1.5 % of reading; SD - Standard Deviation.

Station	Minimum ($g\ m^{-2}d^{-1}$)	Mean ($g\ m^{-2}d^{-1}$)	Median ($g\ m^{-2}d^{-1}$)	Maximum ($g\ m^{-2}d^{-1}$)	SD	No. of data
1	1.9	73.7	79.7	165.4	30.2	2941
2	0.8	55.9	59.7	143.2	21.2	2167
3	11.6	109.5	117.1	198.8	39.1	2399
4	0.4	69.0	63.0	349.3	33.4	2602
5	5	40	36	170.6	17.5	2463
6	7.6	418.4	437.6	725.5	119.8	2640
7	3	120	125.3	222.3	36.4	2669

Table 7.3: Descriptive statistics of atmospheric parameters

Variable	Minimum	Mean	Median	Maximum	SD	No. of data
Atmospheric temperature (°C)	1.8	12.6	11.0	27.3	5.5	2974
Barometric pressure (hPa)	728.1	731.9	731.8	735.7	1.4	2975
Humidity (%)	10.7	74.6	82.0	98.1	20.5	2975
Windspeed (km/h)	0	3.8	1.5	21.3	4.5	2975
Rain (mm)	0	0.13	0	16.54	0.65	3048
Wind direction (°N)	0	-	-	349.6	-	2428

SD – Standard Deviation.

Table 7.4: Results from the stepwise multiple regression analysis (SMLRM) for Station 1. Note: The gray marked row highlights the atmospheric variable that has the strongest influence on the CO_2 flux. SE – Standard Error; tStat - t-statistic for each coefficient to test the null hypothesis that the corresponding coefficient is zero against the alternative that it is different from zero, given the other predictors in the model; pValue - p-value for the t-statistic of the hypothesis test that the corresponding coefficient is equal to zero or not; Adjusted R^2 - The model explains the variability on the response variable (CO_2 flux) caused by the predictor variables (atmospheric parameters).

Station	Estimated coefficients	Estimate	SE	tStat	pValue	Adjusted R^2
1	Intercept	-0.19	0.03	-6.69	2.69E-11	
	Air temperature	-0.16	0.04	-3.63	2.83E-04	0.0165
	Barometric pressure	0.09	0.02	4.9	1.04E-06	0.004
	Humidity	-0.2	0.04	-5.4	7.21E-08	0.0311
	Wind speed	-0.30	0.03	-9.24	4.48E-20	0.0544
	Rain	-0.08	0.02	-4.32	1.61E-05	0.001
	Temp: Prs	0.09	0.03	2.89	0.003	0.002
	Temp: Hu	-0.12	0.03	-4.36	1.35E-05	0.012
	Temp: Ws	0.30	0.05	5.97	2.66E-09	0.003
	Temp: Rain	0.08	0.03	2.31	0.02	0.015
	Prs: Hu	0.11	0.03	4.18	2.95E-05	0.002
	Prs: Ws	0.08	0.03	2.99	0.002	0.006
	Ws: Rain	0.06	0.03	2.22	0.03	0.007
Linear regression model	y ~1 + Temp*Prs + Temp*Hmdt + Temp*Ws + Temp*Prcpt + Prs*Hmdt + Prs*Ws + Hmdt*Ws + Ws*Prcpt					
Model summary statistics	Sum adjusted R^2	0.15				
	Number of observations	2971				
	P-value	2.93E-95				

Table 7.5: Results SMLRM Station 2

Station	Estimated coefficients	Estimate	SE	tStat	pValue	Adjusted R²
2	Intercept	-0.06	0.02	-2.48	0.01	
	Air temperature	-0.3	0.03	-8.99	4.39E-19	0.0234
	Barometric pressure	0.12	0.02	6.39	1.92e-10	0.0126
	Humidity	-0.36	0.03	-11.34	3.24e-29	0.0226
	Rain	-0.05	0.02	-2.3	0.02	0.0011
	Temp: Hu	-0.06	0.02	-3	0.002	0.0033
	Temp: Rain	0.13	0.03	4.23	2.4e-05	0.0038
	Prs: Rain	0.05	0.02	2.26	0.02	0.0012
Linear regression model	y ∼1 + Temp*Hmdt + Temp*Prcpt + Prs*Prcpt					
Model summary statistics	Sum adjusted R²	0.07				
	Number of observations	2971				
	P-value	4.7E-45				

Table 7.6: Results SMLRM Station 3

Station	Estimated coefficients	Estimate	SE	tStat	pValue	Adjusted R²
3	Intercept	0.06	0.02	3.09	2.01E-03	
	Air temperature	-0.49	0.03	-15.16	4.72E-50	0.009
	Barometric pressure	0.09	0.02	5.51	3.85E-08	0.008
	Humidity	-0.30	0.03	-11.69	6.98E-31	0.04
	Wind speed	-0.34	0.03	-13.53	1.54E-40	0.304
	Rain	-0.07	0.02	-4.64	3.65E-06	0.001
	Temp: Hu	-0.14	0.02	-6.35	2.54E-10	0.005
	Prs: Hu	0.03	0.02	1.79	7.33E-02	0.001
	Prs: Ws	0.10	0.02	5.57	2.83E-08	0.003
	Hu: Ws	0.16	0.02	7.82	7.48E-15	0.004
Linear regression model	y ∼1 + Temp*Hmdt + Prs*Hmdt + Prs*Ws + Hmdt*Ws + Ws*Prcpt					
Model summary statistics	Sum adjusted R²	0.39				
	Number of observations	2971				
	P-value	2.94e-309				

Table 7.7: Results SMLRM Station 4

Station	Estimated coefficients	Estimate	SE	tStat	pValue	Adjusted R^2
4	Intercept	0.00	0.02	0.15	8.80E-01	
	Air temperature	-0.30	0.04	-8.39	7.21E-17	0.0192
	Barometric pressure	0.19	0.02	10.34	1.17E-24	0.0251
	Wind speed	-0.29	0.03	-9.72	5.48E-22	0.0019
	Humidity	-0.10	0.03	-3.79	1.51E-04	0.0304
	Prs: Hu	0.05	0.02	2.85	4.45E-03	0.0016
Linear regression model	y $\sim$1 + Temp*Ws + Prs*Ws + Hmdt*Ws					
Model summary statistics	Sum adjusted R^2	0.08				
	Number of observations	2971				
	P-value	2.95E-55				

Table 7.8: Results SMLRM Station 5

Station	Estimated coefficients	Estimate	SE	tStat	pValue	Adjusted R^2
5	Intercept	-0.19	0.02	-8.13	6.49E-16	
	Air temperature	-0.10	0.03	-4.05	5.16E-05	0.009
	Barometric pressure	0.22	0.02	12.75	2.79E-36	0.031
	Wind speed	-0.33	0.03	-11.67	8.68E-31	0.101
	Temp: Prs	0.03	0.02	2.06	3.92E-02	0.01
	Temp: Ws	0.22	0.02	9.73	4.96E-22	0.029
Linear regression model	y ∼1 + Temp*Ws + Prs*Ws + Hmdt*Ws					
Model summary statistics	Sum adjusted R^2	0.18				
	Number of observations	2971				
	P-value	3.89E-120				

Table 7.9: Results SMLRM Station 6

Station	Estimated coefficients	Estimate	SE	tStat	pValue	Adjusted R^2
6	Intercept	0.00	0.02	-0.10	9.21E-01	
	Air temperature	0.10	0.03	2.95	3.22E-03	0.003
	Barometric pressure	0.18	0.02	10.28	2.24E-24	0.045
	Humidity	0.18	0.03	5.71	1.25E-08	0.012
	Wind speed	-0.28	0.03	-10.70	3.05E-26	0.138
	Temp: Prs	-0.08	0.03	-2.71	6.85E-03	0.001
	Prs: Hu	-0.20	0.02	-8.06	1.06E-15	0.018
	Prs: Ws	-0.08	0.02	-3.48	5.05E-04	0.01
	Hu: Ws	0.12	0.02	6.95	4.40E-12	0.012
Linear regression model	y ~1 + Temp*Hmdt + Prs*Hmdt + Prs*Ws + Hmdt*Ws + Ws*Prcpt					
Model summary statistics	Sum adjusted R^2	0.239				
	Number of observations	2971				
	P-value	2.29E-171				

Table 7.10: Results SMLRM Station 7

Station	Estimated coefficients	Estimate	SE	tStat	pValue	Adjusted R²
7	Intercept	-0.28	0.03	-10.39	7.22E-25	
	Air temperature	-0.08	0.04	-2.01	4.46E-02	0.0113
	Barometric pressure	0.25	0.02	13.00	1.33E-37	0.0416
	Humidity	-0.18	0.03	-5.50	4.03E-08	0.0241
	Wind speed	-0.09	0.03	-2.75	6.07E-03	0.024
	Temp: Ws	0.40	0.05	7.81	7.63E-15	0.0215
	Prs: Ws	0.06	0.02	3.48	5.13E-04	0.004
	Hu: Ws	0.13	0.04	3.54	4.04E-04	0.003
	Hu: Ws	0.12	0.02	6.95	4.40E-12	0.012
Linear regression model	y ∼1 + Temp*Ws + Prs*Ws + Hmdt*Ws					
Model summary statistics	Sum adjusted R²	0.113				
	Number of observations	2971				
	P-value	3.72E-74				

Figure 7.7: Photograph of the study area showing four of the seven monitoring stations. Numbers indicate the stations. Photograph is looking to the east towards the Los Humeros fault plane striking NNE-SSW.

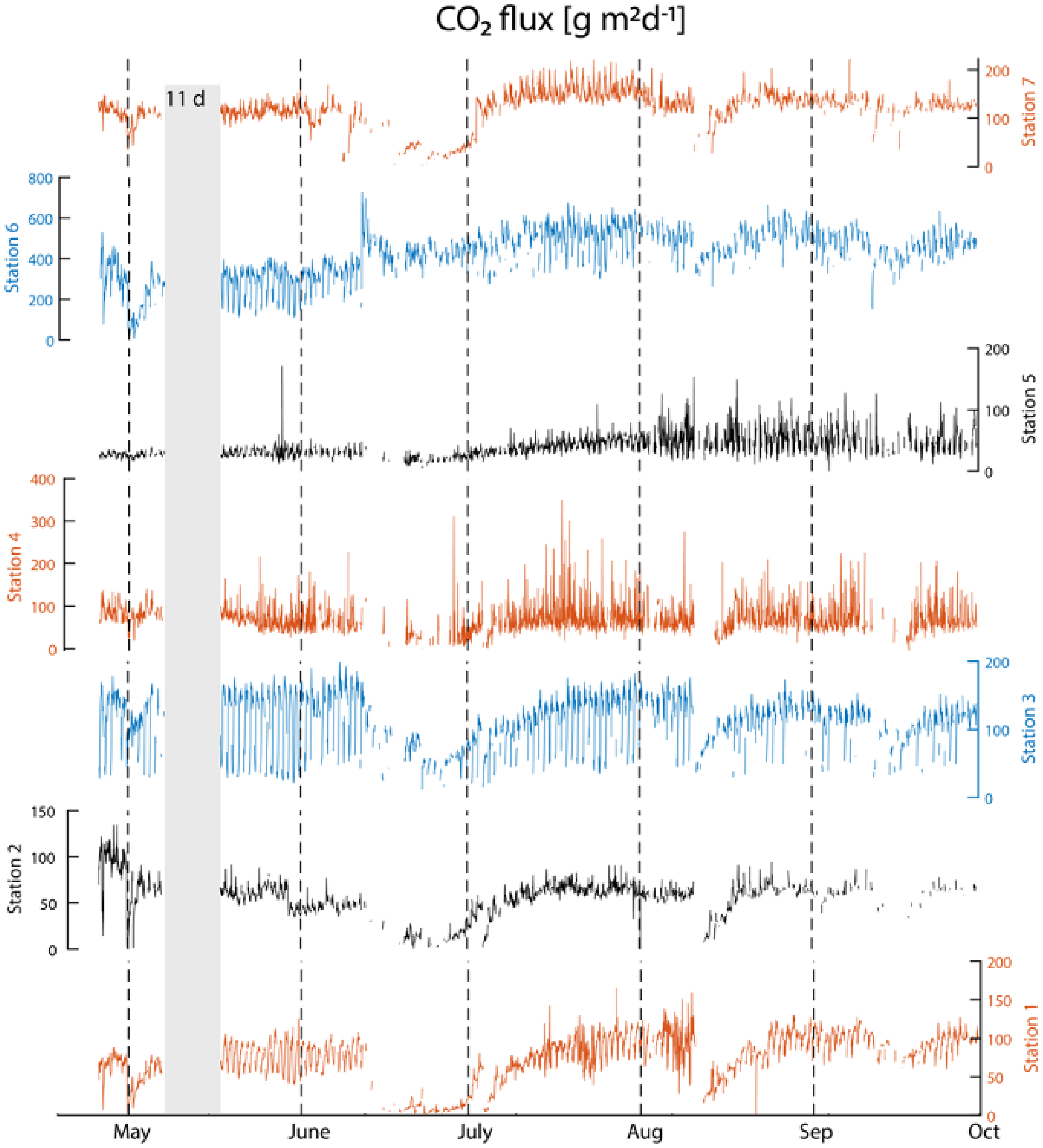

Figure 7.8: Temporal evolution of CO_2 fluxes at all Stations from end of April to end of September 2018. Grey rectangle represents a data gap of 11 days. Black dashed vertical lines indicate the beginning of each month.

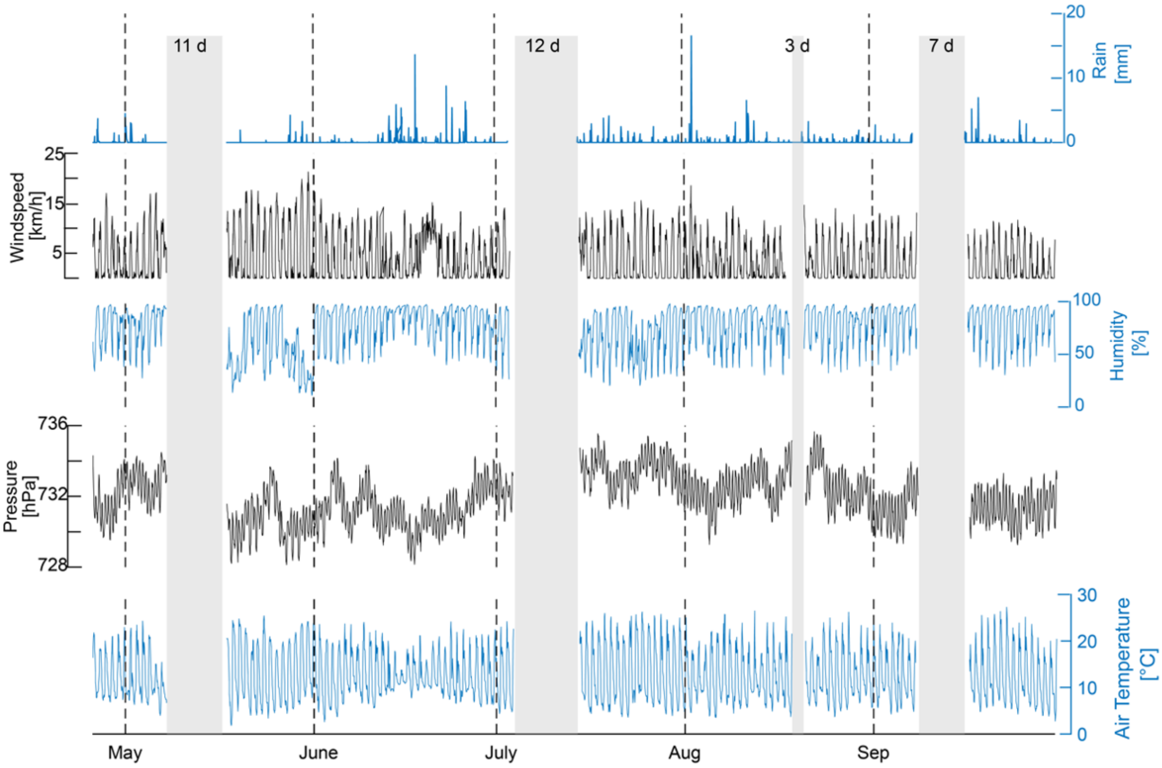

Figure 7.9: Temporal evolution of atmospheric parameters from end of April to end of September 2018. Grey rectangles represent the length of data gaps in days. Black dashed vertical lines indicate the beginning of each month.

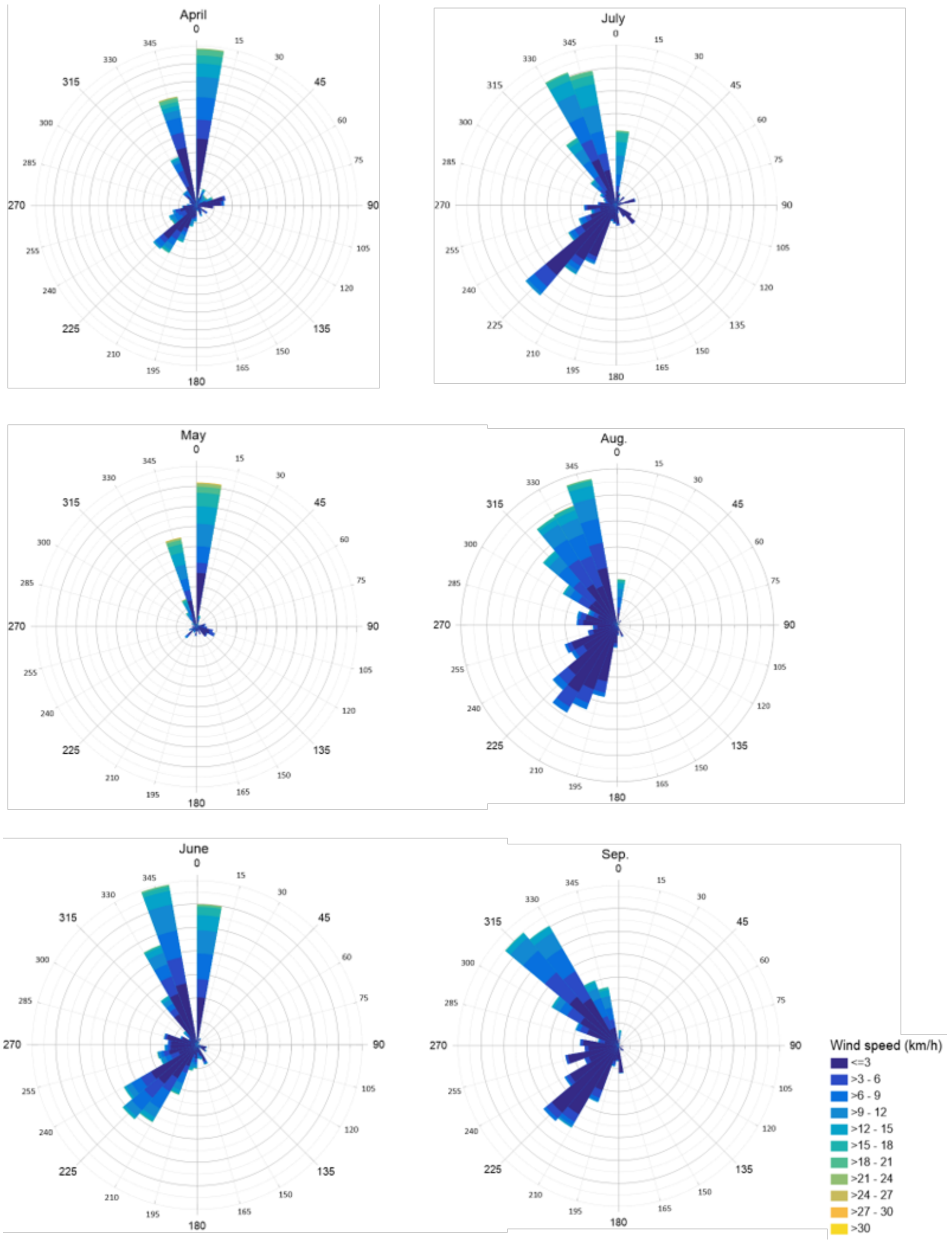

Figure 7.10: Wind speed and wind direction over the course of the monitoring period.

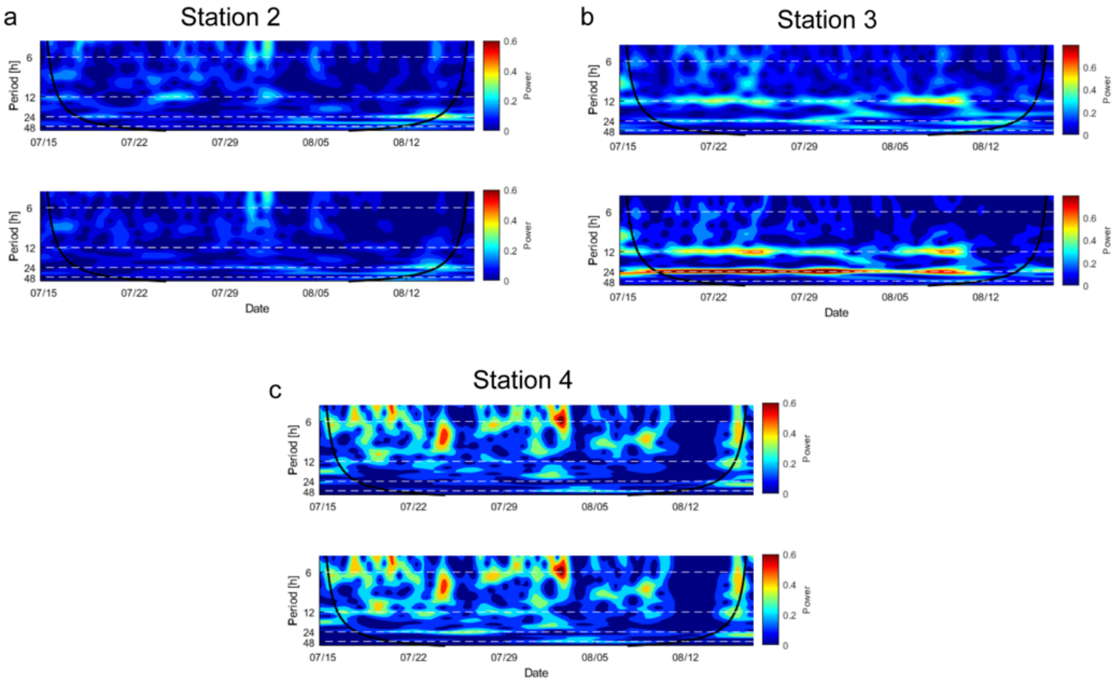

Figure 7.11: Wavelet power spectrum for the period from mid-July to mid-August at: a) station 2, b) station 3, and c) station 4. The lower spectrogram at each station shows the original CO_2 flux while the upper wavelet power spectrum shows the residual CO_2 flux. The time period shown here was chosen because of its continuous data coverage. Black solid lines represent the cone of influence with areas outside the black line potentially affected by edge-effect artifacts.

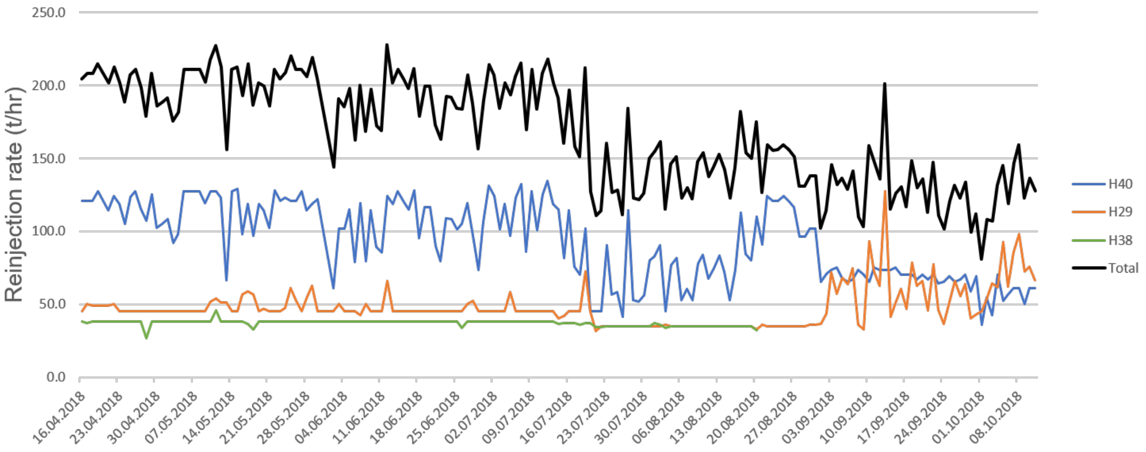

Figure 7.12: Daily reinjection rates for each well and total rate of reinjected fluid (black). For the location of reinjection wells please see Figure 7.1b

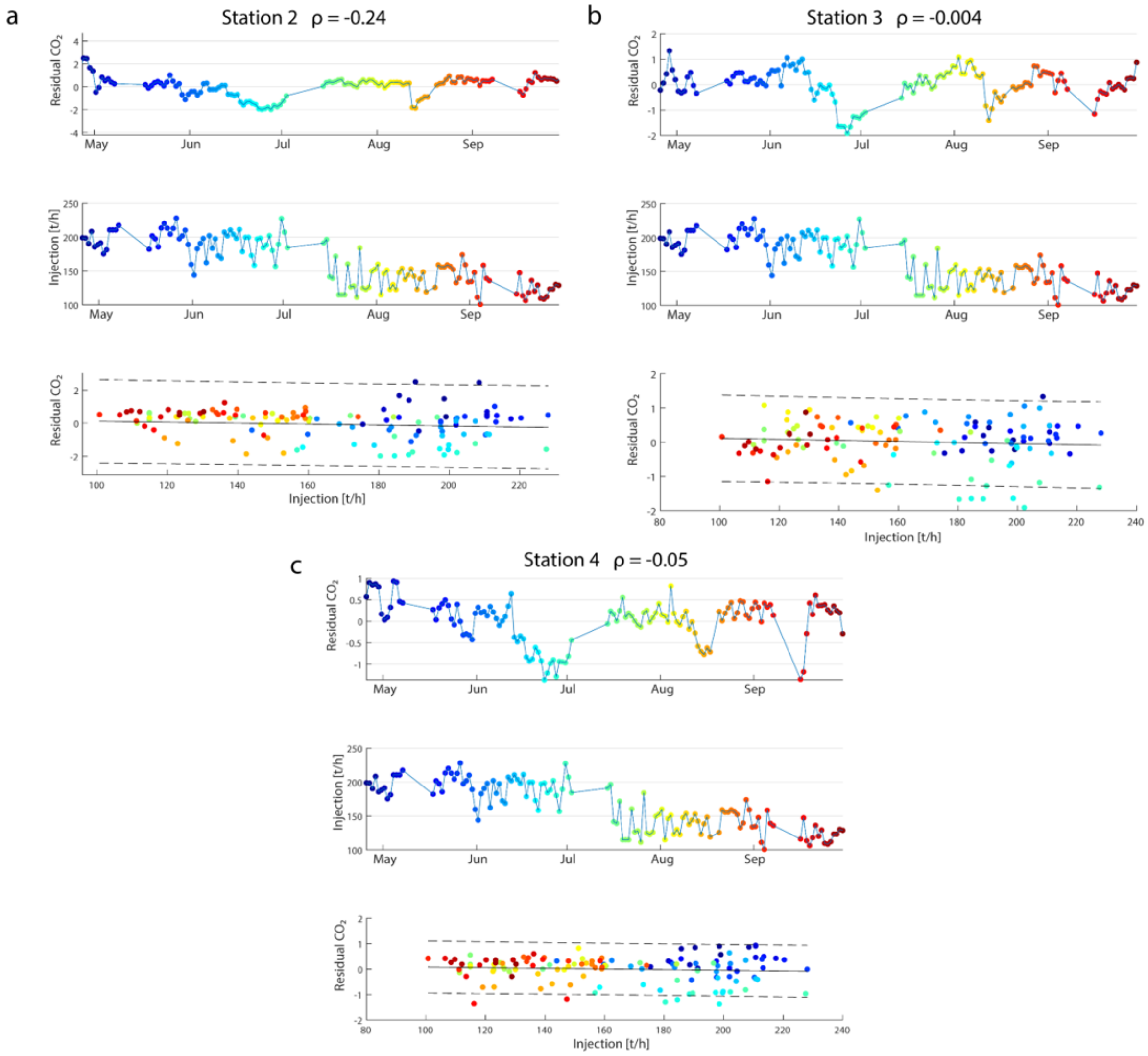

Figure 7.13: Temporal relationship between daily residual CO_2 flux (upper plot) and total reinjected fluids (middle diagram) at: a) station 2, b) station 3, and c) station 4 and corresponding spearman correlation coefficients (ρ). Linear regression analysis (bottom plot) illustrates the relationship between the CO_2 flux residuals and reinjection rates within the 95 % confidence interval. Colours are used to visualize the data of the respective time period.

8

Aluto Exploration

Pinpointing Deep Geothermal Upflow in Zones of Complex Tectono-Volcanic Degassing: New Insights from Aluto Volcano, Main Ethiopian Rift

Egbert Jolie, W. Hutchinson, D.L. Driba, Anna Jentsch, B. Gizaw

Article published in *Geochemistry, Geophysics, Geosystems*, 2019.
`https://doi.org/10.1029/2019GC008309`

Abstract: Active rifts release large amounts of gases from deep sources to the atmosphere by advection and diffusion processes along permeable fracture zones. The objective of this study is to develop geothermal exploration concepts for areas with little or no hydrothermal surface expressions suitable for fluid sampling and analyses (e.g., hot springs, geysers, and fumaroles). In such areas, soil gas surveys can complement established geophysical and geochemical exploration. We report CO_2, ^{222}Rn (radon), and ^{220}Rn (thoron) emission data and ground temperatures from the Aluto volcanic complex in the Main Ethiopian Rift to improve understanding of tectonic and volcanic controls on the existing geothermal system. This suite of gas emission measurements allows us to identify major, deep-rooted permeable structures with active fluid circulation and identify suitable drilling targets for geothermal production wells on Aluto. We show that significant differences in gas signatures (i.e., efflux and spatial pattern) can be used to identify predominantly volcanically and/or tectonically influenced compartments. Major gas emissions indicate significant fluid circulation at depth, which is typical for magmatic systems. Such high gas emissions have been observed in areas affected by major tectonic structures interacting with magmatic bodies at depth (tectono-volcanic). Predominantly fault-controlled sectors also show hydrothermal fluid circulation, but to a lower extent compared to tectono-volcanic sectors. Within the Aluto volcanic complex, geothermal production wells mainly target such fault-controlled domains, whereas results of the study indicate strongest fluid circulation in tectono-volcanic sectors. This result should be considered for the future exploration and development strategy of the site.

Plain Language Summary: Active rifts release large amounts of gases from deep sources to the atmosphere along permeable fracture zones. We report CO_2, ^{222}Rn (radon), and ^{220}Rn (thoron) emission data and ground temperatures from the Aluto volcanic complex in the Main Ethiopian Rift. Results help to improve understanding of tectonic and volcanic controls on the existing geothermal system and are useful to identify suitable drilling targets for geothermal production wells. Variations in gas emissions also allow mapping of permeable structures, even in areas where faults are not obvious. We show that significant differences in gas signatures (i.e., flow rates and spatial pattern) can be used to identify predominantly volcanically and/or tectonically influenced domains. Emissions increase toward the volcanic center implying a deep degassing magmatic body.

8.1 Introduction

The East African Rift System has numerous high-temperature geothermal fields, which offer huge potential for power generation and opportunities for economic development; however, the heterogeneity and complexity of the highly fractured geothermal reservoirs pose major difficulties for their exploration (*Younger*, 2014). Conventional geophysical and geochemical exploration technologies are useful to prove a resource and understand the large-scale architecture of geothermal systems but do not pinpoint preferential locations for targeting expensive production wells into most permeable pathways. Additionally, geophysical data (e.g., resistivity data) often cannot distinguish active from paleo-hydrothermal activity as the resistivity structure will be preserved in the subsurface, even if systems are cooling (*Bibby et al.*, 1992). For a successful exploration strategy in these environments, information on the system's current activity and fault permeability (e.g., upflows and outflows) is required at a high spatial resolution. The best geochemical approach for obtaining such high spatial resolution observations are soil gas surveys (e.g., CO_2, ^{222}Rn, and ^{220}Rn), which help to identify the most permeable structures with highest hydrothermal fluid flow (*Jolie et al.*, 2015a; *Neri et al.*, 2016). In this paper we prove the suitability of these techniques for geothermal exploration projects.

Major faults in the East African Rift System are controlled by tectonic and volcanic mechanisms. Surface gas release and hydrothermal fluid circulation in active rift systems not only are related to its volcanic heat source but also reflect local and regional tectonic controls in the subsurface (*Brune et al.*, 2017; *Goerner et al.*, 2009; *Jolie et al.*, 2016). Increased degassing along fracture zones outlines deep-rooted permeable segments of active faults and points to major upflow and outflow zones of hydrothermal fluids. Depth of faults is at least 5 km, but no distinct structure could be identified below 8 km based on Magnetotelluric (MT) studies by *Samrock et al.* (2015). In Tule Moye, a comparable site to Aluto, faults channel magmatic fluids from a depth of ∼14 km to the surface (*Samrock et al.*, 2018). Fault segments with strong gas emissions are characterized by increased slip and dilation tendencies (*Jolie et al.*, 2015b, 2016). Analyses of a variety of soil gases have proven their suitability for assessing the tectonic and volcanic controls on geothermal systems (*Hunt et al.*, 2017; *Jolie et al.*, 2015a, 2016; *Lee et al.*, 2016). These gases provide vital information for the exploration of geothermal fields and help in targeting wells in the most permeable structures with the greatest flow rates of high-temperature hydrothermal fluids. Soil gas surveys do not require heavy equipment and can be performed in a relatively short time even in some of the most difficult terrain, where other technologies are limited. Many techniques even allow in situ analysis in the field (e.g., accumulation chamber method, alpha spectroscopy, and gas chromatography), which gives much flexibility in the planning of field campaigns (*Jolie et al.*, 2015a).

Aluto offers an ideal location to address some of these issues and understand the architecture of a rift-related alkaline, fault-controlled geothermal system. The volcanic complex has been a target for geothermal exploration and exploitation for several decades (*Gebregzabher*, 1986; *Gianelli and Teklemariam*, 1993; *Gizaw*, 1993; *Hochstein et al.*, 2017; *Teklemariam et al.*, 1996; *Valori et al.*, 1992) as well as recent geological, geochemical, and geophysical investigations (*Biggs et al.*, 2011; *Braddock et al.*, 2017; *Hutchison et al.*, 2015, 2016a,b,c; *Iddon et al.*, 2019; *Nowacki et al.*, 2018; *Saibi et al.*, 2012; *Samrock et al.*, 2015; *Wilks et al.*, 2017) Although Aluto is well studied compared to many of Ethiopia's geothermal prospects, major uncertainties remain about how geothermal fluids are distributed in the subsurface and how they ascend along the mapped fault zones. Answering these questions has implications for understanding Aluto's geothermal system and for characterizing the fault network that might be exploited by future dike intrusions and volcanic events (*Hutchison et al.*, 2015); more generally, it can provide important lessons on how to exploit the complex, highly-fractured alkaline geothermal systems that typify the East African Rift System.

In this study, we show the results of a multi-method approach that focuses on the identification and characterization of degassing fluids that ascend from a magmatic system along tectonic faults (tectono-volcanic interaction). Tectono-volcanic interactions have an effect on soil degassing within the Aluto volcanic complex and result in more intense gas emissions. Our approach consists of a combination of systematic alpha-spectroscopic measurements as well as CO_2 efflux measurements based on an area-wide, regular grid (*Jolie et al.*, 2015a, 2016). Results illustrate that substantial information on permeable subsurface structures and lateral outflows can be obtained by the analysis of surface degassing. This adds more details to the results of conventional structural mapping at the surface, which is often limited in particular in areas with fast geomorphological changes due to strong erosional activity. Soil gas surveys provide useful solutions for a comprehensive analysis of geothermal systems and the identification of suitable areas for geothermal development.

8.2 Geological Setting

8.2.1 Regional Geology – The Main Ethiopian Rift

The ∼600-km-long Main Ethiopian Rift (MER) is an actively extending magmatic rift that forms the northernmost segment of the East African Rift System (*Corti*, 2009). The MER shows clear along-axis variations in rift morphology (*Molin and Corti*, 2015), tectonics (*Agostini* *et al.*, 2011), and crustal structure (*Keir et al.*, 2015; *Maguire et al.*, 2006) and is usually divided into northern, central, and southern sectors (Figure 8.1a).

Normal fault scarps are prominent at the surface, and two dominant fault sets have been identified: (1) Mid-Miocene border faults and (2) Quaternary-Recent Wonji faults aligned along the rift axis (*Boccaletti et al.*, 1998; *Ebinger and Casey*, 2001; *Mohr*, 1967). Rift magmatism has led to surface volcanism across the MER and Quaternary-Recent volcanoes are mostly concentrated along the rift axis (*Di Paola*, 1972).

Although the styles and geochemistry of MER volcanism is diverse (*Fontijn et al.*, 2018), the most attractive geothermal prospects are hosted by chemically evolved, silicic shield volcanoes and calderas, for example, Corbetti, Aluto, or Gedemsa (*Hutchison et al.*, 2016a; *Kebede*, 2012; *Samrock et al.*, 2018).

Satellite remote sensing surveys (e.g., *Biggs et al.* 2011; *Hutchison et al.* 2016b; *Lloyd et al.* 2018) have highlighted episodes of ground deformation at a number of these silicic volcanoes (e.g., Aluto and Corbetti). These observations provide compelling evidence for subsurface fluid movement, although contrasting models have been proposed to explain the causes of deformation, including magmatic intrusions, gas and magmatic fluid pulses, and clay swelling (*Hutchison et al.*, 2016c; *Samrock et al.*, 2018). Despite this uncertainty, there is a consistent view that pre-existing structures (both tectonic and volcanic in origin) play an important role in controlling the movement of magma, hydrothermal fluids, and gases at these volcanoes (*Goerner et al.*, 2009; *Hutchison et al.*, 2015; *Lloyd et al.*, 2018).

8.2.2 Aluto Geology and Geothermal Field

Aluto volcano, the focus of this contribution, is located in the central MER (*Hutchison et al.*, 2015, 2016b,c) and is Ethiopia's only exploited geothermal field (*Kebede*, 2012). Its geological and eruptive history has been the focus of work by *Hutchison et al.* (2015, 2016b,c) who have shown that the complex was initially built up as a trachytic shield before undergoing a series of large caldera-forming eruptions between 320 and 300 ka. Since ∼60 ka, Aluto has been in a post-caldera phase typified by the eruption of small volume ($< 250 \times 106$ m^3) pumice cones and obsidian domes across the complex. The key structural feature of Aluto is a NNE-SSW (Wonji-aligned) fault known as the Artu Jawe Fault Zone (AJFZ; *Hutchison et al.*, 2015), and deep well observations suggest that the AJFZ predates the first eruptions of the silicic complex. Young obsidian lava flows seem to be co-located with this major structure and represent a record of the most active structures across Aluto, which channeled magma during eruptive periods and now channel magmatic gases. The AJFZ together with an elliptical ring fault, assumed to have developed during Aluto's caldera collapse, strongly influences magma ascent and also direct hydrothermal fluids toward the surface. Geothermal surface manifestations (e.g., steam vents, alteration, and warm ground) are widely distributed within the volcanic complex, but strong fumaroles and boiling hot springs only occur outside the complex (Figure 8.1b).

Aluto's geothermal field has also been the focus of numerous surface and deep well investigations (e.g., *Gianelli and Teklemariam* 1993; *Gizaw* 1993; *Teklemariam et al.* 1996). Observations from the wells have been used to infer that the main part of the geothermal reservoir is $> 2{,}000$ m beneath the surface and is sealed by a sequence of intensely altered

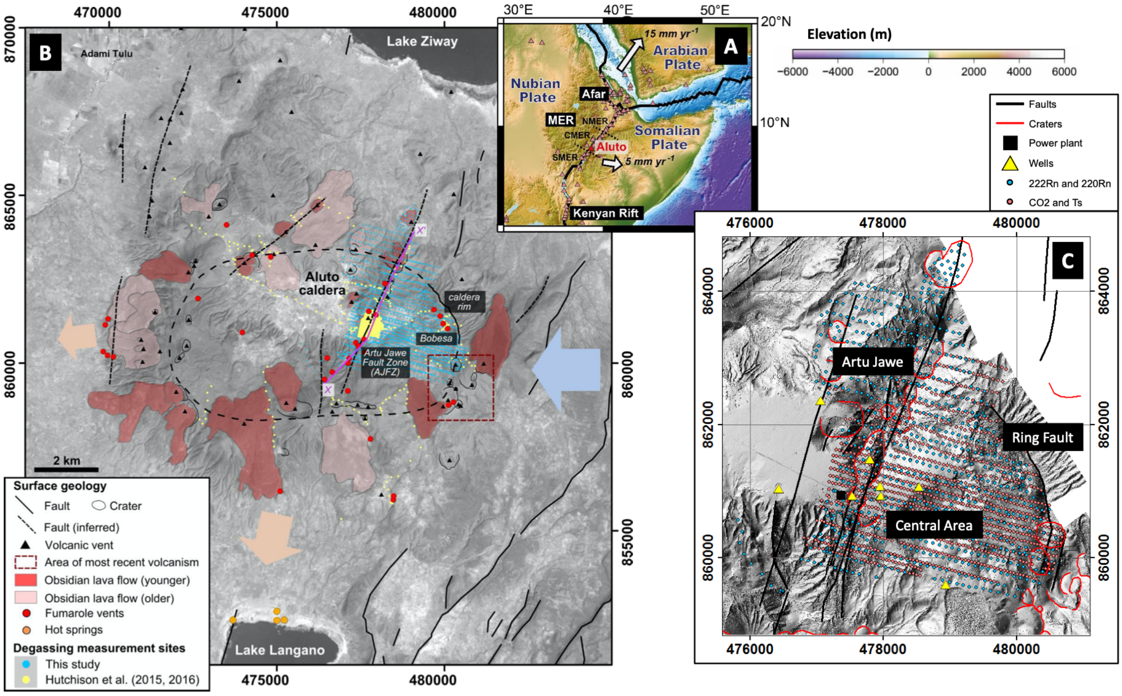

Figure 8.1: (a) Regional topographic map. The black lines represent major plate boundaries, while pink triangles mark all Holocene volcanoes (after Siebert & Simkin, 2002). The Main Ethiopian Rift (MER) is divided into northern (NMER), central (CMER), and southern (SMER) segments. Aluto volcano, the focus of this study, is located in the CMER and is shown in red. White arrows show current extension vectors relative to a fixed Nubian Plate (after *Saria et al.* 2014). In (b), a detailed map of the Aluto volcanic complex with a summary of the geology, hydrothermal manifestations, and degassing studies is shown (coordinate system WGS 1984 UTM Zone 37N). The latest version of the geological map of Aluto is available in *Hutchison et al.* (2016b). The large blue arrow shows the presumed inflow of cool groundwater to the geothermal reservoir (after *Braddock et al.* 2017; *Darling et al.* 1996), while the smaller orange arrows show the shallow outflow of hot geothermal fluids that feed fumaroles and hot springs on the West and South of the complex. In (c), a detailed map of the study area including all sampling sites for ^{222}Rn, ^{220}Rn, CO_2, and T_S is shown.

basalts and tuffs that form a low-permeability, low-resistivity clay cap at ∼500–1,500 m (*Samrock et al.*, 2018). The geothermal fluid appears to be primarily sourced from rainfall on the rift margin (*Darling et al.*, 1996; *Rango et al.*, 2010) rather than the surrounding lakes, and there is good evidence from resistivity soundings for major outflows to the South and West (*Hochstein et al.*, 2017). This and the high temperatures indicated by water chemistry, mineralogy, and downhole temperatures (>300 °C; *Gizaw*, 1993) all suggest that the AJFZ represents a major upflow zone from the deep geothermal reservoir toward the surface. To date, geothermal production wells only target the AJFZ, specifically its Northern Sector (Figure 8.1).

Previous studies of Aluto's gas emissions (*Hutchison et al.*, 2015, 2016b) focused mainly on CO_2 and involved a couple of transects of major structures and a small-scale study of the main AJFZ area (Figure 8.1). These results supported findings from earlier geothermal investigations that identified the AJFZ as the key structure for fluid upflow and geothermal utilization. *Hutchison et al.* (2015) also found significant anomalous degassing in other areas of the complex (specifically around the caldera rim and ring fault on the east of the complex, Bobesa; Figure 8.1). Owing to the limited number of sample sites and the focus on CO_2 data, major uncertainites remain about these degassing regions as well as the upflow along the AJFZ. In particular, it is not clear whether (1) all mapped faults are connected to a deep geothermal reservoir; (2) fluid circulation extends along NNE-striking fault zones beyond the boundaries of Aluto volcanic complex; (3) fault intersections provide enhanced permeability and hence good targets for future exploration; and (4) there is any evidence for lateral fluid outflow. By extensive and systematic soil gas measurements (involving a wide range of parameters, CO_2, ^{222}Rn, and ^{220}Rn), we aim to address these challenges by assessing the variability of gas emissions along fracture zones and identifying further permeable but less prominent or maybe even hidden structures.

8.3 Methods

A large-scale soil gas survey was performed in May 2016 covering a significant area of the two dominating structures (i.e., Artu Jawe and Ring Fault; Figure 8.1c) as well as the area in between the two structures (referred to as "Central Area"), building up on previous efforts by (*Hutchison et al.*, 2015, 2016b). A second small-scale survey was performed in early 2017 to extend the survey area to the North and Northwest for a comprehensive understanding of the NNE continuation of the AJFZ and the continuation of the Ring Fault to the West. The NE-SW extension of the study area is 5.7 km with a maximum NW-SE extension of 3.5 km. The following parameters were determined during the field survey-CO_2 efflux by the accumulation chamber method, ^{222}Rn and ^{220}Rn activity concentration by alpha-spectroscopic measurements, and soil temperatures (T_S) at 50 cm depth (Table 8.1; *Fridriksson et al.* 2016; *Jolie et al.* 2015a). The accumulation chamber method is a technology where a chamber is placed on the ground and the increasing CO_2 concentration in the chamber is measured (2–3 min) by an infrared gas analyzer (LI-COR 820, accuracy <3% of reading). The increase in CO_2 concentration correlates to the CO_2 efflux at the interface from geosphere to atmosphere. Throughout the survey, we used a WEST Systems Type A accumulation chamber (*West Systems*, 2019). Temperature measurements have been performed using a Greisinger GMH 285-BNC thermometer with Pt1000 sensor in a 620-mm-long stainless steel probe (accuracy ±0.1 K). ^{222}Rn and ^{220}Rn activity concentrations are determined by a radiometric measurement (∼15 min), which determines their short-living radon daughter nuclides 218Po and 216Po from soil gas samples collected 1 m below the surface (*Jolie et al.*, 2015a) and pumped to the analyzer. Measurements have been performed by a Sarad RTM 1688 and RTM 2200 using a high-voltage measuring chamber with electrostatic precipitation of ionized nuclides on the surface of a 2 cm2 semiconductor silicon detector (accuracy: 3 counts/min).

8.3.1 Radon Versus Thoron

Radon (^{222}Rn) and thoron (^{220}Rn) activity concentrations have been used for the assessment of hydrothermal upflow zones in geothermal resources (*Jolie et al.*, 2015a). ^{222}Rn activity concentrations above and in the vicinity of hydrothermal upflow zones usually result in increased gas concentrations. In general, measurable activity concentrations of both parameters depend primarily on (1) the depth of the uranium/thorium source in the subsurface, (2) the fluid migration velocity from the subsurface to the surface, and (3) the different decay velocities

Table 8.1: Summary of All Measured Parameters Parameter CO_2.
Note: The maximum encountered CO_2 efflux value was above the detection limit (DL) of the device and therefore set to the maximum measurable CO_2 efflux value.

Parameter	CO_2 ($g \cdot m^{-2} \cdot day^{-1}$)	^{222}Rn ($kBq \cdot m^{-3}$)	^{220}Rn ($kBq \cdot m^{-3}$)	T (°C)
Number of samples	1,280	726	721	885
Min	0.9	558	177	18.1
Max	25,084 (DL*)	1,050.7	562.3	95.1
Mean (arithm.)	333.9	36.2	19.6	27.0
Median	61.6	19.8	12.9	23.6
Grid dimension	55 × 100 m	100 × 175 m	100 × 175 m	55 × 100 m
	55 × 200 m	55 × 200 m		55 × 200 m

for ^{222}Rn ($T_{1/2}$ = 3.8 days) and ^{220}Rn ($T_{1/2}$ = 55.6 s). This means that in areas with fast fluid migration velocities from the geothermal reservoir to the surface ^{220}Rn values can also reach peak values. Assuming that the approximate source for uranium and thorium is at a constant depth level throughout the study area, different fluid migration velocities toward the surface have a strong impact on the ^{222}Rn-^{220}Rn ratios (RTR). In practical terms, it means that multiple RTRs can indicate geothermal upflows from depth, instead of one specific ratio. This requires a careful interpretation. A ^{222}Rn-^{220}Rn plot from the five sectors with the main degassing features allows one to identify major upflow zones. During the migration of fluids to the surface, a lot more ^{220}Rn than ^{222}Rn is lost due to decay as a result of its short half-life of 55.6 s, compared to 3.8 days for ^{222}Rn. This effect causes significantly increased RTRs at medium fluid migration velocity. However, if the transport velocity is high enough, both ^{222}Rn and ^{220}Rn will result in maximum values and consequently intermediate RTRs. Conversely, shallow uranium/thorium sources could also result in increased ^{222}Rn and particularly high ^{220}Rn activity concentrations (low RTRs); however, this would require high-temperature geothermal activity for fluid-rock interaction, which mainly occurs in deep geothermal reservoirs. In that sense, it is possible to differentiate between (1) deep sources/medium upflow velocity (high RTR: 6.7–33), (2) deep sources/fast upflow velocity (intermediate RTR: 1.5–3.9), and (3) shallow sources (low RTR: 0.3–0.7).

8.3.2 Soil Gas Fingerprint

Fingerprint analyses are widely used in geochemistry, but fingerprints for multi-parameter soil gas datasets are still a novel processing and visualization technique and presented herein for the first time. Soil gas fingerprints give a more comprehensive understanding and classification of the spatial variability of gas emissions by plotting maximum (mean) values of each analyzed parameter from selected compartments of a study area, normalized to the maximum (mean) values observed in the entire study area. These compartments define themselves by particularly high or low soil gas emissions and other geological or hydrological conditions (e.g., terrain, known faults, rivers, and geothermal surface manifestations). In some cases, multiple scenarios for compartments need to be defined and tested for one area. The method allows fast comparison of spatial trends and differences for an unlimited number of parameters. Soil gas fingerprints can be determined for any specific area and aerial extent. Ongoing research activities will further improve this novel approach for a fast assessment and comparison of gas emissions from geothermal fields by including more parameters. Based on this technique, we aim to differentiate deep from shallow sources, tectonic from volcanic degassing, and other characteristics. In this study, we present a soil gas fingerprint analysis for the key structures.

8.4 Results

The two major structures in the study area (i.e., Artu Jawe and Ring Fault) have been subdivided (Figures 8.1c and 8.2). Artu Jawe Fault was divided into Northern (A1) and Southern AJFZ (A2), where higher gas emissions were determined. Along the Ring Fault, two major degassing clusters were identified; therefore, the area was subdivided into R1 and R2.

8.4.1 Carbon Dioxide

The CO_2 efflux dataset was statistically separated into different classes based on two major inflection points (CO_2 efflux: 370 and 8,500 $g{\cdot}m^{-2} \cdot day^{-1}$) in the probability plot (Figure 8.3). Peak values above 8,500 up to 25,084 $g{\cdot}m^{-2} \cdot day^{-1}$ (detection limit of the device) are illustrated as points (Figure 8.2). All values below 350 $g{\cdot}m^{-2}day^{-1}$ are considered as background efflux. A more detailed assessment of the background population identified two further inflection points at 35 and 160 $g{\cdot}m^{-2} \cdot day^{-1}$, splitting the background into two distinct populations. Values below 35 $g{\cdot}m^{-2} \cdot day^{-1}$ are likely to be related to a biogenic source with a mean of 24.9 $g{\cdot}m^{-2} \cdot day^{-1}$, whereas values up to 160 $g{\cdot}m^{-2} \cdot day^{-1}$ and above are considered as volcanic background values (*Hutchison et al.*, 2015). Increased CO_2 efflux values have been measured along Artu Jawe and the Ring Fault, as well as in one well-defined zone in the Central Area (Figure 8.2). Peak CO_2 efflux values (>8,500 $g{\cdot}m^{-2} \cdot day^{-1}$) occurred only along the Ring Fault (R1 + R2) and the Southern AJFZ (A2), but not in Northern AJFZ (A1).

A strong segmentation of the degassing pattern was observed along the AJFZ, which resembles partly the location and dimension of volcanic eruption craters (A1). The Central Area (C) hosts two areas with increased degassing rates. A larger anomaly (C1) is located in the Northern part between Artu Jawe and the Ring Fault (referred to as Bobesa) and correlates with increased ^{222}Rn values (without geothermal surface manifestations). Another small anomaly (C2) sits further Southeast where increased T_S and ^{222}Rn were measured (with geothermal surface manifestations). Existing CO_2 efflux data from 2012 to 2014 and 2016 indicate stable degassing features in space and time for a number of years (Figure 8.4). This area also represents the transition zone from a structurally dominated segment in the North to a volcanically dominated segment in the South.

8.4.2 Soil Temperature

Thermal anomalies occur mainly along Artu Jawe (A1 + 2) and the Ring Fault (R1 + 2), plus two areas (C2 + C4) in the eastern Central Area (i.e., steaming ground; Figure 8.2). C2 seems to be connected to R2. Highest T_S was measured in Southern Artu Jawe and the Ring Fault (R2). Soil temperatures along the Northern AJFZ do not exceed 75 °C. A wide area with slightly increased soil temperatures (up to 32 °C) was identified in the northern part of the study area.

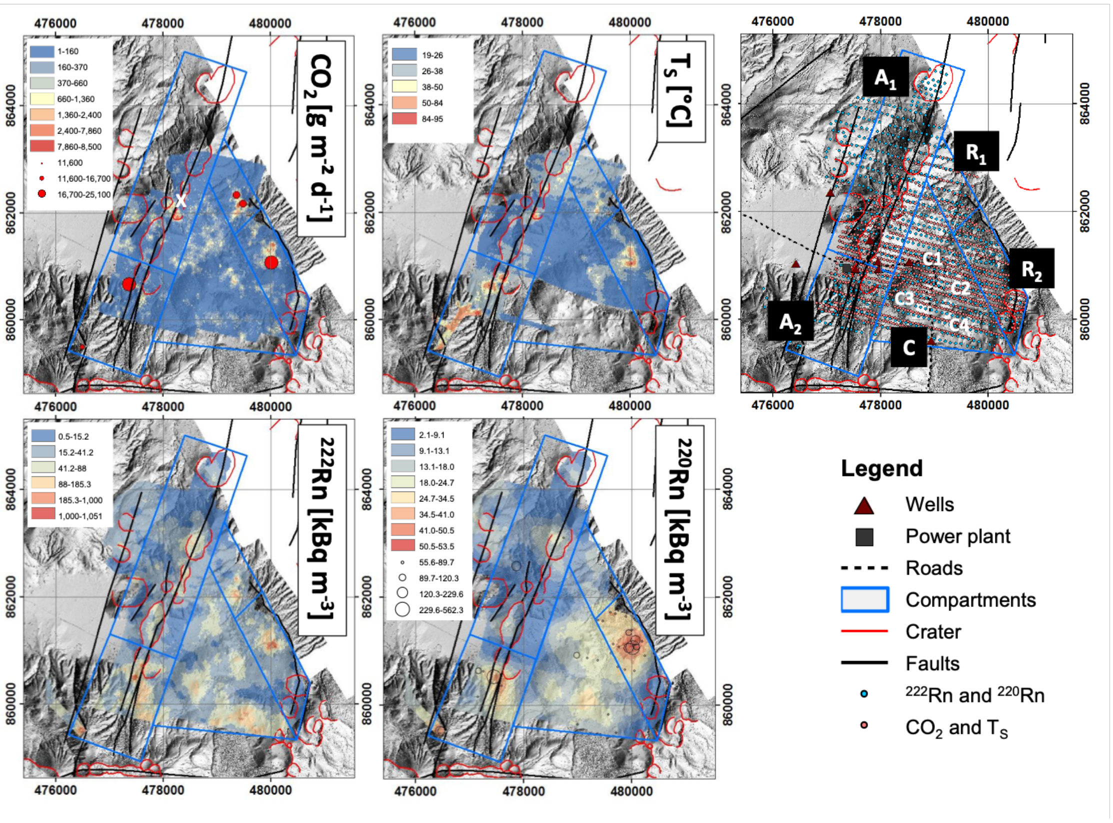

Figure 8.2: Interpolated maps for CO$_2$, T$_S$, ^{222}Rn, and ^{220}Rn. CO$_2$ values >8,500 g·m^{-2} · day^{-1} and ^{220}Rn values >53.5 kBq·m^{-3} are illustrated as points. Fault lines and craters have been digitized on the basis of a map from *Kebede et al.* (1985).

8.4.3 Radon

The ^{222}Rn activity concentration dataset was statistically separated into different classes based on major and minor inflection points in the probability plot (Figure 8.3). Peak activity concentrations (>120.4 kBq·m^{-3}- mean of PIII) occur along the Southern AJFZ with decreasing values toward the North (Figure 8.2). Peaks in the northern sector are located within volcanic eruption craters and appear as elongated anomalies. All values below 15.5 kBq·m^{-3} are considered as pure background. Values between 15.5 and 50.1 kBq·m^{-3} are expected to be a mixture of background and peak values. The map (Figure 8.2) illustrates a segmented, fault-controlled pattern of increased ^{222}Rn activity concentration along Artu Jawe (mainly characterized by dextral offsets). Compared to CO$_2$ efflux and T$_S$, ^{222}Rn gives well-defined anomalies. Two major anomalous, but rather circular areas are located along the Ring Fault (R1 + R2). Three distinct anomalous areas, but with lower magnitudes, were identified in the center (C1 + C2 + C3). The anomaly to the East (C2) coincides with increased soil temperatures. In the northern part of Artu Jawe at the intersection of the Ring Fault and the AJFZ ^{222}Rn values and T$_S$ have only increased minimally. East of the intersection, slightly increased soil temperatures have been measured along a NNE-oriented zone. Anomalous ^{222}Rn values also appear beyond the intersection of the Ring Fault and AJFZ to the NNE in continuation of the AJFZ.

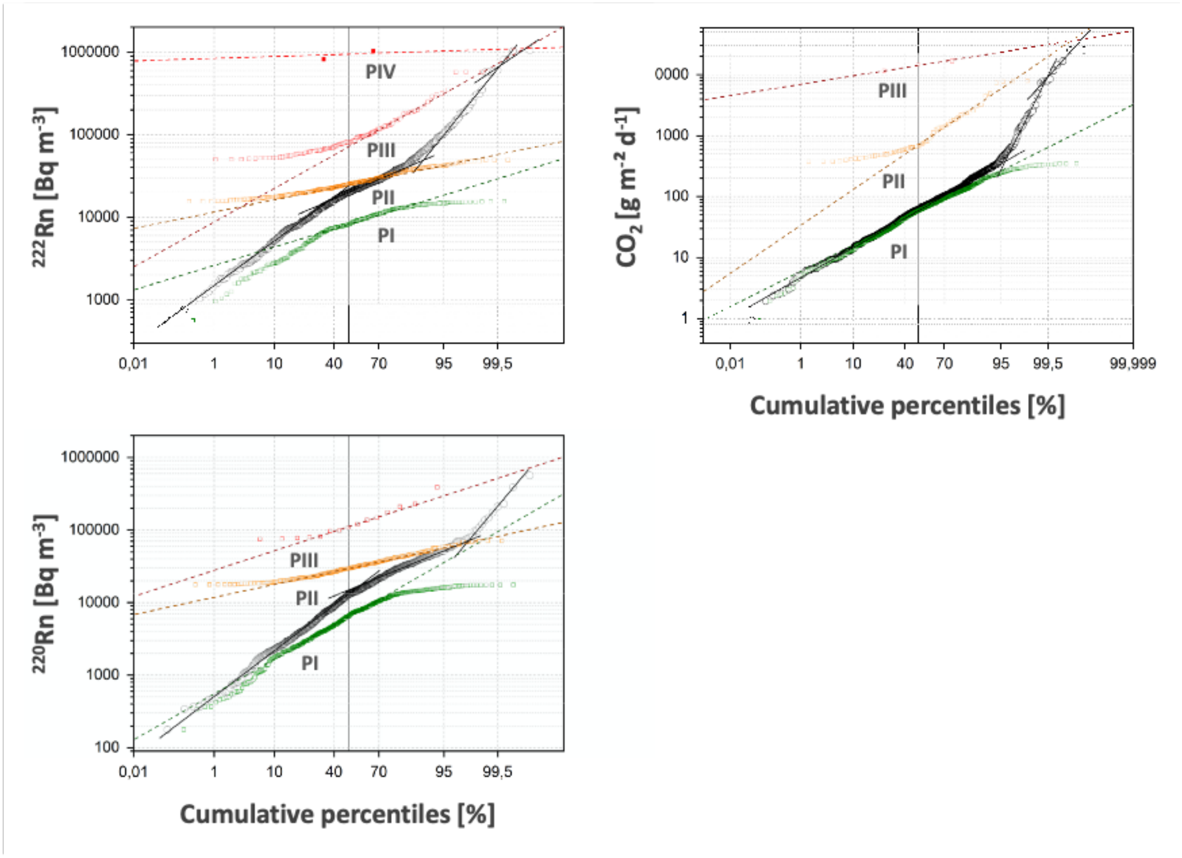

Figure 8.3: Probability plots for interpretation of the data. Following classification was introduced based on major inflection points in the probability plot of each dataset: CO_2 [g·m^{-2} · day^{-1}]: PI (Min–370), PII (370–8,500), PIII (8,500–Max); ^{222}Rn [kBq·m^{-3}]: PI (Min–15.5), PII (15.5–50.1), PIII (50.1–608.4), PIV (608.4–Max); ^{220}Rn [kBq·m^{-3}]: PI (Min–17.6), PII (17.6–71.8), PIII (71.8–Max).

8.4.4 Thoron

The ^{220}Rn activity concentration dataset was separated into different classes based on major and minor inflection points in the probability plot (Figure 8.3). Additional class breaks have been defined for a finer discretization of the map (Figure 8.2). The majority of peak ^{220}Rn values (>71.8 kBq·m^{-3}) was measured at Bobesa. This anomaly extends to the West with decreasing values. Another peak ^{220}Rn cluster occurs in the Southern AJFZ and some medium ^{220}Rn values (17.6–71.8 kBq·m^{-3}) in Northern AJFZ. Activity concentration along Artu Jawe is increasing from the North toward the South. All values below 17.6 kBq·m^{-3} are considered as background.

8.4.5 Along Fault Variations

A profile of gas emissions along the AJFZ (X-X'; Figure 8.1) is shown in Figure 8.5. Fault-controlled emissions occur over a broad zone orthogonal to the fault (Figure 8.2), and so we filtered the emission data so that data within a fixed distance of the line were included in the plot (this is referred to as the buffer zone). For ^{222}Rn, ^{220}Rn, and T_S, a buffer zone of 500 m either side of the profile line was used, while for CO_2 a narrower buffer zone of 300 m was used. The narrower buffer zone for the CO_2 data was selected because data density is greater

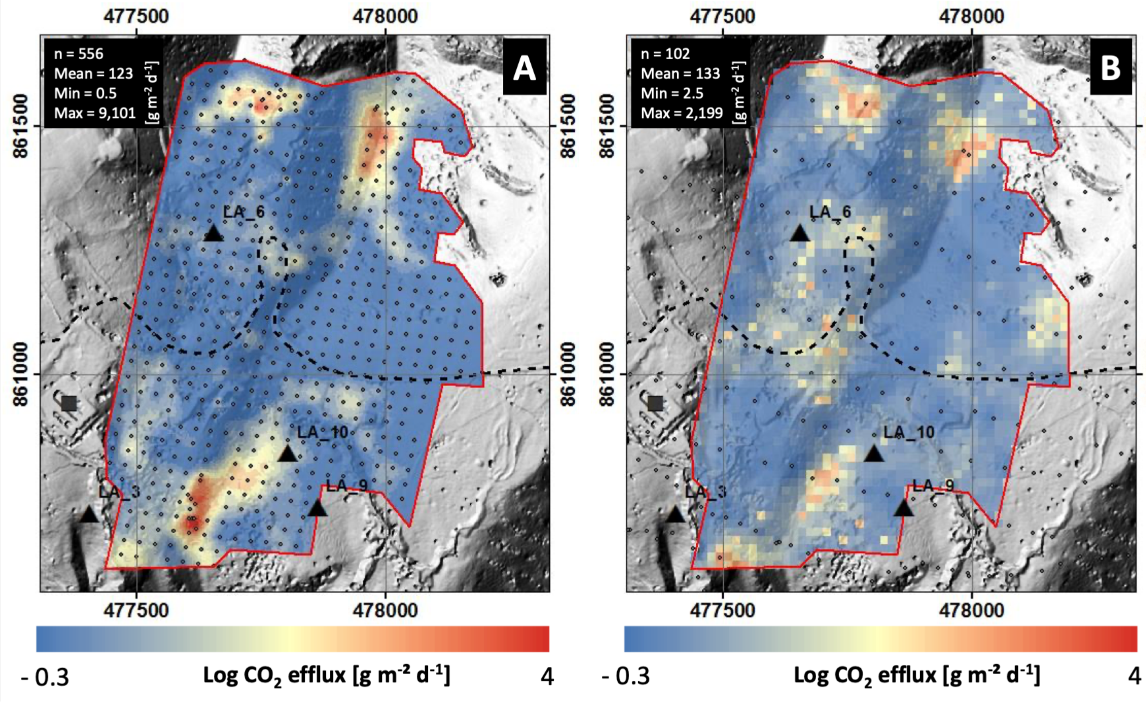

Figure 8.4: Detailed CO_2 efflux map from the transition zone A1 to A2 for the years 2012–2014 (a) from *Hutchison et al.* (2015, 2016b) and 2016 (b) Stable degassing conditions at major degassing spots are indicated.

(as we included the high-spatial resolution survey of *Hutchison et al.* 2015; Figure 8.4). It is important to note that changing this buffer zone does not significantly affect the results and interpretations. We also calculated a running average (Figure 8.5, grey lines), by binning the data in 1 km segments along the fault so that we could identify whether there was any broad (kilometer-scale) change in emissions.

The along-fault plot (Figure 8.5) illustrates the trend of increasing gas emissions from the Northern AJFZ toward the Southern AJFZ. This correlating trend is reflected in all parameters (CO_2, ^{222}Rn, ^{220}Rn, and T_S). A possible explanation for this is the combination of volcanic (vicinity to a magmatic volatile source) and tectonic (structural permeability) impacts in Southern AJFZ, whereas the northern part of Artu Jawe is mainly tectonically influenced (permeable, but distant from magmatic volatile source). For both areas, gas emissions are highly variable over short (1–100 m) length scales, which can be explained by a fault segmentation, non-optimal orientation of the fracture zones in the acting stress field, sealing effects, and multiple upflow zones of geothermal fluids.

8.4.6 Soil Gas Fingerprint

A first attempt of a soil gas fingerprint analysis is presented in Figure 8.6. For each of the five analyzed key compartments (A1, A2, R1, R2, and C), a stacked column is plotted illustrating the maximum and mean values for ^{222}Rn, ^{220}Rn, CO_2 efflux, and T_S normalized to the maximum value in the entire study area. Such plots allow a fast spatial evaluation of the collected data. Here the significant differences in gas emissions originating from A2 and R2 versus A1, R1, and C can be recognized.

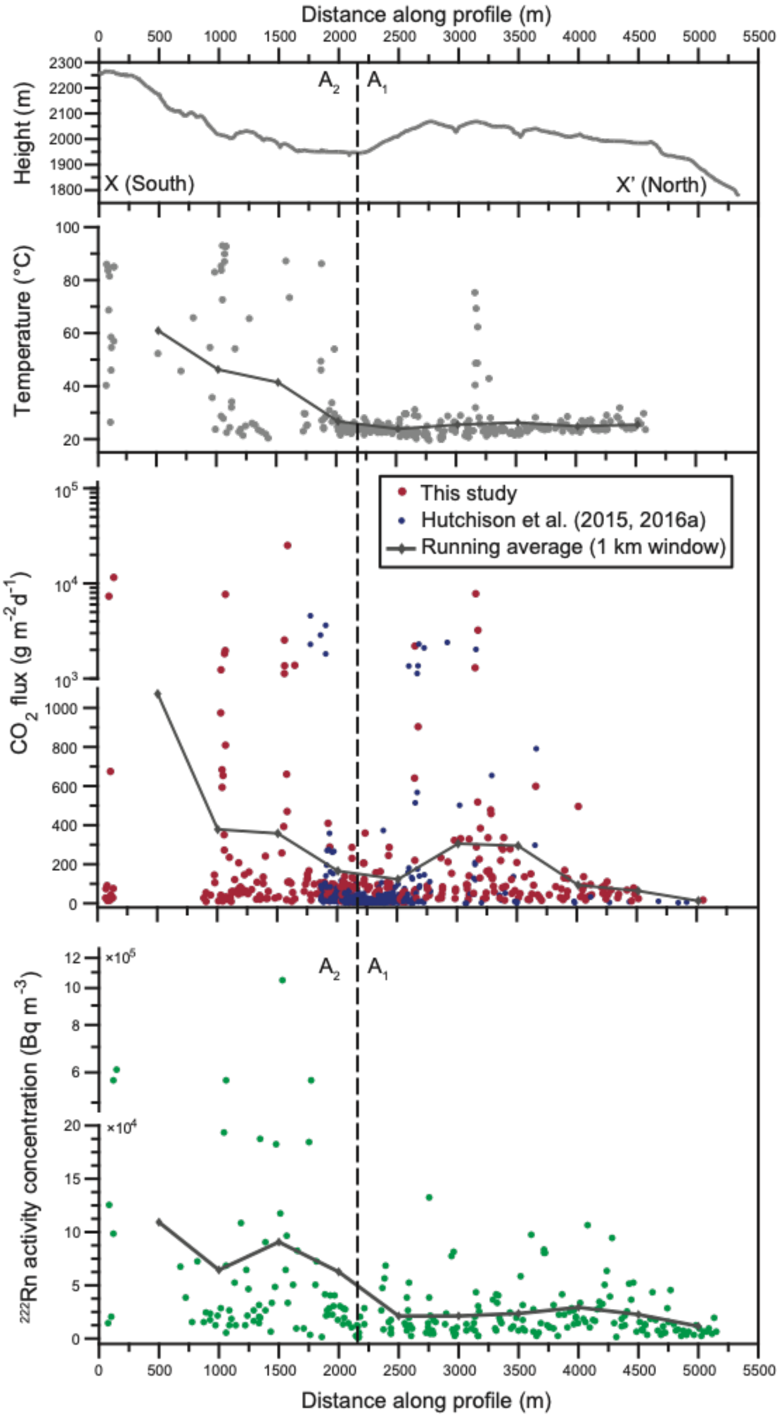

Figure 8.5: Along-fault variations of CO_2, ^{222}Rn, and soil temperature clearly show local peaks along the Artu Jawe Fault Zone and a general increase of gas release toward the South. The profile X-X' along the Artu Jawe Fault Zone is shown in Figure 8.1b. Fault-controlled emissions occur over a broad zone orthogonal to the fault (Figure 8.2). For that reason, data within a fixed distance orthogonal to the fault line was included in the plot (this is referred to as the buffer zone). We also calculated a running average by binning the data in 1 km segments along the fault to identify any broad (kilometer-scale) changes in emissions.

8.4.7 Radon-Thoron and Radon-Thoron-Carbon Dioxide Plots

Figure 8.7a reveals a tendency in all sectors toward increased RTRs (6.7–33) at different magnitudes for ^{222}Rn and ^{220}Rn (see also supporting information S1–S4). This indicates the

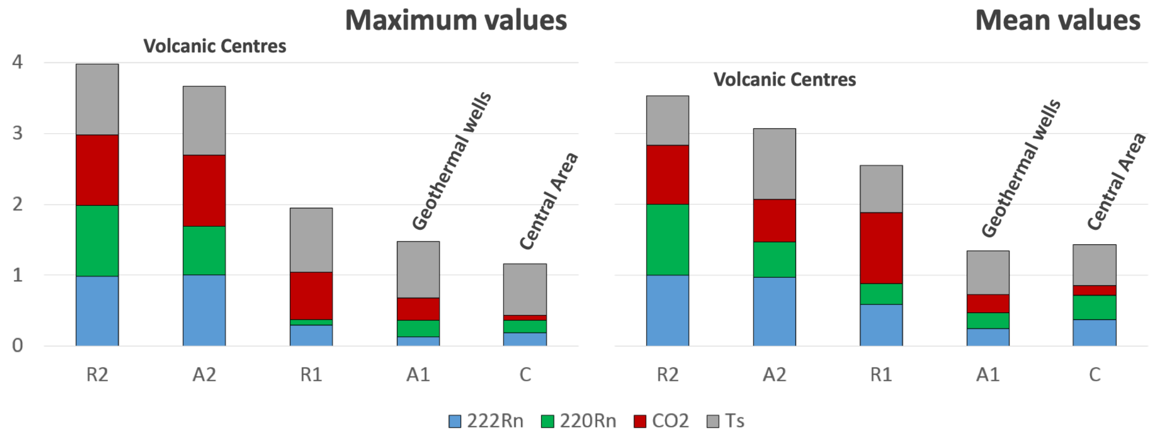

Figure 8.6: Soil gas fingerprint for the Northern and Southern Artu Jawe Fault Zone (A1 and A2), the Ring Fault (R1 and R2), and the Central Area (C) illustrated in a stacked bar chart for maximum and mean values. The compartment-specific maximum and mean values of each parameter have been normalized to the maximum value in the entire study area and are illustrated in a stacked bar chart. Example: In case the maximum values for each parameter have always been measured in the same compartment, the stacked column will have a value of 4.

presence of a significant hydrothermal upflow along permeable fracture zones from a deep source at medium fluid migration velocities. The main uranium and thorium source at Aluto is expected to be Neogene ignimbrites (below 1,400m depth), which are also hosting the geothermal reservoir where intense fluid-rock interaction occurs (*Gizaw*, 1993; *Hutchison et al.*, 2016a,b). Stratigraphic data from well logs show a uniform distribution of the ignimbrites across the study area (e.g.,*Teklemariam et al.* 1996). Due to the lack of chemical information from well cuttings, data from analogue outcrops have been used to assess the chemical composition of the reservoir rocks. Analyses of rock samples from Aluto ignimbrites and basalts have shown that the ignimbrites are much richer in uranium and thorium than basalts (Ignimbrites: 10–20 ppm thorium and 2–4 ppm uranium; basalt: 2–5 ppm thorium; and 0–1 ppm uranium; *Hutchison et al.* 2016a; *Teklemariam et al.* 1996). RTRs from 1.5 to 3.9 indicate a major hydrothermal upflow from a deep source and maximum fluid migration velocities. These ratios have been identified only in A2 and R2. Lower ^{222}Rn and ^{220}Rn magnitudes in A1 and R1, but peak RTRs, are interpreted as dilution effects. Whereas A1, R1, and R2 indicate the presence of deep and shallow sources, no shallow source is indicated for A2, which highlights the presence of a major hydrothermal upflow from a deep source. Selected maximum ^{222}Rn and ^{220}Rn values (^{222}Rn > 149.6 kBq·m^{-3}; ^{220}Rn > 80.7 kBq·m^{-3}) with a trend toward a deep source and maximum fluid migration velocities (RTR 1.5-3.9) are highlighted on the map (Figure 8.8) and illustrate major upflows from a deep source along the Southern AJFZ (A2) and the Ring Fault (R2).

The interpretation of the interpolated maps suggests a correlation of maximum ^{222}Rn, ^{220}Rn, and CO_2 emissions in most of the geothermally active areas. Based on a ternary plot (Figure 8.7b), this obvious correlation was further analyzed. The principle of this concept is to identify sites with simultaneous peaks from all three parameters, even if the actual magnitudes are relatively low. As a novelty, even for areas characterized by low-intermediate gas emissions, signals from deeper sources could be identified with this approach as illustrated in Figure 8.7b. CO_2 efflux values were extracted from the interpolated map based on the ^{222}Rn-^{220}Rn

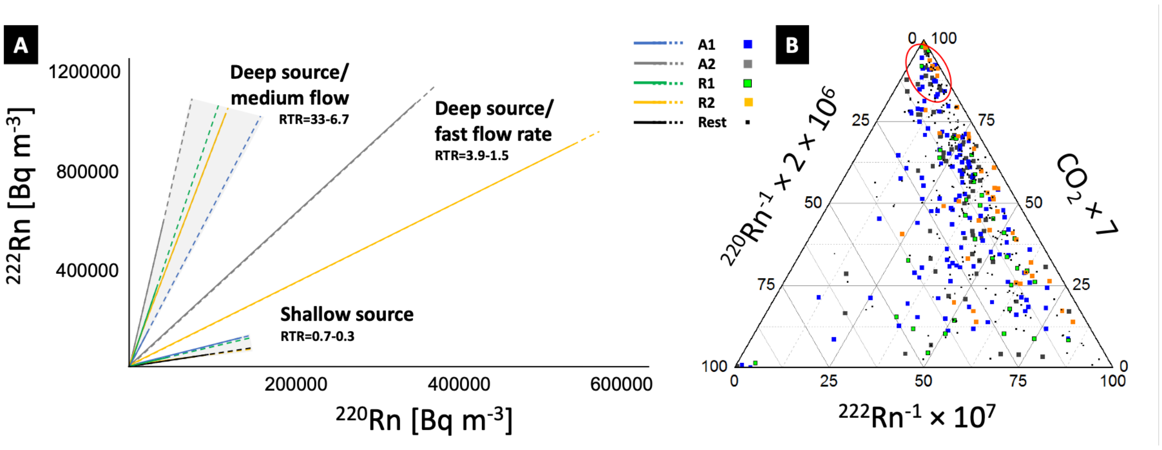

Figure 8.7: (a) ^{222}Rn versus ^{220}Rn plot for data from A1, A2, R1, R2, and Central Area (Rest) as depth indicator (see also supporting information S1–4); (b) ^{222}Rn-^{220}Rn-CO_2 ternary plot. The plot illustrates a cluster of data points with increased CO_2, ^{222}Rn, and ^{220}Rn values.

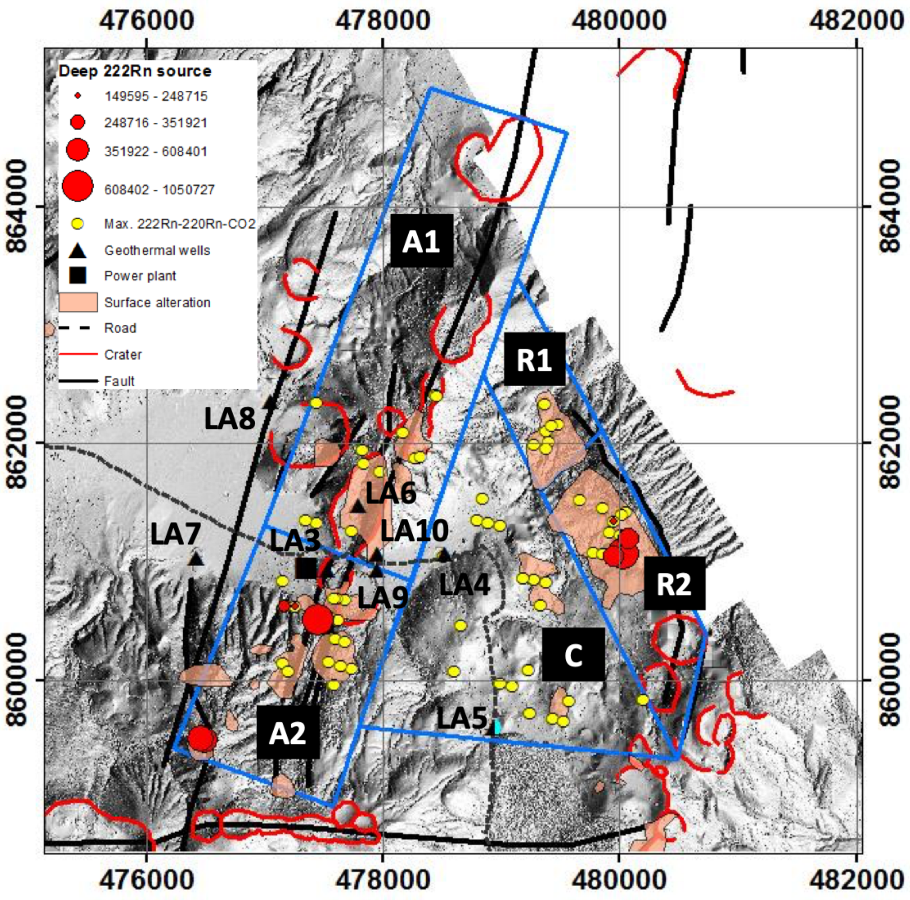

Figure 8.8: Sampling sites with coherent peak values for all three parameters have been extracted (from Figure 8.7b) and are shown on the map (yellow circles). Location of sampling sites with ^{222}Rn and ^{220}Rn values indicating a deep source and fast flow rates are illustrated as red circles (given as ^{222}Rn in Bq·m^{-3}).

sampling grid. This extraction procedure was necessary due to different sampling grids for the two methods. For ^{222}Rn and ^{220}Rn, inverse values are plotted, so that the peak values from all parameter plot in the same corner of the ternary plot. A cluster of data points from all compartments becomes obvious in the CO_2-corner of the ternary plot. These values ($CO_2 >$

84%) have been extracted (manual selection) and plotted on a map (Figure 8.8). Many of the selected data points are constrained to areas with major geothermal anomalies. However, in addition to the well-known geothermal areas, this approach also highlights data points in the central part, which usually appeared less prominent and were therefore often considered as less important for structural permeability. Based on the ternary diagram, we found evidence for the existence of permeable structural pathways in the Central Area (Figure 8.7b and 8.8).

8.5 Discussion

8.5.1 Main Degassing Structures

In all investigated sectors, upflowing geothermal fluids are indicated (Figure 8.2). The pattern analysis of soil gas emissions implies (1) elongated upflows along permeable fracture segments and (2) locally concentrated upflows. Although *Hutchison et al.* (2015, 2016b) identified the major structures, this new work clearly identifies and characterizes the major permeable structures, as well as the strong spatial variation of gas emissions.

8.5.1.1 Artu Jawe

The spatial pattern and variation of gas efflux and soil temperature suggest a strong fault segmentation with dextral displacements of Artu Jawe. Increased values of CO_2 efflux, ^{222}Rn, ^{220}Rn, and T_S have been observed along multiple well-confined NNE-oriented segments and within areas of maximum displacement, indicating major migration pathways of geothermal fluids. In the northern part of Artu Jawe, a significant dextral displacement of about 300 m creates permeability evidenced by increased CO_2 emissions (Figure 8.2; CO_2 map; marked as “X”). Maximum degassing rates occurred mainly within cluster of aligned and elongated volcanic eruption craters, which have not been observed in the southern part of Artu Jawe (A2). Geothermal activity further North of the Aluto volcanic complex is decreasing. Peak CO_2 efflux and ^{222}Rn occurred in the Southern AJFZ, indicating a connection to the deep geothermal reservoir, but their spatial pattern appears to be less defined compared to the North. In contrast to the northern part, geothermal surface activity is indicated to continue Southward as can be seen by the presence of hot springs on the northern shore of Lake Langano in continuation of the structural trend of the AJFZ. Only minor surface alteration was observed in the North compared to the South. Less permeable segments could be affected by (1) silicic mineralization (sealing) of previously permeable fault segments (Teklemariam & Beyene, 2001) or (2) a nonpreferential fracture orientation in the acting stress field causing low structural permeability and hence less fluid circulation.

Along-fault variations on short length scales (100 m) and longer scales (kilometer; running average) are illustrated in Figure 8.5. Short length scale variations indicate fault segmentation and variable structural permeability, whereas long scale variations indicate regional trends, such as a general increase of gas emission to the South of AJFZ indicating a major source of magmatic volatiles.

The pattern of increased CO_2 efflux and ^{222}Rn values is not always congruent in the northern part of Artu Jawe. A possible explanation for this is the maturity of the geothermal manifestations. It is assumed that very young manifestations release mainly CO_2 in its initial phase. CO_2 from exsolution processes in magmatic sources travels to the surface once the magma is emplaced, for example, in dike intrusions. After some reaction time of hot and CO_2 bearing fluids with the reservoir rocks, more and more ^{222}Rn is released, which is ultimately resulting in a combination of increased ^{222}Rn and CO_2. Surface manifestations in its extinction phase seem to emit mainly ^{222}Rn and less CO_2. This could be explained by ongoing reaction processes of reservoir fluids and rocks, but an insufficient supply of new magmatic CO_2.

8.5.1.2 Ring Fault

CO_2 efflux, T_S, and ^{222}Rn anomalies have been detected in two key areas (Figure 8.2) on the western flank of the Ring Fault (Bobesa), but not on the rim itself. It is discussed if these surface manifestations should be considered as solely Ring Fault related features (volcanic) or if they could have evolved as secondary features due to an interaction of the Ring Fault with additional (so far unknown) NNE-oriented tectonic structures (tectono-volcanic) parallel to the NNE-oriented AJFZ.

The area to the Southwest of the Ring Fault (C2) is characterized by widespread soil alteration, a large ^{220}Rn anomaly with decreasing values toward the West, and slightly increased T_S. This area seems to be largely affected by a geothermal outflow from Bobesa to the West. The source of the major degassing vents seems to be deep-rooted (Figure 8.2). Soil gas emissions show similar characteristics as A2.

At the inferred intersection of the Artu Jawe Fault and the Ring Fault, a nested eruption crater ($\sim$580 × 300 m) is located, where intermediate, but no maximum ^{222}Rn and ^{220}Rn values have been measured. CO_2 efflux values and T_S also do not show significantly higher values at the inferred intersection. In conclusion, observed gas emissions do not suggest an eminent permeability structure with a connection to a deep reservoir, although measured gas emissions are above background, indicating some minor fluid circulation.

8.5.1.3 Central Area

Magnitudes of gas emissions range from low to intermediate with a few peak values. Therefore, a hydrothermal system with similar characteristics as A2 or R2 is not expected in that area, though the presence of hydrothermal fluid circulation was proven with our approach. Wide-ranging CO_2 efflux (C1 and C2) and ^{222}Rn activity concentrations (C1–4) of low-intermediate magnitudes were identified in the Central Area (Figure 8.2). Geothermal surface activity was observed in C2 and C4. Increased CO_2 efflux in C1 can be interpreted as (1) a potential eastward directed shallow, lateral outflow from Artu Jawe (similar to a perched aquifer), and/or (2) increased structural permeability along an unknown NNE-oriented fracture zone. A biogenic source for these emissions is unlikely since biological sources (with isotopically light $\delta^{13}C$; *Hutchison et al.* 2016b) show significantly lower fluxes and will not correlate with the high ^{222}Rn in the same area. Another rather small anomaly with increased CO_2 efflux and ^{222}Rn was identified in C2. Here increased T_S has been measured, and geothermal surface manifestations were observed. Possible explanations for this are as follows: (1) Presence of separate structure-controlled geothermal upflow, and/or (2) lateral outflow from Bobesa. An additional ^{222}Rn anomaly was detected in C3, which could be the result of another separate upflow of geothermal fluids along a NNE-oriented fault zone.

A large ^{222}Rn anomaly in the Southeast (C4) without obvious structural trends coincides with multiple, young volcanic eruption centers and lava flows. This area is also characterized by increased T_S, and CO_2 efflux, and seems to be an interesting target, worth more detailed investigation, as some data points show the same trends as observed in Aluto's high-temperature areas. The area has already been drilled (LA5, Figure 8.8), and data indicate the presence of an outflow zone at depth (*Gizaw*, 1993), which is probably due to its location at the boundary of the thermal anomaly. Further investigations could help to confirm or exclude the presence of a deep heat source. In general, NNE-oriented structures are indicated in the Central Area by the orientation of areas with increased gas emissions, but magnitudes are low and a very active hydrothermal system is not expected, though evidence of hydrothermal circulation is given. While we cannot rule out deep penetrating structures in this area, no significant fault scarps are observed at the surface.

8.5.2 Intersecting Faults

Hutchison et al. (2015) hypothesized that the intersection of the Ring Fault and AJFZ could be a spot of high magmatic gas efflux. However, the results from this study do not support a high magmatic gas efflux in this region. While there is a small increase in ^{222}Rn, ^{220}Rn, T_S, and CO_2 indicating a permeability structure, they do not confirm a connection to a deep source. The low gas flux at this intersection could be caused by a low permeability or limited fluids present at depth. The two main areas on the Ring Fault with geothermal surface activity appear to coincide with fault intersections of the Ring Fault and additional NNE-oriented fault zones inferred based on increased gas emissions in the Central Area. These intersections may be important in controlling the upflow of deep fluids.

8.5.3 Implications for Geothermal Exploration

The observation of increased gas flux (in particular CO_2) along the AJFZ to the South is a good evidence for extra degassing by the presence of magma in the crust. Whether it is a mostly cooled plutonic body or large body of melt is still unclear (*Iddon et al.*, 2019), but the along fault plot seems like good evidence for a larger magmatic contribution than typically found along other faults in the rift (*Hunt et al.*, 2017).

From a geothermal perspective, results clearly indicate increased fluid migration from a deep source along permeable fault structures in the southern part of the AJFZ (A2) and in the southeastern segment of the Ring Fault (R2). These areas are not yet targeted for geothermal exploitation but could be interesting prospects for future exploration and development as increased hydrothermal fluid circulation is expected and indicated by soil gas analysis. At this stage, only the northern part of the Artu Jawe Fault (A1) is exploited for geothermal power generation. The gas emissions in this sector point to a deep source as well but do not indicate an area of maximum hydrothermal fluid circulation due to lower gas emission rates compared to A2 or R2. The Southeastern part of the Central Area (C4) also reveals some degassing features with elevated gas efflux in an area with lots of young volcanic landforms. This implies the possibility of a contribution by fluids from a deep source and is worth further exploration efforts.

Generally, the gas emissions from Aluto are comparable to other geothermal systems in volcanic areas where diffuse degassing surveys have been performed for geothermal system analyses. A similar range of gas emissions was also observed in other fields (*Giammanco et al.*, 2007; *Jolie et al.*, 2015a). As a result of our area-wide measuring approach based on a predefined regular grid, we observe a limited number of peak values, and the majority of the data shows low values. This is different in comparison to other soil gas surveys, which usually focus on areas with the strongest gas efflux and obvious volcanic edifices (i.e., steam vents, hot pools, and surface alteration).

8.6 Conclusion

The Aluto volcanic complex is characterized by variable emission rates of volcanic gases and soil gas concentrations, which can be explained by its tectonic, volcanic, and tectono-volcanic setting. Apart from the two main structural features, that is, Artu Jawe Fault and Ring Fault, further sectors with increased gas emissions have been identified in between. Gas release along the Artu Jawe Fault reflects the general NNE-trend of the Wonji faults and is increasing from the tectonically dominated North toward the volcanic center in the South. This trend can be recognized for all investigated parameter. Similar results could be demonstrated in other geothermal fields in tectono-volcanic settings (e.g., *Hernández et al.* 2012). Significant differences in quantity of soil gas between A1 to A2 suggest a differentiation between a tectonic and tectono-volcanic compartment. The transition from the Northern to the Southern AJFZ in the vicinity of the Aluto-Langano geothermal powerplant is a particularly interesting area, since outcropping segments of the Artu Jawe Fault are accessible without a cover of recent eruptive deposits (*Hutchison et al.*, 2015). Here we observe a change from tectonic (North) to tectono-volcanic mode (South). The geothermal surface expressions at the Ring Fault are considered a result of volcanic and tectonic interactions (tectono-volcanic) and are similar to the southern part of the Artu Jawe Fault.

For a comprehensive and integrated interpretation of the identified gas emissions, a conceptual model was developed (Figure 8.9). The existence of two additional so far unknown NNE-oriented fracture zones in the Central Area is proposed. Available soil gas data support the hypothesis of their presence. This assumption is also supported by the ^{222}Rn-^{220}Rn-CO$_2$ plot, on which basis data points in the Central Area with maximum values were highlighted (Figure 8.8). Highlighted sampling sites suggest two NNE oriented corridors of increased gas emissions. However, no obvious structural-geological evidence based on surface mapping was found. The presence of such structures could explain further geothermal surface expressions to the North and South of the study area (e.g., hot springs at northern shore of Lake Langano). They could also explain the two distinct geothermal areas along the Ring Fault as a result of intersecting NNE-oriented structures with the Ring Fault (volcano-tectonic origin). Based on this concept, we expect a continuation of areas with increased gas release toward the North and South as a result of rift-controlled degassing processes.

The results of the soil gas survey have a direct implication for future geothermal exploration and exploitation at the site, since it is indicated that exploration of the southern part of the AJFZ could also be prospective due to its combination of tectono-volcanic conditions (i.e.,

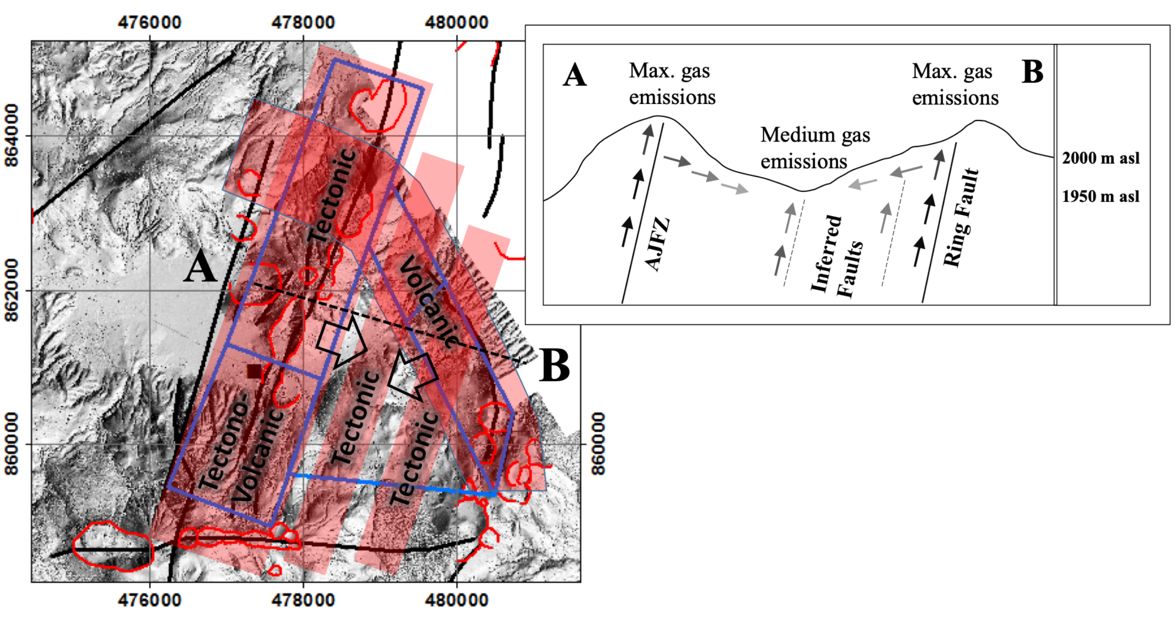

Figure 8.9: The developed conceptual model attempts to simplify the complex tectonic and volcanic setting of the Aluto Volcano. The Southern Artu Jawe Fault Zone is dominated by tectono-volcanic gas emissions. Along the Northern Artu Jawe Fault, the tectonic setting dominates surface gas emissions. The Ring Fault is a volcanic feature, which is likely to be affected by NNE-oriented structural features. Geothermal outflow zones are indicated by arrows.

heat and structures). Further isotopic analyses (e.g., ^{3}He/^{4}He and $\delta^{13}C$) will help to better understand the source of the hydrothermal fluids and allow a direct comparison of Artu Jawe and Bobesa. In addition to the major geothermal areas, hydrothermal fluid circulation is also indicated in multiple areas in the central part, which is worth further investigations.

Acknowledgments

We thank all people from the Geological Survey of Ethiopia and our local field assistants, who helped to make the field work a great success. In particular, we thank Jonas Romrig and Bonso, who was an excellent field assistant. The project was financed in the framework of the Volkswagen Foundation's "Postdoctoral Fellowships for African Researchers in the Engineering Sciences" (reference: 90017). Data are accessible through the Research Data Repository of GFZ Data Services (dataservices.gfz-potsdam.de) or may be obtained from the author by reasonable request. The authors thank the reviewers of the paper for their constructive comments and suggestions.

Appendix 8.A Figures

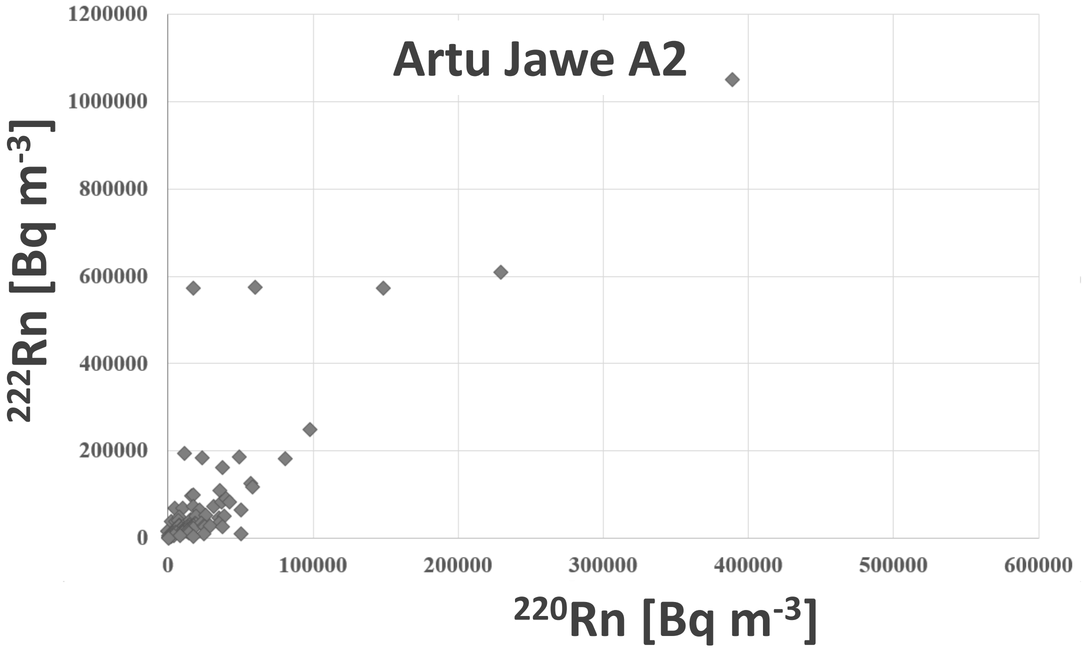

Figure 8.10: 222Rn vs. 220Rn plot for Artu Jawe A1, including data points.

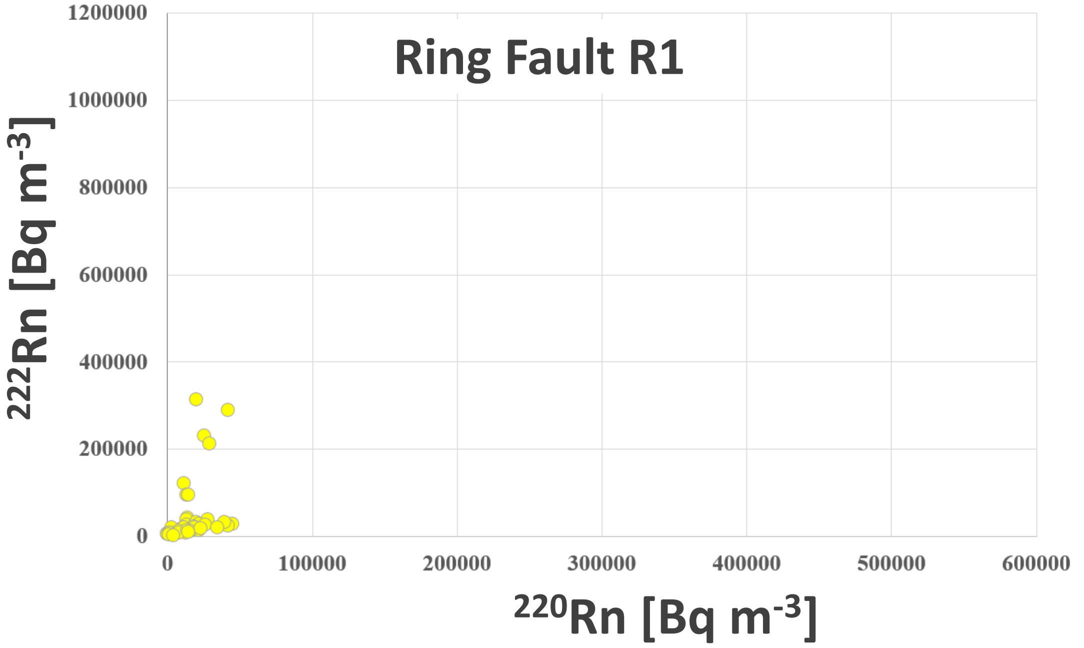

Figure 8.11: 222Rn vs. 220Rn plot for Artu Jawe A2, including data points.

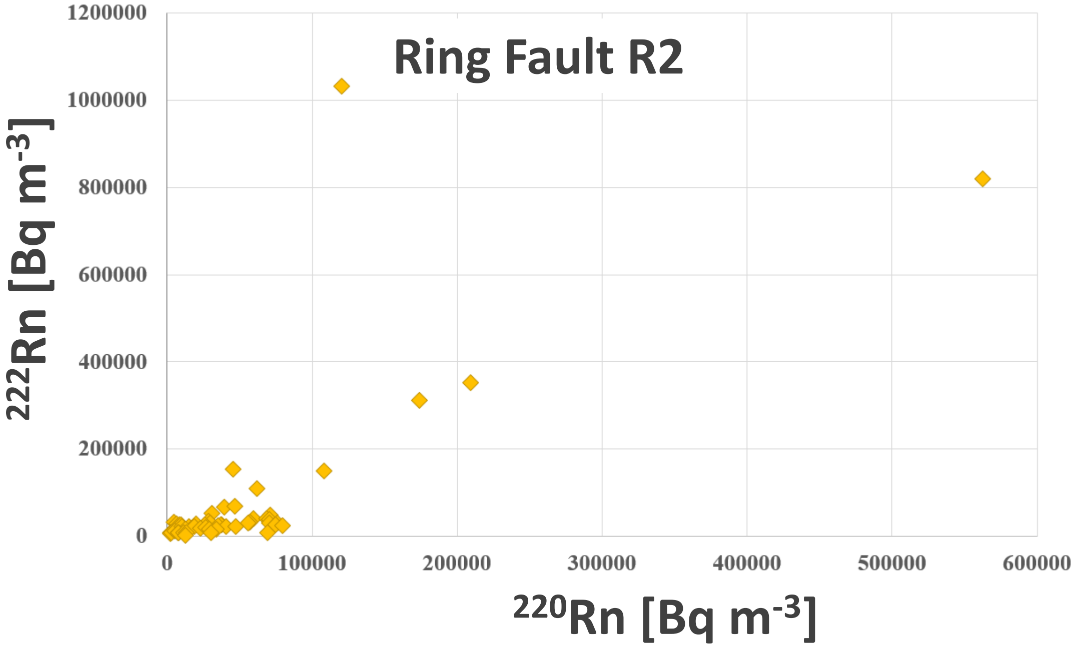

Figure 8.12: 222Rn vs. 220Rn plot for Ring Fault R1, including data points

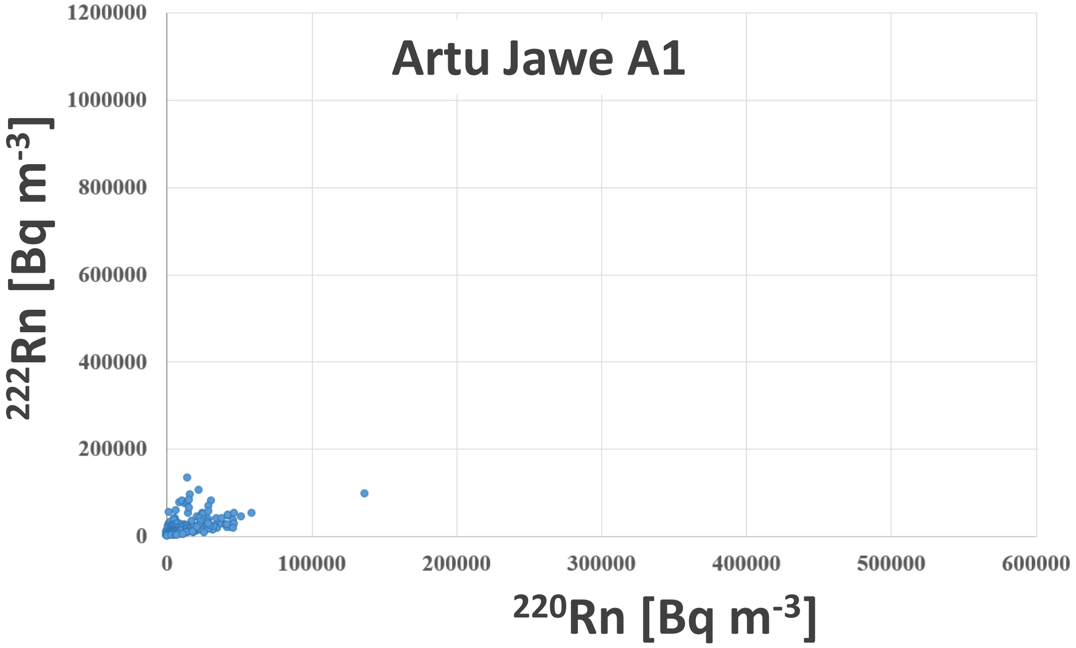

Figure 8.13: 222Rn vs. 220Rn plot for Ring Fault R2, including data points

9

Ngapouri Exploration

Testing the tunable diode laser system in extreme environments: Measuring high and low CO_2 concentrations in both active volcanic and geothermal settings

Agnes Mazot, Andrew Rae, Anna Jentsch, Karen Britten

Article published in *Journal of Volcanology and Geothermal Research*, 2019.
`https://doi.org/10.1016/j.jvolgeores.2019.03.011`

Abstract: Measuring CO_2 emissions in geothermal and volcanic areas is sometimes difficult because of large areas to cover and sites often inaccessible. Measuring high levels of CO_2 concentration can provide information on hidden structure in geothermal areas and recording changes in CO_2 concentration on volcanic areas can help monitor the level of volcanic activity. The purpose of this study was to use the Tunable Laser Diode (TDL) absorption spectroscopy method to test levels of CO_2 concentrations at two extreme environments: White Island volcano, the most active volcano of New Zealand, with large and concentrated gas fluxes, and Ngapouri geothermal area, a small geothermal area in the Taupo Volcanic Zone, New Zealand, with relatively low and diffuse gas emissions. In 2017, for the first time using TDL at White Island, CO_2 concentration measurements performed across the active fumarole fields had the highest CO_2 concentrations of 657 ppm. TDL survey measurements were also conducted across fault strands near the Ngapouri geothermal area, and the results complemented CO_2 flux results obtained with the accumulation chamber method. Higher CO_2 concentrations were measured close to the mapped Ngapouri splays with a maximum of 484 ppm. The maximum CO_2 flux measured in the same area was 100 g m^{-2} day^{-1} however the highest CO_2 fluxes measured along the transects and by the mapped faults were less clear, but the CO_2 concentrations increased closer to the fault splays. Advantages and disadvantages of using a TDL system have been described and compared to the accumulation chamber method. The results from the TDL system demonstrated that CO_2 concentrations can be used as a tool,

with other geophysical tools, for both detecting and highlighting geological structures where no obvious thermal activity is present and for monitoring purposes on active volcanoes.

9.1 Introduction

The Tunable Laser Diode (TDL) absorption spectroscopy method has been mainly used for measuring CO_2 concentrations in different geological settings such as in geothermal and volcanic systems (*Belotti et al.*, 2003; *Carapezza et al.*, 2011; *Cuccoli et al.*, 2007). Recently, CO_2 emissions have been estimated using TDL for an extrapolation of global CO_2 emissions (*Pedone et al.*, 2014a,b, 2015). However, no study has focused on using the TDL for detecting permeable structures (e.g. faults) in geothermal areas where surface discharge features are poorly developed or absent, and only a few studies have been done for monitoring continuous CO_2 concentration over fumaroles or crater lakes in volcanic areas (*Weber et al.*, 2006). The objective of this study is to test the concept of a method sensitive enough to detect any anomalous CO_2 concentration over hidden faults, where no visible geothermal activity was observed and to test the technique for monitoring CO_2 concentration in volcanic craters where high CO_2 emission are observed. The instrument used in this study is a portable Infra-Red (IR) laser system, able to measure the CO_2 concentration along linear paths up to 1 km of length.

The focus on the detection of moderate to low solubility gases (e.g., CO_2, He, CH_4) in the near-surface environment has provided an important tool to discover potentially new resources (*Hanson et al.*, 2014). The studies have been mainly focused on CO_2 concentration measurements at the surface, as CO_2 is considered to be a relatively non-condensable gas present in the geothermal systems, due to its moderate solubility in water. However, CO_2 presence in the atmosphere and that produced in the soil by a variety of biological processes, can hinder the measurement of anomalous geothermal CO_2 (*Raich and Tufekcioglu*, 2000). In volcanic areas CO_2 is the second main gas after H_2O and it is the first to leave the magma rising from depth because of its low solubility in melt ($>$ 6 km) (*Aiuppa et al.*, 2004, 2006; *Carroll and Halloway*, 1994). Monitoring of CO_2 degassing over fumarolic areas and volcanic crater lakes can provide information on the deep volcanic processes and help improve the volcano early warning system (*Caudron et al.*, 2012; *Hernández et al.*, 2001).

TDL measurements were trialed on White Island, New Zealand's most active volcano to test if the TDL system could detect quick changes in CO_2 concentrations over fumarolic areas and over the volcanic lake. We subsequently used the TDL to measure any anomalous CO_2 concentrations across the Ngapouri fault splays, Taupo Volcanic Zone (TVZ), where grassland is the predominant environment. Furthermore, CO_2 flux was measured using the accumulation chamber method in the same volcanic and geothermal areas and advantages and disadvantages of the use of TDL over the accumulation chamber were presented.

9.2 Regional geology

The TVZ is a region of continental crustal extension, trending in a northeasterly direction from the andesite volcanoes of the central North Island (Ruapehu, Ngauruhoe, Tongariro) to the edge of the continental shelf, beyond the Bay of Plenty coastline (Figure 9.1).

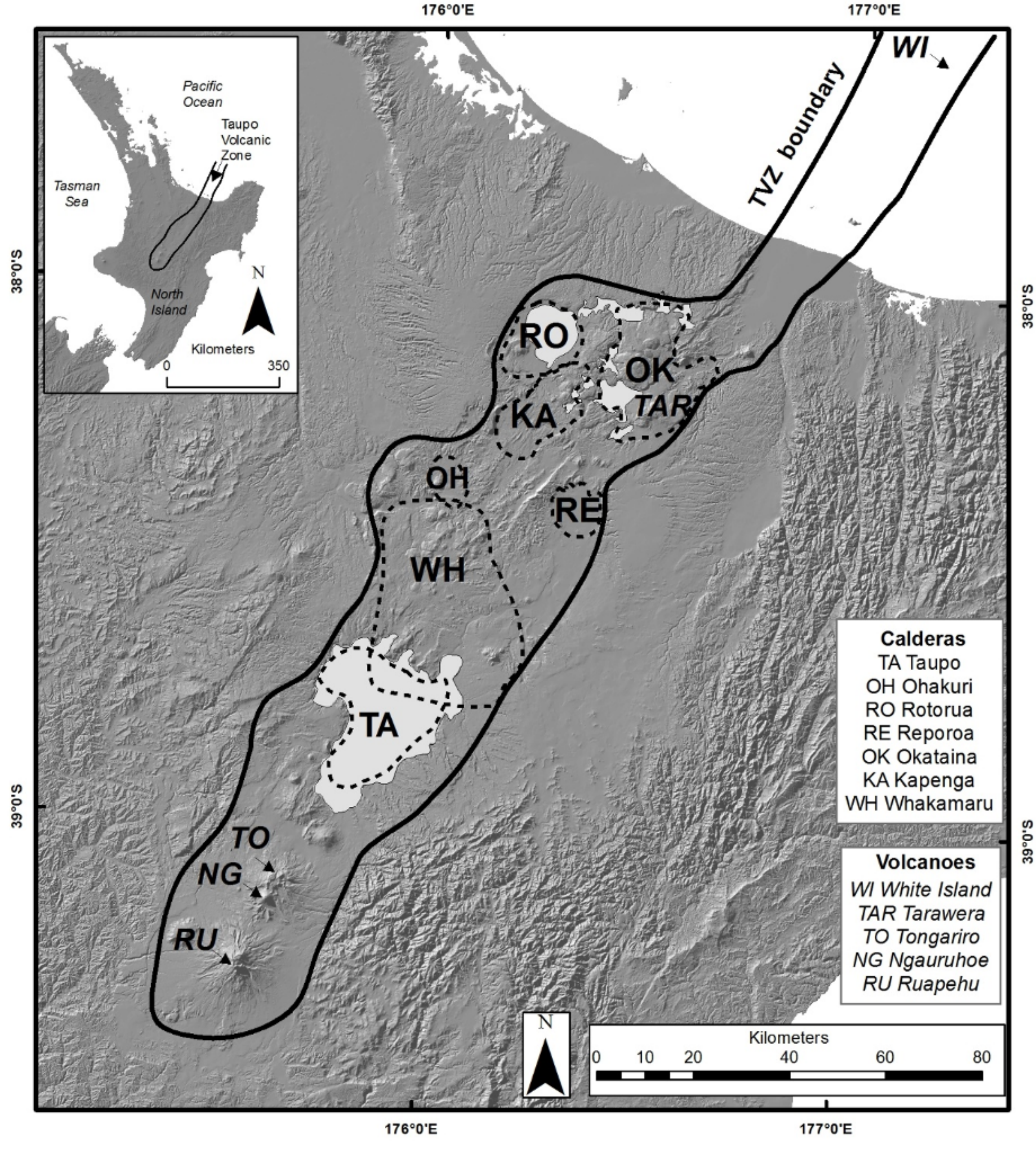

Figure 9.1: Terrain map of the Taupo Volcanic Zone (TVZ) displaying inferred caldera boundaries (Wilson et al., 2009), and the recently active volcanoes

The TVZ is a volcanically segmented rift system, with northern and southern regions dominated by cone-building andesitic volcanism (e.g., White Island and Ruapehu-Tongariro-Ngauruhoe, respectively) and a central region of caldera-forming rhyolitic volcanism (*Wilson et al.*, 1995). At least eight calderas have been identified Mangakino, Whakamaru, Okataina, Rotorua, Ohakuri, Reporoa, Taupo and possibly Kapenga (Figure 9.1), with the most recent eruptions being the 26.5 ka Oruanui and 1.8 ka Taupo (both from Taupo caldera), and the 1314 AD Kaharoa eruption from Mt. Tarawera (Okataina).

More than twenty TVZ geothermal systems are restricted to the central rhyolitic domain (Figure 9.1). Their locations were first defined by electrical resistivity surveys (< 500 m depth *Bibby et al.*, 1995), and more recently by other geophysical techniques (*Hurst et al.*, 2016). The mean spacing and areal extent of the geothermal systems is 10-15 km and 20 km^2, respectively. The systems reflect zones of hydrothermal upflow of high temperature fluids (> 200 °C) above magmatic heat sources that are considered beyond 4 km depth. Hydrothermal circulation is driven by density contrasts between heated water in the geothermal reservoir and the colder surrounding water. Recharge is provided from meteoric waters down flowing to probably >5 km depth (*Rowland and Simmons*, 2012). Geothermal fluids are predominantly meteoric, with a 6-14% magmatic contribution (*Giggenbach*, 1995). Due to the inherently impermeable nature of the basement greywacke rocks, the deep (>3 km depth) upflow zones are inferred to occur in regions of structurally-controlled zones of high permeability, such as those associated with faults and/or volcanic conduits.

9.2.1 Volcanic settings: White Island

White Island volcano is an andesitic-dacitic volcano situated offshore in the Bay of Plenty, approximately 50 km north of the North Island coastline (Figure 9.2). With approximately 70% of the volcano below sea-level, the exposed portion forms a steep-sided and highly eroded volcanic island. The floor of the main crater is covered by a debris avalanche deposit, which formed by crater wall collapse in September 1914, blocking a long-established vent system in the western subcrater. The volcano has seen near continuous activity for 150,000 years, characterised by sporadic eruptive episodes of small phreatic, phreatomagmatic and strombolian eruptions (*Clark et al.*, 1979), associated with historic craters (Western, Central and Eastern subcraters) and the extensive fumarolic activity (Figure; 9.2 *Cole et al.*, 2000). The most recent eruption at White Island in April 2016, was a phreatic explosion through the shallow acidic (pH < 0; 60 °C) crater lake. Presently, active fumaroles (∼150 °C; *Christenson et al.*, 2017), steaming vents, acid streams and pools are confined to the main crater, with the center of the volcanic activity being a smaller western crater filled by an acidic lake (Figure 9.2).

White Island crater floor has a complex morphology with old eruption craters,with lake sediment filling (mostly clay) and covered by debris from the 1914 landslide. *Bloomberg et al.* (2014) suggest that the controls of CO_2 emission are mainly the permeability associated with rims of old subcraters being the main pathway of magmatic gases and the capping clays creating local low permeability. Studies on ground deformation at White Island (*Fournier and Chardot*, 2012) suggested that the ground deformation (uplift) records in the period December 2007- November 2009 were consistent with increase in gas flux and temperature of fumaroles and were related to either an increase of magma degassing at depth (*Giggenbach et al.*, 2003) or a boiling process in the hydrothermal system.

9.2.2 Geothermal settings: Ngapouri

Ngapouri is located at the northern end of the Paeroa Range between the Paeroa Fault to the west and the Ngapouri Fault to the east, and south of the Maungaongaonga dacite dome

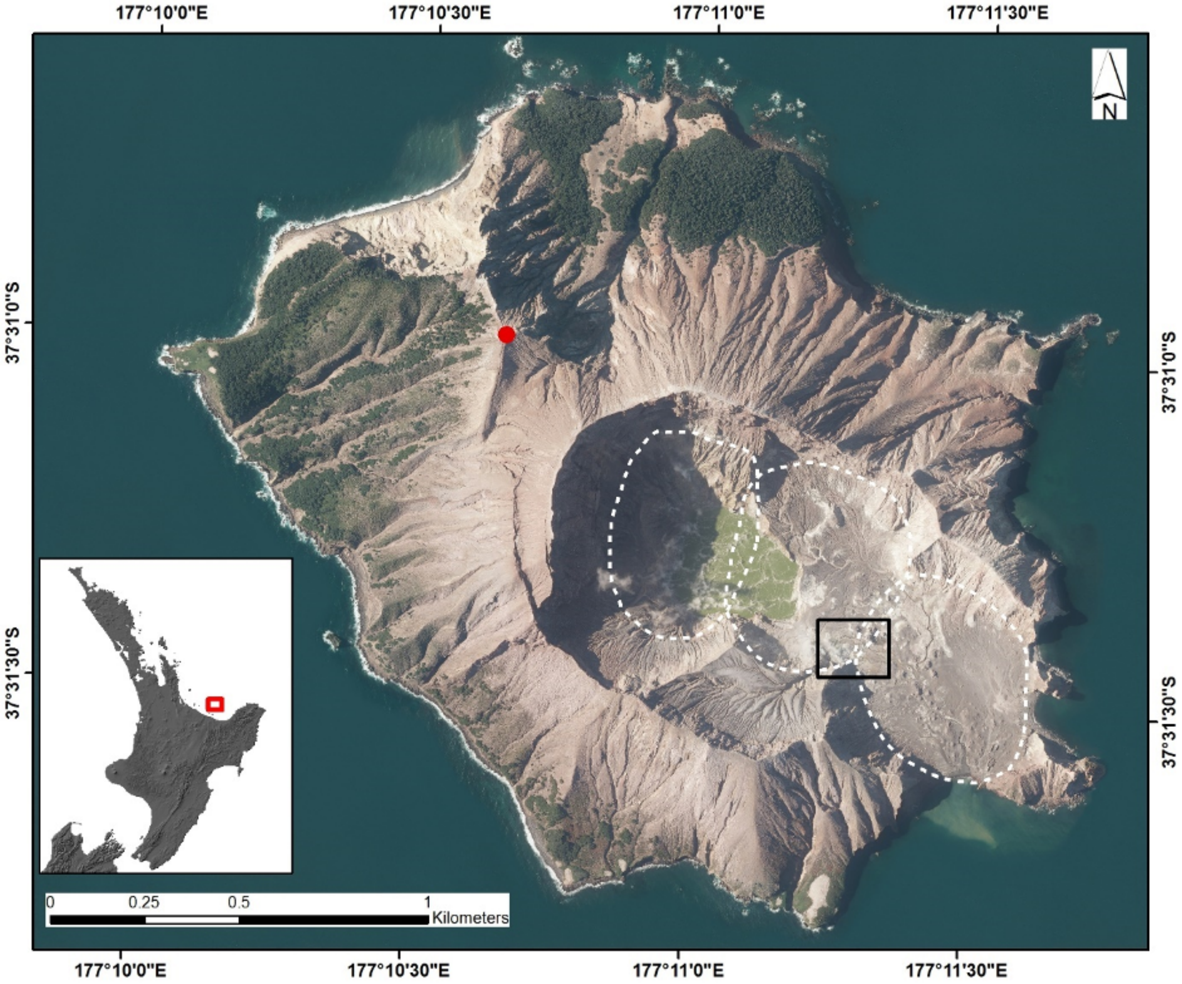

Figure 9.2: Aerial photograph of White Island showing the main crater, with the western crater lake and the active area of the crater floor. The area of where CO_2 concentration measurements were made is located inside the black rectangle. Historic craters are outlined with white dashes (Cole et al., 2000). The red dot is the location of the MetService meteorological station (37.517°S, 177.178°E).

(Figure 9.3). This part of the Paeroa Range, at 480-670 m elevation, is west of the Waiotapu geothermal area, and south-southeast of the Waikite geothermal area. The normal Paeroa Fault (N45E), down thrown to the northwest, defines the western escarpment of the Paeroa Range and the eastern boundary of the Taupo Fault Belt (*Rowland and Sibson*, 2001; *Villamor and Berryman*, 2001).

The normal Ngapouri Fault (N55E) is a northwesterly-dipping major splay of the Paeroa Fault,with a length of about 15 km from Paeroa Trig, where it splays from the Paeroa Fault, to the northeast along the eastern shore of Lake Ngapouri and towards Lake Okaro (*Grindley*, 1963) (Figure 9.3). Several hydrothermal explosion craters (including Lake Ngapouri and Okaro) occur along its length (Figure 9.3; *Healy*, 1974; *Hedenquist and Henley*, 1985; *Nairn et al.*, 2005; *Villamor and Berryman*, 2001). Displacement along the Ngapouri Fault has formed northeast-trending ridges (up to 120 m high) along the eastern side of the northern Paeroa Range. Previous structural studies from excavated trenches across the fault traces (*Nairn et al.*, 2005; *Villamor and Berryman*, 2001) have mapped displaced tephra layers in the trench walls and enabled measurements of displacement and estimates of displacement rates

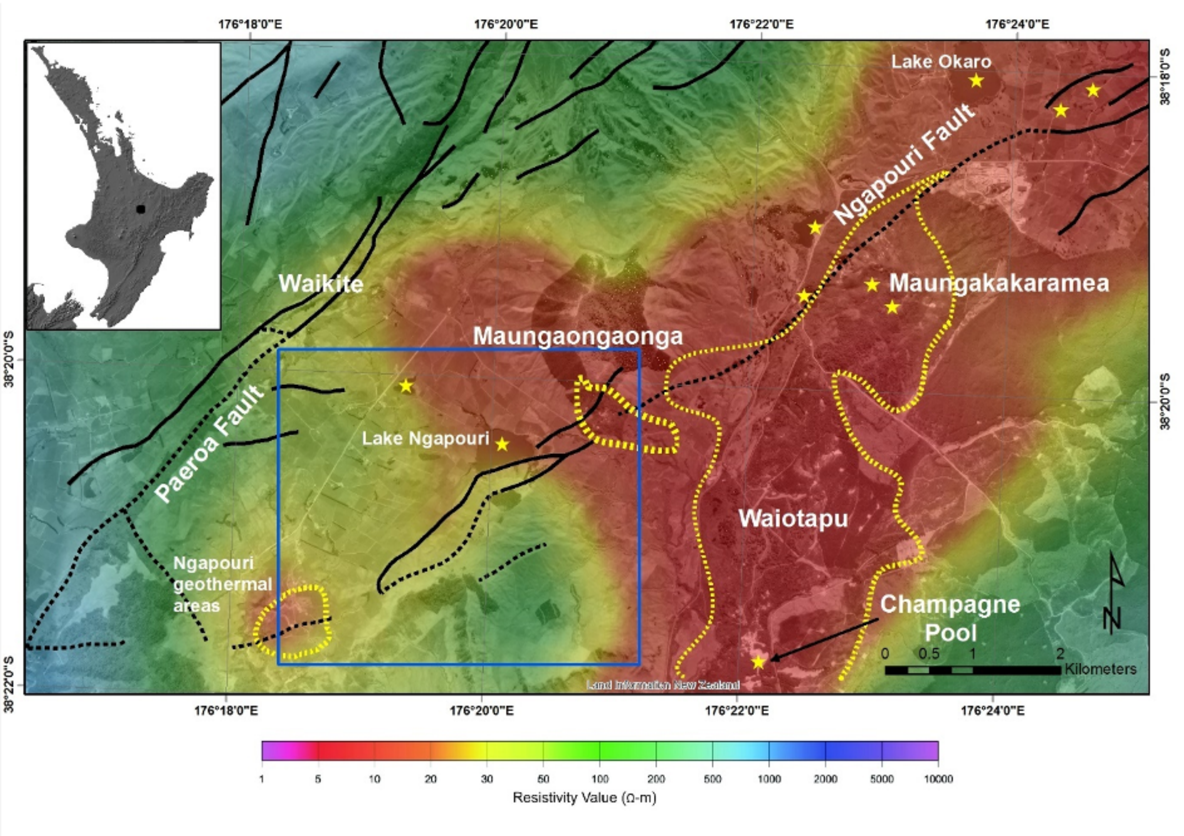

Figure 9.3: Aerial photograph showing mapped active faults (GNS Science active fault database), including the Ngapouri Fault, overlaid onto the electrical resistivity map (nominal array spacing 500 m; *Stagpoole and Bibby*, 1998). The dotted black lines are inferred faults. The yellow dashed lines enclose areas of active thermal ground. Yellow stars indicate some of the hydrothermal eruption centres defined by *Hedenquist and Henley* (1985). The blue rectangle indicates our survey area (shown in Figure 9.4).

(0.23 ± 0.001 mm/yr; *Villamor and Berryman*, 2001). These trenches confirm the location of the Ngapouri Fault splays in our study area.

Geothermal surface activity occurs along parts of the Ngapouri Fault. In the northeast, steaming ground and fumarolic activity occurs on the southern flanks of Maungaongaonga. In the southwest, there are several small areas (< 650 m^2) of steam and gas venting (Figure 9.4), henceforth referred to as the Ngapouri geothermal features (but Schiltz Farm Fumarole in *Glover et al.* 1992). No obvious expressions of surface activity occur along the fault scarps between the Maungaongaonga and Ngapouri geothermal areas.

Electrical resistivity soundings across Ngapouri were included in a district-wide DC resistivity survey of the Waimangu, Waiotapu, Waikite and Reporoa geothermal areas (*Bibby et al.*, 1995). This was done using Schlumberger arrays with AB/2 spacings of 500 m and 1000 m. The AB/2 = 500 m apparent resistivity map shows shallow conductivity ($<$25 Ωm) across northern Ngapouri (corresponding to the Waiotapu geothermal area) that extends westwards to Waikite (Figure 9.3). The Ngapouri geothermal features manifest as a small circular area ($<$1 km^2) of low apparent resistivity ($<$30 Ωm), separated from the Waiotapu-Waikite conductor to the north by an area with higher apparent resistivity (30-50 Ωm). With increasing depth (AB/2 = 1000 m) conductivity increases across the area with a broadening of low apparent resistivity ($<$30 Ωm) on the eastern side of the Ngapouri area of interest (Figure 9.3).

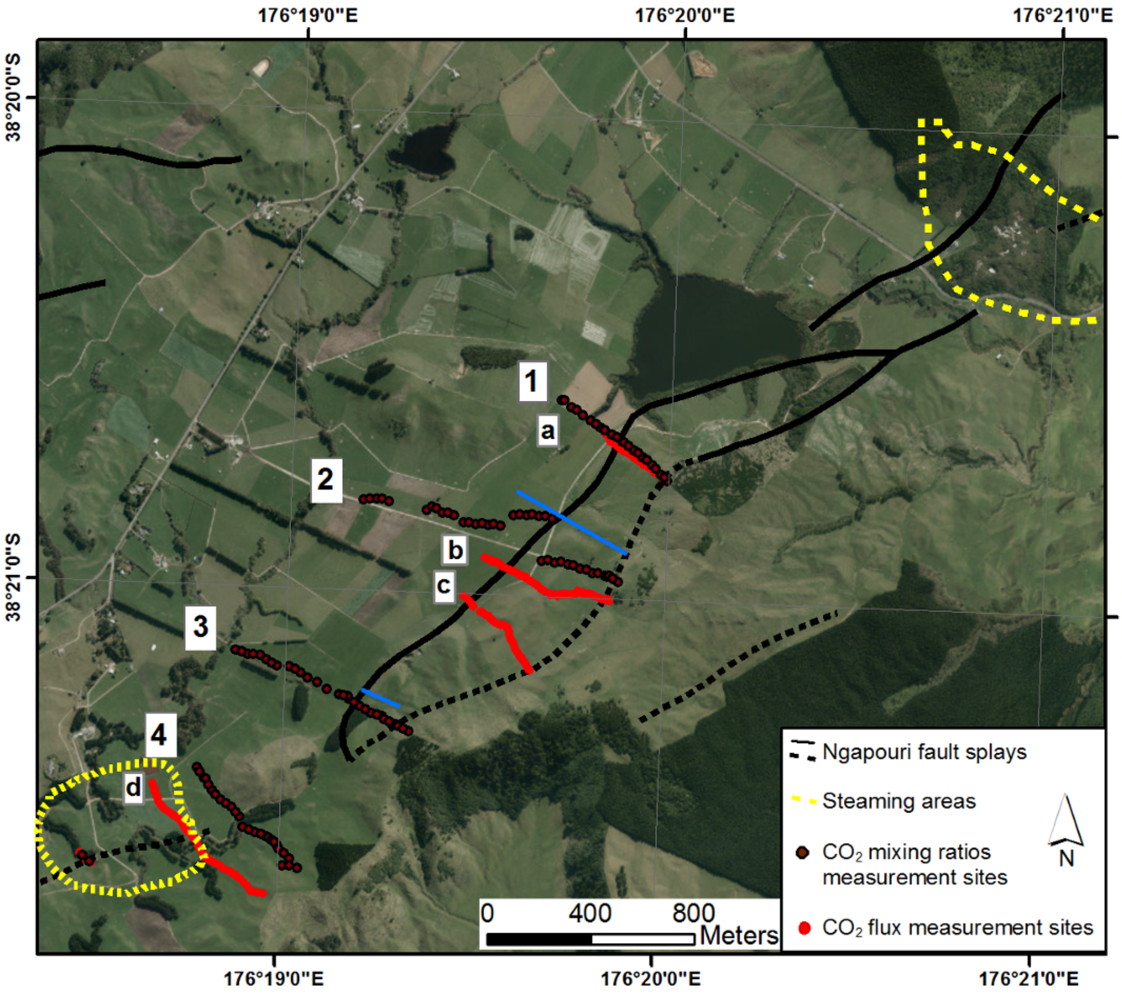

Figure 9.4: Location of the fault traverses numbered 1 to 4 and the CO_2 flux measurement sites at the geothermal area and named a-c (red dots). Brown dots are the midpoints at 50m intervals between transceiver and the retroreflector. The yellow dash are areas of geothermal activity. The blue line represents the location of the mapped trench by Berryman et al. (unpublished results).

9.3 Methodology and field measurements

9.3.1 Tunable diode laser technique

Tunable diode laser (TDL) spectroscopy technique consists of the measurement of gas concentration based on the absorption of Infra-Red radiation by the target gas. TDL is used for accurate measurement of a specific gas as it uses a light source that is tunable over a narrow wavelength range. The IR based laser system used in this study is based on a transmitter/receiver (transceiver) unit able to measure average CO_2 concentrations along an optical path between the transceiver and a passive retroreflector. The measurement principles of the TDL are explained in detail in *Chen* (2011) and *Linnerud et al.* (1998).

The instrument used in this study consists of a GasFinder version 2.0 TDL (Boreal Laser), an Infra-Red transceiver unit that can be used to measure CO_2 concentrations over linear paths of up to 1 km distance (Figure 9.5a). The laser source located in the transceiver is a near-infrared tunable diode laser operating at 1576.9 nm for CO_2 absorption line. A laser light emitted from the transmitter unit propagates through the atmosphere to the retroreflector and returns back to the receiver where it is focused onto a photo diode detector (Figure 9.5a and b).

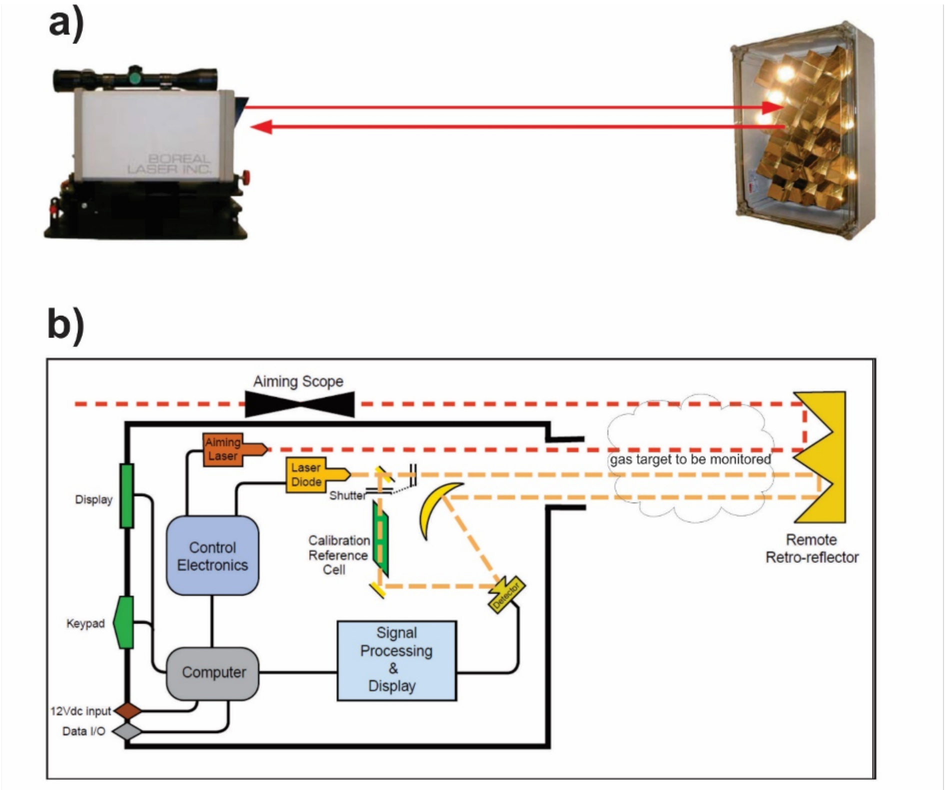

Figure 9.5: a) Photo of the transceiver GasFinder 2.0 and the retroreflector array. b) Schematic representation of the GasFinder 2.0 Tunable diode laser (from GasFinder2 Operation Manual, Boreal Laser Inc., 2012; see Section 9.3.1 for explanation)

The laser emitted from the transceiver is divided by a beam splitter (Figure 9.5b). One laser beam goes along the open path and is reflected back to the photo diode detector by a retroreflector (yellow line in Figure 9.5b). The other beam is reflected by a mirror through the gas reference cell to the photodiode detector. Both laser beams are analyzed at the receiver for the presence of the target gas in the target zone. Effects of instrumental and environmental changes are cancelled because the remote signal and the reference signal are in the same atmospheric conditions. The GasFinder2 performs an automatic calibration at the start and a standard cell with CO_2 gas of known concentration is automatically inserted every minute on the laser path for making adjustments on the measurements with the new atmospheric conditions.

In the field, the GasFinder2 was set to measure CO_2 concentrations at 1 Hz rate for more accurate data. Alignment between the laser unit and the retro reflector mirror was optimized using a visible aiming laser and a sighting scope (Figure 9.5b). The size of the retro reflector was chosen as to adjust the returning light level of the laser beam to a desired value, depending on the path-length and the expected amount of absorbed radiation.

As the TDL system measures gas target in the atmosphere, the meteorological parameters (mostly temperature and pressure) can have an influence on the measurements. If the temperature of the atmosphere is too high (>40 °C) or too low (<-20 °C), it can alter the data acquisition of CO_2 as it can change the absorption wavelength of the laser. Over the ambient range, like in our case, there is no temperature reading drift. The pressure can also alter the results but there is an automatic built in correction of the pressure stored in the computer using calibration equations from laboratory experiments. The humidity and particularly the fog can also be a problem as the beam laser is not strong enough to pass through fog. So, the measurements cannot be performed with this kind of weather condition. Furthermore, when performing measurements on top of a fumarole or across a steaming lake, no data can be recorded. All the measurements were made in dry conditions. During the campaigns weather data (wind direction and wind speed) were recorded by a MetService weather station.

9.3.2 CO_2 flux measurements by accumulation chamber technique

At Ngapouri and White Island areas, soil CO_2 fluxes were measured by the accumulation chamber technique using portable non-dispersive, infrared systems (WS-LI820-CO_2: West Systems S.r.l., Pontedera (PI), Italy; EGM-4: PP Systems, Amesbury, MA, USA) as described in detail in *Chiodini et al.* (1998). As for the CO_2 concentration measurements using the TDL method, meteorological conditions such as rain and soil humidity may influence the soil gas measurements (see *Chiodini et al.* (1998) for details). In our study, CO_2 flux measurements were made under dry conditions. The accumulation chamber method has been widely used for volcano monitoring, geothermal exploration and definition of hidden geological structures (i.e., *Lewicki and Brantley* 2000; *Lewicki et al.* 2005; *Peiffer et al.* 2015, 2018).

9.3.3 Determination of background CO_2 concentrations and fluxes using Graphical statistical approach

Analysis of the CO_2 flux and concentration data using a graphical statistical approach (GSA) (*Cardellini et al.*, 2003; *Chiodini et al.*, 1998), permits differentiation of various CO_2 degassing mechanisms. The GSA consists of the partitioning of soil CO_2 flux and the air CO_2 concentration into different log-normal populations. The proportion, the mean, and the standard deviation of each population are estimated following the procedure introduced by *Sinclair* (1974). This method was used to study the soil CO_2 flux and air CO_2 concentration for Ngapouri area. Their percentages were validated by combining these populations into the different proportion at various levels of log CO_2 flux and log CO_2 concentration. We used Sichel's t-estimator (*David*, 1977) to estimate the arithmetic mean of CO_2 flux and concentration and the 90% confidence interval of each population, following *Chiodini et al.* (1998).

9.3.4 Tunable diode laser field measurements

9.3.4.1 Tunable diode laser measurements in a volcanic area: White Island

A TDL field campaign was performed on 22 April 2014 at White Island crater floor in the most active area and above the crater lake where a dome is present, with the positions of the retroreflector and transceiver shown in Figures 9.6 and 9.7. The retroreflector was positioned downwind from fumaroles located on the west side of the crater floor, at a height of 1 m. This area was chosen because of the main fumarole in the crater floor that discharged gas

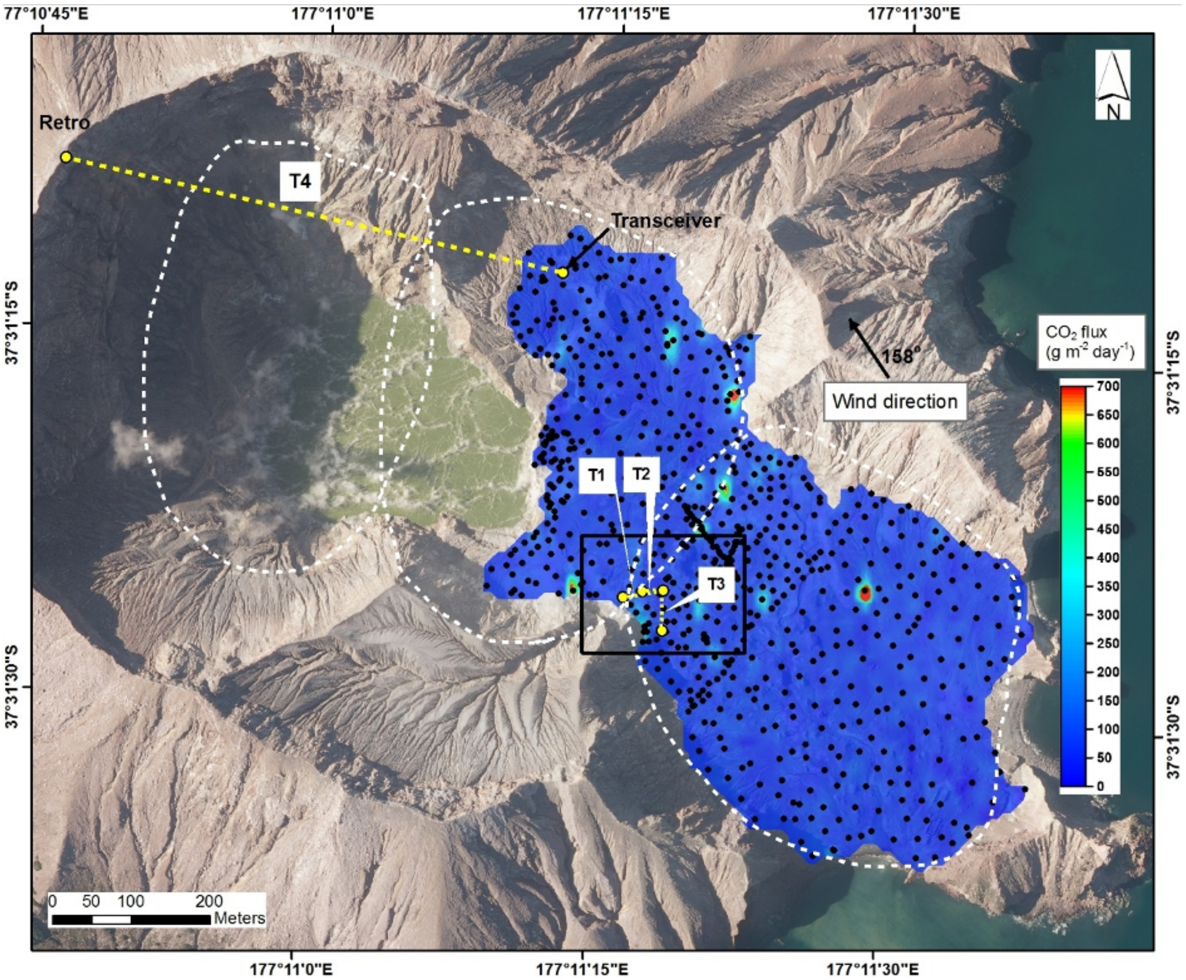

Figure 9.6: CO_2 flux map (in g m^{-2} day^{-1}) obtained by sequential Gaussian simulations of CO_2 flux. The white dashes are the older crater rims formed on White Island crater floor. The black rectangle represents the study area. Yellow dashed lines are the 4 different transects labeled T1, T2, T3 and T4. The average wind direction is also shown.

with clear magmatic compositions (*Christenson et al.*, 2017) and had the highest discharge temperature (150 °C, on 4th of April 2014). Three traverses were made in this area (Figure 9.7). Another series of measurements were made above the crater lake where the volcanic activity is the strongest. The wind direction at the time of the campaign was on average from the south-southeast (158°) in the crater floor, at an average speed of 23.7 ± 2.2 km h^{-1} during the period of measurements (Figure 9.7). The wind speed was measured at the MetService weather station located at the summit of White Island (Figure 9.2 and 9.7) and the wind direction was estimated on site using a handheld anemometer during the day of survey (37.524°S, 177.187°E). On the same day an Infra Red camera was used with images taken on the dome area where the activity was the strongest (Figure 9.8).

In the study of *Bloomberg et al.* (2014), 723 soil CO_2 flux points (Table S1) were measured using the accumulation chamber to cover all the crater floor (Figure 9.6) from January to November 2011 with the purpose of estimating CO_2 emissions from diffuse degassing using sequential Gaussian simulation (sGs; *Deutsch and Journel* 1998) and highlighting CO_2 pathways to the surface. The measured CO_2 fluxes were interpolated over a grid of square cells (7 × 7 m2) covering the study area using the spherical variogram model of *Deutsch and*

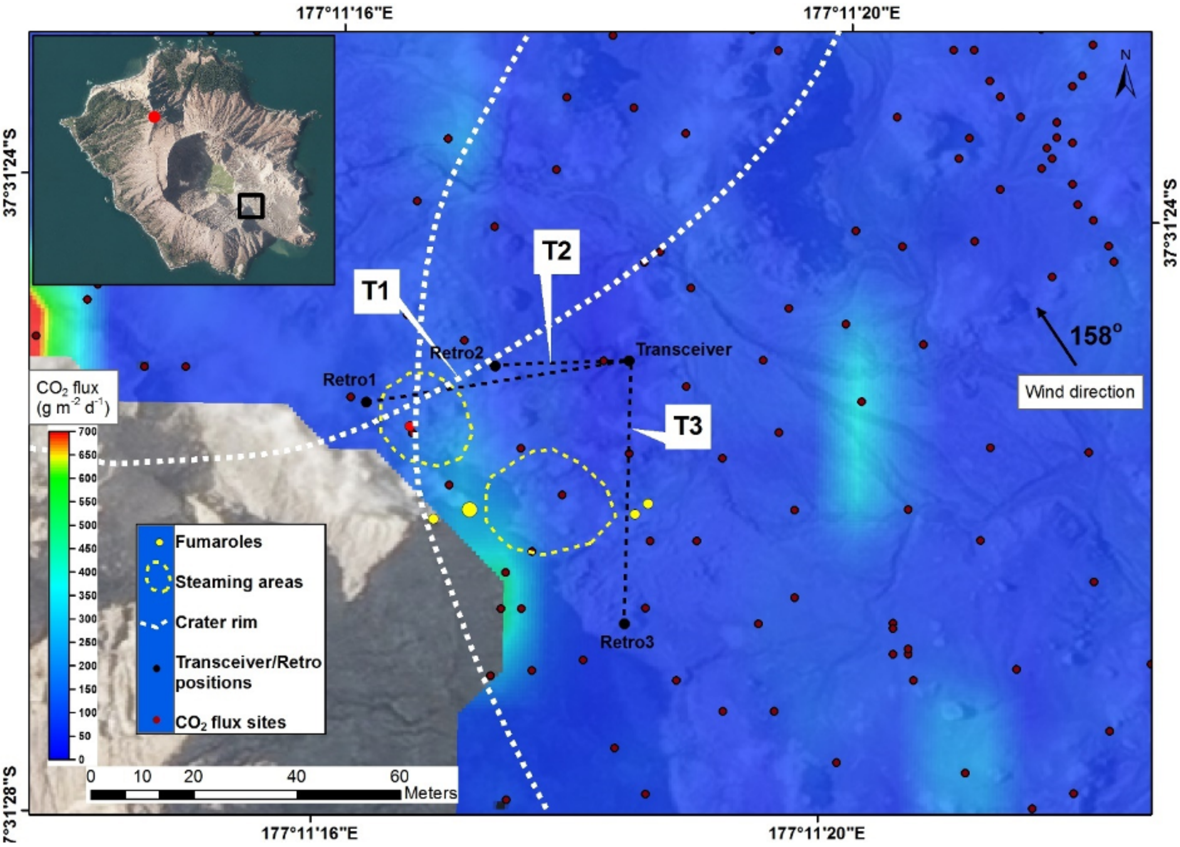

Figure 9.7: Map of an area of the White Island crater floor, western crater floor with location of the fumaroles, the steaming areas, CO_2 flux sites measurements and retroreflector - transceiver positions. Dashed lines are the transects between the transceiver and the retroreflectors 1, 2 and 3 labeled T1, T2 and T3. CO_2 flux measurements sites (purple dots) with the values around the studied area have been shown. The values are in g m^{-2} day^{-1}. The red dot represents the location of the MetService meteorological station. The average wind direction is also shown.

Journel (1998). The parameter values used for this model were 0.4, 1.05, and 55 for nugget, sill, and range, respectively. CO_2 flux values taken on the map along the 3 traverses performed by the TDL were used to build three cross sections using Surfer software. Then, the CO_2 fluxes along the traverses were compared with the CO_2 concentrations. No CO_2 flux could be measured above the crater lake as there was no access to the western crater.

9.3.4.2 Tunable diode laser measurements in a geothermal area: Ngapouri

To test whether geothermal gas is diffusely emitting along fault traces between the Maungaongaonga and Ngapouri geothermal areas, measurements of CO_2 concentration and flux were made along four traverses across strands of the Ngapouri Fault (Figure 9.4). The TDL measurements were made between May and July 2014, whereas the flux measurements were performed from November 2015 to January 2016. Each day of measurement the wind direction and relative strength was recorded using a meteorological station located 23 km from Ngapouri area (Table 9.2).

All fault traverse measurements progressed towards the southeast, with TDL measurements at approximately 50 m intervals with 10 min of data recording at each site, and flux measurements at approximately 10 m intervals. The CO_2 flux measurements were made on similar but shorter traverses that commenced closer to the fault traces. Traverses 1 to 3

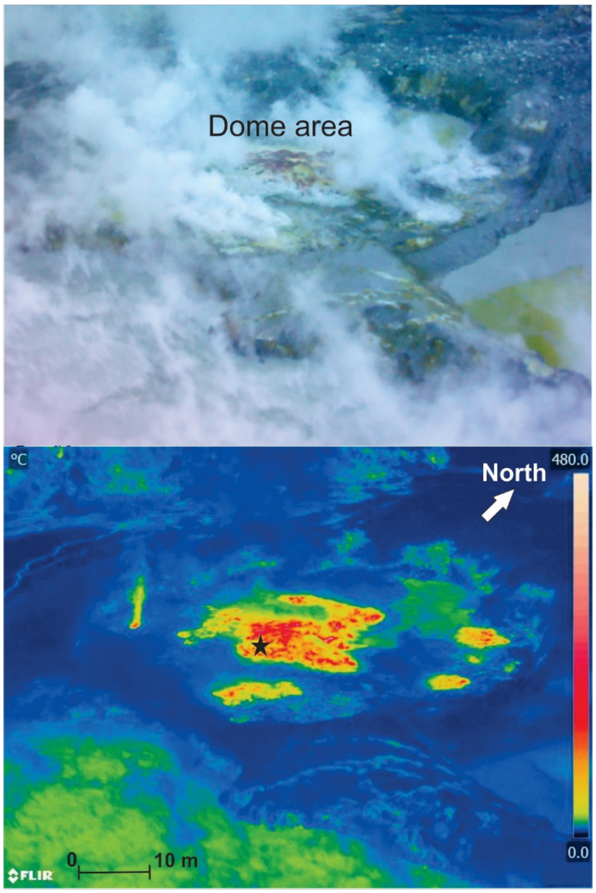

Figure 9.8: General view of the dome area (37°31’16"S, 177°10’57"E) in the White Island crater floor in the spectral range of the visible and Infra-Red using a FLIR T650sc that operates in the spectral range from 7.5 to 14 μm across a 29° × 19° field of view. It is a camera equipped with an uncooled Vanadium Oxide microbolometer detector that produces thermal images of 640 × 480 pixels. The black star shows the highest temperature (458.2 °C).

crossed two Ngapouri Fault splay (Figure 9.4), whereas Traverse 4 was across an area between fault segments, where a topographic expression is not obvious. For Traverse 1 the lines of flux and concentration measurements coincide. Traverse 2, close to an excavated trench location (Berryman et al., unpublished results), the TDL traverse is not a straight line of measurements as it crossed property boundaries that made it difficult to complete as a linear traverse. For this traverse, the line of flux measurements is not perfectly coincident. Traverse 3 does not have coinciding TDL and flux measurements (Figure 9.4) with approximately 600 m separating the lines.

Table 9.1: CO_2 concentrations summary of the four transects performed in the crater floor of White Island. See Table S2 for detailed CO_2 concentration dataset and coordinates of the transceiver and Retroreflectors

	Path Length (m)	Time of acquisition (minutes)	Mean CO_2 concentration (ppm)	Standard Deviation	Minimum concentration (ppm)	Maximum concentration (ppm)
Transect 1	41.2	6	466	35	394	657
Transect 2	22.6	5	465	20	432	555
Transect 3	46	6	402	10	390	443
Transect 4	647	38	477	23	381	549

Table 9.2: Values of average wind direction and speed from the meteorological station located 23 km from Ngapouri area (Rotorua AWS: 38.117°S, 176.317°E).

	Average wind direction (°)	Average wind speed (km h^{-1})
Traverse 1	56 ± 12	27.7 ± 6.5
Traverse 2	242 ± 31	16.2 ± 4.9
Traverse 3	212 ± 18	22.2 ± 2.4
Traverse 4	225 ± 13	25.6 ± 3.6

9.4 Results and discussion

9.4.1 CO_2 concentration at White Island and comparison with CO_2 flux for highlighting structure

CO_2 concentration measurements using the TDL were made through the gas plume emanating from the main fumaroles. The lowest CO_2 concentration measured during the campaign was 380 ppm and considered as the background value for the area of study. The mean CO_2 concentration for the first transect using retroreflector 1 (Table 9.1) was about 466 ppm (± 35 ppm), with the maximum value of 657 ppm. The high CO_2 concentrations measured in the crater floor is explained by the enclosed environment of the crater making difficult for the volcanic gases to escape to the atmosphere and the presence of eddies.

For the second transect, the mean background CO_2 concentration was 465 (± 20 ppm) and the highest value was 555 ppm (Table 9.1). The values are not as high as for the first transect as it is further from the most active fumarole. There were only 170 ppm of difference between the background CO_2 concentration and highest CO_2 concentration measured.

The third transect measurement (Figure 9.7) was performed intercepting two small fumaroles present on the path of the laser. The mean CO_2 concentration value is much lower than the values in the previous transects (402 ± 10 ppm, Table 9.1). And no clear high values were seen during the measurement.

The fourth transect measurement was performed across the carter lake above the most active area (Figure 9.6). The highest CO_2 concentration was 549 ppm with an average of 477 ppm (Table 9.1). The infrared measurements made in the same day on the most active area show temperatures as high as 458.2 °C (Figure 9.8).

The CO_2 flux values acquired from the 3 transects range from 25.5 $g{\cdot}m^{-2} \cdot day^{-1}$ to 127 $g{\cdot}m^{-2} \cdot day^{-1}$ with a mean of 66.2 $g{\cdot}m^{-2} \cdot day^{-1}$. For Transect 1, the CO_2 flux data show an increase when approaching the crater rims (Figure 9.9a). The CO_2 flux along the transect 2 and 3 does not show a clear correlation with the crater rim as shown in transect 1 (Figure 9.9b and 9.10).

Elevated CO_2 flux and CO_2 concentration were measured at White Island crater floor using the accumulation chamber and TDL methods and these data provided more insights in the old crater rims location highlighted by *Cole et al.* 2000 (Figure 9.6). For the first time at White Island, we were able to measure higher CO_2 concentration above fumaroles, steaming ground and crater lake (up to 657 ppm, Table 9.1). TDL can be used as a complementary tool to accumulation chamber method by measuring CO_2 emission from the fumaroles or can be used as a monitoring tool over a specific fumarole. However, the TDL must be setup in a

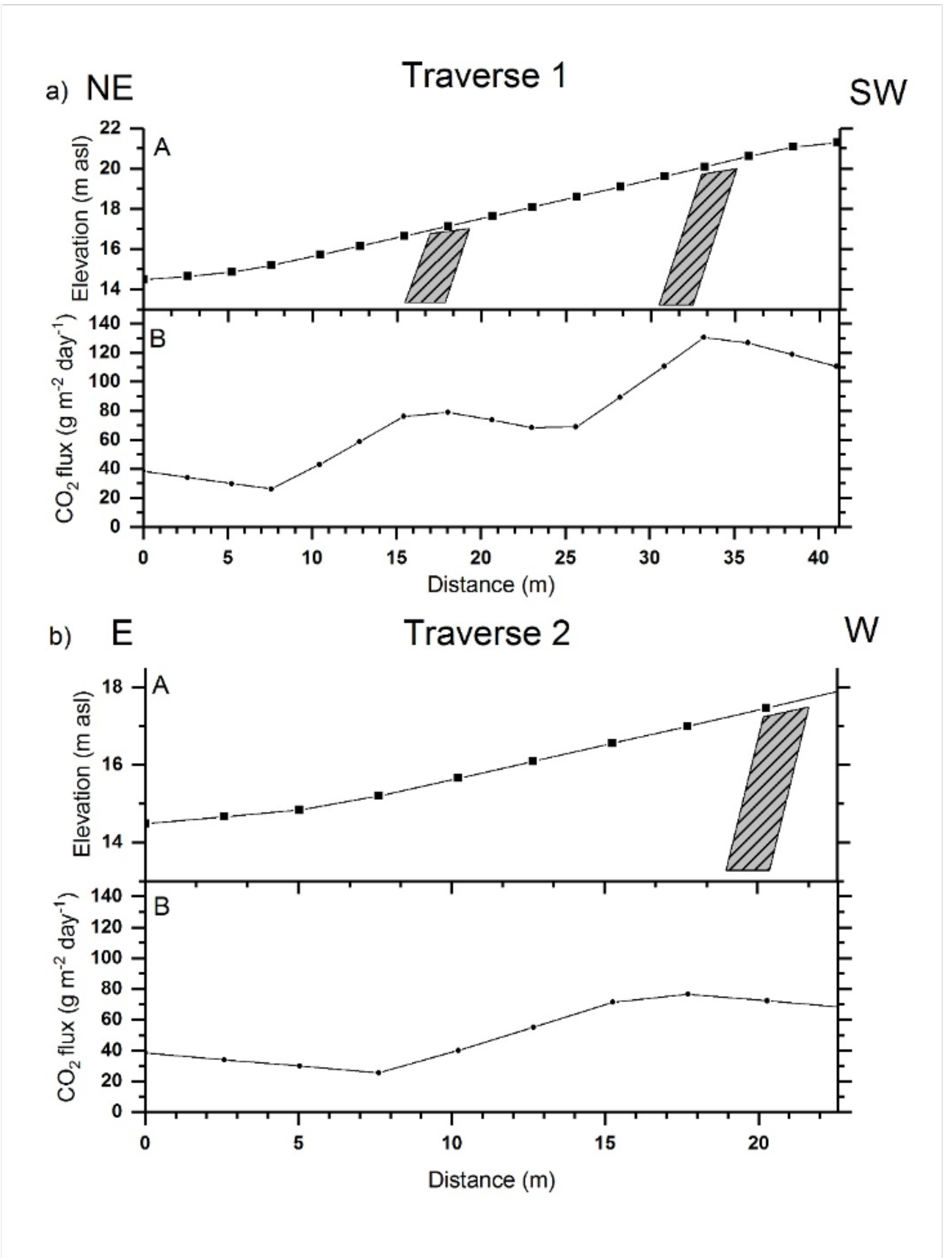

Figure 9.9: Traverses 1 (a) and 2 (b) obtained over vent plumes Retroreflector1-Transceiver (41.2 m) and Retroreflector2-Transceiver (22.6 m), respectively. A: Elevation profiles (masl), fault locations and lateral extent of geothermal activity. The grey dashed areas are the location of the crater rims; B: CO_2 flux (g m^{-2} day^{-1}) along a traverse of the area. The mean CO_2 concentrations on the traverse 1 and were 457 ± 2 ppm and 458 ± 0.9 ppm, respectively.

way that anomalous CO_2 concentration can be recorded because CO_2 is rapidly diluted in the atmosphere. While measuring some of these paths, fluctuations of CO_2 concentrations with time were observed, with cycles of CO_2 variability typically lasting tens of seconds and reflecting changes in plume density (because of fluctuations in gas emission rate at the fumaroles, or, more likely, due to changes in plume transport speed/direction, Figure 9.11). When CO_2 discharged at the surface by advection (fumaroles) or diffusion (soil diffuse degassing), its dispersion depends greatly on the atmospheric conditions, specifically on wind parameters. On Vulcano, Italy, CO_2 dispersion from the volcano in the atmosphere was modeled using a

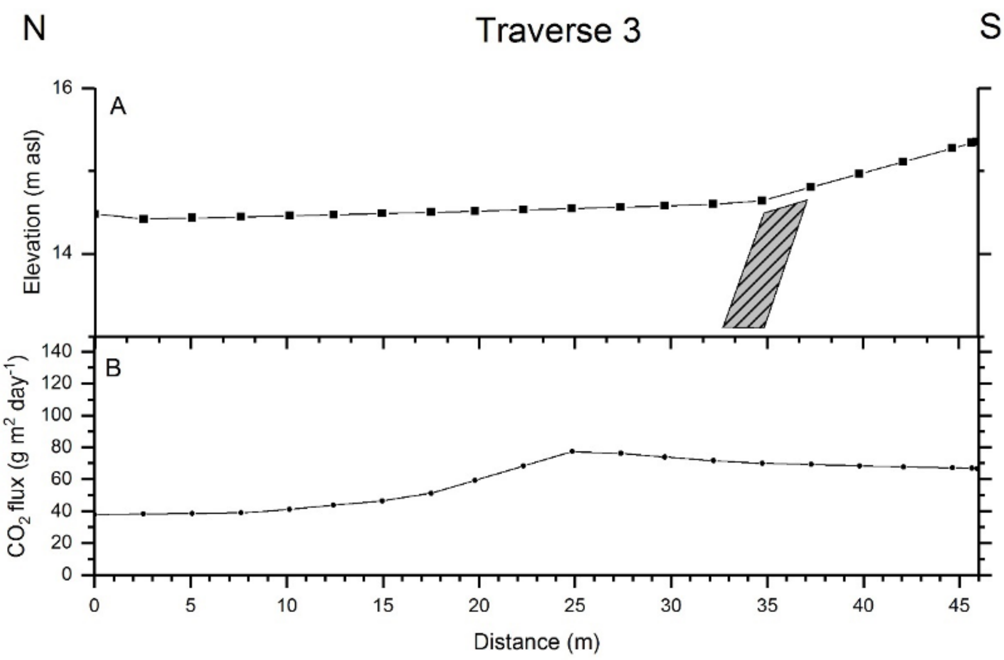

Figure 9.10: Traverse 3 obtained over vent plumes Retroreflector3-Transceiver (46 m). A: Elevation profiles (masl), fault locations and lateral extent of geothermal activity. The grey dashed areas are the location of the crater rim; B: CO_2 flux (g m^{-2} day^{-1}) along a traverse of the area. The mean CO_2 concentration on the traverse was 401 ± 0.9 ppm.

Eulerian model (DISGAS code; *Granieri et al.*, 2014) and the results showed that in the crater area, CO_2 with concentration >5000-7000 ppm was simulated in low-wind conditions.

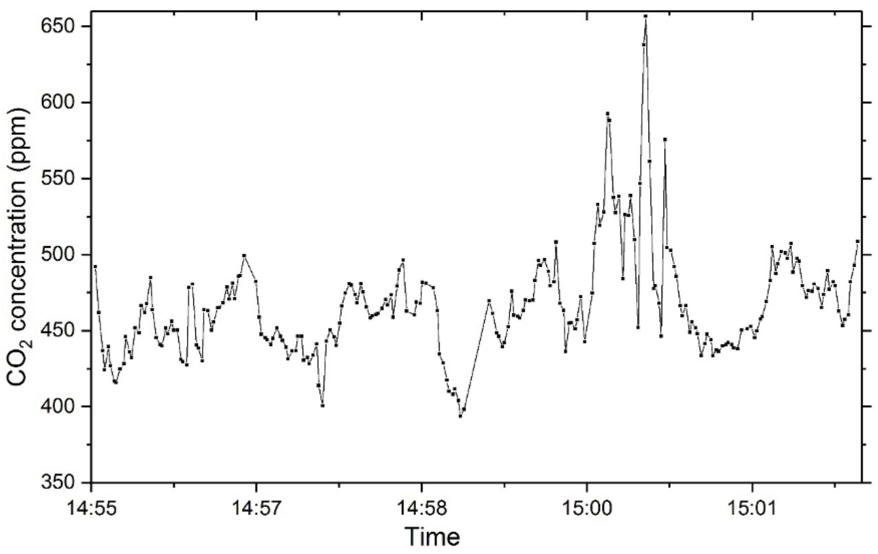

Figure 9.11: CO_2 concentration values measured by the TDL along Transect 1 (Figure 9.7.)

CO_2 emission is controlled by the crater morphology, the permeability and the volcanic activity. By the inspection of the spatial distribution of soil CO_2 fluxes, the highest CO_2 flux measured are mainly associated with the crater rims (Figure 9.6). This suggests that CO_2 degassing is principally controlled by crater morphology. Similar works on Furnas caldera (*Viveiros et al.*, 2010) showed the same control on the CO_2 degassing processes. Furthermore, one of the highest CO_2 flux was measured inside the eastern subcrater at White Island. This anomalous CO_2 flux can be explained by the presence of a lake before the 1914 landslide and the highest flux coincide with the pre-1914 lake shore. A study from *Nairn and Houghton* (1989) suggests that the lake shore seems to be delineated by a crater inside the eastern subcrater. The increase in gas flux showed that the gases were following the pathway through the crater rim and walls that have high-permeability. The same happened at Vulcano, Italy in 2004 and 2005 (*Granieri et al.*, 2006) with increase in soil CO_2 flux suggesting a permeability increase by seismic fracturing below the main edifice and not a magma uprise from a deeper source.

The increase in CO_2 emission rates can also be related to the rising of a new batch of magma at depth. *Hernández et al.* (2001) showed that before the Usu eruption in March 2000, soil CO_2 flux increased 10 times showing how CO_2 emission can be a useful parameter for monitoring volcanic activity. Another example is Stromboli (*Inguaggiato et al.*, 2017), with a significant increase in CO_2 flux before each eruption.

9.4.2 Ngapouri geothermal area

9.4.2.1 Probability distribution of the CO_2 concentration and flux

The determination of background CO_2 concentrations and fluxes are important in areas with low geothermal/volcanic CO_2 emissions, to establish contributions from atmospheric, biogenic, and/or anthropogenic sources. From the TDL measurements, the range of CO_2 concentration measured was from 376 ppm to 563 ppm with a mean CO_2 concentration of 428.9 ± 19.8 ppm for all the study area. Using the GSA, four distinct populations are identified in all the Ngapouri CO_2 concentration data (15,336 measurements including geothermal area in south of Ngapouri area; Figure 9.12a):

- Population A - mean atmospheric CO_2 concentration of 396.34 ppm (90% confidence interval: 396.28-396.40 ppm; 5.4% of the data).
- Population B - mean atmospheric CO_2 concentration of 428.7 ppm (90% confidence interval: 428.6-428.9 ppm; 86.6% of the data).
- Population C - mean atmospheric CO_2 concentration of 463.56 ppm (90% confidence interval: 463.48-463.64 ppm; 7.7% of the data).
- Population D -mean atmospheric CO_2 concentration of 498 ppm(90% confidence interval: 495-504 ppm; 0.3% of the data).

Data representing Population A is considered to be atmospheric background and compare well with the atmospheric CO_2 data monitored at Baring Head, New Zealand (393.9 ppm; April 2014, NIWA data - National Institute of Water and Atmospheric Research). Population B data are also considered background, represented by biogenic sourced CO_2. Data representing Populations C and D are both considered to have geothermal contributions, but

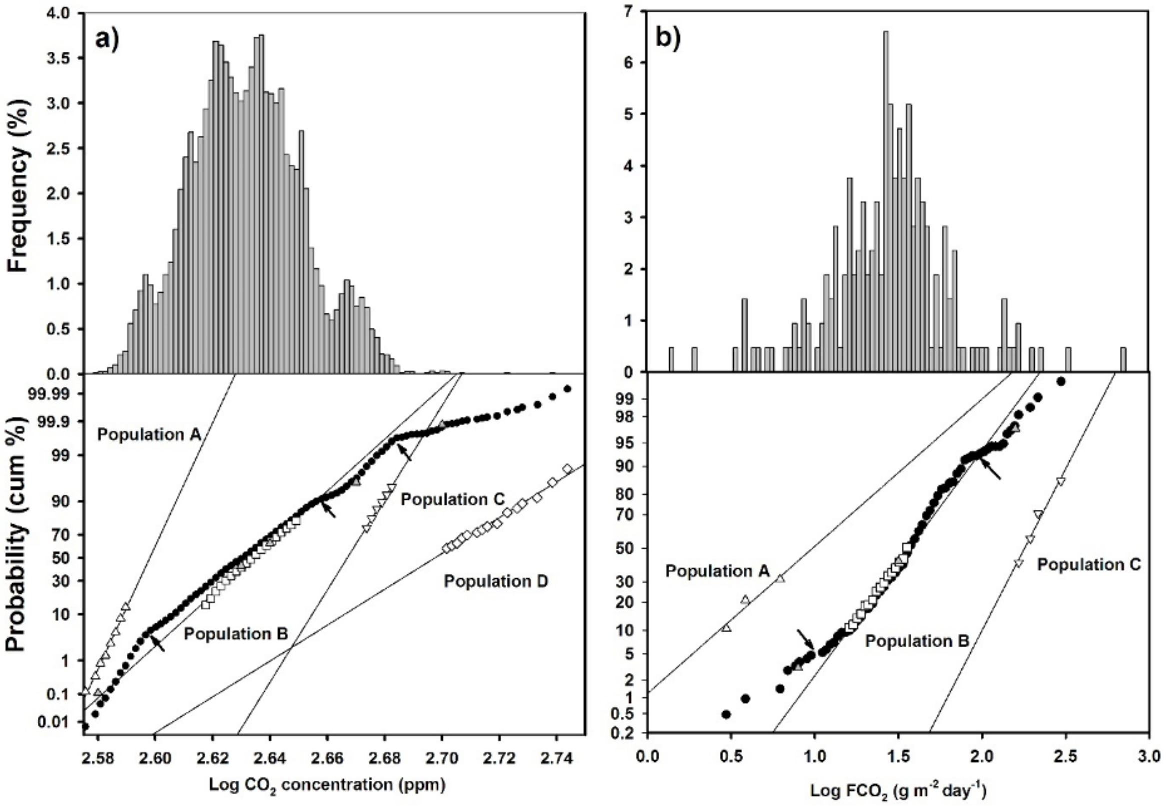

Figure 9.12: Histograms and probability plots of CO_2 concentration (a) and CO_2 flux data (b) (black circles). Populations A (open triangles up), B (open squares), C (open triangles down) and D (open diamond) are shown as straight lines. The grey triangles represent the mixture of population A, B, C and D. The inflection points between each population are indicated by arrows and correspond to the percentage of each population.

the concentration values appear to be dependent on the spatial association to fault splays. Such that, measurements belonging to Population D, which have the higher concentrations, tend to be located closer to the mapped fault. Population C data are from measurements located further from mapped faults, and therefore represent contributions from geothermal and biogenic sources.

From the accumulation chamber measurements, the mean CO_2 flux measured was 48.5 g m^{-2} d^{-1} with a minimum of 2.9 g m^{-2} d^{-1} and a maximum of 575.6 g m^{-2} d^{-1}. In the combined CO_2 flux dataset (213), three populations are identified (Figure 9.12b):

- Population A - corresponds to 4.5% of the data, with a mean CO_2 flux (FCO_2) of 16 g m^{-2} d^{-1} (90% confidence interval: 10-44 g m^{-2} d^{-1}).
- Population B - corresponds to 92.3% of the data,with a mean CO_2 flux of 45 g m^{-2} d^{-1} (90% confidence interval: 41-51 g m^{-2} d^{-1}).
- Population C - corresponds to 3.2% of the data,with a mean CO_2 flux of 212 g m^{-2} d^{-1} (90% confidence interval: 157-396 g m^{-2} d^{-1}).

Mean biogenic flux values from 9.3 and 20.5 gm^{-2} day^{-1} have been measured in Taupo area, 50 km south of Ngapouri area and outside any geothermal system (*Harvey et al.*, 2014). And

CO_2 fluxes between 1 and 52 g m^{-2} d^{-1} (29 - 590 mg C m^{-2} h^{-1}) have been measured from soils in urban lawns and green spaces in the USA and are also considered to have biological origins (*Kaye et al.*, 2005). The Population A flux data fall within both these ranges and is therefore considered representative of a background biogenic CO_2 flux. Population C has the highest flux values, and is most likely representative of geothermal CO_2 degassing. Population B data have intermediate values and are therefore likely to be representative of mixing between Populations A and C.

9.4.2.2 Field measurements of diffuse geothermal CO_2 concentrations and fluxes

During the Traverse 1 measurements (Figure 9.13a) there was a strong northerly wind (Table 9.2). Flux measurements for this transect began approximately 150 m northwest of the western splay and show immediate elevated fluxes (~45 g m^{-2} d^{-1}, Table S8). There are three intervals along the transect where CO_2 flux is greater than background, two of which directly coincide with the location of mapped fault splays (Figure 9.13a). The highest fluxes (~ 60-70 g m^{-2} d^{-1}) are associated with the eastern-most splay. TDL measurements along Traverse 1 started approximately 300 m northwest of the western splay (Table S4). Traverse 1 is represented by a total of 10 transects (10 min acquisition) of 50 m length for each site and has a total length of 500 m. CO_2 concentrations above background coincide with two areas of high gas flux. One is northwest of the mapped splay, and the other, where highest concentrations (484 ppm) occur, is over the eastern-most splay. Despite other intervals along this traverse being below background levels, there is a slight ‘peak’ in background concentrations at the western mapped splay (Figure 9.13a), coincident with the elevated CO_2 fluxes.

On the day of measurements along Traverse 2, approximately 500 m southwest of Traverse 1, the wind direction was from the southwest, and variably of calm to light strength (Table 9.2). The flux traverse begins and ends close to the mapped fault traces and shows a close spatial correspondence with elevated fluxes to both fault splays (Figure 9.13b). Maximum flux (57 g m^{-2} d^{-1}) occurs across the eastern splay (Table S9). TDL measurements on Traverse 2 is represented by a total of 17 transects (10 min acquisition) of approximately 50 m length for each site and has a total length of 850 m. The longer TDL traverse shows four intervals where concentrations are greater than background (Table S5). Two of them correspond to the fault locations and intervals of elevated flux (Figure 9.13b). The highest concentration (467 ppm) occurs over the western splay. The other two intervals occur northwest of the splays, similar to Traverse 1, where surface fault traces are not mapped.

TDL Traverse 3 is located approximately 800 m southwest of Traverse 2, ~450 m northeast of the closest active geothermal area (Fig. 14a). On the day of measurements, wind direction was from the southwest, and variably calm to moderate strength (Table 9.2). Traverse 3 is represented by a total of 12 transects (10 min acquisition) of 50 m length for each site and has a total length of 600 m. Elevated CO_2 concentrations occur above, and between, the mapped fault traces (Table S6). However, the highest concentrations (464 ± 6 ppm) along this transect occur west of the mapped faults (Figure 9.4). The flux measurements for Traverse 3 were made approximately 600 m to the northeast and have been projected onto the Traverse 3 profile (Table S10). Highly variable gas fluxes occur across mapped fault traces, but the highest flux (100 g m^{-2} d^{-1}) occurs between them (Figure 9.14).

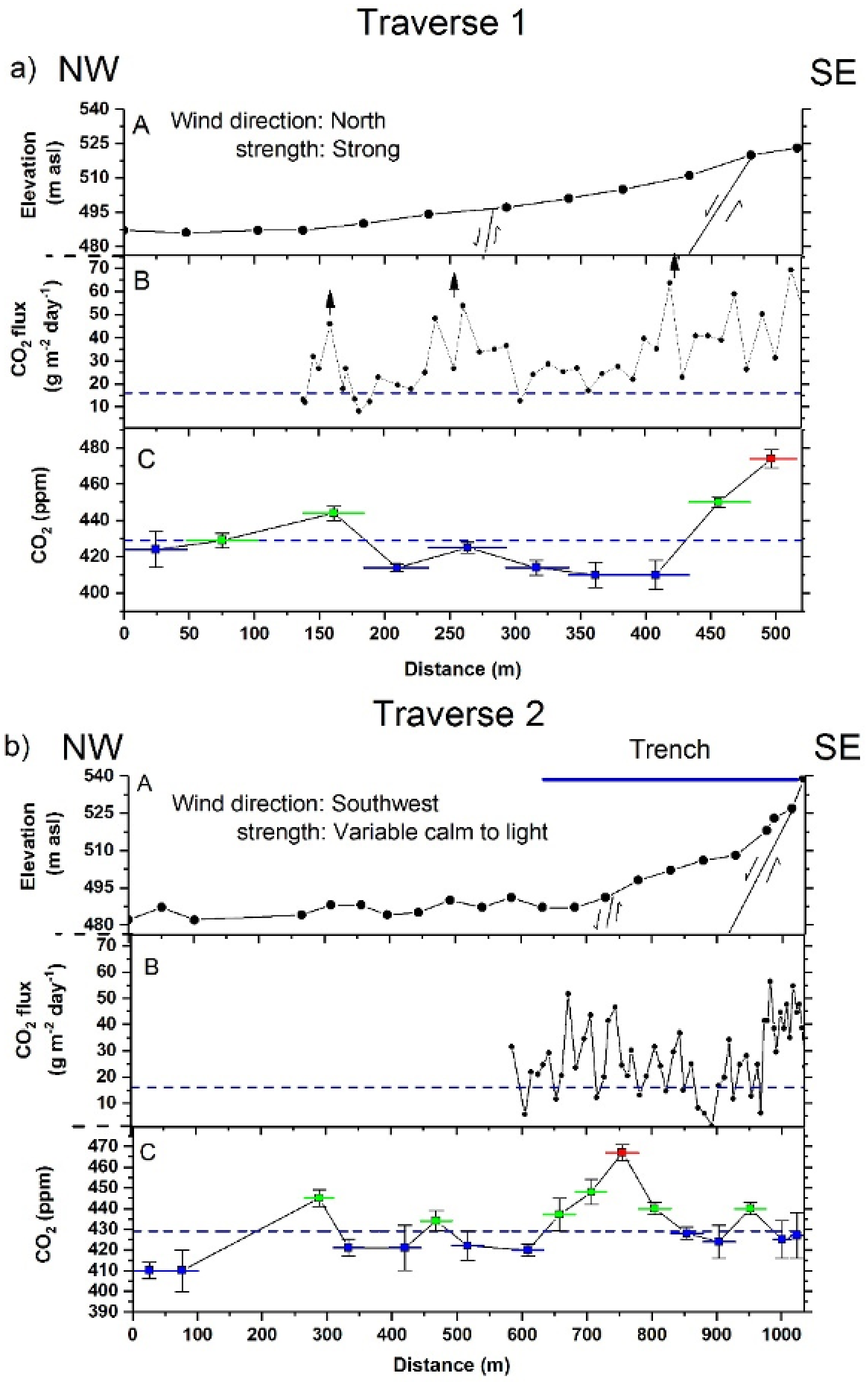

Figure 9.13: Traverses 1 (a) and 2 (b) across the Ngapouri Fault (Figure 9.2), A: Elevation profiles (masl) with fault locations, B: CO_2 flux (g m^{-2} d^{-1}) and C: measured CO_2 concentrations (ppm) along the traverses. Each measurement is a CO_2 concentration within the 50 m path length (represented as a colored horizontal line), with a central point showing standard deviation concentration errors bars. Concentrations for each measurement are color coded: red $\geq$464 ppm, green = 429-464 ppm, blue $\leq$429 ppm. Dashed blue lines represent the mean background CO_2 concentration (429 ppm) and mean background CO_2 flux (16 g m^{-2} d^{-1}). The black arrows in a) correspond to higher CO_2 flux.

Traverse 4 is located approximately 550 m southwest of the TDL Traverse 3 and is the closest to the Ngapouri geothermal area (the northwestern end of Traverse 4 is ~300 m from an area of steaming ground; Figure 9.14b). Traverse 4 is represented by a total of 10 transects

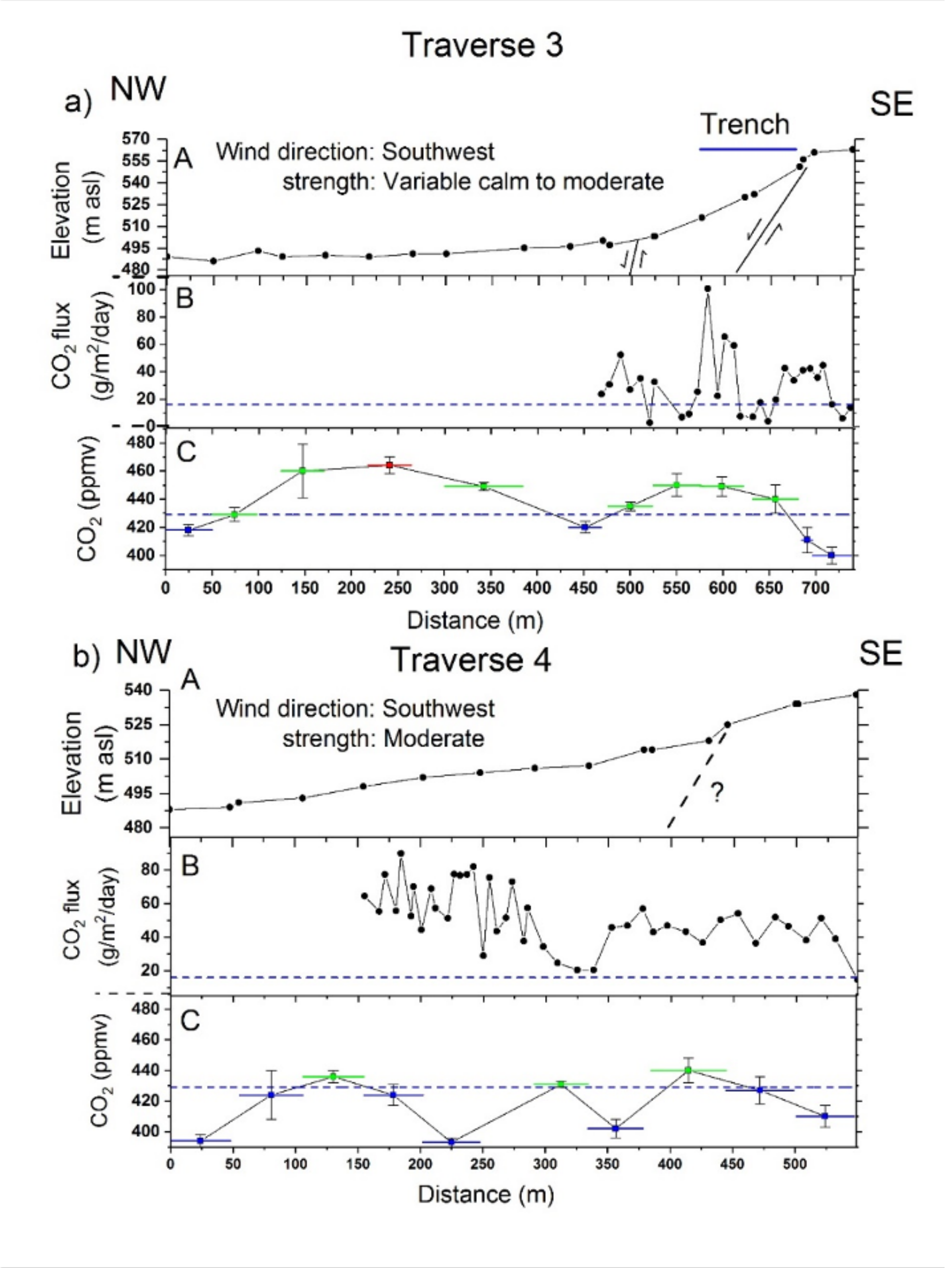

Figure 9.14: Traverses 3 (c) and 4 (d) across the Ngapouri Fault (Figure 9.2), A: Elevation profiles (masl) with fault locations, B: CO_2 flux (g m^{-2} d^{-1}), and C: measured CO_2 concentrations (ppm) along the traverses. Each measurement is a CO_2 concentration within the 50 m path length (represented as a colored horizontal line), with a central point showing standard deviation concentration errors bars. Concentrations for each measurement are color coded: red 464 ppm, green = 429–464 ppm, blue 429 ppm. Dashed blue lines represent the mean background CO_2 concentration (429 ppm) and mean background CO_2 flux (16 g m^{-2} d^{-1}).

(10min acquisition) of 50 m length for each site and has a total length of 500 m. This traverse is across an area where there no mapped surface fault expressions. However, projection of the mapped traces across this area would place the fault close to a ~5 m step in the elevation profile (Fig. 14b). On the day of measurements, the wind direction was from the southwest, and was of moderate strength (Table 9.2). Highest concentrations (440 ± 8 ppm) along this traverse occur above the projected location of the fault trace (Figure 9.14b). However, elevated concentrations (436 ± 7 ppm) are also present at two measurement locations west of the projected fault location (Figure 9.14b, Table S7). The flux measurements for Traverse 4 were made approximately 200 m to the southwest of the TDL Traverse 4 closer to the area of steaming ground. Gas flux along this traverse is variable, but consistently above background values (Figure 9.14b, Table S11).

9.4.2.3 Discussion

The Ngapouri Fault is regarded to have been a focus for the arrested intrusion of basalt dikes that triggered the AD1315 Kaharoa rhyolite eruptions from Tarawera volcanic vents, resulting in phreatic eruptions proximal to the length of the Ngapouri Fault (*Nairn et al.*, 2005). This implies that this fault is a deeply penetrating structural feature that provides favourable permeability for the passage of upwelling geothermal fluids from depth to surface (*Hedenquist and Browne*, 1989; *Lloyd*, 1959).

The results of this study show excellent correlation between elevated atmospheric CO_2 gas fluxes and concentrations with mapped, and projected, Ngapouri Fault traces. This suggests that the fault is diffusely venting CO_2 gas along faults between the northern Maungaongaonga, and the southwestern Ngapouri geothermal areas.

All four CO_2 traverses presented here consistently show elevated CO_2 concentrations at locations west of known mapped fault traces. It is possible that CO_2 is diffusely venting at unmapped (blind) fault splays.

The Direct Current electrical resistivity map ($AB/2 = 500$ m) of the district shows a region of conductive rock extending westwards from Waiotapu to Waikite (Figure 9.11; *Stagpoole and Bibby*, 1998). The Waiotapu geothermal area is regarded to be hydrologically connected to the Waikite geothermal area,with the latter being a western outflow from Waiotapu (*Bibby et al.*, 1994; *Stewart*, 1994). This hypothesis has been successfully modeled by *Kaya et al.* (2014). The implication is that a high temperature geothermal reservoir occurs at depth (i.e., at least $\sim$250 m) beneath Maungaongaonga and the uplifted Paeroa Fault block. The results of our CO_2 surveys suggest that the Waiotapu - Waikite geothermal reservoir also extends southwards to the small Ngapouri geothermal area, with diffuse geothermal gas emissions focused along the Ngapouri Fault splays.

9.5 Advantages and disadvantages of using a TDL over the accumulation chamber

TDL and accumulation chamber methods are able to measure CO_2 concentration and flux respectively. The accumulation chamber has been a proven technique in volcanic and geothermal areas in the past 20 years for measuring CO_2 flux (e.g., *Cardellini et al.* 2003; *Chiodini et al.* 1998; *Viveiros et al.* 2010).

The main advantage of the TDL method is that it can be applied for broader reconnaissance compared to using the accumulation chamber method. The data acquired by the TDL system can highlight anomalies over a path (25-100 m) but can not define exactly where the anomaly is. However, the TDL method can be a complementary tool to the accumulation chamber method in the study of large area (>1 km^2). A preliminary study of the area could be performed for highlighting any anomalous area by narrowing the discharge area performing incrementally smaller measurement paths. The next step would be to make CO_2 flux measurements using the accumulation chamber method.

The second main advantage is that the TDL method can be applied for monitoring purposes. For instance, at White Island the transceiver and the retroreflector would be deployed above the main fumarole areas located west, north west of the crater floor. The TDL measurements made over the White island crater lake was the longest distance ever measured (647 m) and showed high CO_2 concentrations related of the most active fumarole area.

Furthermore, the use of the TDL for CO_2 concentrations measurements over the monitoring area can improve safety because with the long distance (up to 1 km) that the instrument can measure, it is not necessary to be close to the volcanic vents.

Another advantage is that the TDL instrument can detect small changes in CO_2 concentration ($\sim$2 ppm) and so it is sensitive enough to detect anomalies over the area to be monitored. The TDL system detected CO_2 concentration values well above the mean background CO_2 level (410 ppm) on top of the Ngapouri fault splays with values ranging from 420 to 474 ppm. Another example of a work using TDL from *Pedone et al.* (2014a,b) shows similar results. CO_2 concentrations were measured above Solfatara active geothermal area with a maximum of 1400 ppm. The TDL method is an important tool for detecting anomalous CO_2 concentration above faults where no obvious geothermal manifestation is present.

A main disadvantage of using the TDL method is that atmospheric conditions (e.g., fog, wind, clouds) and seasons (e.g., winter, summer) can influence the CO_2 concentration measurements, as well as vegetation cover (*Hu et al.*, 2008), geomorphology, operating vehicles and animal respiration (i.e., cows; *Chianese et al.* 2009). Land use within the survey area at Ngapouri is dairying, and this was something to be aware of if dairy cattle were close by when measuring atmospheric CO_2. When making CO_2 concentration measurements, any of these influences (and possibly others) needs to be considered. On the contrary, CO_2 flux measured using the accumulation chamber is not influenced by other CO_2 contaminants produced in the atmosphere.

A disadvantage of using the accumulation chamber method is that it can't be used over mud pools, cliffs or in fumarolic vent. However, the open path system for the TDL makes the measurement possible where the accumulation chamber measurements are difficult or impossible like over the crater lake on White Island. *Pedone et al.* (2014a,b), made CO_2 concentration measurements over Pisciarelli site where the degassing vents are located at the bottom of a narrow valley. The retroreflector and the transceiver were installed in the outer rim of the valley to have a complete coverage of the fumarolic area. Another study by *Federico et al.* (2019) shows the application of TDL (simultaneously to MultiGas and UAV) in areas in which the use of the accumulation chamber is impossible.

Another main disadvantage of using the accumulation chamber method is the spot measurement. The area of measurement is only a few cm^2 and due to the high variability of the CO_2 flux in only a few meters apart in volcanic/geothermal areas, the spot measurement makes it difficult for highlighting high CO_2 emission sites. Multiple measurement sites need to be chosen for covering all the area of interest (*Granieri et al.*, 2010). Furthermore, if measuring CO_2 flux continuously, the instrument needs to be installed near more active areas and so if a volcanic eruption occurs, the instrument could be damaged and may stop recording data. The TDL instrument can be setup outside the active area, with the transceiver and the retroreflector set up on either side of the crater and so outside the active area, in safety conditions.

9.6 Conclusions

The Tunable diode laser can be used to measure CO_2 air concentrations on geothermal areas where related activity is not obvious in grassland. The results of the study on Ngapouri fault shows excellent correlation between elevated atmospheric CO_2 gas concentrations and the known, and projected, locations of Ngapouri Fault traces.

The major advantage of the TDL system is the high sensitivity for measuring CO_2 concentrations in areas where the average background value is high ($\sim$429 ppm). An additional advantage is that the TDL system can be used as part of broad reconnaissance in complement to the accumulation chamber method that measures soil CO_2 emissions and highlights structures.

While CO_2 accumulation method has served in volcano/geothermal areas admirably for the past 20 years, we believe that the TDL approach now offers tremendous potential and will be of great interest to geologists, volcano observatories and other users.

Acknowledgements

This work was funded by New Zealand Ministry of Science and Innovation (MSI) Geological Hazards Programme (GHZ) and Geothermal Resources of New Zealand (GRN). This manuscript benefited from the thoughtful and constructive reviews of Tony Hurst, Geoff Kilgour, Isabelle Chambefort, Maria Pedone, and anonymous reviewer. We would like to thank Randy Brown and the team from Boreal Laser Inc. for their help in the improvement of the TDL system. The CO_2 concentrations and fluxes data are derived from the GeoNet project.

Electronic supplementary data

All datasets generated and analyzed for this study can be found at: `https://data.mendeley.com/datasets/5tkbh28pd5/1`

Part III

Discussions and Conclusions

10

Discussion

The four publications presented in the previous chapters embrace the range of different soil gas parameters, measurement techniques and sampling designs at three different volcanic-geothermal systems: Los Humeros Volcanic Complex (Mexico), Aluto Volcanic Complex (Ethiopia), and Ngapouri geothermal area (New Zealand). In this chapter the manuscripts are discussed individually and in context to each other. In addition, I discuss the potential application of the used methods and measurement concepts used for future geothermal exploration projects and geothermal fields in utilization.

10.1 Los Humeros Scouting

Chapter 6 presents the first results of a comprehensive and area-wide soil gas survey at the Los Humeros geothermal field. The study focuses on the distribution and origin of area-wide CO_2 degassing across the main geothermal production zone to identify areas of unknown structural controlled permeability with a connection to the superhot geothermal reservoir. Although the Los Humeros geothermal field has been used for power generation since the early nineties, it should be emphasized that half of the drilled wells are not used. This has different reasons such as corrosion of the mechanical construction of wells due to acidic reservoir fluids, (*Diaz et al.*, 2016) or insufficient permeability due to the low permeable andesitic reservoir rocks, and the high spatial variability of lithofacies (*Weydt et al.*, 2018). Consequently, the reservoir permeability is mainly controlled by faults and fractures that cut through the geothermal reservoir and provide ideal pathways for hot fluid migration (*Aragón-Aguilar et al.*, 2017). In many geothermal systems around the world, faults and fractures are favorable targets for wells because the their high permeability relative to the surrounding rock matrix positively influences fluid flow (*Bellani et al.*, 2004; *Faulds and Hinz*, 2015; *Sibson*, 1996). Enhanced CO_2 degassing favoured by faults and fractures has been observed in many volcanic (*Battaglia et al.*, 2019; *Giammanco et al.*, 2007) and hydrothermal systems making the measurement of CO_2 flux and associated carbon isotopes a powerful tool for geothermal exploration (*Fridriksson et al.*, 2016; *Jentsch et al.*, 2020; *Jolie et al.*, 2016; *Klusman et al.*, 2000).

As the geothermal exploration phase marks the most important stage of developing a geothermal project, different techniques are applied and integrated to evolve conceptual models which guide the exploration and field development. In order to obtain a good overview of the characteristics of a potential geothermal resource e.g. depth of reservoir or temperature, a careful selection of exploration studies must be considered to reduce the project risk while keeping costs within an acceptable range.

In addition to geological surface surveys, geophysical surveys are well established in geothermal prospecting, as their application and the experience gained with them already dates back to the exploration of conventional petroleum resources. However, some of these methods are used by default as they are habitual, even though they may not add crucial value to the holistic characterization of the geothermal system (*DiPippo*, 2016). Early work by *Bibby et al.* (1992) reports that resistivity studies can not differentiate between past and active hydrothermal alteration and thus might be misinterpreted if not integrated with other datasets. Compared to geological/geochemical surveys, geophysical exploration campaigns require sophisticated equipment which is expensive, involves large logistical effort, and data processing requires much more time.

On the other hand CO_2 flux measurements are made with portable, lightweight equipment, which allows the user to carry them in difficult terrain. Adjustments to the sampling grid or the addition of further sampling points can be made at any time as a measurement takes no longer than two minutes. Regularly spaced sampling is an unbiased concept to collect spatially correlated data over large areas (geothermal reservoir scale) whilst avoiding interpolation artefacts (*Isaaks and Srivastava*, 1989).

For the CO_2 scouting survey at Los Humeros, we developed a regular sampling grid for an area of 6 km × 4 km adapted specifically to the structural setting by orienting the small 25 m point spacing perpendicular to the main fault strike (NNW-SSE). Afterwards, the most prospective areas were measured with higher resolution to understand the internal degassing structure and a more accurate extent of the degassing area. Knowledge about specific structural settings that favour fluid migration facilitates exploration drilling. As CO_2 degassing does not appear homogeneous along a single fault plane, the observed degassing patterns of the high resolution survey were interpreted to the internal fault zone architecture of individual faults or fault segments according to the work done by *Faulds and Hinz* (2015). The origin of gases was determined by carbon isotopic analysis from areas of low, medium, and high CO_2 flux and the additional sampling of helium isotopes. The results revealed areas connecting the surface with the deep/superhot geothermal reservoir. Furthermore, a previously unknown area of wide structural related degassing, southwest of Humeros village (Area E 6.3) has been identified and may be a future drilling target. This is in agreement with results from passive seismic monitoring, where lowest Vp/Vs values are interpreted as gas bearing regions (*Toledo et al.*, 2020b). Ground temperature measurements complemented the CO_2 surveys and proved to be an additional indicator of the presence of hot fluids migrating along faults without increased gas emissions at the surface. This is due to impermeable soil layers, which hamper gas migration but allow heat to be transferred by thermal conduction (*Bloomberg et al.*, 2012).

In addition to the typical correlation of high CO_2 flux (> 100 g m^{-2} d^{-1}) and associated $\delta^{13}C_{CO_2}$ values of hydrothermal origin ($\delta^{13}C_{CO_2}$ = -3‰), it is worth noting that CO_2 emissions that would be attributed to biogenic CO_2 showed carbon isotope values of the deep geothermal system. Similar findings are reported from the Ngatamariki geothermal field in New Zealand (*Hanson et al.*, 2014) and the hydrothermal-volcanic system of Solfatara di Pozzuoli in Italy (*Chiodini et al.*, 2008). This shows that the combined analysis of CO_2 flux and carbon isotopes for a differentiation of carbon sources is a powerful approach to estimate the actual extent of geothermally active areas, especially where no obvious surface manifestations e.g. fumaroles or steaming ground, are present.

Area-wide soil gas sampling provides a cost-efficient, sustainable and fast exploration method to understand structural controlled gas release. This is also applicable for the identification of blind geothermal systems (*Hanson et al.*, 2014) depending on the sealing capacity of cap rocks (*Carapezza et al.*, 2015; *Taussi et al.*, 2019). Furthermore, CO_2 scouting surveys can establish environmental baseline studies often requested in geothermal exploration programs. To facilitate exploration campaigns of large geothermal fields, CO_2 scouting can be used as an initial exploration survey, and based on the results, geophysical campaigns can be adapted and increase their resolution in areas of increased fluid flow. Finally, this makes it easy to exclude less interesting areas and focus on the most promising ones.

10.2 Los Humeros Monitoring

Chapter 7 presents results of a continuous and multi-chamber CO_2 flux monitoring survey. The main focus was to investigate a potential relationship between CO_2 flux variability induced by changes in reinjection rates in the Los Humeros geothermal system.

Geothermal reservoir monitoring aims to maintain a sustainable geothermal field operation in order to avoid over exploitation of the geothermal resource. Nowadays, reinjection is an integral part of a sustainable geothermal utilization to dispose geothermal brine, reduce pressure draw-down, and recharge water to the system especially when the natural recharge is low (*Kamila et al.*, 2021). Geothermal operators are responsible to overview reservoir conditions related to geothermal production and injection, and to respond in a timely manner to unwanted changes regarding mass flow, discharge enthalpy and reservoir pressure. The most direct information from the reservoir can be obtained from wells. This means either shutting down a production or injection well during testing or using an unproductive well for monitoring. A distinction is made between surface and underground monitoring, in which equipment has to be installed at the bottom of the well or at the wellhead. In both cases though, the costly equipment must withstand high temperatures and pressures and sometimes acidic liquids (*Grant et al.*, 1982). Other monitoring concepts that are applied at the surface include gravity and seismic measurements. These however require extensive monitoring networks that are ideally deployed before exploitation in order to understand the natural state of the system. Both methods are able to track the redistribution or recharge of fluids connected to areas of higher permeability/faults, but seismic monitoring also recognizes fluid-generated stress changes in the subsurface resulting in induced seismicity, a hot topic in geothermal exploitation (*Gaucher et al.*, 2015; *Grant et al.*, 1982).

Monitoring of CO_2 flux does not require extensive set-ups, but can still provide substantial data regarding changes in the deep geological system. A link between anomalous soil CO_2 flux and seismic activity has already been found in tectonically active areas like Central and South Italy (*Chiodini et al.*, 2004) as well as in active volcanic areas (*Liuzzo et al.*, 2013; *PADRON et al.*, 2008). This can further highlight the potential use of continuous CO_2 monitoring as a precursor to changes at depth.

This was the motivation to investigate whether there is also a link between geothermal reservoir operations and CO_2 flux variability. Therefore, we deployed a CO_2 flux monitoring system within the damage zone of a large normal fault crossing the Los Humeros geothermal field in combination with an on-site meteorological station. Increased CO_2 degassing, hot ground temperatures (97 °C) and intense hydrothermal alteration already evidenced the connection of the fault to the deep geothermal reservoir (*Jentsch et al.*, 2020). Furthermore it is targeted by several production and injection wells which made the fault an ideal study site to monitor CO_2 variability in response to reinjection rates.

From the continuous measurements of CO_2 flux over a period of five months, a negative correlation was found between changes in reinjection rates and surface CO_2 degassing. The correlation was calculated after the data was filtered from atmospheric influences by a stepwise multiple regression analysis (*Jentsch et al.*, 2021). This is a common method applied in geochemical monitoring studies to determine the potential influence on CO_2 emissions by endogenous processes (*Liuzzo et al.*, 2013; *Oliveira et al.*, 2018; *Viveiros et al.*, 2015).

Nevertheless, there are several unmonitored variables such as soil temperature and -humidity and non linear processes like fluid-rock interactions or changes in effective stresses by pore pressure perturbations from ascending fluids, which are expected to have an influence on the variability of CO_2 emissions. A comprehensive discussion on these parameters is given in chapter 7. The different response of the individual monitoring chambers to changes in reinjection rates is related to the heterogeneous subsurface at the monitoring site. The monitoring site is located within a fault damage zone where pumice and scoria fall deposits are affected by varying degrees of hydrothermal alteration that consequently decrease or increase the permeability of the rock-matrix and fracture network.

The results lead to a better understanding of the small-scale and temporal variability of CO_2 flux and build awareness for choosing a suitable monitoring site. A thorough understanding about the structural geology and mapping of geothermal surface manifestations and their extent is recommended prior to installing a monitoring system. Finally, this finding has implications for novel reservoir monitoring approaches, and seems to be a promising concept to understand real-time changes in geothermal reservoirs associated with their operation. Such observations also allow to estimate fluid migration velocities, which is a key constraint for conceptual and numerical modelling of fluid flow in fracture-dominated systems. The installation of a CO_2 monitoring system can also be conducted before any exploitation starts to provide a data baseline for later comparison.

10.3 Aluto Exploration

Chapter 8 presents results from the Aluto Volcanic Complex (AVC) in Ethiopia where a comprehensive dataset consisting of CO_2 flux, ^{222}Rn, and ^{220}Rn activity concentrations and ground temperatures were collected at high spatial resolution. The aim of this study was to identify hidden and deep reaching permeable structures. Since the Aluto geothermal field is located in the East African Rift System, hydrothermal fluid circulation is influenced by both, its volcanic heat source and local to regional tectonic forces (*Lloyd et al.*, 2018). From the eight wells that were drilled in Aluto, only two are productive and located adjacent to the major Artu Jawe fault zone (AJFZ) representing the main upflow area. A small segment of the fault is exposed and accompanied by several fumaroles that continue in a NNE to SSW direction, giving indication to the buried part of the fault zone. Indeed, the deep well stratigraphy indicates large displacements between the main lithologies suggesting the presence of additional faults, but without surface expressions (*Hutchison et al.*, 2015). A few areas of major hydrothermal degassing have been mapped by *Hutchison et al.* (2015) and are related to the caldera rim structure (referred to as Bobesa).

The major advantage of this exploration campaign was the combined measurement of all parameters at each individual sampling site. This resulted in the development of soil gas fingerprints that simplifies the spatial analysis and comparison of areas with each other. The application of geochemical fingerprints has a long tradition and their development aimed to easily identify specific geological reservoirs on Earth (*Hoefs*, 2009). Furthermore, by simply calculating the ratio of ^{222}Rn-^{220}Rn activity concentrations (RTR) the source (deep or shallow) and migration velocities of the gases can be estimated due to their different element half life (^{222}Rn = 3.8 days and ^{220}Rn = 55 s; *Giammanco et al.* 2007). In this way, major hydrothermal upflow zones are highlighted. The extraction of coherent peak values from CO_2 flux, ^{222}Rn, and ^{220}Rn activity concentrations and their spatial distribution revealed the existence of two unknown zones of increased permeability. Potentially, they represent NNE-SSW oriented faults following the regional structural trend of the area (*Hutchison et al.*, 2015) and intersecting with the Ring fault that would explain the appearance of two distinct clusters of hydrothermal features at the surface (*Jolie et al.*, 2019). Coherent peak values of the four parameters together with determined RTR's allowed to divide the study site into volcanic (heat), tectonic (structures), or volcano-tectonic dominated areas. The most promising settings represent a combination of both, as there are sufficient hot fluids that can migrate along permeable faults. This applies to areas to the south and southeast that are not yet used for geothermal exploitation but are promising targets for geothermal drilling (*Jolie et al.*, 2019). The multi parameter approach revealed that anomalous ^{222}Rn and ^{220}Rn activity concentrations generally correlated with areas of increased CO_2 emissions and ground temperatures. However, solely radon and thoron measurements allowed us to identify two areas in the central part of the study site with a possible connection to the geothermal reservoir that would not have been found by measuring CO_2 flux and ground temperatures alone. These areas can either represent lateral outflow zones from major hydrothermal upflow zones (AJFZ and Bobesa), or separate structural controlled permeabilities. Data from the only well drilled in the south (LA5) indicate an outflow zone at depth (*Gizaw*, 1993). Although no surface fault scarps are exposed, increased gas emissions indicate the presence of fluid pathways.

10.4 Ngapouri Exploration

Paper 9 presents results from CO_2 concentration measurements at two field sites, a low degassing geothermal area called Ngapouri and White Island, New Zealand's most active volcano. The aim of this study was to test if the Tunable Diode Laser (TDL) absorption spectroscopy method is sensitive enough to detect any anomalous CO_2 concentrations in two very different volcanic/geothermal systems. Another goal was to compare the TDL method to CO_2 flux measurements by means of the accumulation chamber method. In this discussion, however, I focus only on the Ngapouri geothermal area because it contributes to the overall concept and goal of this thesis, which is to examine different methods for exploring geothermal energy.

The study area is characterized by two subparallel, partially inferred NE-SW trending faults. Two prominent areas of steaming ground and fumarolic activity are located at the NE (Maungaongaonga volcano) and to the SW, referred to as Ngapouri geothermal area, while no evidence of geothermal activity is visible along the faults. Furthermore, the study area is located between two active geothermal systems, Waiotapu to the east and Waikite to the west. Previous studies discuss that the Waikiti geothermal system presents a hydrothermal outflow from Waiotapu (*Bibby et al.*, 1994; *Stewart*, 1994) which was successfully modelled by *Kaya et al.* (2014). However, no connection to the Ngapouri geothermal area has been discussed/proposed.

So far, the TDL method has been used mainly for studies in volcanically active areas, to monitor gas concentrations (*De Natale et al.*, 2001; *De Rosa et al.*, 2007). Here, for the first time, the TDL method was applied in a low degassing geothermal area to investigate its potential to identify areas of structural controlled permeability.

CO_2 flux and CO_2 concentration were measured along four profiles (1km) crossing the two fault splays. Results show a large variability of CO_2 fluxes and concentrations along the profiles but increased CO_2 concentrations and fluxes can be related with known fault structures (*Mazot et al.*, 2019). Previous studies excavated trenches and proved the existence of the faults (*Villamor and Berryman*, 2001). However, the fault progression is not known for the entire study area. Therefore, increased CO_2 degassing occurring outside the mapped faults can be related to buried fault splays. Increased CO_2 fluxes and concentrations also support the hypothesis that the Waiotapu-Waikite geothermal areas are hydrologically linked and suggest that the systems extend even further south to the Ngapouri geothermal area. Thus, enhanced structural permeability along the Ngapouri faults facilitates hydrothermal fluid flow and may explain the occurence of the isolated Ngapouri geothermal area.

The accumulation chamber is a proven technique in volcanic and geothermal areas (*Chiodini et al.*, 1998; *Jentsch et al.*, 2020) while the TDL method is still new to the field of geothermal exploration. The study by *Mazot et al.* (2019) showed that the TDL method can serve as a preliminary exploration approach for large and unknown geothermal areas before fine-tuning is completed by high-resolution CO_2 flux measurements.

10.5 Cumulative discussion

For the geothermal systems studied here, the application of gas geochemistry has proven to be a reliable and simple technique, on different scales. The decision of whether or not an area is investigated by profiles or regular grids of different resolution depends on the objective of the survey, time, accessibility to the area, site-specific characteristics, and budget. For correlation purposes it is recommended to perform all measurements in the same season and at the same sampling points. Measuring soil gases at regular spaced sampling grids is an unbiased measurement concept (*Isaaks and Srivastava*, 1989) to understand the spatial distribution of gas emissions and determine background levels of soil degassing at a study site (*Jentsch et al.*, 2020; *Jolie et al.*, 2015a, 2019).

Large sampling grids (25 x 200 m) can be useful for a first scouting of an area and proved to be successful in the determination of area wide degassing and the identification of gas migration pathways (*Jentsch et al.*, 2020; *Jolie et al.*, 2015a, 2019). In contrast, domain-based sampling (25 x 50 m) allows the areas of interest to be investigated at higher resolution to determine their actual extent, interpret degassing patterns to structural settings at depth, and calculate the total CO_2 output (*Jentsch et al.*, 2020). A priori information are not necessary but always helpful.

The application of profiles does require a priori information about e.g. known faults or geothermal features, since these determine the orientation of the profiles. Their application is especially useful when fast information is needed about a large area within a short time. Given that there are usually large gaps between profiles, an interpolation algorithm e.g., kriging should not be applied as a poor spatial prediction and artefacts will be produced (*Li and Heap*, 2014). Therefore, widely spaced profiles do not contribute to a robust understanding about the spatial distribution of gas emissions, but rather to specific degassing segments (*Mazot et al.*, 2019).

Overall, the combined measurement of several gas parameters contributes to a holistic interpretation of a geothermal system. Each gas species can give specific information on the conditions that allow their formation, accumulation and/or migration. Ultimately, the time available to explore an area determines how many gas species can be measured.

CO_2 flux and ground temperatures are by far the fastest and easiest parameters to measure and are therefore the most suitable ones for a scouting survey. Together with the sampling of carbon isotopes, the spatial distribution of CO_2 and its origin can be linked to permeable pathways in the subsurface. A preliminary survey with the TDL method could be less time consuming, if the morphology of the study area is not too variable. Based on the TDL results, areas with anomalous CO_2 degassing can then be investigated using the domain-based approach by measuring the CO_2 flux. Helium sampling is more limited to areas of intense degassing to avoid the high level of atmospheric contamination from ^{4}He at diffuse degassing sites. However, the ^{3}He/^{4}He ratio plotted against atmospheric components ^{4}He/^{2}0Ne allows to compute the percentage of mantel, crust, and atmosphere helium, locations directly associated with the deep superhot geothermal system have been identified (*Jentsch et al.*, 2020). The results are supported by a nearby production well showing geothermal reservoir temperatures > 390 °C (*Lorenzo Pulido*, 2008). Thus, it is recommended to take samples where possible.

I also showed that the spatial distribution of ^{222}Rn, and ^{220}Rn activity concentrations give promising results about areas of increased structural permeability. In most cases, high ^{222}Rn activity concentrations at the surface correlate with increased CO_2 emissions, as CO_2 acts as a carrier for radon (*Giammanco et al.*, 2007). Considering the long measurement time of ^{222}Rn activity concentrations (15 minutes per sampling site), I propose its measurement at a later stage of the exploration and not during the scouting. Therefore, a domain based sampling of ^{222}Rn, and ^{220}Rn activity concentrations based on the results of the CO_2 flux scouting survey seems to be a reasonable concept here.

The selection of a suitable site for a CO_2 flux monitoring station should be based on the results of the CO_2 scouting and domain-based surveys (*Jentsch et al.*, 2021). This ensures, that the monitoring site has a good connection to the geothermal reservoir through a permeable fault. Figure 10.1 describes the workflow that not only combines the above steps but also is seen as a target-oriented approach for a successful geothermal exploration and monitoring.

Finally, gas geochemistry is not a standalone method, however the joint interpretation with geological, structural, and geophysical data sets provides a comprehensive overview of the dynamics and structure of geothermal systems (*Toledo et al.*, 2020b). Moreover, it substantially contributes to the development of conceptual models.

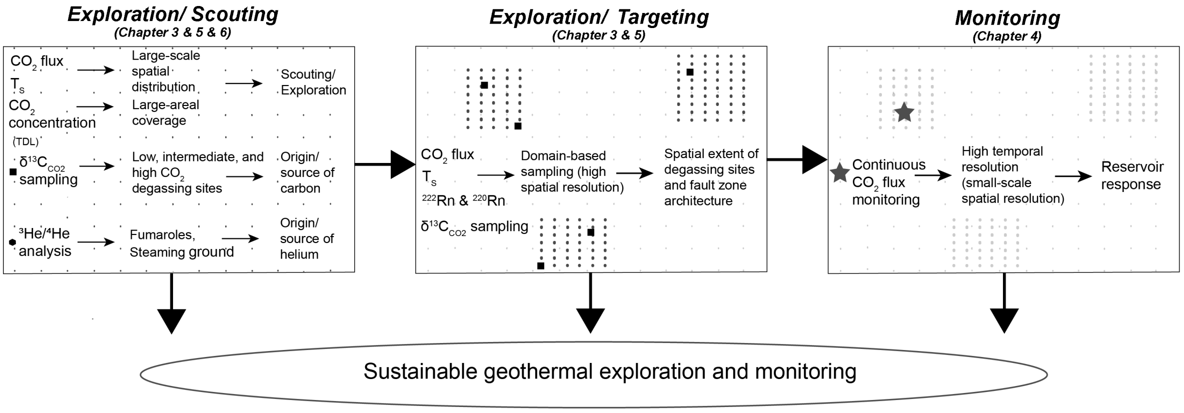

Figure 10.1: Proposed workflow for a successful geothermal exploration and monitoring survey based on the results obtained in this thesis. The different sampling networks are shown as regular spaced sampling points. The strength of the proposed workflow lies in the combined execution of the individual measurement concepts.

11

Conclusions

To date, no comprehensive attempt has been made to verify the area-wide application of soil gas analysis for geothermal exploration purposes. Nor has the continuous measurement of CO_2 flux been used to monitor changes in a geothermal reservoir. This thesis provides an overview of the most suitable gas parameters and sampling concepts tested in three volcanic-geothermal systems. It is intended to be established as a guide for future geothermal exploration and monitoring projects. Moreover, each of the applied approaches provides valuable information for a comprehensive and sustainable exploration and monitoring of the geothermal underground. The most important outcomes of this thesis are:

(1) The development of site specific sampling concepts related to known structural and geothermal surface conditions are fundamental to determine both area-wide and domain-based soil degassing and relate them to permeable structures in the subsurface.

(2) Domain-based sampling concepts facilitate the determination of the actual extent of an active geothermal area and the interpretation of soil degassing patterns in terms of specific structural conditions that favour fluid flow.

(3) The combined measurement of CO_2 flux and $\delta^{13}C_{CO_2}$ revealed that important information is transferred also by low/background CO_2 emissions increasing the size of diffuse degassing domains potentially connected with the deep geothermal reservoir. For this reason, it is recommended to take samples for carbon isotopic analysis also from low CO_2 degassing areas.

(4) Helium isotopic analyses allows to identify areas with a connection to the hydrothermal or superhot geothermal reservoir.

(5) Background CO_2 fluxes related to biogenic origin can be highly variable in convection-dominated geothermal systems as shown at the three study sites in this thesis. For a successful exploration, it is therefore essential to choose a grid spacing that covers a meaningful surface area and is of high enough resolution, to account for the unpredictable. The determination of background gas emissions ultimately contributes to environmental baseline studies of geothermal projects.

(6) The installation of a permanent CO_2 flux monitoring system with seven accumulation chambers proved to be a useful method to monitor temporal changes caused by reinjection

into the deep geothermal reservoir. Thus, it provides an alternative and cost-effective method for monitoring geothermal reservoir dynamics. This study also showed that information from the deep geothermal reservoir can be transferred by lower CO_2 fluxes.

(7) The strong small-scale variability of CO_2 flux underlines the anisotropic and heterogeneous properties of fault zones, which directly influence the gas flux. This should be taken into account when choosing a location for a monitoring station. This accounts not only for geothermal reservoir monitoring but also in volcano surveillance.

(8) The development of soil gas fingerprints is a novel approach for the visualization of spatial distribution of soil gas parameters. Based on CO_2 flux, ground temperatures, ^{222}Rn and ^{220}Rn activity concentrations a simplified spatial analysis based on site specific characteristics of the study area allowed to assess areas directly linked with the geothermal reservoir.

(9) The tunable diode laser is a convenient method for the fast observation of diffuse degassing along profiles. Increased CO_2 concentrations were detected in association with permeable fault segments. Even though originally used in atmospheric and volcanic research, this thesis demonstrates how significant its application is for geothermal exploration.

For the utilisation of geothermal energy, a thorough knowledge of the geological structure of the underground is compulsory. The application of soil gas analytics contributes to this understanding and helps to improve the prospect of success for the exploitation of geothermal energy. Furthermore, it can reduce the costs of exploration and monitoring surveys and thus lowers the development risk. The measurement concepts and methods tested in this thesis can be applied to other subsurface energy and disposal activities such as carbon capture and storage, landfills, or radioactive waste disposals.

Overall, soil gas analysis is not intended to replace existing exploration and monitoring methods but to complement them in a meaningful way.

References

Aben, F. M., M. Doan, T. M. Mitchell, R. Toussaint, T. Reuschlé, M. Fondriest, J. Gratier, and F. Renard (2016), Dynamic fracturing by successive coseismic loadings leads to pulverization in active fault zones, *Journal of Geophysical Research: Solid Earth*, pp. 3782–3803, doi:https://doi.org/10.1002/2015JB012542.

Agostini, A., M. Bonini, G. Corti, F. Sani, and P. Manetti (2011), Distribution of Quaternary deformation in the central Main Ethiopian Rift, East Africa, *Tectonics*, *30*(4), doi:10.1029/2010TC002833.

Aiuppa, A., and F. Gaillard (2016), Volcanic gases, *Encyclopedia of Earth Sciences Series*, pp. 1476–1479, doi:10.2307/1776906.

Aiuppa, A., C. Federico, G. Giudice, S. Gurrieri, A. Paonita, and M. Valenza (2004), Plume chemistry provides insights into mechanisms of sulfur and halogen degassing in basaltic volcanoes, *Earth and Planetary Science Letters*, *222*(2), 469–483, doi:10.1016/j.epsl.2004.03.020.

Aiuppa, A., C. Federico, G. Giudice, S. Gurrieri, M. Liuzzo, H. Shinohara, R. Favara, and M. Valenza (2006), Rates of carbon dioxide plume degassing from Mount Etna volcano, *Journal of Geophysical Research: Solid Earth*, *111*(B9), doi:https://doi.org/10.1029/2006JB004307.

Allard, P. (1983), The origin of water, carbon, sulphur, nitrogen and rare gases in volcanic exhalations; evidence from isotope geochemistry, in *Forecasting Volcanic Events*, edited by T. H and S. J, pp. 337–386, New York: Elsevier, Berlin, Heidelberg.

Amanda, F. F., R. Yamada, M. Uno, and S. Okumura (2019), Evaluation of caldera hosted geothermal potential during volcanism and magmatism in subduction system, NE Japan, *Geofluids*, *2019*, 1–14, doi: https://doi.org/10.1155/2019/3031586.

Aragón-Aguilar, A., G. Izquierdo-montalvo, S. López-blanco, and V. Arellano-gómez (2017), Analysis of heterogeneous characteristics in a geothermal area with low permeability and high temperature, *Geoscience Frontiers*, *8*(5), 1039–1050, doi:10.1016/j.gsf.2016.10.007.

Arellano, V. M., A. García, R. M. Barragán, G. Izquierdo, A. Aragón, and D. Nieva (2003), An updated conceptual model of the Los Humeros geothermal reservoir (Mexico), *Journal of Volcanology and Geothermal Research*, *124*(1-2), 67–88, doi:10.1016/s0377-0273(03)00045-3.

Arellano, V. M., R. M. Barragán, M. Ramírez, S. López, A. Paredes, A. Aragon, and R. Tovar (2015), The Response to Exploitation of the Los Humeros (México) Geothermal Reservoir, *World Geothermal Congress 2015*, *2*(April), 7.

Arzate, J., F. Corbo-Camargo, G. Carrasco-Núñez, J. Hernández, and V. Yutsis (2018), The Los Humeros (Mexico) geothermal field model deduced from new geophysical and geological data, *Geothermics*, *71*(September 2017), 200–211, doi:10.1016/j.geothermics.2017.09.009.

Azadi, M., S. A. Northey, S. H. Ali, and M. Edraki (2020), Transparency on greenhouse gas emissions from mining to enable climate change mitigation, *Nature Geoscience*, *13*(2), 100–104, doi:10.1038/s41561-020-0531-3.

Banerjee, A., et al. (2011), Deep permeable fault-controlled helium transport and limited mantle flux in two extensional geothermal systems in the Great Basin, United States, *Geology*, *39*(3), 195–198, doi: 10.1130/G31557.1.

Baskaran, M. (2016), Radon in Groundwater System, in *Radon: A Tracer for Geological, Geophysical and Geochemical Studies*, pp. 167–188, Springer International Publishing, doi:10.1007/978-3-319-21329-3_8.

Batista Cruz, R. Y., A. L. Rizzo, F. Grassa, R. Bernard Romero, A. González Fernández, T. G. Kretzschmar, and E. Gómez-Arias (2019), Mantle degassing through continental crust triggered by active faults: The case of the Baja California Peninsula, Mexico, *Geochemistry, Geophysics, Geosystems*, *20*(4), 1912–1936, doi:10.1029/2018GC007987.

Battaglia, A., et al. (2019), Insights Into the Mechanisms of Phreatic Eruptions From Continuous High Frequency Volcanic Gas Monitoring : Rincón de la Vieja, *Frontiers in Earth Science*, *6*(January), 1–20, doi:10.3389/feart.2018.00247.

Belin, R. E. (1959), Radon in the New Zealand geothermal regions, *Geochimica et Cosmochimica Acta*, *16*(1-3), 181–191, doi:10.1016/0016-7037(59)90053-5.

Bellani, S., A. Brogi, A. Lazzarotto, D. Liotta, and G. Ranalli (2004), Heat flow, deep temperatures and extensional structures in the Larderello Geothermal Field (Italy): Constraints on geothermal fluid flow, *Journal of Volcanology and Geothermal Research*, *132*(1), 15–29, doi:10.1016/S0377-0273(03)00418-9.

Belotti, C., F. Cuccoli, L. Facheris, and O. Vaselli (2003), An application of tomographic reconstruction of atmospheric CO2 over a volcanic site based on open-path IR laser measurements, *IEEE Transactions on Geoscience and Remote Sensing*, *41*(11), 2629–2637, doi:10.1109/TGRS.2003.815400.

Benediktsdóttir, Á., G. P. Hersir, A. M. Vilhjálmsson, A. Manzella, A. Santilano, and S. Held (2019), Final report on resistivity modelling and comparison with other SHGS, GEMex deliverable 5.2, *Tech. rep.*

Bennati, L., et al. (2011), Fluid circulation in a complex volcano-tectonic setting, inferred from self-potential and soil CO2 flux surveys: The Santa María-Cerro Quemado-Zunil volcanoes and Xela caldera (Northwestern Guatemala), *Journal of Volcanology and Geothermal Research*, *199*(3-4), 216–229, doi:10.1016/j.jvolgeores.2010.11.008.

Bense, V. F., T. Gleeson, S. E. Loveless, O. Bour, and J. Scibek (2013), Fault zone hydrogeology, *Earth-Science Reviews*, *127*, 171–192, doi:10.1016/j.earscirev.2013.09.008.

Bergfeld, D., F. Goff, and C. J. Janik (2001), Elevated carbon dioxide flux at the Dixie Valley geothermal field, Nevada; relations between surface phenomena and the geothermal reservoir, *Chemical Geology*, *177*(1-2), 43–66, doi:10.1016/S0009-2541(00)00381-8.

Bernard, R., Y. Taran, M. Pennisi, E. Tello, and A. Ramirez (2011), Chloride and Boron behavior in fluids of Los Humeros geothermal field (Mexico): A model based on the existence of deep acid brine, *Applied Geochemistry*, *26*(12), 2064–2073, doi:10.1016/j.apgeochem.2011.07.004.

Bertrami, R., G. Buonasorte, A. Ceccarelli, S. Lombardi, S. Pieri, and G. Scandiffio (1990), Soil gases in geothermal prospecting: two case histories (Sabatini Volcanoes and Alban Hills, Latium, central Italy), *Journal of Geophysical Research*, *95*(B13), doi:10.1029/jb095ib13p21475.

Bibby, H., G. Dawson, H. Rayner, S. Bennie, and C. Bromley (1992), Electrical resistivity and magnetic investigations of the geothermal systems in the Rotorua area, New Zealand, *Geothermics*, *21*(1-2), 43–64, doi:10.1016/0375-6505(92)90067-J.

Bibby, H., S. Bennie, V. Stagpoole, and T. Caldwell (1994), Resistivity structure of the Waimangu, Waiotapu, Waikite and Reporoa geothermal areas, New Zealand, *Geothermics*, *23*(5-6), 445–471, doi:10.1016/0375-6505(94)90013-2.

Bibby, H. M., T. G. Caldwell, F. J. Davey, and T. H. Webb (1995), Geophysical evidence on the structure of the Taupo Volcanic Zone and its hydrothermal circulation, *Journal of Volcanology and Geothermal Research*, *68*(1-3), 29–58, doi:10.1016/0377-0273(95)00007-H.

Biggs, J., I. D. Bastow, D. Keir, and E. Lewi (2011), Pulses of deformation reveal frequently recurring shallow magmatic activity beneath the main ethiopian rift, *Geochemistry, Geophysics, Geosystems*, *12*, doi:10.1029/2011GC003662.

Bignall, G., A. Rae, and M. Rosenberg (2010), Rationale for Targeting Fault Versus Formation-Hosted Permeability in High-Temperature Geothermal Systems of the Taupo Volcanic Zone, New Zealand, in *Proceedings World Geothermal Congress*, vol. 5, pp. 25–29.

Bloomberg, S., C. Werner, C. Rissmann, A. Mazot, T. Horton, D. Gravley, B. Kennedy, and C. Oze (2014), Soil CO2 emissions as a proxy for heat and mass flow assessment, Taupō Volcanic Zone, New Zealand, *Geochemistry, Geophysics, Geosystems*, *15*(12), 4885–4904, doi:https://doi.org/10.1002/2014GC005327.

Bloomberg, S., et al. (2012), Soil gas flux exploration at the Rotokawa Geothermal field and White Island, New Zealand, in *36th Workshop on Geothermal Reservoir Engineering Standford University, Standford, California*, January, pp. 1–11, doi:10.1016/j.neucom.2012.04.020.

Boccaletti, M., M. Bonini, R. Mazzuoli, B. Abebe, L. Piccardi, and L. Tortorici (1998), Quaternary oblique extensional tectonics in the ethiopian rift (horn of africa), *Tectonophysics*, *287*, doi:10.1016/S0040-1951(98)80063-2.

Bodvarsson, G. (1989), Some theoretical and field aspects of reinjection in geothermal reservoirs, *Water Resources Research*, *25*(6), 1235–1248.

Bödvarsson, G., and C. Tsang (1982), Injection and thermal breakthrough in fractures geothermal reservoirs, *Journal of Geophysical Research*, *87*(B2), 1031–1048.

Boudoire, G., et al. (2018), Small-scale spatial variability of soil CO2 flux: Implication for monitoring strategy, *Journal of Volcanology and Geothermal Research*, *366*, 13–26, doi:10.1016/j.jvolgeores.2018.10.001.

Braddock, M., J. Biggs, I. M. Watson, W. Hutchison, D. M. Pyle, and T. A. Mather (2017), Satellite observations of fumarole activity at aluto volcano, ethiopia: Implications for geothermal monitoring and volcanic hazard, *Journal of Volcanology and Geothermal Research*, *341*, doi:10.1016/j.jvolgeores.2017.05.006.

Brune, S., S. E. Williams, and R. D. Müller (2017), Potential links between continental rifting, CO2 degassing and climate change through time, *Nature Geoscience*, *10*(12), 941–946, doi:10.1038/s41561-017-0003-6.

Buttitta, D., A. Caracausi, L. Chiaraluce, R. Favara, M. Gasparo Morticelli, and A. Sulli (2020), Continental degassing of helium in an active tectonic setting (northern Italy): the role of seismicity, *Scientific Reports*, *10*(1), 1–13, doi:10.1038/s41598-019-55678-7.

Caine, J. S., J. P. Evans, and C. B. Forster (1996), Fault zone architecture and permeability structure, *Geology*, *24*(11), 1025–1028.

Camarda, M., S. De Gregorio, R. Favara, and S. Gurrieri (2007), Evaluation of carbon isotope fractionation of soil CO2 under an advective-diffusive regimen: A tool for computing the isotopic composition of unfractionated deep source, *Geochimica et Cosmochimica Acta*, *71*(12), 3016–3027, doi:10.1016/j.gca.2007.04.002.

Camarda, M., S. De Gregorio, R. Di Martino, R. Favara, and V. Prano (2020), Relationship between soil CO2 flux and tectonic structures in SW Sicily, *Annals of Geophysics*, *63*, doi:10.4401/ag-8264.

Campos-Enriquez, J., and V. H. Garduño-Monroy (1987), The shallow structure of Los Humeros and Las Derrumbadas geothermal fields, Mexico, *Geothermics*, *16*(5-6), 539–554, doi:10.1016/0375-6505(87)90038-1.

Campos-Enriquez, J. O., and J. J. Arredondo-Fragoso (1992), Gravity study of Los Humeros caldera complex, Mexico: Structure and associated geothermal system, *Journal of Volcanology and Geothermal Research*, *49*(1-2), 69–90, doi:10.1016/0377-0273(92)90005-X.

Cannata, A., G. Giudice, S. Gurrieri, P. Montalto, S. Alparone, G. Di Grazia, R. Favara, S. Gresta, and M. Liuzzo (2010), Relationship between soil CO2 flux and volcanic tremor at Mt. Etna: Implications for magma dynamics, *Environmental Earth Sciences*, *61*(3), 477–489, doi:10.1007/s12665-009-0359-z.

Carapezza, M., et al. (2011), Diffuse CO2 soil degassing and CO2 and H2S concentrations in air and related hazards at Vulcano Island (Aeolian arc, Italy), *Journal of Volcanology and Geothermal Research*, *207*(3-4), 130–144, doi:10.1016/j.jvolgeores.2011.06.010.

Carapezza, M. L., and D. Granieri (2004), Co2 soil flux at vulcano (italy): comparison between active and passive methods, *Applied Geochemistry*, *19*(1), 73–88, doi:10.1016/S0883-2927(03)00111-2.

Carapezza, M. L., T. Ricci, M. Ranaldi, and L. Tarchini (2009), Active degassing structures of Stromboli and variations in diffuse CO2 output related to the volcanic activity, *Journal of Volcanology and Geothermal Research*, *182*(3-4), 231–245, doi:10.1016/j.jvolgeores.2008.08.006.

Carapezza, M. L., M. Ranaldi, A. Gattuso, N. M. Pagliuca, and L. Tarchini (2015), The sealing capacity of the cap rock above the Torre Alfina geothermal reservoir (Central Italy) revealed by soil CO2 flux investigations, *Journal of Volcanology and Geothermal Research*, *291*, 25–34, doi:10.1016/j.jvolgeores.2014.12.011.

Cardellini, C., G. Chiodini, and F. Frondini (2003), Application of stochastic simulation to CO2 flux from soil: Mapping and quantification of gas release, *Journal of Geophysical Research: Solid Earth*, *108*(B9), doi:10.1029/2002JB002165.

Cardellini, C., G. Chiodini, F. Frondini, R. Avino, E. Bagnato, S. Caliro, M. Lelli, and A. Rosiello (2017), Monitoring diffuse volcanic degassing during volcanic unrests: the case of Campi Flegrei (Italy), *Scientific Reports*, *7*(1), 6757, doi:10.1038/s41598-017-06941-2.

Carrasco-Núñez, G., J. Hernández, L. De León, P. Dávila-Harris, G. Norini, J. P. Bernal, B. Jicha, M. Navarro, and P. López-Quiroz (2017a), Geologic Map of Los Humeros volcanic complex and geothermal field, eastern Trans-Mexican Volcanic Belt, *Terra Digitalis*, *1*(2), 1–11, doi:10.22201/igg.terradigitalis.2017.2.24.78.

Carrasco-Núñez, G., M. López-Martínez, J. Hernández, and V. Vargas (2017b), Subsurface stratigraphy and its correlation with the surficial geology at Los Humeros geothermal field, eastern Trans-Mexican Volcanic Belt, *Geothermics*, *67*, 1–17, doi:10.1016/j.geothermics.2017.01.001.

Carrasco-Núñez, G., J. P. Bernal, P. Davila, B. Jicha, G. Giordano, and J. Hernandez (2018), Reappraisal of Los Humeros Volcanic Complex by new U/Th Zircon and 40Ar/39Ar dating: Implications for greater geothermal potential, *Geochemistry, Geopysics, Geosystems*, *19*, 132–149, doi:10.1002/2017GC007044.

Carroll, M., and J. Halloway (1994), *Volatiles in Magmas*, 517 pp., Mineralogical Society of America.

Caudron, C., A. Mazot, and A. Bernard (2012), Carbon dioxide dynamics in kelud volcanic lake, *Journal of Geophysical Research: Solid Earth*, *117*, doi:10.1029/2011JB008806.

Cavazos-Álvarez, J. A., and G. Carrasco-Núñez (2020), Anatomy of the Xáltipan ignimbrite at Los Humeros Volcanic Complex ; the largest eruption of the Trans-Mexican Volcanic Belt, *Journal of Volcanology and Geothermal Research*, *392*, 106,755, doi:10.1016/j.jvolgeores.2019.106755.

Chatterjee, S., C. Deering, G. Waite, C. Prandi, and P. Lin (2019), An adaptive sampling strategy developed for studies of diffuse volcanic soil gas emissions, *Journal of Volcanology and Geothermal Research*, doi: 10.1016/j.jvolgeores.2019.06.006.

Chen, J. (2011), Compact laser-spectroscopic gas sensors using vertical-cavity surface emitting lasers, Ph.D. thesis, Technische Universität München.

Chester, F. M., and J. M. Logan (1986), Implications for mechanical properties of brittle faults from observations of the Punchbowl fault zone, California, *pure and applied geophysics*, *124*(1), 79–106, doi:10.1007/BF00875720.

Chianese, D., C. Rotz, and T. Richard (2009), Simulation of carbon dioxide emissions from dairy farms to assess greenhouse gas reduction strategies, *Transactions of the ASABE*, *52*(4), 1301–1312.

Chiodini, G., F. Frondini, and F. Ponziani (1995), Deep structures and carbon dioxide degassing in Central Italy, *Geothermics*, *24*(1), 81–94, doi:10.1016/0375-6505(94)00023-6.

Chiodini, G., R. Cioni, M. Guidi, B. Raco, and L. Marini (1998), Soil CO2 flux measurements in volcanic and geothermal areas, *Applied Geochemistry*, *13*(5), 543–552, doi:10.1016/S0883-2927(97)00076-0.

Chiodini, G., C. Cardellini, A. Amato, E. Boschi, S. Caliro, F. Frondini, and G. Ventura (2004), Carbon dioxide Earth degassing and seismogenesis in central and southern Italy, *Geophysical Research Letters*, *31*(7), 1–4, doi:10.1029/2004GL019480.

Chiodini, G., A. Baldini, F. Barberi, M. L. Carapezza, C. Cardellini, F. Frondini, D. Granieri, and M. Ranaldi (2007), Carbon dioxide degassing at Latera caldera (Italy): Evidence of geothermal reservoir and evaluation of its potential energy, *Journal of Geophysical Research: Solid Earth*, *112*(12), 1–17, doi:10.1029/2006JB004896.

Chiodini, G., S. Caliro, C. Cardellini, R. Avino, D. Granieri, and A. Schmidt (2008), Carbon isotopic composition of soil CO2 efflux, a powerful method to discriminate different sources feeding soil CO2 degassing in volcanic-hydrothermal areas, *Earth and Planetary Science Letters*, *274*(3-4), 372–379, doi:10.1016/j.epsl.2008.07.051.

Chiodini, G., C. Cardellini, F. Di Luccio, J. Selva, F. Frondini, S. Caliro, A. Rosiello, G. Beddini, and G. Ventura (2020), Correlation between tectonic CO2 Earth degassing and seismicity is revealed by a 10-year record in the Apennines, Italy, *Science Advances*, *6*(35), eabc2938, doi:10.1126/sciadv.abc2938.

Chiodini, G., et al. (2015), Carbon dioxide diffuse emission and thermal energy release from hydrothermal systems at Copahue-Caviahue Volcanic Complex (Argentina), *Journal of Volcanology and Geothermal Research*, *304*, 294–303, doi:10.1016/j.jvolgeores.2015.09.007.

Christenson, B. W., S. White, K. Britten, and B. J. Scott (2017), Hydrological evolution and chemical structure of a hyper-acidic spring-lake system on Whakaari/White Island, NZ, *Journal of Volcanology and Geothermal Research*, *346*, 180–211, doi:10.1016/j.jvolgeores.2017.06.017.

Ciais, P., et al. (1995), Partitioning of ocean and land uptake of CO2 as inferred by carbon isotopic measurements from the NOAA Climate Monitoring and Diagnostics Laboratory Global Air Sampling Network, *Journal of Geophysical Research*, *100*(94), 5051–5070.

Cigolini, C., M. Laiolo, and D. Coppola (2007), Earthquake–volcano interactions detected from radon degassing at Stromboli (Italy), *Earth and Planetary Science Letters*, *257*(3-4), 511–525, doi:10.1016/j.epsl.2007.03.022.

Ciotoli, G., M. Guerra, S. Lombardi, and E. Vittori (1998), Soil gas survey for tracing seismogenic faults: A case study in the Fucino Basin, central Italy, *Journal of Geophysical Research: Solid Earth*, *103*(B10), 23,781–23,794, doi:https://doi.org/10.1029/98JB01553.

Clark, R. H., J. W. Cole, I. A. Nairn, and C. P. Wood (1979), Magmatic eruption of White Island volcano, New Zealand, December 1976–April 1977, *New Zealand Journal of Geology and Geophysics*, *22*(2), 175–190, doi:10.1080/00288306.1979.10424217.

Cole, J. W., T. Thordarson, and R. M. Burt (2000), Magma Origin and Evolution of White Island (Whakaari) Volcano, Bay of Plenty, New Zealand, *Journal of Petrology*, *41*(6), 867–895, doi:10.1093/petrology/41.6.867.

Corti, G. (2009), Continental rift evolution: From rift initiation to incipient break-up in the main ethiopian rift, east africa, *Earth-Science Reviews*, *96*, doi:10.1016/j.earscirev.2009.06.005.

Cuccoli, F., L. Facheris, O. Vasselli, and F. Tassi (2007), Five years measurements of CO2 air concentrations by DSA IR laser devices. Results and perspectives for laser remote sensing systems of gas emissions by critical areas, in *Geoscience and Remote Sensing Symposium*, pp. 4280–4283.

Curewitz, D., and J. A. Karson (1997), Structural settings of hydrothermal outflow: Fracture permeability maintained by fault propagation and interaction, *Journal of Volcanology and Geothermal Research*, *79*(3-4), 149–168, doi:10.1016/S0377-0273(97)00027-9.

D'Amore, F., and A. H. Truesdell (1988), A review of solubilities and equilibrium constants for gaseous species of geothermal interest., *Sciences Géologiques. Bulletin*, *41*(3), 309–332, doi:10.3406/sgeol.1988.1801.

Darling, W., B. Gizaw, and M. K. Arusei (1996), Lake-groundwater relationships and fluid-rock interaction in the east african rift valley: isotopic evidence, *Journal of African Earth Sciences*, *22*, doi:10.1016/0899-5362(96)00026-7.

Daskalopoulou, K., A. L. Gagliano, S. Calabrese, L. Li Vigni, M. Longo, K. Kyriakopoulos, G. Pecoraino, and W. D'Alessandro (2019), Degassing at the Volcanic/Geothermal System of Kos (Greece): Geochemical Characterization of the Released Gases and CO2 Output Estimation , *Geofluids*, *2019*, 1–16, doi:10.1155/2019/3041037.

David, M. (1977), *Geostatistical ore reserve estimation. Developments in geomathematics 2*, Elsevier, Amsterdam.

Davidson, J. R. J., J. Fairley, A. Nicol, D. Gravley, and U. Ring (2016), The origin of radon anomalies along normal faults in an active rift and geothermal area, *Geosphere*, *12*(5), 1656–1669, doi:10.1130/GES01321.1.

Dávila-Harris, P., and G. Carrasco-Núñez (2014), An unusual syn-eruptive bimodal eruption: The Holocene Cuicuiltic Member at Los Humeros caldera, Mexico, *Journal of Volcanology and Geothermal Research*, *271*, 24–42, doi:10.1016/j.jvolgeores.2013.11.020.

De Natale, P., L. Gianfrani, and G. De Natale (2001), Optical methods for monitoring of volcanoes: Techniques and new perspectives, *Journal of Volcanology and Geothermal Research*, *109*(1-3), 235–245, doi:10.1016/S0377-0273(00)00314-0.

De Rosa, M., G. Gagliardi, A. Rocco, R. Somma, P. De Natale, and G. De Natale (2007), Continuous in situ measurements of volcanic gases with a diode-laser-based spectrometer: CO2 and H2O concentration and soil degassing at Vulcano (Aeolian islands: Italy), *Geochemical Transactions*, *8*(1), 5, doi:10.1186/1467-4866-8-5.

Deutsch, C., and A. Journel (1998), *Geostatistical Software Library and User's Guide*, Oxford University Press, New York, doi:DOI:https://doi.org/10.1017/S0016756899531774.

Di Paola, G. M. (1972), The Ethiopian Rift Valley (between 7° 00' and 8° 40' lat. north), *Bulletin Volcanologique*, *36*(4), 517–560, doi:10.1007/BF02599823.

Diaz, A. R., E. Kaya, and S. J. Zarrouk (2016), Reinjection in geothermal fields - A worldwide review update, *Renewable and Sustainable Energy Reviews*, *53*, 105–162, doi:10.1016/j.rser.2015.07.151.

DiPippo, R. (2007), *Geothermal Power Plants. Principles, Applications, Case Studies and Environmental Impact*, 2nd ed., 520 pp., Elsevier.

DiPippo, R. (2016), *Geothermal power generation: Developments and Innovation*, 854 pp., Woodhead Publishing.

Dlugokencky, E., and P. Tans (2020), Trends in atmospheric carbon dioxide, *www.gml.noaa.gov/ccgg/trends*, (Accessed: 05.05.2021).

Duddridge, G. A., P. Grainger, and E. M. Durrance (1991), Fault detection using soil gas geochemistry, *Quarterly Journal of Engineering Geology and Hydrogeology*, *24*(4), 427–435, doi:10.1144/GSL.QJEG.1991.024.04.09.

Ebinger, C., and M. Casey (2001), Continental breakup in magmatic provinces: An ethiopian example, *Geology*, *29*, doi:10.1130/0091-7613(2001)029<0527:CBIMPA>2.0.CO;2.

Edmonds, M., and P. J. Wallace (2017), Volatiles and exsolved vapor in volcanic systems, *Elements*, *13*(1), 29–34, doi:10.2113/gselements.13.1.29.

Elders, W. A., G. M. Izquierdo, A. Alfonso, R. A. Tovar, and M. A. Flores (2014), Significance of deep zones of intense bleaching and silicification in the Los Humeros high-temperature geothermal field, Mexico: Evidence of the effects of acid alteration, *Transactions - Geothermal Resources Council*, *38*, 497–502.

Erees, F. S., G. Yener, M. Salk, and Ö. Özbal (2006), Measurements of radon content in soil gas and in the thermal waters in Western Turkey, *Radiation Measurements*, *41*(3), 354–361, doi:10.1016/j.radmeas.2005.06.030.

Espinosa-Paredes, G., and A. Garcia-Gutierrez (2003), Estimation of static formation temperatures in geothermal wells, *Energy Conversion and Management*, *44*(8), 1343–1355, doi:10.1016/S0196-8904(02)00117-6.

Etiope, G., and R. W. Klusman (2010), Microseepage in drylands: Flux and implications in the global atmospheric source/sink budget of methane, *Global and Planetary Change*, *72*(4), 265–274, doi:10.1016/j.gloplacha.2010.01.002.

Etiope, G., and G. Martinelli (2002), Migration of carrier and trace gases in the geosphere: an overview, *Physics of the Earth and Planetary Interiors*, *129*(3-4), 185–204, doi:10.1016/S0031-9201(01)00292-8.

Fairley, J. P., and J. J. Hinds (2004a), Field observation of fluid circulation patterns in a normal fault system, *Geophysical Research Letters*, *31*(19), L19,502 1–4, doi:10.1029/2004GL020812.

Fairley, J. P., and J. J. Hinds (2004b), Rapid transport pathways for geothermal fluids in an active Great Basin fault zone, (9), 825–828, doi:10.1130/G20617.1.

Faulds, J. E., and N. H. Hinz (2015), Favorable Tectonic and Structural Settings of Geothermal Systems in the Great Basin Region , Western USA: Proxies for Discovering Blind Geothermal Systems, in *World Geothermal Congress, Melbourne, Australia*, April, pp. 1–6.

Faulds, J. E., et al. (2018), Discovery of a blind geothermal system in southern Gabbs Valley, western Nevada, through application of the play fairway analysis at multiple scales, *Transactions - Geothermal Resources Council*, *42*, 452–465.

Federico, C., M. Liuzzo, G. Giudice, G. Capasso, A. Pisciotta, and M. Pedone (2019), Variations in CO2 emissions at a mud volcano at the southern base of Mt Etna: are they due to volcanic activity interference or a geyser-like mechanism?, *Bulletin of Volcanology*, *81*(2), doi:10.1007/s00445-018-1261-x.

Ferriz, H., and G. A. Mahood (1984), Eruption rates and compositional trends at Los Humeros volcanic center, Puebla, Mexico., *Journal of Geophysical Research*, *89*(B10), 8511–8524, doi:10.1029/JB089iB10p08511.

Finizola, A., F. Sortino, J. F. Lénat, M. Aubert, M. Ripepe, and M. Valenza (2003), The summit hydrothermal system of Stromboli. New insights from self-potential, temperature, CO2 and fumarolic fluid measurements, with structural and monitoring implications, *Bulletin of Volcanology*, *65*(7), 486–504, doi:10.1007/s00445-003-0276-z.

Fischer, T. P., and G. Chiodini (2015), Volcanic, Magmatic and Hydrothermal Gases, in *The Encyclopedia of Volcanoes*, 2nd ed. ed., pp. 779–797, Elsevier, doi:10.1016/B978-0-12-385938-9.00045-6.

Fontijn, K., K. McNamara, A. Z. Tadesse, D. M. Pyle, F. Dessalegn, W. Hutchison, T. A. Mather, and G. Yirgu (2018), Contrasting styles of post-caldera volcanism along the main ethiopian rift: Implications for contemporary volcanic hazards, *Journal of Volcanology and Geothermal Research*, *356*, doi:10.1016/j.jvolgeores.2018.02.001.

Forde, O. N., A. G. Cahill, R. D. Beckie, and K. U. Mayer (2020), Barometric-pumping controls fugitive gas emissions from a vadose zone natural gas release, *Scientific Reports*, (November 2018), 1–9, doi:10.1038/s41598-019-50426-3.

Fossen, H. (2010), *Faults*, pp. 151–188, Cambridge University Press, doi:10.1017/CBO9780511777806.010.

Fournier, N., and L. Chardot (2012), Understanding volcano hydrothermal unrest from geodetic observations: Insights from numerical modeling and application to White Island volcano, New Zealand, *Journal of Geophysical Research: Solid Earth*, *117*(B11), doi:https://doi.org/10.1029/2012JB009469.

Francis, P., and C. Oppenheimer (2004), *Volcanoes*, 2nd ed., Oxford University Press, New York, United States.

Fridriksson, T., B. R. Kristjánsson, H. Ármannsson, E. Margrétardóttir, S. Ólafsdóttir, and G. Chiodini (2006), CO2 emissions and heat flow through soil, fumaroles, and steam heated mud pools at the Reykjanes geothermal area, SW Iceland, *Applied Geochemistry*, *21*(9), 1551–1569, doi:10.1016/j.apgeochem.2006.04.006.

Fridriksson, T., E. Padrón, F. Óskarsson, and N. M. Pérez (2016), Application of diffuse gas flux measurements and soil gas analysis to geothermal exploration and environmental monitoring: Example from the Reykjanes geothermal field, SW Iceland, *Renewable Energy*, *86*, 1295–1307, doi:10.1016/j.renene.2015.09.034.

Friedlingstein, P., et al. (2020), Global Carbon Budget 2020, *Earth System Science Data*, *12*(4), 3269–3340, doi:10.5194/essd-12-3269-2020.

Frondini, F., S. Caliro, C. Cardellini, G. Chiodini, and N. Morgantini (2009), Carbon dioxide degassing and thermal energy release in the Monte Amiata volcanic-geothermal area (Italy), *Applied Geochemistry*, *24*(5), 860–875, doi:10.1016/j.apgeochem.2009.01.010.

Frondini, F., C. Cardellini, S. Caliro, G. Beddini, A. Rosiello, and G. Chiodini (2018), Measuring and interpreting CO 2 fluxes at regional scale: the case of the Apennines, Italy , *Journal of the Geological Society*, *176*(2), 408–416, doi:10.1144/jgs2017-169.

Fu, C. C., et al. (2017), Exploring the relationship between soil degassing and seismic activity by continuous radon monitoring in the Longitudinal Valley of eastern Taiwan, *Chemical Geology*, *469*, 163–175, doi: 10.1016/j.chemgeo.2016.12.042.

Gaucher, E., M. Schoenball, O. Heidbach, A. Zang, P. A. Fokker, J. D. Van Wees, and T. Kohl (2015), Induced seismicity in geothermal reservoirs: A review of forecasting approaches, *Renewable and Sustainable Energy Reviews*, *52*(December 2017), 1473–1490, doi:10.1016/j.rser.2015.08.026.

Gebregzabher, Z. (1986), Hydrothermal alteration minerals in Aluto Langano geothermal wells, Ethiopia, *Geothermics*, *15*(5-6), 735–740, doi:10.1016/0375-6505(86)90086-6.

Giammanco, S., K. W. W. Sims, and M. Neri (2007), Measurements of 220 Rn and 222 Rn and CO2 emissions in soil and fumarole gases on Mt. Etna volcano (Italy): Implications for gas transport and shallow ground fracture, *Geochemistry, Geopysics, Geosystems*, *8*(10), 1–14, doi:10.1029/2007GC001644.

Gianelli, G., and M. Teklemariam (1993), Water-rock interaction processes in the Aluto-Langano geothermal field (Ethiopia), *Journal of Volcanology and Geothermal Research*, *56*(4), 429–445, doi:10.1016/0377-0273(93) 90007-E.

Giggenbach, W., H. Shinohara, M. Kusakabe, and T. Ohba (2003), Formation of acid volcanic brines through interaction of magmatic gases, seawater, and rock within the White Island volcanic-hydrothermal system, New Zealand, *Society of Economic Geologists*, *10*, 19–40.

Giggenbach, W. F. (1995), Variations in the chemical and isotopic composition of fluids discharged from the Taupo Volcanic Zone, New Zealand, *Journal of Volcanology and Geothermal Research*, *68*(1-3), 89–116, doi:10.1016/0377-0273(95)00009-J.

Gingrich, J. E. (1984), Radon as a geochemical exploration tool, *Journal of Geochemical Exploration*, *21*(1-3), 19–39, doi:10.1016/0375-6742(84)90032-3.

Gizaw, B. (1993), Aluto-Langano geothermal field, Ethiopian rift valley: Physical characteristics and the effects of gas on well performance, *Geothermics*, *22*(2), 101–116, doi:10.1016/0375-6505(93)90050-W.

Glover, R., L. Klyen, and Crump (1992), Spring chemistry of the Waikite-Puakohurea thermal area, in *Proceedings of the New Zealand Geothermal Workshop*, pp. 63–72.

Goerner, A., E. Jolie, and R. Gloaguen (2009), Non-climatic growth of the saline Lake Beseka, Main Ethiopian Rift, *Journal of Arid Environments*, *73*(3), doi:10.1016/j.jaridenv.2008.09.015.

González-Partida, E., R. M. Barragán, and D. Nieva-G (1993), Análisis geoquímico-isotópico de las especies carbónicas del fluido geotérmico de Los Humeros, Puebla, México, *Geofísica Internacional*, *32*, 299–309.

Graham, D. W. (2002), Noble Gas Isotope Geochemistry of Mid-Ocean Ridge and Ocean Island Basalts: Characterization of Mantle Source Reservoirs, *Reviews in Mineralogy and Geochemistry*, *47*(1), 247–317, doi:10.2138/rmg.2002.47.8.

Graham, D. W. (2008), Noble Gas Isotope Geochemistry of Mid-Ocean Ridge and Ocean Island Basalts: Characterization of Mantle Source Reservoirs, *Reviews in Mineralogy and Geochemistry*, *47*(1), 247–317, doi:10.2138/rmg.2002.47.8.

Granieri, D., M. L. Carapezza, G. Chiodini, R. Avino, S. Caliro, M. Ranaldi, T. Ricci, and L. Tarchini (2006), Correlated increase in CO2 fumarolic content and diffuse emission from la Fossa crater (Vulcano, Italy): Evidence of volcanic unrest or increasing gas release from a stationary deep magma body?, *Geophysical Research Letters*, *33*(13), 2–5, doi:10.1029/2006GL026460.

Granieri, D., R. Avino, and G. Chiodini (2010), Carbon dioxide diffuse emission from the soil: ten years of observations at Vesuvio and Campi Flegrei (Pozzuoli), and linkages with volcanic activity, *Bulletin of Volcanology*, *72*(1), 103, doi:10.1007/s00445-009-0304-8.

Granieri, D., G. Chiodini, R. Avino, and S. Caliro (2014), Carbon dioxide emission and heat release estimation for Pantelleria Island (Sicily, Italy), *Journal of Volcanology and Geothermal Research*, *275*, 22–33, doi: 10.1016/j.jvolgeores.2014.02.011.

Grant, M., I. Donaldson, and P. Bixley (1982), *Geothermal Reservoir Engineering*, 370 pp., Academic Press, New York.

Grindley, G. (1963), Geology and structure of Waiotapu geothermal field, *In Waiotapu Geothermal Field. NZ Department of Scientific and Industrial Research Bulletin*, *155*, 10–25.

Gunnarsson, I., E. S. Aradóttir, and B. Sigfússon (2014), Geothermal Gas Emission From Hellisheiði and Nesjavellir Power Plants , Iceland, *37*.

Gutiérrez-Negrín, L. C. A. (2019), Current status of geothermal-electric production in Mexico, in *IOP Conf. Series: Earth and Environmental Science 249 (012017)*, doi:10.1088/1755-1315/249/1/012017.

Gutierrez-Negrin, L. C. A., and G. Izquierdo-Montalvo (2010), Review and Update of the Main Features of the Los Humeros Geothermal Field, Mexico, in *Proceedings World Geothermal Congress 2010 Bali, Indonesia, 25–29 April 2010*, pp. 1–7.

Hanson, M. C., C. Oze, and T. W. Horton (2014), Identifying blind geothermal systems with soil CO2 surveys, *Applied Geochemistry*, *50*, 106–114, doi:10.1016/j.apgeochem.2014.08.009.

Harvey, M. C., K. Britten, and L. Schwendenmann (2014), A review of approaches to distinguish between biological and geothermal soil diffuse CO2 flux ., in *New Zealand Geothermal Workshop 2014, Auckland, New Zealand*.

Healy, J. (1974), Waiotapu geothermal field: Minerals of New Zealand (Part D-Geothermal Resources) Report NZGS 38D., *Tech. rep.*, NZ Geological Survey, Rotorua, NZ.

Hedenquist, J. W., and P. R. Browne (1989), The evolution of the Waiotapu geothermal system, New Zealand, based on the chemical and isotopic composition of its fluids, minerals and rocks, *Geochimica et Cosmochimica Acta*, *53*(9), 2235–2257, doi:10.1016/0016-7037(89)90347-5.

Hedenquist, J. W., and R. W. Henley (1985), Hydrothermal eruptions in the Waiotapu geothermal system, New Zealand: their origin, associated breccias, and relation to precious metal mineralization., *Economic Geology*, *80*(6), 1640–1668, doi:10.2113/gsecongeo.80.6.1640.

Henley, R. W., and A. J. Ellis (1983), Geothermal systems ancient and modern: a geochemical review, *Earth Science Reviews*, *19*(1), 1–50, doi:10.1016/0012-8252(83)90075-2.

Hernández, P., N. Pérez, J. Salazar, M. Reimer, K. Notsu, and H. Wakita (2004), Radon and helium in soil gases at Cañadas caldera, Tenerife, Canary Islands, Spain, *Journal of Volcanology and Geothermal Research*, *131*(1-2), 59–76, doi:10.1016/S0377-0273(03)00316-0.

Hernández, P. A., J. M. Salazar, Y. Shimoike, T. Mori, K. Notsu, and N. Pérez (2001), Diffuse emission of CO2 from Miyakejima volcano, Japan, *Chemical Geology*, *177*(1-2), 175–185, doi:10.1016/S0009-2541(00)00390-9.

Hernández, P. A., et al. (2012), Diffuse volcanic degassing and thermal energy release from Hengill volcanic system, Iceland, *Bulletin of Volcanology*, *74*(10), 2435–2448, doi:10.1007/s00445-012-0673-2.

Hilton, D. R., T. P. Fischer, and B. Marty (2002), 9 Noble Gases and Volatile Recycling at Subduction Zones, doi:10.2138/rmg.2002.47.9.

Hochstein, M. P. (1988), Assessment and modelling of geothermal reservoirs (small utilization schemes), *Geothermics*, *17*(1), 15–49, doi:https://doi.org/10.1016/0375-6505(88)90004-1.

Hochstein, M. P., B. Oluma, and H. Hole (2017), Early exploration of the Aluto geothermal field, Ethiopia (History of discovery well LA-3), *Geothermics*, *66*, 73–84, doi:10.1016/j.geothermics.2016.11.010.

Hoefs, J. (2004), *Stable Isotope Geochemistry*, 5th, compl ed., 244 pp., Springer Berlin Heidelberg.

Hoefs, J. (2009), Geochemical fingerprints: a critical appraisal, *European Journal of Mineralogy*, *22*(1), 3–15, doi:10.1127/0935-1221/2010/0022-1997.

Horne, R. (1985), Reservoir engineering aspects of reinjection, *Geothermics*, *14*(2), 449–457.

Hu, L., Q. Jianjun, and W. Ligang (2008), Characterization of farmland soil respiration and modeling analysis of contribution of root respiration, *Transactions of the Chinese Society of Agricultural Engineering*, *4*.

Hunt, J. A., A. Zafu, T. A. Mather, D. M. Pyle, and P. H. Barry (2017), Spatially Variable CO2 Degassing in the Main Ethiopian Rift: Implications for Magma Storage, Volatile Transport, and Rift-Related Emissions, *Geochemistry, Geophysics, Geosystems*, *18*(10), 3714–3737, doi:10.1002/2017GC006975.

Hurst, T., W. Heise, S. Hreinsdottir, and I. Hamling (2016), Geophysics of the Taupo Volcanic Zone: A review of recent developments, *Geothermics*, *59*, 188–204, doi:10.1016/j.geothermics.2015.09.008.

Hutchison, W., T. A. Mather, D. M. Pyle, J. Biggs, and G. Yirgu (2015), Structural controls on fluid pathways in an active rift system: A case study of the aluto volcanic complex, *Geosphere*, *11*, doi:10.1130/GES01119.1.

Hutchison, W., D. M. Pyle, T. A. Mather, G. Yirgu, J. Biggs, B. E. Cohen, D. N. Barfod, and E. Lewi (2016a), The eruptive history and magmatic evolution of aluto volcano: new insights into silicic peralkaline volcanism in the ethiopian rift, *Journal of Volcanology and Geothermal Research*, *328*, doi:10.1016/j.jvolgeores.2016.09.010.

Hutchison, W., et al. (2016b), Causes of unrest at silicic calderas in the east african rift: New constraints from insar and soil-gas chemistry at aluto volcano, ethiopia, *Geochemistry, Geophysics, Geosystems*, *17*, doi:10.1002/2016GC006395.

Hutchison, W., et al. (2016c), A pulse of mid-pleistocene rift volcanism in ethiopia at the dawn of modern humans, *Nature Communications*, *7*, doi:10.1038/ncomms13192.

Huttrer, G. W. (2020), Geothermal Power Generation in the World 2015-2020 Update Report, in *Proceedings World Geothermal Congress 2020 Reykjavik, Iceland, April 26 – May 2, 2020*, pp. 1–17.

Iddon, F., C. Jackson, W. Hutchison, K. Fontijn, D. M. Pyle, T. A. Mather, G. Yirgu, and M. Edmonds (2019), Mixing and crystal scavenging in the main ethiopian rift revealed by trace element systematics in feldspars and glasses, *Geochemistry, Geophysics, Geosystems*, *20*, doi:10.1029/2018GC007836.

Iglesias, E. R., M. Flores-Armenta, R. J. Torres, M. Ramirez-Montes, N. Reyes-Picaso., and I. Cruz-Grajales (2015), Tracer testing at Los Humeros, Mexico, High-enthalpy geothermal field, in *Proceedings World Geothermal Congress 2015, Melbourne, Australia, 19-25 April 2015*.

Inguaggiato, S., F. Vita, M. Cangemi, A. Mazot, A. Sollami, L. Calderone, S. Morici, and M. P. Jacome (2017), Stromboli volcanic activity variations inferred from observations of fluid geochemistry: 16 years of continuous monitoring of soil CO2 fluxes (2000 – 2015), *Chemical Geology*, *469*, 69–84, doi:10.1016/j.chemgeo.2017.01.030.

IPCC (2013), *Climate Change 2013: The Physical Science Basis. Contribution of Working Group I to the Fifth Assessment Report of the Intergovernmental Panel on Climate Change*, 1535 pp pp., Cambridge University Press.

IRENA (2020), *Renewable Energy Statistics 2020*, 408 pp.

Isaaks, E. D., and R. M. Srivastava (1989), *An Introduction to Applied Geostatistics*, 561 pp., Oxford University Press, New York.

Jafari, A., and T. Babadagli (2011), Effective fracture network permeability of geothermal reservoirs, *Geothermics*, *40*(1), 25–38, doi:10.1016/j.geothermics.2010.10.003.

Jentsch, A., E. Jolie, D. G. Jones, H. Taylor-curran, L. Peiffer, M. Zimmer, and B. Lister (2020), Magmatic volatiles to assess permeable volcano-tectonic structures in the Los Humeros geothermal field , Mexico, *Journal of Volcanology and Geothermal Research*, *394*, 1–14, doi:10.1016/j.jvolgeores.2020.106820.

Jentsch, A., W. Duesing, E. Jolie, and M. Zimmer (2021), Monitoring the response of volcanic CO2 emissions to changes in the Los Humeros hydrothermal system., *Submitted for publication at Nature Scientific Reports.*

Jolie, E. (2019), Detecting gas-rich hydrothermal vents in Ngozi Crater Lake using integrated exploration tools, *Scientific Reports*, *9*(1), 12,164, doi:10.1038/s41598-019-48576-5.

Jolie, E., M. Klinkmueller, and I. Moeck (2015a), Diffuse surface emanations as indicator of structural permeability in fault-controlled geothermal systems, *Journal of Volcanology and Geothermal Research*, *290*, 97–113, doi:10.1016/j.jvolgeores.2014.11.003.

Jolie, E., I. Moeck, and J. E. Faulds (2015b), Quantitative structural-geological exploration of fault-controlled geothermal systems - A case study from the Basin-and-Range Province, Nevada (USA), *Geothermics*, *54*, 54–67, doi:10.1016/j.geothermics.2014.10.003.

Jolie, E., M. Klinkmueller, I. Moeck, and D. Bruhn (2016), Linking gas fluxes at Earth's surface with fracture zones in an active geothermal field, *Geology*, *44*(3), 187–190, doi:10.1130/G37412.1.

Jolie, E., W. Hutchison, D. Driba, A. Jentsch, and B. Gizaw (2019), Pinpointing Deep Geothermal Upflow in Zones of Complex Tectono-Volcanic Degassing: New Insights from Aluto Volcano, Main Ethiopian Rift, *Geochemistry, Geophysics, Geosystems*, *20*(8), 4146–4161, doi:10.1029/2019gc008309.

Jolie, E., et al. (2018), GEMex – A Mexican-European Research Cooperation on Development of Superhot and Engineered Geothermal Systems, in *43rd Workshop on Geothermal Reservoir Engineering, Stanford University, Standford, California*, pp. 1–10.

Jolie, E., et al. (2021), Geological controls on geothermal resources for power generation, *Nature Reviews Earth & Environment*, pp. 1–16.

Kamila, Z., E. Kaya, and S. J. Zarrouk (2021), Reinjection in geothermal fields: An updated worldwide review 2020, *Geothermics*, *89*(September 2020), 101,970, doi:10.1016/j.geothermics.2020.101970.

Karion, A., et al. (2013), Methane emissions estimate from airborne measurements over a western United States natural gas field, *Geophysical Research Letters*, *40*(16), 4393–4397, doi:10.1002/grl.50811.

Karlstrom, K. E., L. J. Crossey, D. R. Hilton, and P. H. Barry (2013), Mantle 3He and CO2 degassing in carbonic and geothermal springs of Colorado and implications for neotectonics of the Rocky Mountains, *Geology*, *41*(4), 495–498, doi:10.1130/G34007.1.

Kaya, E., and S. J. Zarrouk (2017), Reinjection of greenhouse gases into geothermal reservoirs, *International Journal of Greenhouse Gas Control*, *67*(November), 111–129, doi:10.1016/j.ijggc.2017.10.015.

Kaya, E., S. J. Zarrouk, and M. J. O. Sullivan (2011), Reinjection in geothermal fields : A review of worldwide experience, *Renewable and Sustainable Energy Reviews*, *15*(1), 47–68, doi:10.1016/j.rser.2010.07.032.

Kaya, E., M. J. O'Sullivan, and M. P. Hochstein (2014), A three dimensional numerical model of the Waiotapu, Waikite and Reporoa geothermal areas, New Zealand, *Journal of Volcanology and Geothermal Research*, *283*, 127–142, doi:10.1016/j.jvolgeores.2014.07.008.

Kaye, J. P., R. L. McCulley, and I. C. Burke (2005), Carbon fluxes, nitrogen cycling, and soil microbial communities in adjacent urban, native and agricultural ecosystems, *Global Change Biology*, *11*(4), 575–587, doi:https://doi.org/10.1111/j.1365-2486.2005.00921.x.

Kebede, S. (2012), Geothermal exploration and development in Ethiopia: status and future plan, in *Short Course VII on Exploration for Geothermal Resources*, pp. 1–16.

Kebede, S., T. Mamo, and T. Abebe (1985), Geological report and explanation to the geological map of Aluto-Langano geothermal area, *Tech. rep.*, Ethiopian Institute of Geological Surveys, Addis Ababa.

Keir, D., I. D. Bastow, G. Corti, F. Mazzarini, and T. O. Rooney (2015), The origin of along-rift variations in faulting and magmatism in the ethiopian rift, *Tectonics*, *34*, doi:10.1002/2014TC003698.

Kennedy, B. M., and M. C. van Soest (2006), A helium isotope perspective on the Dixie Valley, Nevada, hydrothermal system, *Geothermics*, *35*(1), 26–43, doi:10.1016/j.geothermics.2005.09.004.

Keppler, H., M. Wiedenbeck, and S. S. Shcheka (2003), Carbon solubility in olivine and the mode of carbon storage in the Earth's mantle, *Nature*, *424*(6947), 414–416, doi:10.1038/nature01828.

Kis, B. M., A. Ionescu, C. Cardellini, S. Harangi, C. Baciu, A. Caracausi, and F. Viveiros (2017), Quantification of carbon dioxide emissions of Ciomadul, the youngest volcano of the Carpathian-Pannonian Region (Eastern-Central Europe, Romania), *Journal of Volcanology and Geothermal Research*, doi:10.1016/j.jvolgeores.2017.05.025.

Klusman, R. W., J. N. Moore, and M. P. LeRoy (2000), Potential for surface gas flux measurements in exploration and surface evaluation of geothermal resources, *Geothermics*, *29*(6), 637–670, doi:10.1016/S0375-6505(00)00036-5.

Kohn, M. J. (2010), Carbon isotope compositions of terrestrial C3 plants as indicators of (paleo)ecology and (paleo)climate, *Proceedings of the National Academy of Sciences*, *107*(46), 19,691–19,695, doi:10.1073/pnas.1004933107.

Kristmannsdóttir, H., and H. Ármannsson (2003), Environmental aspects of geothermal energy utilization, *Geothermics*, *32*(4-6), 451–461, doi:10.1016/S0375-6505(03)00052-X.

Kämpf, H., K. Bräuer, J. Schumann, K. Hahne, and G. Strauch (2013), Co2 discharge in an active, non-volcanic continental rift area (czech republic): Characterisation (δ13c, 3he/4he) and quantification of diffuse and vent co2 emissions, *Chemical Geology*, *339*, 71–83, doi:https://doi.org/10.1016/j.chemgeo.2012.08.005, frontiers in Gas Geochemistry.

Laiolo, M., M. Ranaldi, L. Tarchini, M. L. Carapezza, D. Coppola, T. Ricci, and C. Cigolini (2016), The effects of environmental parameters on diffuse degassing at Stromboli volcano : Insights from joint monitoring of soil CO2 flux and radon activity, *Journal of Volcanology and Geothermal Research*, *315*, 65–78, doi:10.1016/j.jvolgeores.2016.02.004.

Lautze, N., D. Thomas, N. Hinz, G. Apuzen-Ito, N. Frazer, and D. Waller (2017), Play fairway analysis of geothermal resources across the State of Hawaii: 1. Geological, geophysical, and geochemical datasets, *Geothermics*, *70*, 376–392, doi:10.1016/j.geothermics.2017.02.001.

Lee, H., J. D. Muirhead, T. P. Fischer, C. J. Ebinger, S. A. Kattenhorn, Z. D. Sharp, and G. Kianji (2016), Massive and prolonged deep carbon emissions associated with continental rifting, *Nature Geoscience*, *9(2)*(January), 1–6, doi:10.1038/NGEO2622.

Lee, K. C. (2001), Classification of geothermal resources by exergy, *Geothermics*, *30*(4), 431–442, doi:10.1016/S0375-6505(00)00056-0.

Lelli, M., and R. Villanueva Alfaro Cuevas (2019), WP 4 – Tectonic control on fluid flow Task 4.3 – Final Report on geochemical characterization and origin of cold and thermal fluids, *Tech. rep.*

Lewicki, J., and S. Brantley (2000), CO<inf>2</inf> degassing along the San Andreas fault, Parkfield, California, *Geophysical Research Letters*, *27*(1), 5–8, doi:10.1029/1999GL008380.

Lewicki, J. L., and G. E. Hilley (2014), Multi-scale observations of the variability of magmatic CO2 emissions, Mammoth Mountain, CA, USA, *Journal of Volcanology and Geothermal Research*, *284*, 1–15, doi:10.1016/j.jvolgeores.2014.07.011.

Lewicki, J. L., and C. M. Oldenburg (2004), Strategies for detecting hidden geothermal systems by near-surface gas monitoring, *Lawrence Berkeley National Laboratory*, p. 48.

Lewicki, J. L., D. Bergfeld, C. Cardellini, G. Chiodini, D. Granieri, N. Varley, and C. Werner (2005), Comparative soil CO2 flux measurements and geostatistical estimation methods on Masaya volcano, Nicaragua, *Bulletin of Volcanology*, *68*, 76–90, doi:10.1007/s00445-005-0423-9.

Lewicki, J. L., J. Birkholzer, and C.-f. Tsang (2007), Natural and industrial analogues for leakage of CO2 from storage reservoirs: identification of features, events, and processes and lessons learned, *Environmental Geology*, *52*(3), 457–467, doi:10.1007/s00254-006-0479-7.

Li, J., and A. D. Heap (2014), Spatial interpolation methods applied in the environmental sciences: A review, *Environmental Modelling and Software*, *53*, 173–189, doi:10.1016/j.envsoft.2013.12.008.

Linnerud, I., P. Kaspersen, and T. Jæger (1998), Gas monitoring in the process industry using diode laser spectroscopy, *Applied Physics B: Lasers and Optics*, *67*(3), 297–305, doi:10.1007/s003400050509.

Liuzzo, M., S. Gurrieri, G. Giudice, G. Giuffrida, I. Nazionale, and S. Palermo (2013), Ten years of soil CO2 continuous monitoring on Mt. Etna: Exploring the relationship between processes of soil degassing and volcanic activity, *Geochemistry, Geophysics, Geosystems*, *14*(8), 2886–2899, doi:10.1002/ggge.20196.

Lloyd, E. F. (1959), The hot springs and hydrothermal eruptions of Waiotapu, *New Zealand Journal of Geology and Geophysics*, *2*(1), 141–176, doi:10.1080/00288306.1959.10431319.

Lloyd, R., J. Biggs, M. Wilks, A. Nowacki, J.-M. Kendall, A. Ayele, E. Lewi, and H. Eysteinsson (2018), Evidence for cross rift structural controls on deformation and seismicity at a continental rift caldera, *Earth and Planetary Science Letters*, *487*, 190–200, doi:10.1016/j.epsl.2018.01.037.

Lombardi, S., and N. Voltattorni (2010), Rn, He and CO2 soil gas geochemistry for the study of active and inactive faults, *Applied Geochemistry*, *25*(8), 1206–1220, doi:10.1016/j.apgeochem.2010.05.006.

Lorenzo Pulido, C. D. (2008), Borehole Geophysics and Geology of Well H-43 , Los Humeros Geothermal Field , Puebla , México, *Geothermal training program, Iceland*, (23).

Lucci, F., F. Carrasco-Núñez, G., Rossetti, T. Theye, J. C. White, S. Urbani, H. Azizi, Y. Asahara, and G. Giordano (2019), Anatomy of the magmatic plumbing system of Los Humeros Caldera (Mexico): implications for geothermal systems, *Solid Earth Discuss., in review*, doi:https://doi.org/10.5194/se-2019-86.

Lund, J. W., and A. N. Toth (2020), Direct Utilization of Geothermal Energy 2020 Worldwide Review, in *Proceedings World Geothermal Congress 2020 Reykjavik, Iceland, April 26 – May 2, 2020*, pp. 1–39.

Maguire, P., et al. (2006), Crustal structure of the northern main ethiopian rift from the eagle controlled-source survey; a snapshot of incipient lithospheric break-up, *Geological Society, London, Special Publications*, *259*, doi:10.1144/GSL.SP.2006.259.01.21.

Mahon, W. A. (1970), Chemistry in the exploration and exploitation of hydrothermal systems, *Geothermics*, *2*, 1310–1322, doi:10.1016/0375-6505(70)90449-9.

Martínez-Serrano, R. G. (2002), Chemical variations in hydrothermal minerals of the Los Humeros geothermal system, Mexico, *Geothermics*, *31*(5), 579–612, doi:10.1016/S0375-6505(02)00015-9.

Marty, B., and L. Zimmermann (1999), Volatiles (He, C, N, Ar) in mid-ocean ridge basalts: Assesment of shallow-level fractionation and characterization of source composition, *Geochimica et Cosmochimica Acta*, *63*(21), 3619–3633, doi:10.1016/S0016-7037(99)00169-6.

Mason, E., M. Edmonds, and A. V. Turchyn (2017), Remobilization of crustal carbon may dominate volcanic arc emissions, *Science*, *294*(July), 290–294, doi:10.1126/science.aan5049.

Mazot, A., A. Rae, A. Jentsch, and K. Britten (2019), Testing the tunable diode laser system in extreme environments: Measuring high and low CO 2 concentrations in both active volcanic and geothermal settings, *Journal of Volcanology and Geothermal Research*, *376*, 1–14, doi:10.1016/j.jvolgeores.2019.03.011.

Moeck, I. S. (2014), Catalog of geothermal play types based on geologic controls, *Renewable and Sustainable Energy Reviews*, *37*, 867–882, doi:10.1016/j.rser.2014.05.032.

Mohr, P. A. (1967), Major volcano–tectonic lineament in the ethiopian rift system, *Nature*, *213*, doi:10.1038/213664a0.

Molin, P., and G. Corti (2015), Topography, river network and recent fault activity at the margins of the central main ethiopian rift (east africa), *Tectonophysics*, *664*, doi:10.1016/j.tecto.2015.08.045.

Mörner, N.-A., and G. Etiope (2002), Carbon degassing from the lithosphere, *Global and Planetary Change*, *33*(1-2), 185–203, doi:10.1016/S0921-8181(02)00070-X.

Muffler, P., and R. Cataldi (1978), Methods for regional assessment of geothermal resources, *Geothermics*, *7*(2-4), 53–89, doi:10.1016/0375-6505(78)90002-0.

Nairn, I., and B. Houghton (1989), Formation of collapse craters and morphological changes in the main crater of White Island volcano during the 1976-82 eruption sequence, *N. Z. Geol. Surv. Bull.*, *103*, 25–34.

Nairn, I. A., J. W. Hedenquist, P. Villamor, K. R. Berryman, and P. A. Shane (2005), The ˜AD1315 Tarawera and Waiotapu eruptions, New Zealand: contemporaneous rhyolite and hydrothermal eruptions driven by an arrested basalt dike system?, *Bulletin of Volcanology*, *67*(2), 186–193, doi:10.1007/s00445-004-0373-7.

Neri, M., E. Ferrera, S. Giammanco, G. Currenti, R. Cirrincione, G. Patanè, and V. Zanon (2016), Soil radon measurements as a potential tracer of tectonic and volcanic activity, *Scientific Reports*, *6*(1), 24,581, doi:10.1038/srep24581.

Nicholson, K. (1993), *Geothermal Fluids*, 268 pp., Springer Berlin Heidelberg, Berlin, Heidelberg, doi:10.1007/978-3-642-77844-5.

Niedermann, S., W. Bach, and J. Erzinger (1997), Noble gas evidence for a lower mantle component in MORBs from the southern East Pacific Rise: Decoupling of helium and neon isotope systematics, *Geochimica et Cosmochimica Acta*, *61*(13), 2697–2715, doi:10.1016/S0016-7037(97)00102-6.

Noack, K. (1998), Control of gas emissions in underground coal mines, *International Journal of Coal Geology*, *35*(1-4), 57–82, doi:10.1016/S0166-5162(97)00008-6.

Norini, G., G. Groppelli, R. Sulpizio, G. Carrasco-Núñez, P. Dávila-Harris, C. Pellicioli, F. Zucca, and R. De Franco (2015a), Structural analysis and thermal remote sensing of the Los Humeros Volcanic Complex: Implications for volcano structure and geothermal exploration, *Journal of Volcanology and Geothermal Research*, *301*, 221–237, doi:10.1016/j.jvolgeores.2015.05.014.

Norini, G., G. Groppelli, R. Sulpizio, C.-N. nez, P. G., Dávila-Harris, C. Pellicioli, F. Zucca, and R. De Franco (2015b), Structural analysis and thermal remote sensing of the Los Humeros Volcanic Complex: Implications for volcano structure and geothermal exploration, *Journal of Volcanology and Geothermal Research*, *301*, 221–237, doi:10.1016/j.jvolgeores.2015.05.014.

Norini, G., et al. (2019), The structural architecture of the Los Humeros volcanic complex and geothermal field, *Journal of Volcanology and Geothermal Research*, *381*, 312–329, doi:https://doi.org/10.1016/j.jvolgeores.2019.06.010.

Notsu, K., S. Nakai, G. Igarashi, J. Ishibashi, T. Mori, M. Suzuki, and H. Wakita (2001), Spatial distribution and temporal variation of 3He/4He in hot spring gas released from Unzen volcanic area, Japan, *Journal of Volcanology and Geothermal Research*, *111*, 89–98.

Nowacki, A., M. Wilks, J.-M. Kendall, J. Biggs, and A. Ayele (2018), Characterising hydrothermal fluid pathways beneath aluto volcano, main ethiopian rift, using shear wave splitting, *Journal of Volcanology and Geothermal Research*, *356*, doi:10.1016/j.jvolgeores.2018.03.023.

Obermann, A., T. Kraft, E. Larose, and S. Wiemer (2015), Potential of ambient seismic noise techniques to monitor the St. Gallen geothermal site (Switzerland), *Journal of Geophysical Research: Solid Earth*, *120*(6), 4301–4316, doi:10.1002/2014JB011817.

Oliveira, S., F. Viveiros, C. Silva, and J. E. Pacheco (2018), Automatic filtering of soil CO2 flux data; different statistical approaches applied to long time series, *Frontiers in Earth Science*, *6*(208), 1–14, doi:10.3389/feart.2018.00208.

Oppenheimer, C., T. Fischer, and B. Scaillet (2014), Volcanic Degassing: Process and Impact, in *Treatise on Geochemistry*, vol. 4, edited by H. Holland and K. Turekian, 2 ed., chap. 4.4, pp. 111–179, Elsevier, Amsterdam, doi:10.1016/B978-0-08-095975-7.00304-1.

Ozima, M. and Podosek, F. A. (2002), *Noble gas geochemistry.*, 2nd ed., 286 pp., Cambridge University Press, United Kingdom.

PADRON, E., G. MELIAN, R. MARRERO, D. NOLASCO, J. BARRANCOS, G. PADILLA, P. A. HERNANDEZ, and N. M. PEREZ (2008), Changes in the Diffuse CO 2 Emission and Relation to Seismic Activity in and around El Hierro , Canary Islands, *Pure and Applied Geophysics*, *165*, 95–114, doi:10.1007/s00024-007-0281-9.

Parisio, F., V. Vilarrasa, W. Wang, O. Kolditz, and T. Nagel (2019), The risks of long-term re-injection in supercritical geothermal systems, *Nature Communications*, *10*(4391), doi:10.1038/s41467-019-12146-0.

Parkinson, K. . J. . (1981), An improved method for measuring soil respiration in the field, *Journal of Applied Ecology*, *18*(1), 221–228.

Parks, M. M., S. Caliro, G. Chiodini, D. M. Pyle, T. A. Mather, K. Berlo, M. Edmonds, J. Biggs, and P. Nomikou (2013), Distinguishing contributions to diffuse CO2 emissions in volcanic areas from magmatic degassing and thermal decarbonation using soil gas Rn – δ13C systematics : Application to Santorini volcano, Greece, *Earth and Planetary Science Letters*, *377-378*, 180–190, doi:10.1016/j.epsl.2013.06.046.

Pedone, M., A. Aiuppa, G. Giudice, F. Grassa, C. Cardellini, G. Chiodini, and M. Valenza (2014a), Volcanic CO2 flux measurement at Campi Flegrei by tunable diode laser absorption spectroscopy, *Bulletin of Volcanology*, *76*(4), 812, doi:10.1007/s00445-014-0812-z.

Pedone, M., A. Aiuppa, G. Giudice, F. Grassa, V. Francofonte, B. Bergsson, and E. Ilyinskaya (2014b), Tunable diode laser measurements of hydrothermal/volcanic CO2 and implications for the global CO2 budget, *Solid Earth*, *5*(2), 1209–1221, doi:10.5194/se-5-1209-2014.

Pedone, M., F. Viveiros, A. Aiuppa, G. Giudice, F. Grassa, A. L. Gagliano, V. Francofonte, and T. Ferreira (2015), Total (fumarolic + diffuse soil) CO2 output from Furnas volcano, *Earth, Planets and Space*, *67*(1), 174, doi:10.1186/s40623-015-0345-5.

Peiffer, L., R. Bernard-Romero, A. Mazot, Y. A. Taran, M. Guevara, and E. Santoyo (2014), Fluid geochemistry and soil gas fluxes (CO2-CH4-H2S) at a promissory Hot Dry Rock Geothermal System: The Acoculco caldera, Mexico, *Journal of Volcanology and Geothermal Research*, *284*, 122–137, doi:10.1016/j.jvolgeores.2014.07.019.

Peiffer, L., C. Wanner, and L. Pan (2015), Numerical modeling of cold magmatic CO2 flux measurements for the exploration of hidden geothermal systems, *Journal of Geophysical Research: Solid Earth*, *120*(10), 6856–6877, doi:10.1002/2015JB012258.

Peiffer, L., G. Carrasco-Núñez, A. Mazot, R. E. Villanueva-Estrada, C. Inguaggiato, R. Bernard Romero, R. Rocha Miller, and J. Hernández Rojas (2018), Soil degassing at the Los Humeros geothermal field (Mexico), *Journal of Volcanology and Geothermal Research*, *356*, 163–174, doi:10.1016/j.jvolgeores.2018.03.001.

Pérez-Campos, X., et al. (2008), Horizontal subduction and truncation of the Cocos Plate beneath central Mexico, *Geophysical Research Letters*, *35*(18), 1–6, doi:10.1029/2008GL035127.

Pinti, D. L., Y. Gelinas, A. M. Moritz, M. Larocque, and Y. Sano (2016), Anthropogenic and natural methane emissions from a shale gas exploration area of Quebec, Canada, *Science of the Total Environment*, *566-567*, 1329–1338, doi:10.1016/j.scitotenv.2016.05.193.

Pinti, D. L., M. C. Castro, A. Lopez-Hernandez, G. Han, O. Shouakar- Stash, C. M. Hall, and M. Ramírez-Montes (2017), Fluid circulation and reservoir conditions of the Los Humeros Geothermal Field (LHGF), Mexico, as revealed by a noble gas survey, *Journal of Volcanology and Geothermal Research*, *333-334*(January 2015), 104–115, doi:10.1016/j.jvolgeores.2017.01.015.

Pistone, S., R. Stacey, and R. Horne (2011), The significance of CO2 Solubility in Geothermal Reservoirs, in *PROCEEDINGS, Thirty-Sixth Workshop on Geothermal Reservoir Engineering Stanford University, Stanford, California*.

Portugal, E., M. Verma, R. Barragán, and A. Mañón (1994), Geoquímica isotópica de 13C, D, y 18Ode fluidos del sistema geotérmico Los Humeros Puebla (México), *Geofis. Int.*, *33*, 607–618.

Prol-Ledesma, R. (1998), Pre- and post-exploitation variations in hydrothermal activity in Los Humeros geothermal field, Mexico, *Journal of Volcanology and Geothermal Research*, *83*, 313–333.

Prol-Ledesma, R. M., and P. R. L. Browne (1988), Fluid inclusion analysis in core samples from the Los Humeros geothermal field, Mexico., *Geothermal Resources Council Transactions*, *12*, 197–202.

Raich, J., and A. Tufekcioglu (2000), Vegetation and Soil Respiration: Correlations and Controls, *Biogeochemistry*, *48*(1), 71–90, doi:https://doi.org/10.1023/A:1006112000616.

Rango, T., R. Petrini, B. Stenni, G. Bianchini, F. Slejko, L. Beccaluva, and T. Ayenew (2010), The dynamics of central main ethiopian rift waters: Evidence from δd, δ18o and 87sr/86sr ratios, *Applied Geochemistry*, *25*, doi:10.1016/j.apgeochem.2010.10.001.

Regmi, B. P., and M. Agah (2018), Micro gas chromatography: An overview of critical components and their integration, *Analytical Chemistry*, *90*(22), 13,133–13,150, doi:10.1021/acs.analchem.8b01461, pMID: 30359512.

Reth, S., M. Reichstein, and E. Falge (2005), The effect of soil water content, soil temperature, soil pH-value and the root mass on soil CO2 efflux - A modified model, *Plant and Soil*, *268*(1), 21–33, doi: 10.1007/s11104-005-0175-5.

Richard, L., D. L. Pinti, J. F. Hélie, A. L. Hernández, T. Shibata, M. C. Castro, Y. Sano, O. Shouakar-Stash, and F. Sandoval-Medina (2019), Variability of deep carbon sources in Mexican geothermal fluids, *Journal of Volcanology and Geothermal Research*, *370*, 1–12, doi:10.1016/j.jvolgeores.2018.11.026.

Rinaldi, A. P., J. Vandemeulebrouck, M. Todesco, and F. Viveiros (2012), Effects of atmospheric conditions on surface diffuse degassing, *Journal of Geophysical Research*, *117*(September), 1–14, doi:10.1029/2012JB009490.

Rissmann, C., B. Christenson, C. Werner, M. Leybourne, J. Cole, and D. Gravley (2012), Surface heat flow and CO2 emissions within the Ohaaki hydrothermal field, Taupo Volcanic Zone, New Zealand, *Applied Geochemistry*, *27*(1), 223–239, doi:10.1016/j.apgeochem.2011.10.006.

Rissmann, C., et al. (2011), Fluid flow associated with silicic lava domes and faults, Ohaaki hydrothermal field, New Zealand, *Journal of Volcanology and Geothermal Research*, *204*(1-4), 12–26, doi:10.1016/j.jvolgeores.2011.05.002.

Rodríguez, F., et al. (2015), Surface geochemical and geophysical studies for geothermal exploration at the southern volcanic rift zone of Tenerife, Canary Islands, Spain, *Geothermics*, *55*, 195–206, doi:10.1016/j.geothermics.2015.02.007.

Rossetti, F., L. Aldega, F. Tecce, F. Balsamo, A. Billi, and M. Brilli (2011), Fluid flow within the damage zone of the Boccheggiano extensional fault (Larderello–Travale geothermal field, central Italy): structures, alteration and implications for hydrothermal mineralization in extensional settings, *Geological Magazine*, *148*(4), 558–579, doi:10.1017/s001675681000097x.

Rowland, J. V., and R. H. Sibson (2001), Extensional fault kinematics within the Taupo Volcanic Zone, New Zealand: Soft-linked segmentation of a continental rift system, *New Zealand Journal of Geology and Geophysics*, *44*(2), 271–283, doi:10.1080/00288306.2001.9514938.

Rowland, J. V., and R. H. Sibson (2004), Structural controls on hydrothermal flow in a segmented rift system, Taupo Volcanic Zone, New Zealand, *Geofluids*, *4*(4), 259–283, doi:10.1111/j.1468-8123.2004.00091.x.

Rowland, J. V., and S. F. Simmons (2012), Hydrologic, Magmatic, and Tectonic Controls on Hydrothermal Flow, Taupo Volcanic Zone, New Zealand: Implications for the Formation of Epithermal Vein Deposits, *Economic Geology*, *107*(3), 427–457, doi:10.2113/econgeo.107.3.427.

Sabbarese, C., et al. (2020), Continuous radon monitoring during seven years of volcanic unrest at Campi Flegrei caldera (Italy), *Scientific Reports*, *10*(1), 1–10, doi:10.1038/s41598-020-66590-w.

Saemundsson, K. (2016), Geothermal systems in global perspective, *Short Course I on Exploration and Development of Geothermal Resources*, pp. 1–12.

Saibi, H., E. Aboud, and S. Ehara (2012), Analysis and interpretation of gravity data from the aluto-langano geothermal field of ethiopia, *Acta Geophysica*, *60*, doi:10.2478/s11600-011-0061-x.

Samrock, F., A. Kuvshinov, J. Bakker, A. Jackson, and S. Fisseha (2015), 3-D analysis and interpretation of magnetotelluric data from the Aluto-Langano geothermal field, Ethiopia, *Geophysical Journal International*, *202*(3), 1923–1948, doi:10.1093/gji/ggv270.

Samrock, F., A. V. Grayver, H. Eysteinsson, and M. O. Saar (2018), Magnetotelluric Image of Transcrustal Magmatic System Beneath the Tulu Moye Geothermal Prospect in the Ethiopian Rift, *Geophysical Research Letters*, *45*(23), doi:10.1029/2018GL080333.

Sano, Y., and T. P. Fischer (2013), *The Analysis and Interpretation of Noble Gases in Modern Hydrothermal Systems*, pp. 249–317, Springer Berlin Heidelberg, Berlin, Heidelberg, doi:10.1007/978-3-642-28836-4_10.

Sano, Y., and H. Wakita (1985), Geographical distribution of 3He/4He ratios in Japan: implications for arc tectonics and incipient magmatism., *Journal of Geophysical Research*, *90*(B10), 8729–8741, doi:10.1029/JB090iB10p08729.

Sanyal, S. K. (2005), Classification of Geothermal Systems- A Possible Scheme, in *Thirtieth Workshop on Geothermal Reservoir Engineering, Stanford University*, pp. 1–8.

Saria, E., E. Calais, D. S. Stamps, D. Delvaux, and C. J. H. Hartnady (2014), Present-day kinematics of the east african rift, *Journal of Geophysical Research: Solid Earth*, *119*, doi:10.1002/2013JB010901.

Schön, J. H. (2015), Chapter 9 - Thermal Properties, in *Physical Properties of Rocks*, *Developments in Petroleum Science*, vol. 65, edited by J. H. Schön, pp. 369–414, Elsevier, doi:https://doi.org/10.1016/B978-0-08-100404-3.00009-3.

Scott, S., T. Driesner, and P. Weis (2015), Geologic controls on supercritical geothermal resources above magmatic intrusions, *Nature Communications*, *6*, 1–6, doi:10.1038/ncomms8837.

Sharp, Z. D. (2017), *Principles of stable isotope geochemistry 2nd Edition*, 385 pp., doi:10.5072/FK2GB24S9F.

Sibson, R. H. (1996), Structural permeability of fluid-driven fault-fracture meshes, *Journal of Structural Geology*, *18*(8), 1031–1042, doi:10.1016/0191-8141(96)00032-6.

Sigurdsson, H., B. Houghton, S. McNutt, H. Rymer, and J. Stix (2015), in *The Encyclopedia of Volcanoes*, edited by H. Sigurdsson, 2nd ed., p. 1393, Academic Press, Amsterdam, doi:10.1016/B978-0-12-385938-9.12001-2.

Siler, D. L., and J. D. Pepin (2021), 3-d geologic controls of hydrothermal fluid flow at brady geothermal field, nevada, usa, *Geothermics*, *94*, 102,112, doi:https://doi.org/10.1016/j.geothermics.2021.102112.

Siler, D. L., N. H. Hinz, and J. E. Faulds (2018), Stress concentrations at structural discontinuities in active fault zones in the western United States: Implications for permeability and fluid flow in geothermal fields, *Geological Society of America Bulletin*, *130*(7), 1273–1288.

Sinclair, A. J. (1974), Selection of threshold values in geochemical data using probability graphs, *Journal of Geochemical Exploration*, *3*(2), 129–149, doi:10.1016/0375-6742(74)90030-2.

Sorey, M. L. (1985), Evolution and present state of the hydrothermal system in Long Valley Caldera, *Journal of Geophysical Research*, *90*, 11,219–11,228.

Stagpoole, V. M., and H. M. Bibby (1998), Electrical resistivity map of the Taupo Volcanic Zone, New Zealand, nominal array spacing 500 m, 1: 250,000, version 1.0, *Institute of Geological & Nuclear Sciences Geophysical Map*, *11*.

Stefansson, V. (1997), Geothermal reinjection experience, *Geothermics*, *26*(1), 99–139.

Stelling, P., L. Shevenell, N. Hinz, M. Coolbaugh, G. Melosh, and W. Cumming (2016), Geothermal systems in volcanic arcs : Volcanic characteristics and surface manifestations as indicators of geothermal potential and favorability worldwide, *Journal of Volcanology and Geothermal Research*, *324*, 57–72, doi:10.1016/j.jvolgeores.2016.05.018.

Stewart, M. K. (1994), Groundwater contributions to Waikite geothermal fluids, in *16th New Zealand Geothermal Workshop*, pp. 109–114.

Stimac, J., F. Goff, and C. J. Goff (2015), Chapter 46 - intrusion-related geothermal systems, in *The Encyclopedia of Volcanoes*, edited by H. Sigurdsson, 2nd ed. ed., pp. 799–822, Academic Press, Amsterdam, doi:https://doi.org/10.1016/B978-0-12-385938-9.00046-8.

Stober, I., and K. Bucher (2013), *Geothermal Energy: From Theoretical Models to Exploration and Development*, 291 pp., Springer-Verlag Berlin Heidelberg, doi:10.1007/978-3-642-13352-7.

Suñe-Puchol, I., et al. (2019), The Ilopango caldera complex, El Salvador: Origin and early ignimbrite-forming eruptions of a graben/pull-apart caldera structure, *Journal of Volcanology and Geothermal Research*, *371*, 1–19, doi:10.1016/j.jvolgeores.2018.12.004.

Talwani, P., L. Chen, and K. Gahalaut (2007), Seismogenic permeability, ks, *Journal of Geophysical Research: Solid Earth*, *112*(7), doi:10.1029/2006JB004665.

Tamburello, G., S. Pondrelli, G. Chiodini, and D. Rouwet (2018), Global-scale control of extensional tectonics on CO 2 earth degassing, *Nature Communications*, *9*(1), doi:10.1038/s41467-018-07087-z.

Taussi, M., B. Nisi, M. Pizarro, D. Morata, E. A. Veloso, G. Volpi, O. Vaselli, and A. Renzulli (2019), Sealing capacity of clay-cap units above the Cerro Pabellón hidden geothermal system (northern Chile) derived by soil CO2 flux and temperature measurements, *Journal of Volcanology and Geothermal Research*, *384*, 1–14, doi:10.1016/j.jvolgeores.2019.07.009.

Taussi, M., B. Nisi, O. Vaselli, S. Maza, D. Morata, and A. Renzulli (2021), Soil Co2 Flux and Temperature From a New Geothermal Area in the Cordón De Inacaliri Volcanic Complex (Northern Chile), *Geothermics*, *89*(June 2020), 101,961, doi:10.1016/j.geothermics.2020.101961.

Teklemariam, M., S. Battaglia, G. Gianelli, and G. Ruggieri (1996), Hydrothermal alteration in the Aluto-Langano geothermal field, Ethiopia, *Geothermics*, *25*(6), 679–702, doi:10.1016/S0375-6505(96)00019-3.

Toledo, T., E. Gaucher, P. Jousset, A. Jentsch, C. Haberland, H. Maurer, C. Krawczyk, M. Calò, and A. Figueroa (2020a), Local earthquake tomography at the Los Humeros geothermal field in Mexico, *Journal of Geophysical Research - Solid Earth*.

Toledo, T., E. Gaucher, P. Jousset, A. Jentsch, C. Haberland, H. Maurer, C. Krawczyk, M. Calò, and A. Figueroa (2020b), Local earthquake tomography at Los Humeros geothermal field (Mexico), *Journal of Geophysical Research: Solid Earth*, *125*, doi:10.1029/2020JB020390.

Toth, A., and E. Bobok (2017), What Is Geothermal Energy?, in *Flow and Heat Transfer in Geothermal Systems*, pp. 1–19, Elsevier, doi:10.1016/B978-0-12-800277-3.00001-3.

Townend, J., et al. (2017), Petrophysical, Geochemical, and Hydrological Evidence for Extensive Fracture-Mediated Fluid and Heat Transport in the Alpine Fault's Hanging-Wall Damage Zone, *Geochemistry, Geophysics, Geosystems*, *18*(12), 4709–4732, doi:https://doi.org/10.1002/2017GC007202.

Truesdell, A., and J. Quijano (1988), Datos isotópicos de CO2 en la descarga total de pozos en Los Humeros, Pue. Comisión Federal de Electricidad, Reporte Interno 6/88 (5 pp), *Tech. rep.*

Urban, E., and J. Lermo (2017), Fracture and stress evaluation using well logs and microseismicity, in the exploitation of Los Humeros geothermal field, Mexico, *Transactions - Geothermal Resources Council*, *41*, 1756–1780.

Urbani, S., G. Giordano, F. Lucci, F. Rossetti, V. Acocella, G. Carrasco-núñez, S. Roma, and L. S. L. Murialdo (2020), Estimating the depth and evolution of intrusions at resurgent calderas: Los Humeros (Mexico), pp. 527–545.

Valori, A., M. Teklemariam, and G. Gianelli (1992), Evidence of temperature increase of CO2-bearing fluids from Aluto-Langano geothermal field (Ethiopia): a fluid inclusions study of deep wells LA-3 and LA-6, *European Journal of Mineralogy*, *4*(5), 907–920, doi:10.1127/ejm/4/5/0907.

Verma, S. P. (2000), Geochemical Evidence for a Lithospheric Source for Magmas from Acoculco Caldera, Eastern Mexican Volcanic Belt Geochemical Evidence for a Lithospheric Source for Magmas from Acoculco Caldera, Eastern Mexican Volcanic Belt, *Chemical Geology*, *164*, 35–60, doi:10.2747/1938-2839.43.1.51.

Villamor, P., and K. Berryman (2001), A late quaternary extension rate in the Taupo Volcanic Zone, New Zealand, derived from fault slip data, *New Zealand Journal of Geology and Geophysics*, *44*(2), 243–269, doi:10.1080/00288306.2001.9514937.

Viveiros, F., C. Cardellini, T. Ferreira, S. Caliro, G. Chiodini, and C. Silva (2010), Soil CO2 emissions at Furnas volcano, São Miguel Island, Azores archipelago: Volcano monitoring perspectives, geomorphologic studies, and land use planning application, *Journal of Geophysical Research: Solid Earth*, *115*(12), 1–17, doi:10.1029/2010JB007555.

Viveiros, F., T. Ferreira, C. Silva, J. C. Vieira, J. L. Gaspar, G. Virgili, and P. Amaral (2015), Permanent monitoring of soil CO2 degassing at Furnas and Fogo volcanoes (São Miguel Island, Azores), in *Volcanic Geology of S. Miguel Island (Azores archipelago)*, edited by J. L. Gaspar, J. E. Guest, A. M. Duncan, F. J. A. S. Barriga, and D. K. Chester, chap. 20, pp. 271–288, Geological Society London, London, doi: https://doi.org/10.1144/M44.20.

Viveiros, F., G. Chiodini, C. Cardellini, S. Caliro, V. Zanon, C. Silva, A. L. Rizzo, A. Hipólito, and L. Moreno (2020), Deep CO2 emitted at Furnas do Enxofre geothermal area (Terceira Island, Azores archipelago). An approach for determining CO2 sources and total emissions using carbon isotopic data, *Journal of Volcanology and Geothermal Research*, *401*, 106,968, doi:10.1016/j.jvolgeores.2020.106968.

Voltattorni, N., A. Sciarra, and F. Quattrocchi (2010), The Application of Soil-Gas Technique to Geothermal Exploration: Study of Hidden Potential Geothermal Systems, *Proceedings World Geothermal Congress 2015*, (April), 6 p.

Weber, K., et al. (2006), Ground-based remote sensing of gas emissions from Teide volcano (Tenerife, Canary Islands, Spain): first results, in *Remote Sensing of Clouds and the Atmosphere XI*, vol. 6362, edited by J. R. Slusser, K. Schäfer, and A. Comerón, pp. 384–393, International Society for Optics and Photonics, SPIE, doi:10.1117/12.714411.

Werner, C., and C. Cardellini (2006), Comparison of carbon dioxide emissions with fluid upflow, chemistry, and geologic structures at the Rotorua geothermal system, New Zealand, *Geothermics*, *35*(3), 221–238, doi:10.1016/j.geothermics.2006.02.006.

Werner, C., S. L. Brantley, K. Boomer, and A. A (2000), CO2 emissions related to the Yellowstone volcanic system sampling , total degassing , and transport mechanisms diffuse soil fluxes emission rates from thermal vents yr were measured in thermal fluxes observed in most nonthermal regions were similar to val, *Journal of Geophysical Research*, *105*, 10,810–831,846.

West Systems (2019), Portable diffuse flux meter WEST Systems, Handbook, Release 9.1.

Weydt, L. M., et al. (2018), Outcrop analogue study to determine reservoir properties of the Los Humeros and Acoculco geothermal fields , Mexico, *Advances in Geosciences*, (45), 281–287, doi:https://doi.org/10.5194/adgeo-45-281-2018.

Whitehead, N. E. (1984), Geothermal prospecting by ground radon measurements, *Journal of Volcanology and Geothermal Research*, *20*, 213–229.

Widén, B., and H. Majdi (2011), Soil CO2 efflux and root respiration at three sites in a mixed pine and spruce forest: seasonal and diurnal variation, *Canadian Journal of Forest Research*, *31*(5), 786–796, doi:10.1139/x01-012.

Wilks, D. (2006), *Statistical Methods in the Atmospheric Sciences*, 2nd, inter ed., 627 pp., Academic Press.

Wilks, M., J.-M. Kendall, A. Nowacki, J. Biggs, J. Wookey, Y. Birhanu, A. Ayele, and T. Bedada (2017), Seismicity associated with magmatism, faulting and hydrothermal circulation at aluto volcano, main ethiopian rift, *Journal of Volcanology and Geothermal Research*, *340*, doi:10.1016/j.jvolgeores.2017.04.003.

Willcox, P. (2011), Eruptive, magmatic and structural evolution of a large explosive caldera volcano: Los Humeros, Central Mexico, Ph.D. thesis, PhD Thesis, University of Leicester.

Williams, C. F., M. J. Reed, and A. F. Anderson (2011), Updating the Classification of Geothermal Resources, in *Proceedings of 36th workshop on Geothermal Reservoir Engineering, Stanford University*, p. 7.

Wilson, C., B. Houghton, M. McWilliams, M. Lanphere, S. Weaver, and R. Briggs (1995), Volcanic and structural evolution of Taupo Volcanic Zone, New Zealand: a review, *Journal of Volcanology and Geothermal Research*, *68*(1-3), 1–28, doi:10.1016/0377-0273(95)00006-G.

Wohletz, K., and H. Grant (1992), *Volcanology and Geothermal Energy*, 432 pp., Berkeley: University of California Press, Berkeley.

Wyering, L. D., M. C. Villeneuve, I. C. Wallis, P. A. Siratovich, B. M. Kennedy, D. M. Gravley, and J. L. Cant (2014), Mechanical and physical properties of hydrothermally altered rocks, Taupo Volcanic Zone, New Zealand, *Journal of Volcanology and Geothermal Research*, *288*, 76–93, doi:10.1016/j.jvolgeores.2014.10.008.

Yehya, A., and J. R. Rice (2020), Influence of fluid-assisted healing on fault permeability structure, *Journal of Geophysical Research: Solid Earth*, *125*(10), doi:10.1029/2020JB020553.

Younger, P. L. (2014), Missing a trick in geothermal exploration, *Nature Geoscience*, *7*(7), 479–480, doi:10.1038/ngeo2193.

Zhang, Y., P. M. Schaubs, C. Zhao, A. Ord, B. E. Hobbs, and A. C. Barnicoat (2008), Fault-related dilation, permeability enhancement, fluid flow and mineral precipitation patterns: Numerical models, *Geological Society Special Publication*, *299*(January), 239–255, doi:10.1144/SP299.15.

A

Statutory declaration

I declare that I have authored this thesis independently, that I have not used any other than the declared sources, and that I have explicitly marked all the material which has been quoted either literally or by content from the used sources. The thesis has not been submitted to any other examining body and has not been published.

....
Date and signature